A Combined Computational and Experimental Investigation of Polynucleotide Binding Polymers for Therapeutic Applications

by

Deniz Meneksedag Erol

A thesis submitted in partial fulfillment of the requirements for the degree of

Doctor of Philosophy
in
Department of Biomedical Engineering
and
Department of Chemical and Materials Engineering

University of Alberta

Abstract

Polynucleotide binding polymers have a wide range of therapeutic applications including delivery systems for therapeutic polynucleotides, and antithrombotic drugs for extracellular nucleic acid-mediated thrombogenic events. This dissertation explores polynucleotide binding polymers in these two avenues, with combined computational and experimental approaches. Particular emphasis was placed on computational studies to probe structural features of polymers and polymer-polynucleotide complexes at the all-atom level. The first line of studies in this dissertation explored polymers employed in the delivery of short interfering RNA (siRNA), a synthetic polynucleotide capable of silencing the overly-expressed genes in malignant cells. Particularly, polymer design and dynamics of polymer-siRNA complex formation, structural features of polymer-siRNA complexes for enhanced functional performance, and the effect of anionic substances of the physiological milieu on polymer-siRNA complex integrity were investigated. The results demonstrated that there exists a hydrophobic-hydrophilic balance in designing siRNA delivery systems, determining the functional performance of the resulting complexes. Polymer-siRNA complexes were found to accommodate the presence of other polynucleotides in their periphery without losing their integrity; however, they experienced a vast variety of conformational states in the presence of heparin, a sulfated glycosaminoglycan found on cell membrane and extracellular milieu. Our efforts to investigate the polynucleotide binding polymers designed to arrest the prothrombotic activity of DNA revealed the importance of polymer structural design; self-interacting polymers exhibited poor DNA binding, which could be detrimental for their functional antithrombotic performance. This dissertation demonstrated the proof-of-concept for employing computational

approaches in conjunction with experimental studies where applicable, in efforts to develop "better" polymer therapeutics for different applications.

Preface

Parts of this thesis have been previously published, as described below. Thus, their structures are mostly maintained; i.e., each chapter has its own introduction, methods, results, discussion, and references, and abbreviations are defined at their first appearance. Specific acknowledgements are provided within each chapter.

Chapter 2 includes portions from a previously published review paper and a book chapter. A major part is adapted from the review paper Meneksedag-Erol D, Tang T, & Uludağ H (2014) Molecular Modeling of Polynucleotide Complexes. *Biomaterials* 35: 7068-7076. As the first author, I was responsible for concept formation, conducting the literature review and writing the manuscript. Dr. Tian Tang and Dr. Hasan Uludağ were the supervisory authors who were involved in concept formation and revision of the manuscript. Some sections of Chapter 2 were adapted from the book chapter Meneksedag-Erol D**,** Sun C, Tang T, & Uludağ H (2014) Molecular Dynamics Simulations of Polyplexes and Lipoplexes Employed in Gene Delivery. *Intracellular Delivery II, Fundamental Biomedical Technologies,* eds Prokop A, Iwasaki Y, Harada A (Springer Netherlands), Vol 7, pp 277-311. As the primary author, I was responsible for concept formation, conducting the literature review, and writing the manuscript. Dr. Chongbo Sun contributed to manuscript revision. Dr. Tian Tang and Dr. Hasan Uludağ were the supervisory authors who were involved in concept formation and revision of the manuscript.

A version of **Chapter 3** of this thesis has been published as Meneksedag-Erol D, KC RB, Tang T, & Uludağ H (2015) A Delicate Balance When Substituting a Small Hydrophobe onto Low Molecular Weight Polyethylenimine to Improve Its Nucleic Acid Delivery Efficiency. *ACS Appl. Mater. Interfaces* 7: 24822−24832. As the primary author, I was responsible for concept formation, conducting the molecular simulations, data analysis, assisting the *in vitro*

experimental studies, and writing the manuscript. Dr. Remant Bahadur KC performed the synthesis and characterization of the polymers, prepared the cell culture, helped with *in vitro* experimental studies; and edited part of the manuscript on the experimental studies. Dr. Tian Tang and Dr. Hasan Uludağ were the supervisory authors who contributed to concept formation, checked the accuracy of the results, and revised the manuscript.

A version of **Chapter 4** of this thesis has been published as Meneksedag-Erol D, Tang T, & Uludağ H (2015) Probing the Effect of miRNA on siRNA−PEI Polyplexes. *J. Phys. Chem. B* 119: 5475−5486. I was responsible of conducting the molecular simulations and physicochemical studies, analyzing the data, and writing the manuscript. Dr. Tian Tang and Dr. Hasan Uludağ were the supervisory authors who contributed to concept formation, checked the accuracy of the results, and revised the manuscript.

Chapter 6 will be submitted for publication as Meneksedag-Erol D, Tang T, & Uludağ H, Mechanistic Insights into the Role of Glycosaminoglycans in Delivery of Polymeric Nucleic Acid Nanoparticles by Molecular Dynamics Simulations. **Chapter 5** constitutes some of the supporting information to this future paper. The restrained electrostatic potential charges from quantum mechanical calculations in Chapter 5 was carried out by Dr. Morteza Chehel Amirani.

The research conducted for **Chapter 7** is part of a research collaboration with Dr. Jayachandran N. Kizhakkedathu (Department of Chemistry, Center for Blood Research and Department of Pathology and Laboratory Medicine, University of British Columbia), under NSERC Collaborative Research and Training Experience Program for Regenerative Medicine (NCPRM). The data presented in this chapter will be included in a future paper.

Chapter 8 includes revised versions of the future perspectives/studies sections from the two papers described above, Meneksedag-Erol D *et al*. (2014) *Biomaterials* 35: 7068-7076, and

Meneksedag-Erol D *et al.* (2015) *J. Phys. Chem. B* 119: 5475−5486, in addition to the original discussion written on the basis of the research conducted in this dissertation.

Acknowledgements

I have had the privilege of working with distinguished academics and wonderful colleagues during my PhD program, and I would like to take this opportunity to express my gratitude for their involvement in my personal and professional development. First of all, I would like to thank my supervisors, Dr. Tian Tang and Dr. Hasan Uludağ, for guiding me with their expertise, supporting me through challenging tasks, and helping me grow as an independent researcher and instructor. I couldn't be more grateful to have them as my mentors in this academic journey.

I would like to thank our collaborator, Dr. Jayachandran N. Kizhakkedathu, for giving me the opportunity to expand my knowledge in the new avenues of polymer science, and for his help and insightful discussions.

I also would like to acknowledge the financial support from NSERC Collaborative Research and Training Experience Program for Regenerative Medicine (NCPRM), and DB Robinson Graduate Scholarship in Chemical and Materials Engineering.

Special thanks to Dr. Laura Rose for her help and encouragement in the beginning of my PhD program, and Dr. Chongbo Sun for passing on his knowledge in modeling studies. Many thanks to Dr. Morteza Chehel Amirani for his help in the molecular model development with quantum mechanical level calculations, and Dr. Remant Bahadur KC for mentoring me in the experimental studies. I also would like to thank my friends and colleagues in Tang and Uludağ research groups for insightful scientific discussions, and for their support and encouragement.

I would like to dedicate this thesis to the memory of my mother, Nesrin Meneksedag (1958-1995). From the bottom of my heart, I am thankful to my grandmother, Yuksel Meneksedag, the wonderful woman who raised me into the person I am today, and my husband, Fatih Erol, for their endless love and support. Without them, none of this would have been possible.

Table of Contents

List of Tables

List of Figures

List of Abbreviations

AA	All-atom
CG	Coarse-grained
CGENFF	CHARMM General Force Field
CME	Clathrin-mediated endocytosis
CML	Chronic myeloid leukemia
COM	Center of mass
CS	Chondroitin sulfate
CvME	Caveolae/raft-mediated endocytosis
DAP	1,3-diaminopropane
DAPMA	N,N-di-(3-aminopropyl)-N-(methyl)amine
DFT	Density functional theory
DMPC	Dimyristoylphosphatidylcholine
DMSO	Dimethyl sulfoxide
DMTAP	Dimyristoyltrimethylammonium propane
DOPE	1,2-dioleoyl-sn-glycero-3-phosphoethanolamine
DPD	Dissipative particle dynamics
DPPE	1,2-dipalmitoyl-sn-glycero-3-phosphoethanolamine
DS	Dermatan sulfate
dsRNA	double-stranded RNA
EDC	N-(3-dimethylaminopropyl)-N′-ethylcarbodiimide hydrochloride
EMSA	Electrophoresis mobility shift assays
FF	Force field
GAG	Glycosaminoglycan
GFP	Green fluorescent protein
GlcA	β-D-glucuronic acid
GlcN	D-glucosamine
GlcNS(6S)	N,O6-disulfo-glucosamine
HA	Hyaluronic acid
HMW	High molecular weight
HS	Heparan sulfate
IdoA	α-L-iduronic acid
IdoA2S	2-O-sulfo-alpha-L-idopyranuronic acid
KS	Keratan sulfate
LMW	Low molecular weight
MC	Monte Carlo
Mcl-1	Myeloid cell leukemia 1
MD	Molecular dynamics
MFI	Mean fluorescence intensity

miRNA	microRNA
miR-21	miRNA-21
MM	Molecular mechanics
MM-PBSA	Molecular Mechanics Poisson-Boltzmann Surface Area
MTT	3-(4,5-dimethylthiazol-2-yl)-2,5-diphenyl-tetrazolium bromide
MW	Molecular weight
NA	Nucleic acid
NHS	N-hydroxysuccinimide
NMR	Nuclear magnetic resonance
PAMAM	Polyamidoamine
PBC	Periodic boundary conditions
PC	Phosphatidylcholine
PDB	Protein data bank
PEI	Polyethylenimine
PG	Proteoglycan
PLL	Poly-L-lysine
PME	Particle mesh Ewald
PMF	Potential of mean force
PrA	Propionic acid
QM	Quantum mechanics
R_g	Radius of gyration
RISC	RNA-induced silencing complex
RMSD	Root mean square deviation
RNAi	RNA interference
siRNA	short interfering RNA
US	Umbrella sampling
WHAM	Weighted histogram analysis method

1. Introduction: Scope of the Dissertation

"Polymer therapeutics", i.e., polymers employed as pharmaceuticals in the form of drugs, conjugates, or supramolecular assemblies [1], have been under the spotlight in laboratorial and clinical settings, in efforts to develop versatile platforms for the treatment of a wide range of diseases. Much attention has been paid for designing polymer therapeutics for cancer treatment [2], mainly as delivery vehicles for polynucleotide cargos to correct defective genes (DNA delivery) or silence the aberrantly expressed genes (short interfering RNA (siRNA) delivery) in malignant cells [3]. Multifaceted ability of polymeric materials to bind to polynucleotides opened new avenues for therapeutic applications; recent studies have shown the potential of cationic polymers to act as safe antithrombotics, by neutralizing the exposed polynucleotides [4-6]. This dissertation aims at exploring polynucleotide binding polymers employed in the treatment of cancer and cancer associated thrombosis, with a particular focus on (*i*) cationic polymer – siRNA nanoparticles as cancer therapeutics, and (*ii*) cationic polymers as antithrombotics against DNA-mediated activation of blood coagulation. A combined computational and experimental approach is adopted, with a major emphasis on computational studies, to provide insights into the structural and compositional features of the polymers/polymer-polynucleotide complexes from an atomistic perspective. Experiments were carried out on siRNA nanoparticulate systems either to explore their physicochemical properties or to test their functional performance.

The work described in this dissertation starts with a comprehensive review of the molecular simulation studies performed on polynucleotide complexes in **Chapter 2**. Particularly, the studies investigating polymeric carrier–polynucleotide complexation, condensation, and aggregation; as well as nanoparticle intracellular trafficking are presented. The current progress in the field shows a major focus on the design of polymeric carriers and their complexation

mechanisms, while questions surrounding the integrity of nanoparticles in the subsequent stages of their delivery remain to be addressed. The existing knowledge gaps constitute the motivation for the following chapters exploring polymeric siRNA nanoparticles.

Chapter 3 investigates systematic modification of an otherwise non-functional low molecular weight polymer with a small hydrophobe for the development of a siRNA delivery system into leukemic cells. The impetus behind the hydrophobic modification of the polymers is to promote cellular uptake of the nanoparticles through hydrophobic attraction to cell membrane. However, systematic investigation is needed for every substituent, as the extent of modification may influence the performance of the delivery system. In this chapter, the synthesized polymers were tested with *in vitro* functional assays, followed by all-atom simulations to explore the effect of hydrophobic modification on nanoparticle formation. The combined approach allowed us to correlate the hydrophilic-hydrophobic balance of nanoparticles with functional performance.

Chapters 4 to **6** explore the integrity of siRNA nanoparticles in the presence of endogenous molecules, as to mimic the environments the siRNA nanoparticles can face along their delivery route. This is a particularly under-studied area from an all-atom simulation perspective, given the current challenges in the atomistic models. **Chapter 4** investigates the influence of an endogenous microRNA molecule on siRNA nanoparticle integrity, with physicochemical studies and all-atom simulations. The work presented in this chapter demonstrated the capability of polymeric siRNA nanoparticles in accommodating anionic substances such as microRNA into their structure without compromising their integrity; however, raised some intriguing questions on how the siRNA nanoparticles are disrupted by other anionic biomolecules such as glycosaminoglycans of the cell membrane milieu. We then directed our efforts to investigate

the mechanisms by which heparin, a sulfated member of the glycosaminoglycan family, acts on the siRNA nanoparticles. **Chapter 5** presents the molecular model development for heparin. Using this model, **Chapter 6** investigates the mechanistic details of heparin-mediated changes in the conformational states of siRNA nanoparticles, with a series of all-atom simulations. This chapter demonstrated that in the presence of heparin, siRNA nanoparticles can visit a number of different conformational states ranging in stability, which can give rise to a variety of therapeutic outcomes.

Polynucleotide binding polymers are explored in the context of a different therapeutic application, namely as antithrombotic drugs, in **Chapter 7**. Extracellular nucleic acids are one of the proposed activators of thrombogenic events [7-9]; and of particular interest to cancer, their level in circulation is elevated in comparison to healthy individuals [10-12]. Inhibiting prothrombotic activity of extracellular nucleic acids with cationic polymers has shown to be a promising, and safer alternative to current antithrombotics [4]. In this chapter, a series of all-atom simulations were performed to monitor and compare DNA binding performance of cationic polymers possessing different architectures, in search for polymer structural features needed for stronger DNA binding. Aside from binding to DNA, there might exist other mechanisms contributing to the therapeutic effect of the polymers *in vivo*; however, our computational approach is expected to give structural insights into polymer design, and help screen different candidates prior to functional testing.

The results presented in this dissertation contributed to our understanding on the design of polynucleotide binding polymers to achieve enhanced stability and performance in the context of two specific therapeutic applications. Our research highlighted potential areas for future consideration, and the challenges in simulating supramolecular assemblies with all-atom

approaches. In **Chapter 8**, we provided overall conclusions and future perspectives for each chapter, and suggested advanced techniques to circumvent the limitations of atomistic simulations.

References

1. Duncan R (2003) The Dawning Era of Polymer Therapeutics. *Nat. Rev. Drug Discov.* 2(5):347-360.
2. Duncan R (2006) Polymer Conjugates as Anticancer Nanomedicines. *Nat. Rev. Cancer* 6(9):688-701.
3. Lachelt U & Wagner E (2015) Nucleic Acid Therapeutics Using Polyplexes: A Journey of 50 Years (and Beyond). *Chem. Rev.* 115(19):11043-11078.
4. Jain S, Pitoc GA, Holl EK, Zhang Y, Borst L, Leong KW, Lee J, & Sullenger BA (2012) Nucleic Acid Scavengers Inhibit Thrombosis Without Increasing Bleeding. *Proc. Natl. Acad. Sci. U.S.A.* 109(32):12938-12943.
5. Smith SA, Choi SH, Collins JN, Travers RJ, Cooley BC, & Morrissey JH (2012) Inhibition of Polyphosphate as a Novel Strategy for Preventing Thrombosis and Inflammation. *Blood* 120(26):5103-5110.
6. Travers RJ, Shenoi RA, Kalathottukaren MT, Kizhakkedathu JN, & Morrissey JH (2014) Nontoxic Polyphosphate Inhibitors Reduce Thrombosis While Sparing Hemostasis. *Blood* 124(22):3183-3190.
7. Renne T, Schmaier AH, Nickel KF, Blomback M, & Maas C (2012) In Vivo Roles of Factor XII. *Blood* 120(22):4296-4303.
8. Kannemeier C, Shibamiya A, Nakazawa F, Trusheim H, Ruppert C, Markart P, Song Y, Tzima E, Kennerknecht E, Niepmann M, von Bruehl ML, Sedding D, Massberg S, Gunther A, Engelmann B, & Preissner KT (2007) Extracellular RNA Constitutes a Natural Procoagulant Cofactor in Blood Coagulation. *Proc. Natl. Acad. Sci. U.S.A.* 104(15):6388-6393.
9. Demers M, Krause DS, Schatzberg D, Martinod K, Voorhees JR, Fuchs TA, Scadden DT, & Wagner DD (2012) Cancers Predispose Neutrophils to Release Extracellular DNA Traps That Contribute to Cancer-associated Thrombosis. *Proc. Natl. Acad. Sci. U.S.A.* 109(32):13076-13081.
10. Leon SA, Shapiro B, Sklaroff DM, & Yaros MJ (1977) Free DNA in the Serum of Cancer Patients and the Effect of Therapy. *Cancer Res.* 37(3):646-650.
11. Kopreski MS, Benko FA, Kwak LW, & Gocke CD (1999) Detection of Tumor Messenger RNA in the Serum of Patients with Malignant Melanoma. *Clin. Cancer Res.* 5(8):1961-1965.

12. Ng EK, Tsui NB, Lam NY, Chiu RW, Yu SC, Wong SC, Lo ES, Rainer TH, Johnson PJ, & Lo YM (2002) Presence of Filterable and Nonfilterable mRNA in the Plasma of Cancer Patients and Healthy Individuals. *Clin. Chem.* 48(8):1212-1217.

2. Molecular Modeling of Polynucleotide Complexes[X]

[X] Versions of sections of this chapter have been published. Adapted from Meneksedag-Erol D, Tang T, & Uludağ H (2014) Molecular Modeling of Polynucleotide Complexes. *Biomaterials* 35: 7068-7076, Copyright (2014), with permission from Elsevier.

[X] Versions of sections of this chapter have been published. Adapted from Meneksedag-Erol D**,** Sun C, Tang T, & Uludağ H (2014) Molecular Dynamics Simulations of Polyplexes and Lipoplexes Employed in Gene Delivery. *Intracellular Delivery II, Fundamental Biomedical Technologies,* eds Prokop A, Iwasaki Y, Harada A (Springer Netherlands), Vol 7, pp 277-311, Copyright (2014), with permission of Springer.

2.1. Introduction

Gene therapy aims to treat a wide range of disorders by altering gene expression with the delivery of genetic materials (polynucleotides). The initial impetus behind gene therapy was the desire to synthesize therapeutic proteins *in situ* with functional DNA expression vectors. Exogenous DNA has to reach the cell nucleus and produce mRNAs for desired proteins by recruiting the appropriate transcription factors. With the discovery of RNA interference (RNAi [1]), the scope of gene therapy was expanded. In RNAi, relatively long double-stranded RNAs (dsRNAs) are cleaved by the enzyme Dicer into short (21-22 nucleotide) RNAs. The guide strand in truncated dsRNAs, after dissociation, gets incorporated into RNA-induced silencing complex (RISC) to identify complementary sequence in mRNAs, leading to mRNA cleavage. The therapeutic use of RNAi relies on short interfering RNAs (siRNAs), synthetic ~22 nucleotide dsRNAs. The challenges in the delivery of polynucleotides, however, have dampened the great interest in DNA and siRNA therapeutics.

The anionic polynucleotides cannot efficiently cross hydrophobic and anionic lipid bilayers of cell membranes. This limitation stimulated design of delivery systems (also known as carriers) to neutralize and compact the polynucleotides. Polynucleotides complexed with cationic polymers and lipids are known as ‘polyplexes’ and ‘lipoplexes’ (Figure 2.1), respectively [2]. Binding of complexes to cell surface is governed by electrostatic interactions between cationic carriers and anionic membrane proteins and/or cell-surface receptors. Endocytosis follows via a variety of mechanisms, such as clathrin- and caveolin-1 independent, clathrin-mediated (CME), caveolae/raft-mediated (CvME) and micropinocytosis [3]. Uptake of the complexes depends on many factors and there have been some contradictory proposals on most effective endocytosis mechanism(s). While some studies proposed CvME to be the most

conducive, others suggested CME as well as macropinocytosis for larger complexes that cannot be trafficked with CvME or CME [4].

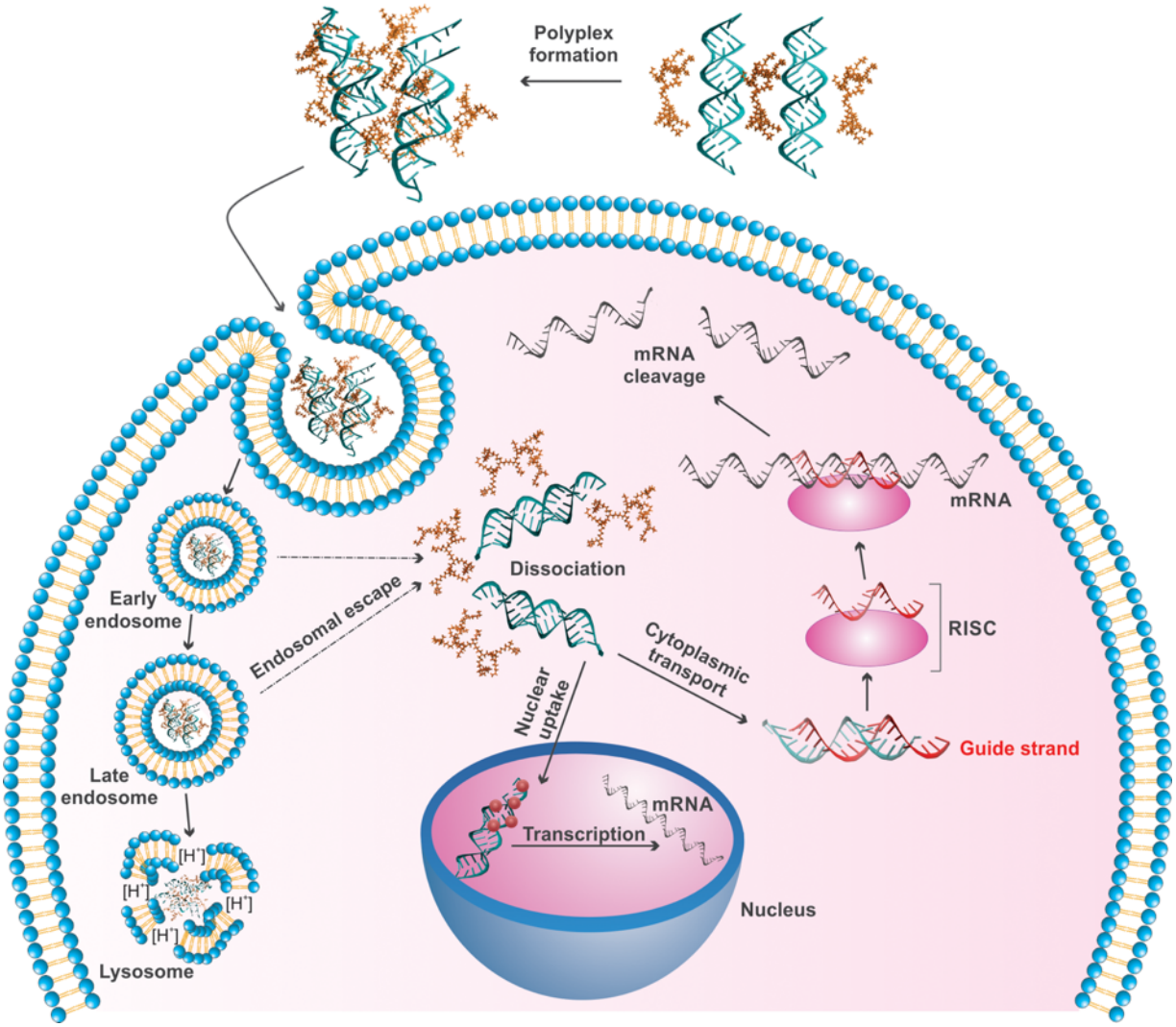

Figure 2.1. Main steps involved in gene delivery.
While siRNA (in red) gets incorporated into RISC in cytosol, DNA gets trafficked to nucleus to recruit transcription factors (represented as red spheres) to produce desired mRNAs.

Intracellular trafficking of complexes starts in early endosomes, which generally fuse into late endosomes (pH~5-6) and lysosomes (pH~4.5). Complexes must efficiently escape into cytosol before lysosomal degradation (Figure 2.1). It is possible to facilitate endosomal escape

by combining polynucleotides with fusogenic ligands, pH-sensitive carriers, and photosensitive agents [5]. Endosomal escape is also possible through 'proton-sponge effect' if the carriers possess H-buffering properties, such as polyethylenimine (PEI) [6]. Upon release into cytoplasm, polynucleotide dissociation takes place and anionic molecules such as cytoplasmic RNA and heparin-like glycosaminoglycans are thought to be involved in this process [7]. After release, DNA has to be trafficked to the nucleus for transcription, and siRNA has to get incorporated into RISC in the cytoplasm to give mRNA cleavage for gene silencing (Figure 2.1).

Many issues related to the mechanism(s) of action of carriers cannot be directly addressed due to instrumental limitations at atomic resolution. Molecular modeling is beginning to be employed to overcome some of these limitations. Via computer simulations, motions of individual or groups of atoms are obtained, and physical properties can be extracted from time average of equilibrated systems. Since the first simulation on a biological macromolecule in 1977 [8], molecular modeling has become a unique tool for analyzing complex biosystems. Features of complexes and critical mechanisms in delivery have been explored, placing experimental observations in a better context. An overview of molecular modeling techniques will be first given, followed by a review on modeling of polyplexes and lipoplexes.

2.2. Molecular Modeling Employed in Gene Delivery[1]

Molecular modeling aims at studying the behavior of molecules through model building and numerical simulation over a range of length and time scales (Figure 2.2). The established

[1]The Nobel Prize in Chemistry 2013 was awarded jointly to Martin Karplus, Michael Levitt and Arieh Warshel for *"the development of multiscale models for complex chemical systems"*. Their discoveries have laid the foundation for the application of molecular simulations bridging different scales to biological systems, the theme of this Chapter.

approaches include quantum mechanical (QM) methods, all atom molecular mechanics (MM), hybrid QM/MM methods, Monte-Carlo (MC) and coarse-grained (CG) simulations. QM methods, such as *ab initio*, density functional theory (DFT) and semi-empirical approaches, determine the detailed electron distribution. It is often used when electron transfer and chemical reaction is important, an issue not generally applicable for gene delivery. All-atom (AA) molecular dynamics (MD) is based on MM, where intra- and intermolecular interactions are described by a force field (FF) that specifies the potential energy in terms of geometrical variables, e.g., atom distances and bond angles [9]. Parameters in the FF are obtained through QM calculations or comparison to experimental data. Force on each atom is calculated from the potential energy and numerically integrating equations of motion provides time trajectory of the system [9]. One way to increase time efficiency is to constrain some intramolecular interactions, such as bond lengths and angles. Constraints in MD can also be applied when the system has a high tendency to be trapped in free energy wells, resulting in poor sampling. Umbrella sampling (US) method [9] is one such approach, where certain degrees of freedom are restrained by applying a biasing potential. US generally requires performing a series of simulations with different biasing potentials. Unbiased results are then obtained with statistical methods like weighted histogram analysis method (WHAM) [10]. Current state-of-the-art in AA-MD allows simulating systems that are $<10^6$ atoms for less than one μs, which is much smaller than experimental systems. Another challenge is the accuracy of FFs [11], but the fast growing computing power and extensive studies on more reliable FFs are facilitating MD simulations at realistic time and length scales.

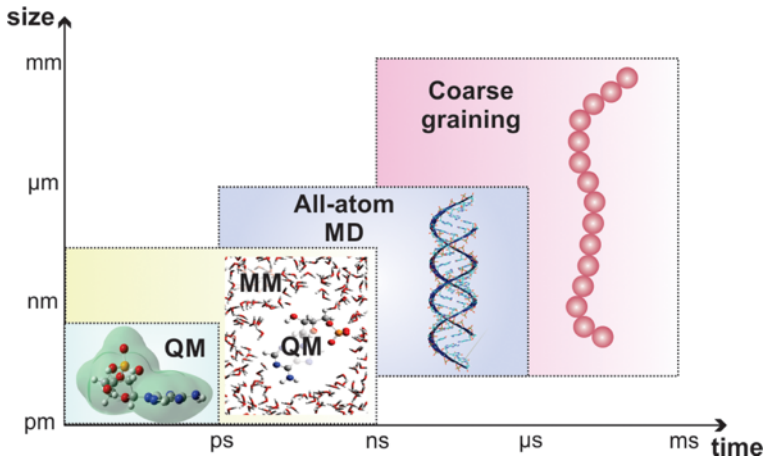

Figure 2.2. Time and length scales typically used by different modeling approaches.

Hybrid QM/MM approach provides a compromise between maintaining a reasonable size of simulated system and accurately describing certain chemically active regions: the reactive part is described by QM and the rest by a FF. An effective potential energy function describes the interactions within each region and on the QM-MM interface. Since its introduction [12], QM/MM method has been widely used in modeling biomolecular systems [13]. Because of the high computational cost associated with QM calculations, current QM/MM simulations can only be performed for hundreds of ps at *ab initio* or DFT levels, although this can be 100 times larger with semi-empirical approaches. Furthermore, most QM/MM simulations have been performed for structural optimization rather than unrestrained dynamics [13].

To overcome the computational limits, approaches that can bridge atomistic and mesoscopic scales have been developed. CG is one such approach where a number of atoms are clustered into beads, namely CG sites. Interactions among CG sites are described by parameterized potential energy functions and time trajectory can be obtained by solving equations of motions [14]. Dissipative particle dynamics (DPD) is an example of CG simulations where the force acting on each CG site ('DPD particle') is a sum of conservative,

dissipative and stochastic forces. The reduced degrees of freedom have allowed CG simulations to reach ms range, facilitating direct comparison to experiments [15]. Treating several atoms as a group, however, causes loss of atomistic information, and may lead to inaccuracy [15].

Unlike deterministic MD, stochastic MC approach samples the phase space by using a random number generator to obtain new coordinates and performing trial moves [11]. These trial moves are either accepted or rejected according to probability distribution for the specific ensemble under consideration. Many MC simulations have been performed for biomolecules and the majority of them are coupled with CG approach.

2.3. Modeling on Complexation of Polynucleotides with Carriers

Most molecular simulations performed on gene delivery focused on complexation of polynucleotides with cationic carriers and their aggregation into larger structures, while other steps of the delivery process are only now beginning to be addressed (Figure 2.3).

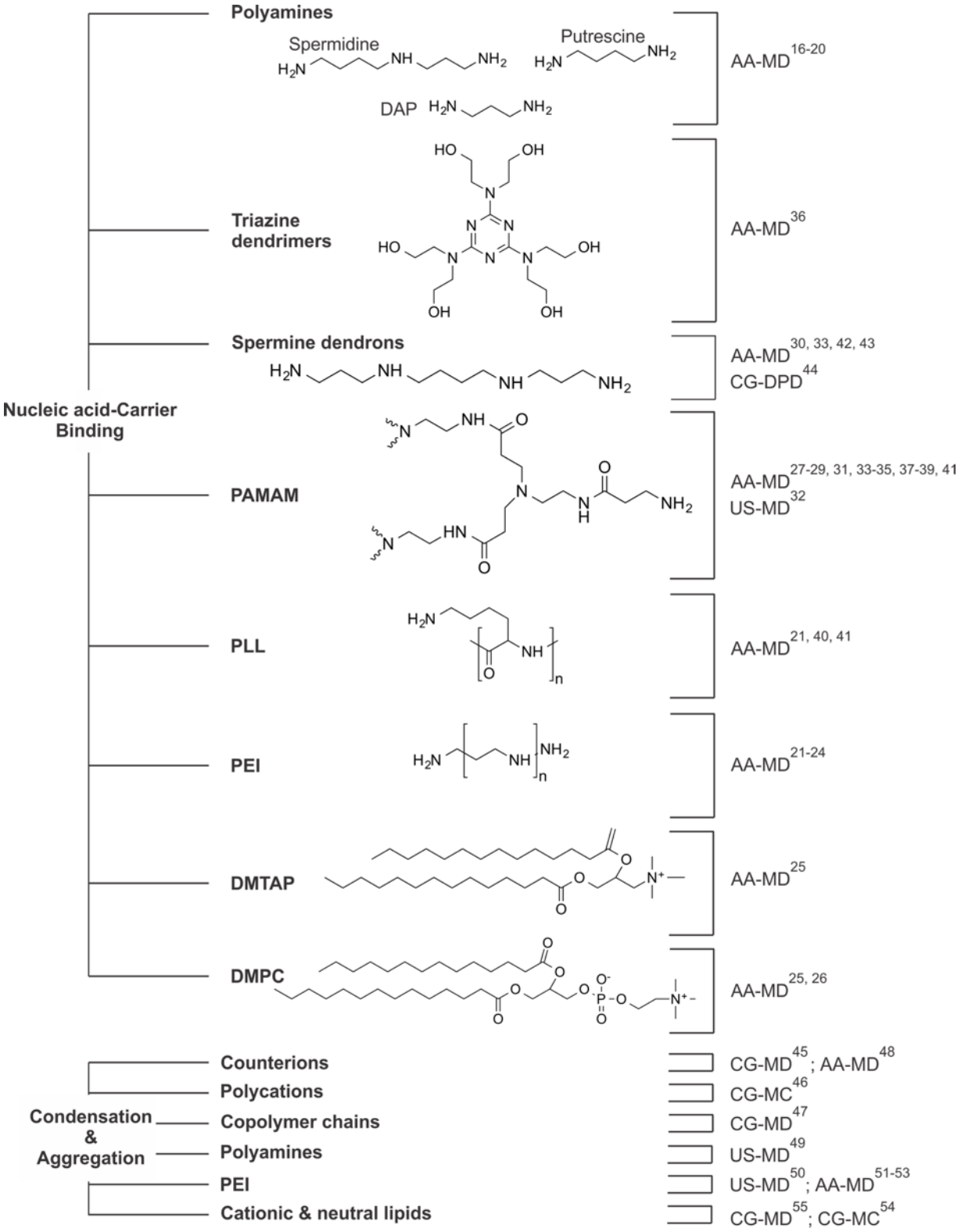

Figure 2.3. Summary of the reviewed concepts, carriers and approaches used in their modeling.

2.3.1. Complexation of Carriers with Polynucleotides

Significant efforts have been spent on understanding how carriers bind to individual polynucleotides. DNA binding of small oligoamines, such as putrescine (2^+), spermidine (3^+) and spermine (4^+), which stabilize DNA in cells, was investigated in a series of MD studies. These oligoamines were shown to bind DNA through the backbone O1P and O2P atoms [16-20]. Similarly, different groups reported the main interactions of PEI with DNA and siRNA to be between PEI amines and backbone phosphates in polynucleotides [21-24]. The first study on DNA-lipid systems probed the interactions of dimyristoyltrimethylammonium propane (DMTAP) and dimyristoylphosphatidylcholine (DMPC) bilayers with DNA and showed that zwitterionic phosphatidylcholine (PC) head groups competed with cationic trimethylammonium moieties for screening of DNA charges [25]. Simulations of DMPC monolayers with DNA showed that although DNA was able to conserve its double helical structure, its base pairing was affected by the interactions with lipid head groups [26]. More systematic studies have been conducted with polycationic carriers employed for experimental gene delivery.

2.3.1.1. Effect of pH, H_2O and salt (NaCl)

Dendrimers with variable extent of protonation were simulated to better understand pH ($[H^+]$) effects during delivery. In line with experiments, a more favorable attraction between dendrimers and siRNA was present under low pH (~5) compared to neutral pH (~7), as indicated by Molecular Mechanics Poisson-Boltzmann Surface Area (MM-PBSA) analysis [27-29]. In our simulation, a decrease in PEI's protonation ratio caused formation of less stable complexes due to the loss of direct H-bonding to DNA [22]. While increased salt concentrations did not affect the binding affinity of a 2nd generation (G2) spermine dendrimer to DNA, this was not the case for G1 [30]. A reduced affinity was also found when salt was introduced to a G5

polyamidoamine (PAMAM)-DNA system [31]. Therefore, screening from salt seems to become important for small or rigid carriers that have limited interaction with polynucleotides. H_2O molecules were also critical in binding dynamics; in a DNA-G3 PAMAM system, US-MD simulations revealed that ordered H_2O was capable of bridging DNA and a highly charged dendrimer [32]. Our own work indicated the release of H_2O from the hydration shell surrounding either DNA or PEIs, as complexes evolve from individual molecules [23]. H_2O molecules can also affect the structures of carriers themselves; PAMAM (G3 to G5) was reported to swell due to H_2O penetration, which was proportional to dendrimer generation [31].

2.3.1.2. Effect of Carrier Architecture

Flexibility of carriers is a critical issue for polyplex/lipoplex formation. For PAMAM dendrimers, rigidity was reported to increase with an increase in size/generation [33-35]. Among the G4 to G6 dendrimers, G4 showed higher binding affinity to siRNA due to its flexibility, while the affinity was lost with G6 due to its rigidity [33]. A comparison among G1, G4 and G7 PAMAM dendrimers showed that the increased rigidity associated with larger size caused higher entropic cost in binding to siRNA [35]. However, Pavan and coworkers published a contradictory report on beneficial effect of flexibility. Flexible G2 triazine dendrimers designed with ethyleneglycol chains could not establish efficient interactions either with siRNA or DNA, due to their compact structure formed by the collapse of flexible linkers in salt environment, whereas rigid dendrimers with piperazine rings resulted in more favorable binding [36]. G5 dendrimers showed a transition from a flexible to a rigid structure with a change in protonation; flexibility observed at neutral pH (pH~7.4) was lost with a decrease in pH to <5, causing a lower affinity towards siRNA [33]. Binding affinity varied with dendrimer generation. Some studies reported reduced affinity with an increase in generation, possibly due to increased rigidity, while

high generation PAMAMs were found to bind more favorably to single-stranded DNA [37], dsDNA [31] and siRNA [29, 38, 39]. The latter should be attributed to increased number of positive charges, and not to the context of carrier flexibility/rigidity.

Our group focused on the influence of PEI molecular weight and structure on its complexation with DNA and siRNA. Degree of branching in 570 Da PEI did not cause any significant changes in binding dynamics [22], but modifications in 2 kDa PEI's architecture resulted in different binding patterns. Flexible linear PEI was observed to bind like cords and covering DNA's surface efficiently, whereas branched PEIs bound like beads, thus allowed bridging multiple DNAs [23]. In addition, DNA charges were screened more efficiently with 2 kDa PEI [23], in comparison with 570 Da PEI [22]. Zheng and coworkers studied a high molecular weight (25 kDa) PEI-DNA system, and reported that one PEI molecule was not sufficient for a stable DNA complex to form [24].

In comparison with linear poly-L-lysine (PLL)s, graft PLLs (where lysines are located on the branches) showed less favorable binding to DNA due to the steric hindrance caused by their hydrophobic backbone [40]. If the charge densities of the carriers are equivalent, binding pattern was found to be similar for linear PLL and PAMAM dendrimers [38, 41], which indicated electrostatic interactions to be the main driving force rather than molecular architecture of the carriers.

2.3.1.3. Effect of Functional Groups

Functional groups can be incorporated into carriers for controlling binding to polynucleotides. MM-PBSA analysis on DNA binding to G1 and G2 dendrons functionalized with spermine, 1,3-diaminopropane (DAP) and N,N-di-(3-aminopropyl)-N-(methyl)amine (DAPMA) showed that surface charges participated in enthalpic interactions. Spermine (9^+ in G1 and 27^+ in G2) had

the most favorable interaction due to its highest surface charges. G2 DAPMA (18^{+}) was found to be similar to G1 and G2 spermine in terms of binding affinity toward DNA. This observation, however, was attributed to favorable enthalpic interactions arising from dendrimer backfolding and DNA bending, rather than surface charges [42]. Functionalization of dendrons with photolabile linkers using UV-degradable spermine resulted in branched structures. These branched structures led to a uniform vibrational behavior of the dendron amines and DNA phosphates, which reduced the entropic cost upon binding compared to non-degradable dendrons, resulting in more stable interactions [43]. CG-DPD simulations showed that modification of spermine dendrons with hydrophobic cholesterol caused self-assembly of G1 dendrons and consequently higher charge density compared to G2, thus enabling more effective DNA binding [44].

2.3.1.4. Nature of Polynucleotide

siRNA was able to establish stronger interactions with carriers due to its more flexible structure compared to DNA, as reported in several studies [24, 36, 43]. This observation was concurrent to previous results seen with PAMAMs, where the rigidity of the carrier reduced the binding strength.

2.3.2. Condensation and Aggregation

Condensing agents (i.e., gene carriers) can lead to formation of self-assembled (ordered) or aggregated (disordered) structures as a result of dramatic change in volume. Under practical conditions, these structures could end up in ~100 nm (‘characteristic’ length) nanoparticles. Condensation is crucial for efficient DNA delivery, while siRNA delivery relies on aggregation; both have been probed by molecular modeling.

2.3.2.1. Condensation

CG-MD simulations on di-, tri- and tetravalent counterion-DNA systems showed the effect of valence on DNA condensation. While DNA was effectively condensed with tri- and tetravalent counterions, divalent counterions lacked this ability [45]. Increasing the numbers of either polycations or polycation charges was reported to be beneficial in polyanion condensation and collapse. While condensation occurred when the carrier to polynucleotide charge ratio >1, only small deformations on polyanion chains were observed with charge ratio <1 [46]. In the case of copolymers, effect of charge was probed by varying the length of copolymers containing both neutral and poycationic parts. Effective condensation was visible with copolymer chains that were longer than four cationic blocks [47].

2.3.2.2. Aggregation

DNA aggregation by counterions, polyamines and polymers was investigated in several studies. In a system involving two DNAs and salt (KCl and NaCl), DNA charges were screened more effectively with Na^+ than K^+, indicated by the steeper DNA repulsion profile in the presence of KCl [48]. Effect of valence was probed for DNA-oligoamine (putrescine, spermidine and spermine) systems. Concurrent with previous observations on counterion-induced condensation [45], increasing valence of oligoamines was reported to provide stronger DNA-DNA attraction [49]. Compared to oligoamines, we reported better DNA-DNA attraction with 568 Da PEI, indicated by a larger depth in the potential of mean force (PMF) curves for DNA interactions. In addition, we reported formation of more stable aggregates with an increase either in N/P (ratio of PEI Ns to DNA Ps) or PEI protonation ratio [50]. In a series of recent publications [51-53], we focused on PEI mediated aggregation of multiple (>2) DNA and siRNA molecules. With 568 Da PEI, aggregation occurred via efficient screening of DNA charges and polyion bridging

(Figure 2.4a) between DNAs [51]. Oleic acid (OA, C18) modification on PEI, which resulted in 831 Da PEI, brought up an additional aggregation pattern, the association of lipid tails (Figure 2.4a) [52]. In addition to oleic acid, we also simulated substitutions on 1874 Da PEI with caprylic acid (CA, C8) and linoleic acid (LA, C18). More stable lipid association was achieved with LAs than CAs, due to the longer length of LA. Level of lipid substitution per PEI was important; while at one lipid substitution per PEI, a fraction of PEIs stayed in solution rather than approaching and binding to siRNA; all PEIs contributed to complex formation at three lipid substitutions per PEI. Compared with native PEI systems, more compact and stable siRNA aggregates were obtained as a result of lipid substitution (Figure 2.4b) [53].

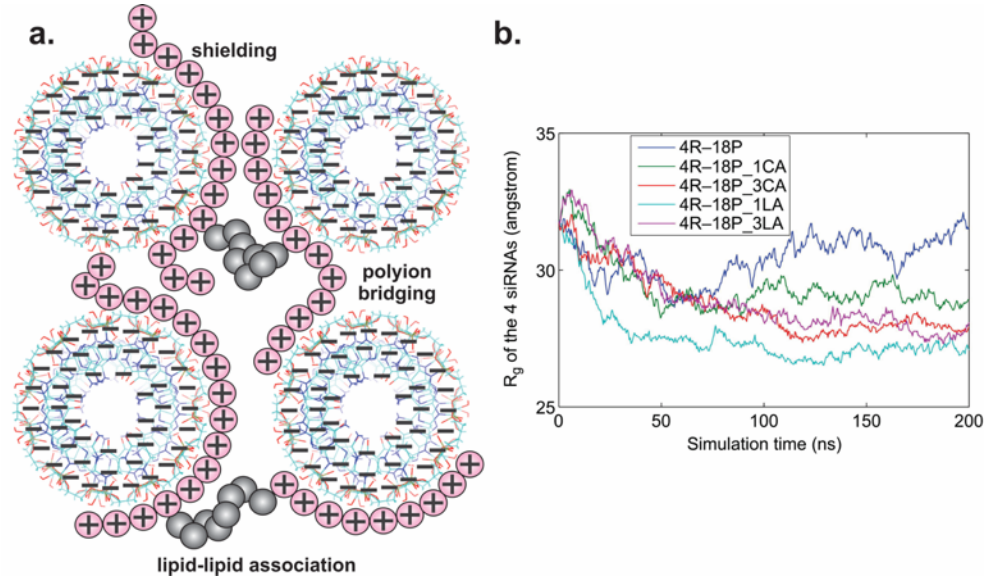

Figure 2.4. Mechanisms of polynucleotide aggregation by polycationic carriers, and the effect carrier functionalization with lipid moieties on the compactness of siRNA complexes.
a. A schematic of polycationic carrier-mediated polynucleotide aggregation. **b.** Radius of gyration of four siRNAs in complex with native and lipid substituted (CA and LA) PEIs. Reprinted from: Biomaterials, Vol. 34 (11), Sun, C., Tang, T., Uludag, H., A Molecular Dynamics Simulation Study on the Effect of Lipid Substitution on Polyethylenimine Mediated siRNA Complexation, Pages: 2822-2833, Copyright (2013), with permission from Elsevier.

Randomly distributed lipids around DNAs gave a self-assembled lipid bilayer comprising DNAs sandwiched in the middle [54]. A larger system involving 32 DNA molecules and > 1000 neutral and cationic lipids was studied, where the charge density of the system (ϕ_c, % cationic lipids) and the membrane stiffness (κ_s) were systematically varied. An optimal self-assembly threshold was evident in terms of these parameters. There were two main self-assembled phases of interest: inverted hexagonal phase where DNAs were packed inside cylindrical lipid micelles, and lamellar phase where DNA monolayers were sandwiched between lipid bilayers. Transitions between the two phases were observed at different ϕ_c and κ_s [55].

2.4. Modeling of Intracellular Trafficking

There have been only a few modeling works that investigated the intracellular trafficking of gene delivery. The very first model of complex attachment to cell membrane studied a simple dendrimer-DNA system using CG-MC simulations. Increasing charge density of membrane or decreasing Debye length of the solution resulted in poor attachment to cell membrane. Dendrimers were observed to dissociate from DNA with increased membrane charge densities, indicating the destabilizing effect of membrane on complexes under certain conditions [56].

Endocytosis of complexes was recently investigated by a CG model for a DNA particle coated with polymers containing protonable charges and surface ligands. While ligand-receptor interactions dominated endocytosis patterns, increasing charge density of polymeric carrier led to partial to full endocytosis. DNA length and concentration, as well as the anionic charge of the membrane were shown to significantly influence the process [57]. For a target membrane, these molecular parameters have to be optimized to achieve optimal endocytosis.

Dinh et al. employed a stochastic simulation for 25 kDa PEI-DNA complexes and studied the transition between distinct states (membrane binding to unpacking). The probability of a

successful DNA delivery was 5% when the complexes escaped in the supranuclear region, compared to 1% for escape in cytoplasm. In the supranuclear region, later escape led to lower probability, most likely due to lysosomal degradation. Cell geometry was shown to be critical; greater delivery efficiency was observed for elongated and smaller cells, since such cells had relatively larger perinuclear space and escape location could be closer to the nucleus [58].

Finally, decompaction of polyanion/polycation complexes was investigated through CG-MC simulations. Decompaction was shown to be possible with heparin-like molecules and it was of higher degree in the presence of Fe(III), which might indicate the importance of Fe(III) in facilitating polynucleotide release [59].

2.5. Conclusions

In this chapter, we provided a detailed review of the simulation work performed to-date on the formation of polyplexes and lipoplexes, as well as their intracellular delivery stages. There has been a great interest towards determining optimal carriers for nucleic acid delivery; and detailed atomic and mesoscopic level data regarding optimal conditions for polyplex/lipoplex formation are now beginning to be available in the literature. However, given the low amount of work pursued on the intracellular events of the delivery process, and the lack of atomistic level details in the existing work, there is an urgent need to fill the gap in theoretical modeling of these crucial stages.

The molecular modeling studies reported in the literature provided unique insights into the atomistic structure of polyplexes and lipoplexes, especially with the multifunctional carriers composed of different chemical domains, and helped to develop a better understanding of the outcomes observed in cellular systems. This is critical since it may facilitate the design of next-generation delivery systems based on known experimental and theoretical aspects of the current

delivery systems. It must be stated that most MD simulations have relied on existing experimental studies for validation and it might be misleading to employ results derived from systems where there is a discrepancy between experimental conditions and theoretical predictions (such as the hydration, salt concentrations, differences in molecular weight of employed species). Conducting simultaneous studies where the experimental and theoretical conditions are harmonized will be beneficial not only for better predictions, but also to improve the theoretical calculations if significant deviations from experimental data are observed.

2.6. Acknowledgements

We acknowledge financial support for our nucleotide delivery and modeling studies from Natural Sciences and Engineering Research Council of Canada (NSERC), Canadian Institute of Health Research (CIHR), Alberta Innovates Technology Futures (AITF), and Canada Foundation for Innovation (CFI).

2.7. References

1. Fire A, Xu S, Montgomery MK, Kostas SA, Driver SE, & Mello CC (1998) Potent and Specific Genetic Interference by Double-stranded RNA in Caenorhabditis Elegans. *Nature* 391(6669):806-811.
2. Guo P, Coban O, Snead NM, Trebley J, Hoeprich S, Guo S, & Shu Y (2010) Engineering RNA for Targeted siRNA Delivery and Medical Application. *Adv. Drug Deliv. Rev.* 62(6):650-666.
3. Hillaireau H & Couvreur P (2009) Nanocarriers' Entry into the Cell: Relevance to Drug Delivery. *Cell. Mol. Life. Sci.* 66(17):2873-2896.
4. Hsu CY & Uludag H (2012) Cellular Uptake Pathways of Lipid-modified Cationic Polymers in Gene Delivery to Primary Cells. *Biomaterials* 33(31):7834-7848.
5. Dominska M & Dykxhoorn DM (2010) Breaking Down the Barriers: siRNA Delivery and Endosome Escape. *J. Cell Sci.* 123(Pt 8):1183-1189.
6. Boussif O, Lezoualc'h F, Zanta MA, Mergny MD, Scherman D, Demeneix B, & Behr JP (1995) A Versatile Vector for Gene and Oligonucleotide Transfer into Cells in Culture and In vivo: Polyethylenimine. *Proc. Natl. Acad. Sci. U.S.A.* 92(16):7297-7301.

7. Moret I, Esteban Peris J, Guillem VM, Benet M, Revert F, Dasi F, Crespo A, & Alino SF (2001) Stability of PEI-DNA and DOTAP-DNA Complexes: Effect of Alkaline pH, Heparin and Serum. *J. Control. Release* 76(1-2):169-181.

8. McCammon JA, Gelin BR, & Karplus M (1977) Dynamics of Folded Proteins. *Nature* 267(5612):585-590.

9. Torrie GM & Valleau JP (1977) Nonphysical Sampling Distributions in Monte Carlo Free-energy Estimation: Umbrella Sampling. *J. Comput. Phys.* 23(2):187-199.

10. Kumar S, Rosenberg JM, Bouzida D, Swendsen RH, & Kollman PA (1992) The Weighted Histogram Analysis Method for Free-energy Calculations on Biomolecules. I. The Method. *J. Comput. Chem.* 13(8):1011−1021.

11. Schlick T (2010) *Molecular Modeling and Simulation: An Interdisciplinary Guide* (Springer, New York, USA), pp 265-298.

12. Warshel A & Levitt M (1976) Theoretical Studies of Enzymic Reactions: Dielectric, Electrostatic and Steric Stabilization of the Carbonium Ion in the Reaction of Lysozyme. *J. Mol. Biol.* 103(2):227-249.

13. Groenhof G (2013) Chapter 3: Introduction to QM/MM Simulations. *Biomolecular Simulations: Methods and Protocols,* Methods in Molecular Biology, eds Monticelli L & Salonen E (Springer Science Business Media, New York), Vol 924, pp 43-66.

14. Takada S (2012) Coarse-grained Molecular Simulations of Large Biomolecules. *Curr. Opin. Struc. Biol.* 22(2):130-137.

15. Voth GA (2009) Chapter 1: Introduction. *Coarse-graining of Condensed Phase and Biomolecular Systems*, ed Voth GA (CRC Press/Taylor and Francis Group, Boca Raton).

16. Korolev N, Lyubartsev AP, Nordenskiold L, & Laaksonen A (2001) Spermine: An "Invisible" Component in the Crystals of B-DNA. A Grand Canonical Monte Carlo and Molecular Dynamics Simulation Study. *J. Mol. Biol.* 308(5):907-917.

17. Korolev N, Lyubartsev AP, Laaksonen A, & Nordenskiold L (2002) On the Competition between Water, Sodium Ions, and Spermine in Binding to DNA: A Molecular Dynamics Computer Simulation Study. *Biophys. J.* 82(6):2860-2875.

18. Korolev N, Lyubartsev AP, Laaksonen A, & Nordenskiold L (2003) A Molecular Dynamics Simulation Study of Oriented DNA with Polyamine and Sodium Counterions: Diffusion and Averaged Binding of Water and Cations. *Nucleic Acids Res.* 31(20):5971-5981.

19. Korolev N, Lyubartsev AP, Laaksonen A, & Nordenskiold L (2004) A Molecular Dynamics Simulation Study of Polyamine- and Sodium-DNA. Interplay Between Polyamine Binding and DNA Structure. *Eur. Biophys. J.* 33(8):671-682.

20. Korolev N, Lyubartsev AP, Laaksonen A, & Nordenskiold L (2004) Molecular Dynamics Simulation Study of Oriented Polyamine- and Na-DNA: Sequence Specific Interactions and Effects on DNA Structure. *Biopolymers* 73(5):542-555.

21. Ziebarth J & Wang Y (2009) Molecular Dynamics Simulations of DNA-Polycation Complex Formation. *Biophys. J.* 97(7):1971-1983.

22. Sun C, Tang T, Uludag H, & Cuervo JE (2011) Molecular Dynamics Simulations of DNA/PEI Complexes: Effect of PEI Branching and Protonation State. *Biophys. J.* 100(11):2754-2763.

23. Sun C, Tang T, & Uludag H (2012) Molecular Dynamics Simulations for Complexation of DNA with 2 kDa PEI Reveal Profound Effect of PEI Architecture on Complexation. *J. Phys. Chem. B.* 116(8):2405-2413.

24. Zheng M, Pavan GM, Neeb M, Schaper AK, Danani A, Klebe G, Merkel OM, & Kissel T (2012) Targeting the Blind Spot of Polycationic Nanocarrier-based siRNA Delivery. *ACS Nano* 6(11):9447-9454.

25. Bandyopadhyay S, Tarek M, & Klein ML (1999) Molecular Dynamics Study of a Lipid-DNA Complex. *J. Phys. Chem. B.* 103(46):10075-10080.

26. Braun CS, Jas GS, Choosakoonkriang S, Koe GS, Smith JG, & Middaugh CR (2003) The Structure of DNA within Cationic Lipid/DNA Complexes. *Biophys. J.* 84(2):1114-1123.

27. Ouyang D, Zhang H, Parekh HS, & Smith SC (2011) The Effect of pH on PAMAM Dendrimer-siRNA Complexation: Endosomal Considerations as Determined by Molecular Dynamics Simulation. *Biophys. Chem.* 158(2-3):126-133.

28. Pavan GM, Posocco P, Tagliabue A, Maly M, Malek A, Danani A, Ragg E, Catapano CV, & Pricl S (2010) PAMAM Dendrimers for siRNA Delivery: Computational and Experimental Insights. *Chemistry* 16(26):7781-7795.

29. Karatasos K, Posocco P, Laurini E, & Pricl S (2012) Poly(amidoamine)-based Dendrimer/siRNA Complexation Studied by Computer Simulations: Effects of pH and Generation on Dendrimer Structure and siRNA Binding. *Macromol. Biosci.* 12(2):225-240.

30. Pavan GM, Danani A, Pricl S, & Smith DK (2009) Modeling the Multivalent Recognition between Dendritic Molecules and DNA: Understanding How Ligand "Sacrifice" and Screening Can Enhance Binding. *J. Am. Chem. Soc.* 131(28):9686-9694.

31. Nandy B & Maiti PK (2011) DNA Compaction by a Dendrimer. *J. Phys. Chem. B.* 115(2):217-230.

32. Mills M, Orr BG, Banaszak Holl MM, & Andricioaei I (2013) Attractive Hydration Forces in DNA-Dendrimer Interactions on the Nanometer Scale. *J. Phys. Chem. B.* 117(4):973-981.

33. Pavan GM, Albertazzi L, & Danani A (2010) Ability to Adapt: Different Generations of PAMAM Dendrimers Show Different Behaviors in Binding siRNA. *J. Phys. Chem. B.* 114(8):2667-2675.

34. Jensen LB, Mortensen K, Pavan GM, Kasimova MR, Jensen DK, Gadzhyeva V, Nielsen HM, & Foged C (2010) Molecular Characterization of the Interaction between siRNA and PAMAM G7 Dendrimers by SAXS, ITC, and Molecular Dynamics Simulations. *Biomacromolecules* 11(12):3571-3577.

35. Jensen LB, Pavan GM, Kasimova MR, Rutherford S, Danani A, Nielsen HM, & Foged C (2011) Elucidating the Molecular Mechanism of PAMAM-siRNA Dendriplex Self-assembly: Effect of Dendrimer Charge Density. *Int. J. Pharm.* 416(2):410-418.

36. Pavan GM, Mintzer MA, Simanek EE, Merkel OM, Kissel T, & Danani A (2010) Computational Insights into the Interactions between DNA and siRNA with "Rigid" and "Flexible" Triazine Dendrimers. *Biomacromolecules* 11(3):721-730.

37. Maiti PK & Bagchi B (2006) Structure and Dynamics of DNA-Dendrimer Complexation: Role of Counterions, Water, and Base Pair Sequence. *Nano Lett.* 6(11):2478-2485.

38. Ouyang D, Zhang H, Herten DP, Parekh HS, & Smith SC (2010) Structure, Dynamics, and Energetics of siRNA-Cationic Vector Complexation: A Molecular Dynamics Study. *J. Phys. Chem. B.* 114(28):9220-9230.

39. Vasumathi V & Maiti PK (2010) Complexation of siRNA with Dendrimer: A Molecular Modeling Approach. *Macromolecules* 43:8264–8274.

40. Elder RM, Emrick T, & Jayaraman A (2011) Understanding the Effect of Polylysine Architecture on DNA Binding Using Molecular Dynamics Simulations. *Biomacromolecules* 12(11):3870-3879.

41. Ouyang D, Zhang H, Parekh HS, & Smith SC (2010) Structure and Dynamics of Multiple Cationic Vectors-siRNA Complexation by All-atomic Molecular Dynamics Simulations. *J. Phys. Chem. B.* 114(28):9231-9237.

42. Jones SP, Pavan GM, Danani A, Pricl S, & Smith DK (2010) Quantifying the Effect of Surface Ligands on Dendron-DNA Interactions: Insights into Multivalency through a Combined Experimental and Theoretical Approach. *Chemistry* 16(15):4519-4532.

43. Pavan GM, Kostiainen MA, & Danani A (2010) Computational Approach for Understanding the Interactions of UV-degradable Dendrons with DNA and siRNA. *J. Phys. Chem. B.* 114(17):5686-5693.

44. Posocco P, Pricl S, Jones S, Barnard A, & Smith DK (2010) Less Is More – Multiscale Modelling of Self-assembling Multivalency and Its Impact on DNA Binding and Gene Delivery. *Chem. Sci.* 1:393–404.

45. Stevens MJ (2001) Simple Simulations of DNA Condensation. *Biophys. J.* 80(1):130-139.

46. Dias RS, Pais AACC, Miguel MG, & Lindman B (2003) Modeling of DNA Compaction by Polycations. *J. Chem. Phys.* 119:8150-8157.

47. Ziebarth J & Wang Y (2010) Coarse-grained Molecular Dynamics Simulations of DNA Condensation by Block Copolymer and Formation of Core-corona Structures. *J. Phys. Chem. B.* 114(19):6225-6232.

48. Savelyev A & Papoian GA (2007) Inter-DNA Electrostatics from Explicit Solvent Molecular Dynamics Simulations. *J. Am. Chem. Soc.* 129(19):6060-6061.

49. Dai L, Mu Y, Nordenskiold L, & van der Maarel JR (2008) Molecular Dynamics Simulation of Multivalent-ion Mediated Attraction between DNA Molecules. *Phys. Rev. Lett.* 100(11):118301.

50. Bagai S, Sun C, & Tang T (2013) Potential of Mean Force of Polyethylenimine-mediated DNA Attraction. *J. Phys. Chem. B.* 117(1):49-56.

51. Sun C, Tang T, & Uludag H (2011) Molecular Dynamics Simulations of PEI Mediated DNA Aggregation. *Biomacromolecules* 12(10):3698-3707.

52. Sun C, Tang T, & Uludag H (2012) Probing the Effects of Lipid Substitution on Polycation Mediated DNA Aggregation: A Molecular Dynamics Simulations Study. *Biomacromolecules* 13(9):2982-2988.

53. Sun C, Tang T, & Uludag H (2013) A Molecular Dynamics Simulation Study on the Effect of Lipid Substitution on Polyethylenimine Mediated siRNA Complexation. *Biomaterials* 34(11):2822-2833.

54. Farago O, Gronbech-Jensen N, & Pincus P (2006) Mesoscale Computer Modeling of Lipid-DNA Complexes for Gene Therapy. *Phys. Rev. Lett.* 96(1):018102.

55. Farago O & Gronbech-Jensen N (2009) Simulation of Self-assembly of Cationic Lipids and DNA into Structured Complexes. *J. Am. Chem. Soc.* 131(8):2875-2881.

56. Voulgarakis NK, Rasmussen KO, & Welch PM (2009) Dendrimers as Synthetic Gene Vectors: Cell Membrane Attachment. *J. Chem. Phys.* 130(15):155101.

57. Ding HM & Ma YQ (2013) Design Maps for Cellular Uptake of Gene Nanovectors by Computer Simulation. *Biomaterials* 34(33):8401-8407.

58. Dinh AT, Pangarkar C, Theofanous T, & Mitragotri S (2007) Understanding Intracellular Transport Processes Pertinent to Synthetic Gene Delivery via Stochastic Simulations and Sensitivity Analyses. *Biophys. J.* 92(3):831-846.

59. Jorge AF, Dias RS, & Pais AA (2012) Enhanced Condensation and Facilitated Release of DNA Using Mixed Cationic Agents: A Combined Experimental and Monte Carlo Study. *Biomacromolecules* 13(10):3151-3161.

3. A Delicate Balance When Substituting a Small Hydrophobe onto Low Molecular Weight Polyethylenimine to Improve Its Polynucleotide Delivery Efficiency[X]

[X] A version of this chapter has been published. Adapted with permission from Meneksedag-Erol D, KC RB, Tang T, & Uludağ H (2015) A Delicate Balance When Substituting a Small Hydrophobe onto Low Molecular Weight Polyethylenimine to Improve Its Nucleic Acid Delivery Efficiency. *ACS Appl. Mater. Interfaces* 7: 24822−24832. Copyright (2015) American Chemical Society.

3.1. Introduction

Delivery of genetic material, either DNA or RNA, into cells and tissues to cope with defective physiology has proven to be a promising alternative in treating genetic disorders and cancers [1]. Silencing aberrant gene expression with synthetic double-stranded short interfering RNAs (siRNAs), in particular, has gained attention since Fire and coworkers [2] revealed the concept of RNA interference (RNAi) in nematode *Caenorhabditis elegans*. Successful delivery of siRNA into the targeted cells is of vital importance in the suppression of abnormal gene expression at therapeutic level. Susceptibility of genetic material to serum nucleases, however, hindered the delivery of naked siRNAs and led to the requirement of a delivery system in therapeutic applications. An efficient delivery system should facilitate the targeting of siRNAs to desired cells and tissues with minimal off-site effects, protect the siRNAs from nucleases, promote the cellular uptake of the cargo by endocytosis, and facilitate its intracellular trafficking [1]. Non-viral carriers have acquired considerable attention in this context, due to their relatively safe and easy to engineer nature in comparison to their viral counterparts.

Polyethylenimine (PEI) is a polymeric carrier that displays beneficial properties especially in the endosomal stages of delivery, hypothesized to originate from its uncharged nitrogens acting as a proton sponge to delay acidification in the endocyctic vesicles [3, 4]. It has been tested extensively for its gene delivery performance in a number of cell lines [5]. Its efficacy in transfecting DNA was found to increase with its molecular weight (MW) [6, 7]; however, high molecular weight (HMW) PEIs possess a considerable amount of toxicity, by inducing damage to the plasma membrane hence causing loss of metabolic activity [7, 8]. In search for a safer, non-toxic and non-immunogenic alternative to HMW PEI, research has focused on improving the performance of non-toxic low molecular weight (LMW) PEI via various modifications.

Polynucleotide complexes have to translocate through a lipid-based plasma membrane, where they are expected to preserve their integrity to effectively deliver their cargo to the cell interior [9]. Modification of carriers with hydrophobic moieties may facilitate the entry to cells by promoting hydrophobic interactions with membrane lipids [10]. Improvements in LMW PEI's gene delivery efficacy were reported with substitution of various hydrophobic molecules, including bulky hydrophobe groups such as cholesterol [11-13] and phospholipids such as phosphoethanolamine (DOPE and DPPE) and phosphocholine (PC) [14], which yielded enhanced transfection and/or silencing efficacy. Modification of 1.8 kDa PEI with hydrophobic alkyl groups such as ethyl, octyl, deodecyl, induced higher transfection efficiencies than that of unmodified PEI [14]. Toward this end, aliphatic lipids were also investigated. A previous study from our group explored a variety of aliphatic substituents, such as caprylic (8C), myristic (14C), palmitic (16C), stearic (18C), oleic (18C with a double bond), and linoleic acid (18C with 2 double bonds). Regardless of the type of the engrafted substituent, performance of 2 kDa PEI was increased in transfecting the genes compared to its unmodified counterpart, and the efficacy of the modified polymers were comparable to HMW 25 kDa PEI [9].

In this chapter, to have a better control over the grafting reactions, we explored the beneficial effect of a short aliphatic substituent, propionic acid (PrA, 3C) on the transfection ability of 1.2 kDa PEI. PrA moieties were grafted onto PEI at different substitution amounts and siRNA delivery capability of the PrA-modified PEIs was systematically assessed in K562 cell line, a chronic myeloid leukemia (CML) model. Surprisingly, a non-monotonic trend was observed between the uptake and gene silencing capability of the siRNA complexes and the amount of PrA substitution, with intermediate substitution amounts yielding the highest efficacy. To elucidate the molecular level details behind this unexpected phenomenon,

molecular dynamics (MD) simulations were performed on the designed complexes, and we proposed molecular basis for the unexpected performance of the engineered polymers.

3.2. Methods

3.2.1. Experimental

3.2.1.1. Materials

Branched 25 kDa PEI, PrA, *N*-(3-dimethylaminopropyl)-*N*′-ethylcarbodiimide hydrochloride (EDC), *N*-hydroxysuccinimide (NHS) were obtained from Sigma-Aldrich (St. Louis, MO). Branched 1.2 kDa PEI was purchased from Polysciences, Inc. (Warrington, PA). RPMI medium containing L-glutamine, 25 mM HEPES, penicillin and streptomycin was obtained from Gibco (Grand Island, NY). Custom-synthesized green fluorescent protein (GFP) siRNA (5'-GAACUUCAGGGUCAGCUUGCCG-3' and 3' UACUUGAAGUCCCAGUCGAACG-5'), and 5'-carboxyfluorescein (FAM)-labeled scrambled siRNA (5'-AACCAGUCGCA AACGCGACUGTT-3' and 5'-TTUUGGUCAGCGUUUGCGCUGAC-5') were obtained from Integrated DNA Technologies, Inc. (IDT; Coralville, IA). All solvents used in the synthesis procedure were obtained from Sigma-Aldrich, and used without any further purification.

3.2.1.2. Synthesis and Characterization of PrA-Modified Polymers

Hydrophobic modification of PEI with PrA was performed via *N*-acylation (Figure 3.1a). Briefly, PrA (3.34 mM, in $CHCl_3$) was activated with EDC (5 mM, in $CHCl_3$) for 30 min and then with NHS (5 mM, in MeOH), at room temperature. The activated PrA solutions were added drop-wise to each PEI solution (3.34 mM, in $CHCl_3$), and stirred overnight at room temperature. The crude products of PrA substituted PEIs of the four PrA/PEI feed ratios (0.5, 1, 2 and 4 mol/mol) were precipitated (3X) in ice cold diethyl ether and dried under vacuum for 48 h. Structural compositions of PrA substituted PEIs and the amount of PrA substitution (α) were

elucidated through ^{1}H-NMR spectroscopy (Bruker 300 MHz, Billerica, MA) using TMS as an internal standard in D_2O. Detailed information on the efficiency of the reactions and the characterization of the polymers is given in Section A.1 of Appendix A. Polymers will be referred to by their substitution amounts calculated from ^{1}H-NMR spectrum given on the right column of Figure 3.1b.

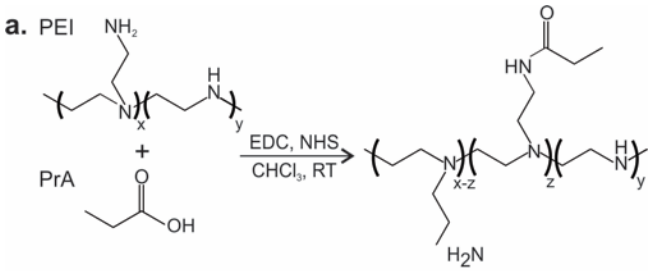

b.

Feed ratio PrA/PEI (mol/mol)	Calculated substitution amount (α) PrA/PEI (mol/mol)
0.50	0.26
1.00	0.69
2.00	1.14
4.00	1.59

Figure 3.1. Chemical synthesis of PrA conjugated PEIs.
(a) Scheme for the synthesis of PrA conjugated PEIs. **(b)** Details on the synthesis of the polymers. The substitution amount (α) is calculated from ^{1}H-NMR spectrum.

3.2.1.3. Cell culture

Wild type and permanently GFP-expressing K562 cells were used as the CML model. Cells were maintained in RPMI medium containing 10% fetal bovine serum (FBS), 100 U/ml penicillin and 100 μg/ml streptomycin, and routinely grown on 75 cm^2 plates. Cells were passaged when they reached ~80% confluence by simply dilution of the cell suspension by 1:10.

3.2.1.4. siRNA/Polymer Complex Preparation

For the preparation of siRNA/polymer complexes, 1.1 μg siRNA was mixed with polymers (dissolved in ddH_2O) at polymer:siRNA weight ratio of 6:1, then incubated in 300 μL RPMI (without FBS) for 30 min at room temperature. 100 μL of siRNA complexes were added to the

cells in 48 well-plates (in 300 μL volume) in triplicate to give a final concentration of 60 nM siRNA in cell suspension.

3.2.1.5. Physicochemical Characterization of siRNA/Polymer Complexes

siRNA/polymer complexes were prepared in 100 μl (total final volume) ultra-pure distilled H_2O by incubating 1.1 μg scrambled siRNA with different amounts of polymers to achieve polymer:siRNA weight ratio of 6:1 for particle size, and 1:1, 3:1 and 6:1 for zeta (ζ) potential measurements. Hydrodynamic diameter and ζ-potential of the particles were investigated by dynamic light and electrophoretic light scattering methods using Zetasizer (Nano ZS; Malvern Instruments, UK). The measurements were carried out at least in triplicates.

3.2.1.6. siRNA Delivery to K562 Cells

For cellular uptake studies, complexes were prepared with FAM-labeled scrambled siRNA with the procedure described above. K562 wild type cells (300 μL, 100,000 cells/mL) were then added on top of the complexes in 48-well plates. Cells were incubated for 24 h at 37 ºC in a humidified atmosphere. After incubation for a desired period, cells were processed for flow cytometry. Briefly, cells were transferred into 1.5 mL tubes and centrifuged at 1400 rpm for 5 min, washed twice with HBSS (pH 7.4), and fixed with formalin (3.7% in HBSS). FAM-siRNA positive cell population was quantified by Beckman Coulter QUANTA^{TM} SC Flow Cytometer using $FL1^{+}$ channel (3000 events/sample). The setting of the instrument was calibrated for each run to obtain FAM-siRNA positive cell population of 1-2% for control samples (i.e., untreated cells). The mean fluorescence intensity (MFI) and the percentage of FAM-siRNA positive cells were determined.

3.2.1.7. GFP Silencing in GFP Positive K562 Cells

Silencing activity of the complexes was determined by quantifying the decrease in GFP fluorescence in GFP-expressing K562 cells. Complexes were prepared with GFP siRNA with the procedure described above, then GFP-expressing K562 cells were seeded on top of the complexes and grown for 72 h. For the first time point (day 3), 300 μL of the cells was transferred into 1.5 mL tubes and centrifuged at 1400 rpm for 5 min, washed twice with HBSS (pH 7.4), and fixed with formalin (3.7% in HBSS). The remaining 100 μL of the cells was mixed with 300 μL fresh media and incubated for next time points (days 6 and 9). GFP silencing was quantified by flow cytometry using $FL1^{-}$ channel. The results were expressed as either mean GFP fluorescence after treatment, or percentage of cells displaying GFP silencing after the treatment, as determined by a shift from native GFP-expressing cell population.

3.2.1.8. Cytotoxicity of the siRNA/Polymer Complexes

In vitro cytotoxicity of the complexes was studied in K562 wild type cells by MTT (3-(4,5-dimethylthiazol-2-yl)-2,5-diphenyl-tetrazolium bromide) assay. First, complexes were prepared in Eppendorf tubes by incubating (in 300 μL RPMI) 1 μg siRNA with various amounts of polymers for the final polymer:siRNA weight ratios ranging from 1:1 to 40:1. Upon 30 min incubation at room temperature, complexes were transferred to 48 well plates in triplicates. K562 wild type cells were then added on top of the complexes (60,000 cells/well), and incubated for 72 h at 37 ºC in a humidified atmosphere. After incubation for the desired period, MTT reagent was added to each well in final concentration of 1 mg/ml and further incubated for 2 h. Deposited formazan crystals were dissolved by replacing the medium with dimethyl sulfoxide (DMSO, 200 μl). Optical density was measured at λ = 570 nm by using universal microplate

reader (ELx; Bio-Tech Instrument, Inc.). Cell viability was expressed as percentage relative to the viability of the cells without any treatment.

3.2.2. Computational

3.2.2.1. Simulated systems

The simulated siRNA has the following sequence: sense strand: 5′-CGCCGAAUUCAUUAAUUUATT-3′, antisense strand: 5′-UAAAUUAAUGAAUUCGGCG GG-3′, capable of silencing myeloid cell leukemia 1 (Mcl-1) protein. The total charge of siRNA is –40 in the fully deprotonated state. Its initial structure is created with UCSF Chimera [15] to be in canonical A-form. The 3′-overhangs were created with the manipulation of the structure via the mutation and/or deletion of the terminal bases. The simulated native PEI is branched and has a MW of 1205 Da. Its chemical structure is given in Figure 3.2. It consists of 27 primary, secondary or tertiary amine groups, of which 12 are protonated (indicated with '+' in Figure 3.2) corresponding to the protonation ratio of 44.4%, which is close to the experimentally determined ratio at pH=6 [16]. The protonation sites were assigned to primary and secondary amines, and were distributed in a way to minimize the nonspecific attractions between protonated amine groups [17]. For the substitution of hydrophobic moieties into PEI's structure, two ratios were chosen: PEI-1PrA with one PrA molecule per PEI and PEI-2PrA with two PrA molecules per PEI. In PEI-1PrA, PrA is substituted into the structure of PEI at the site marked as #1; and in PEI-2PrA, two PrAs were substituted at sites #1 and #2 (Figure 3.2). Initial structures of the native and modified PEIs were built in Maestro 9.8 [18] and VMD [19] software, and equilibrated for 10 ns (restrained) + 10 ns (free) with MD package of NAMD [20]. The structures of the polymers at the end of the simulations were adopted as initial structures for the main simulations.

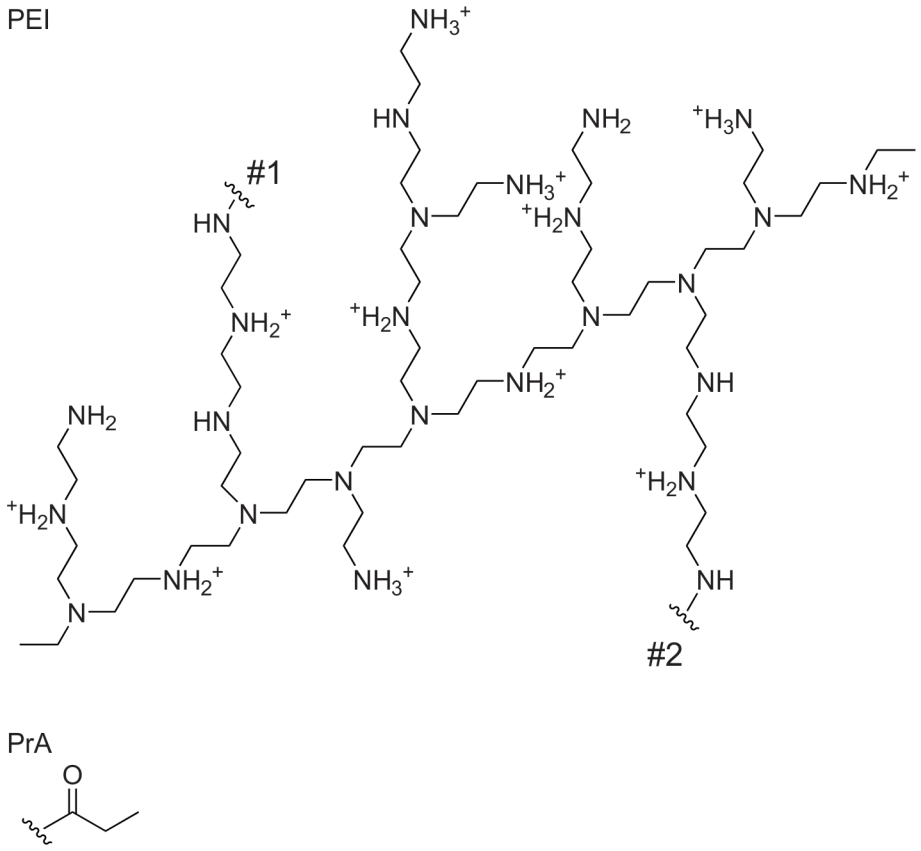

Figure 3.2. Molecular structures of the simulated PEI and PrA.
Protonation sites of PEI are marked with '+', and PrA substitution sites are indicated with '#'.

In order to explore the effect of hydrophobic modification, five simulation systems were then designed with varying PrA substitution amounts. To be consistent with the experimental section, simulated systems will be referred to by the amount of PrA substitution (α) they carry. Each system consists of 4 siRNAs and 16 PEIs, while the number of native and modified PEIs is varied to achieve the desired substitution amounts. For example, in system α = 0.25, we placed 12 native PEIs and 4 PEI-1PrAs, and α is calculated based on the ratio of the number of modified PEIs to the total number of native and modified PEIs, i.e. 4/(4+12) = 0.25. Similarly, in system α = 0.75, we placed 4 native PEIs and 12 PEI-1PrAs, and α is 12/(4+12) = 0.75. Composition and details of the studied systems are given in Table 3.1. In the initial configurations of the

simulations systems (Figure 3.3, left and middle panels), the principal axes of all the molecules were aligned parallel to one another. Four siRNA molecules were then placed on the corners of a square with a side length of 13 Å. Center of mass (COM) of the PEIs, native and/or modified, was positioned 17 Å away from the COM of their neighboring siRNAs. In each system studied, four PEIs were placed amidst the 4 siRNAs, and the remaining 12 PEIs were placed symmetrically to surround the siRNAs. Systems were solvated in a rectangular TIP3P water box with a minimum margin of 15 Å from all the sides. Proper amount of K^+ and Cl^- ions were then added to achieve 150 mM physiological salt concentration to mimic intracellular environment. Note that TIP3P water model [21] is used throughout this thesis due to following reasons: (*i*) the force field for our polymers [22] is a CHARMM-based force field devised by following CHARMM General Force Field (CGENFF) methodology [23]; and (*ii*) the parameterization scheme in CHARMM force fields involves the consideration of interactions with TIP3P water for the optimization of the assigned parameters [23]. Other water models are available; for example, SPC [24], TIP4P [21], and TIP5P [25]; but care should be taken when using these water models in conjunction with CHARMM force fields. Since TIP3P water model is integrated into CHARMM force fields as a part of the parameterization scheme, detailed analysis is needed to ensure accuracy of the interactions involving water when other water models are used [26].

Table 3.1. Details of the five simulated systems.

Substitution amount (α)	PEIs simulated	siRNA/PEI charge ratio	Number of atoms	Number of K^+/Cl^-	Size of the simulation box ($Å^3$)
0	16 native PEI	160/192	106,781	92/124	104 x 114 x 99
0.25	12 native PEI 4 PEI-1PrA	160/192	106,813	92/124	104 x 114 x 99
0.75	4 native PEI 12 PEI-1PrA	160/192	111,514	96/128	108 x 114 x 99
1	16 PEI-1PrA	160/192	108,324	93/125	107 x 112 x 99
2	16 PEI-2PrA	160/192	108,086	93/125	105 x 115 x 99

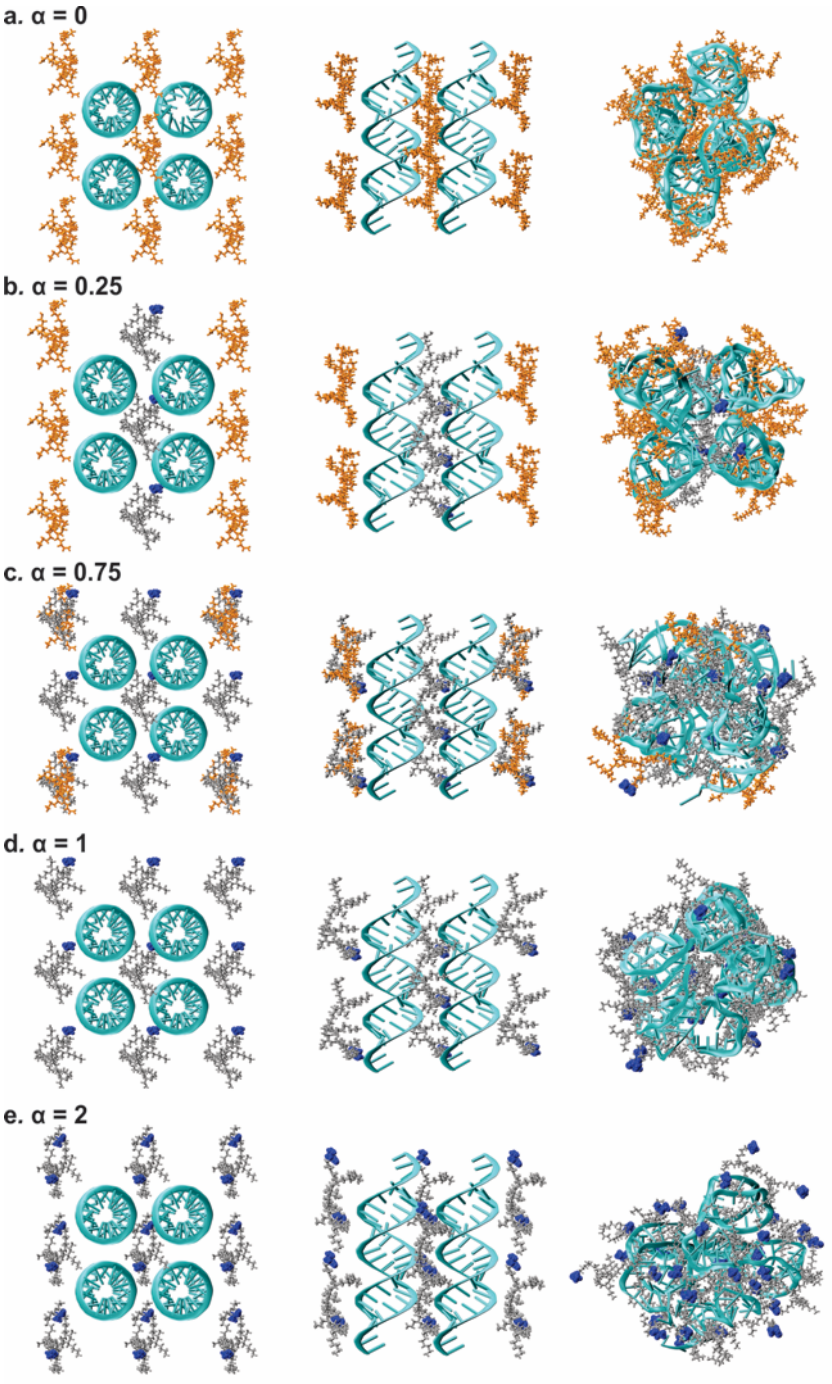

Figure 3.3. **Initial and final configurations of the simulated systems.**
Initial (left panel: top view, middle panel: side view) and final (right panel: top view) configurations of the systems **(a)** α = 0, **(b)** α = 0.25, **(c)** α = 0.75, **(d)** α = 1, **(e)** α = 2. siRNAs are given in cyan, native PEIs are in orange, and modified PEIs are in silver. PrA substitutions are represented as blue spheres. Water and ions are removed for clarity.

3.2.2.2. Simulation details

PEI topology was constructed by adopting the parameters of analogous molecules from CHARMM force field as outlined in CHARMM General Force Field (CGENFF) methodology [23]. The validation for this approach of creating PEI topology was carried out in our previous work [17, 22]. For all the other molecules, CHARMM27 force field [27-30] was used. All the simulations were performed with MD package of NAMD [20] with a time step of 2 fs and periodic boundary conditions (PBC). Cut-off for van der Waals and pairwise electrostatic interactions was set to 12 Å, particle mesh Ewald (PME) [31] was used in the treatment of electrostatic interactions. Bonds involving H atoms were constrained with SHAKE algorithm [32]. All systems were first minimized for 5000 steps, and then heated for 20 ps from 0 K to 300 K, with a harmonic restraint (10 kcal/mol·$Å^2$) on solute's non-H atoms. Restraint on the non-H atoms of the solute was kept for another 10 ns. Restraint was then removed, and NPT simulations were performed for 200 ns. Langevin dynamics thermostat was used for temperature control, with thermostat damping coefficient of 10 ps^{-1} for all the non-H atoms. Pressure control was carried out with Nosé-Hoover Langevin barostat, with damping time scale of 100 fs and Langevin piston oscillation period of 200 fs. Visualization and analysis of the trajectories are carried out with VMD [19]. For all the systems studied, dynamic equilibrium was observed to be achieved by 120 ns of the simulations. Therefore, unless otherwise specified, the data analysis will be based on the last 80 ns.

3.3. Results

3.3.1. siRNA Delivery and Its Silencing Activity in K562 Cells

Delivery of FAM-labeled siRNA with native and PrA-modified PEIs was investigated in K562 cells. The cellular uptake and silencing data are presented in Figure 3.4. From flow cytometry

analysis, substitution of PrA at low amounts, $\alpha = 0.26$ and $\alpha = 0.69$, resulted in substantially higher delivery than the native PEI ($\alpha = 0$); FAM-siRNA delivery was 11- and 10-fold greater than $\alpha = 0$ in $\alpha = 0.26$ and 0.69 systems, respectively (based on the MFI of FAM-siRNA). Increasing the substitution amount α further to 1.14 and 1.59, however, resulted in a significant decrease in the uptake efficiency of siRNA, where the mean delivery became almost comparable to that of native PEI (Figure 3.4a). Proportion of FAM-siRNA positive cells was well correlated with the change in MFI. Delivery with native PEI resulted in 2.7 ± 0.8% FAM-siRNA positive population, while PEIs with $\alpha = 0.26$ and $\alpha = 0.69$ yielded 48.4 ± 2.5% and 44.1 ± 0.5% FAM-siRNA-positive cells, respectively. Further increase in the substitution amount decreased the positive population, where the smallest proportion (4.1 ± 1.4%) of siRNA-positive cells was obtained at the highest $\alpha = 1.59$ (Figure 3.4b). We also compared the performance of PrA-modified 1.2 kDa PEIs in delivering the siRNA with that of versatile carrier HMW (25 kDa) branched PEI. Low substitution ratios displayed a comparable performance to that of 25 kDa PEI, i.e. in comparison to MFI of 25 kDa PEI, ~2-fold decrease in MFI was observed in systems $\alpha = 0.26$ and $\alpha = 0.69$ (Figure A.2a, b in Appendix A).

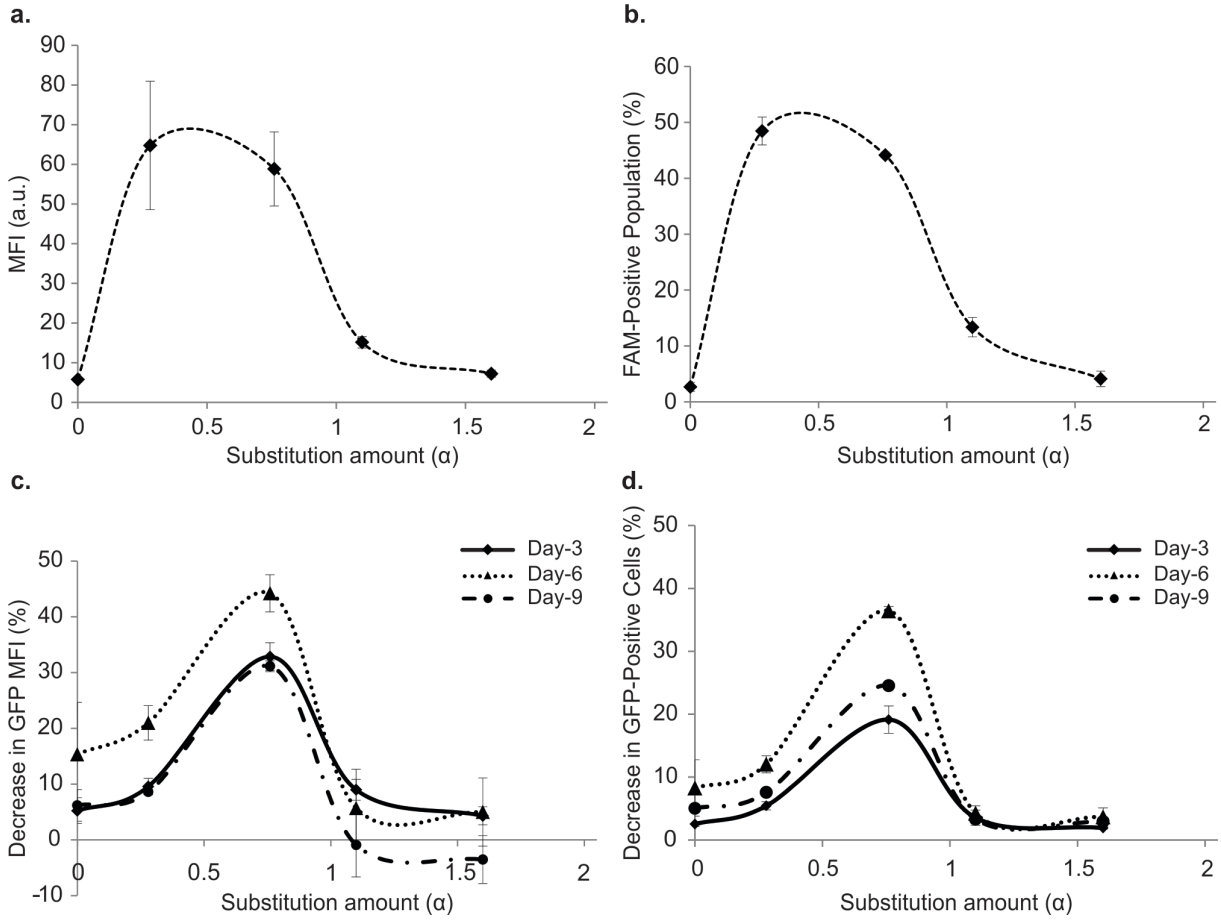

Figure 3.4. Delivery of FAM-labeled siRNA into K652 cells, and GFP silencing in GFP-expressing K652 cells, as a function of the PrA substitution amount in the polymers.
(a) Mean fluorescence intensity (MFI) and **(b)** percentage of FAM-siRNA positive K562 cells after 24 h exposure to complexes prepared with FAM-labeled siRNA and native or modified PEIs at polymer:siRNA ratio of 6:1 (w:w), with final siRNA concentration of 60 nM. **(c)** Decrease in mean GFP fluorescence and, **(d)** decrease in GFP-positive cell population after 3, 6 and 9 days of treatment with final siRNA concentration of 60 nM at polymer:siRNA ratio of 6:1 (w:w).

To explore the effect of PrA substitution on resulting silencing activity of delivered siRNA, we investigated GFP silencing in GFP-expressing K562 cells. GFP silencing was measured 3, 6 and 9 days post transfection, and represented with percent decrease in GFP MFI (normalized against no treatment) (Figure 3.4c) and decrease in the proportion of GFP-positive cells (Figure

3.4d). After 3 days, native PEI (α = 0) resulted in 5.2 ± 2.3% decrease in GFP MFI, while PEIs with α = 0.26 and α = 0.69 yielded 9.6 ± 1.5% and 32.9 ± 2.5% decrease, respectively. Substitution of more PrAs on PEI, however, decreased siRNA silencing activity; percent reduction in GFP MFI was 9.0 ± 1.9% and 4.3 ± 1.6% in polymers with α = 1.14 and α = 1.59, respectively **(**Figure 3.4c). The extent of silenced cell population was well correlated with the percent decrease in GFP MFI, i.e. 2.5 ± 0.4%, 5.4 ± 0.7%, 19.1 ± 2.2%, 3.5 ± 1.2% and 1.9 ± 0.2% of the population was silenced with polymers α = 0, α = 0.26, α = 0.69, α = 1.14 and α = 1.59 systems, respectively, 3 days after treatment **(**Figure 3.4d). The silencing activity of siRNA reached maximum 6 days post transfection, after which a reduction in silencing efficiency was observed on day 9. For example, the decrease in GFP MFI was 32.9 ± 2.5%, 44.2 ± 3.3% and 31.2 ± 1.0% for 3, 6 and 9 days with the polymer with α = 0.69 (best performing polymer). We also compared the efficacy of PrA conjugated 1.2 kDa PEIs with 25 kDa PEI in terms of the silencing activity of the delivered siRNAs (Figure A.2c, d in Appendix A). Among others, PEI with α = 0.69 displayed a comparable albeit not superior performance to that of 25 kDa PEI.

In order to further examine the effect of PrA substitution on the cellular interactions of complexes, we investigated the cytotoxicity of siRNA complexes prepared with polymers of different substitution amounts (Figure 3.5). Toxicity of the complexes increased with the increase in the polymer:siRNA weight ratio regardless of the PrA substitution amount (with α = 0 reaching plateau after polymer:siRNA ratio of 20:1); and >85% of the cells were viable at the polymer:siRNA weight ratio used in transfection studies (6:1). At the highest polymer:siRNA weight ratio tested, among different substitution amounts, α = 0.69 induced the highest toxicity followed by α = 0.26, with 28.4 ± 1.1% and 36.9 ± 3.6% cell viabilities, respectively. While α = 1.14 displayed intermediate toxicity levels with 52.3 ± 3.9% cell

viability; toxicity is significantly reduced in α = 1.59, and was similar to that of the native PEI (α = 0), 77.9 ± 2.3% of cells were viable in α = 1.59 compared to 79.7 ± 8.6% in the unmodified system (Figure 3.5, inset). In line with the trends observed in the cellular uptake and silencing experiments, PrA substitution at low amounts (α = 0.26 and 0.69), resulted in increased cellular interactions (hence cytotoxicity), while further increase in the substitution amount gradually reduced the toxicity of the polymers, with highest substitution reaching the toxicity of the native PEI. We also compared the cytotoxicity of native and PrA modified 1.2 kDa PEIs with 25 kDa PEI, and reported LMW native and/or modified PEIs to be substantially less toxic than their HMW counterpart at the highest polymer:siRNA weight ratios studied (Figure A.3).

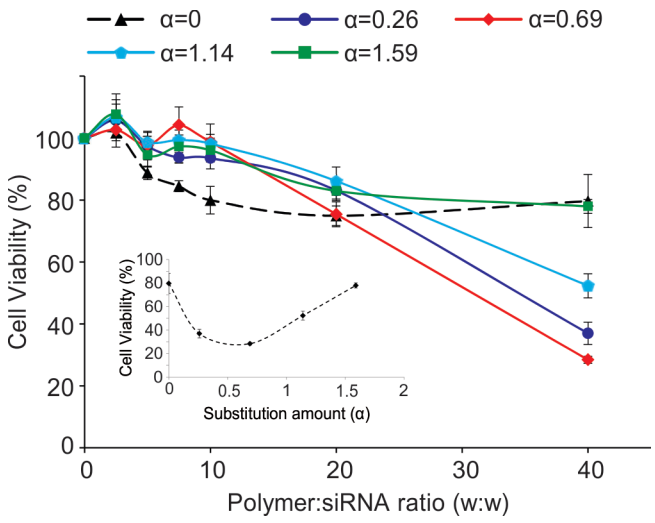

Figure 3.5. Cytotoxicity of siRNA complexes bearing polymers of different PrA substitution amounts prepared at various polymer:siRNA (weight:weight) ratios.
Relative viability of K562 cells after 72 h exposure to complexes of different PrA substitution amounts prepared at polymer:siRNA (w:w) ratios ranging from 0 to 40. The inset shows the relative cell viability as a function of PrA substitution amount (α) at polymer:siRNA (w:w) ratio of 40:1.

3.3.2. Mechanism for the Existence of Optimal Modification

From the experiments, it is clear that there is an optimal ratio for the modification of PEI with PrA groups, since grafting excess PrAs into PEI's structure abolished the siRNA delivery and its silencing activity in K562 cells. We therefore performed all-atom MD simulations to gain a better understanding of the change in PEI's performance by monitoring the molecular level interactions governing the complexation of siRNAs with hydrophobically modified PEIs. Final configurations of the simulation systems are given in right panel of Figure 3.3. The abilities of native and modified PEIs to complex and compact the siRNAs were assessed by calculating the radii of gyration (R_g) of 4 siRNAs in each system **(**Figure 3.6a). The decreasing R_g observed in the first 120 ns of the simulations is an indicator of the complexation process of siRNAs with the PEIs. Differences were observed in the kinetics of complexation among different simulation systems, i.e., in the system $\alpha = 0.75$, R_g of the 4 siRNAs is lower than that of others between ~38 and 73 ns, while $\alpha = 1$ gives higher R_g values among all systems within the first 30 ns and between 70 – 100 ns. Despite the differences observed in complexation kinetics, all the simulation systems reached plateau over the last 80 ns of the simulations. The average R_g values were calculated to be 25.86 ± 0.19 Å, 25.71 ± 0.17 Å, 25.94 ± 0.17 Å, 25.85 ± 0.14 Å, 26.00 ± 0.16 Å for the systems $\alpha = 0$, $\alpha = 0.25$, $\alpha = 0.75$, $\alpha = 1$ and $\alpha = 2$, respectively (Figure 3.6b). Given the similar values of R_g observed in each system, substitution of PrA did not seem to affect PEI's ability to compact siRNAs. We also explored the influence of PrA substitution on the compactness of the complexes by including all the siRNA and PEIs in the calculation of R_g; and again observed the almost negligible effect of modification (Figure A.4 in Appendix A). The sizes of the particles, prepared at polymer:siRNA weight ratio of 6:1, were experimentally

measured; the PrA substitution on the polymers did not show a clear trend on the hydrodynamic size of complexes, with particles ranging between 150 – 400 nm (Figure A.5 in Appendix A).

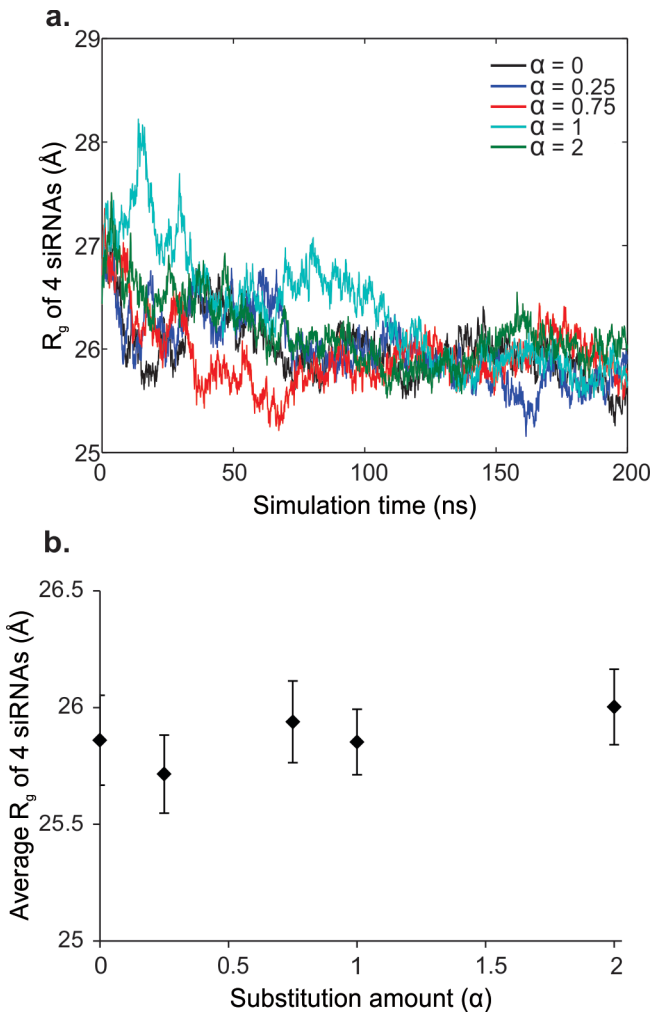

Figure 3.6. Compactness of the siRNAs within the complexes comprising PEIs with different PrA substitution amounts.
(a) R_g of the 4 siRNAs as a function of simulation time, and **(b)** average R_g values of the 4 siRNAs calculated over the last 80 ns of the simulations as a function of substitution amount.

The motion and the location of the hydrophobic moieties during complex formation are expected to be critical in determining the performance of the complexes. In order to monitor the location of PrA moieties, we calculated the radial distribution function (RDF) of PrA carbon

atoms as a function of the distance from the center of mass (COM) of the complex, r (Å) (Figure 3.7). Initial distribution of PrA carbons (Figure 3.7, left panel) is similar for systems $\alpha = 0.25$, $\alpha = 0.75$ and $\alpha = 1$ due to the similar arrangement of molecules in the initial configurations. The decrease in peak heights as α increases indicates the distribution of PrA becomes more homogenous with the increase in the substitution amount. In the system $\alpha = 2$, the most pronounced peak appears at smaller r because of the much more PrA carbon atoms it involves, which resulted in denser distribution of PrA close to the COM of the complex. As the systems reach dynamic equilibrium (Figure 3.7, right panel), in the system with $\alpha = 0.25$, the first and most prominent peak is observed at r = 13.88 Å, followed by the second peak located at r = 18.88 Å. Similarly, in the system $\alpha = 0.75$, two peaks are present, the first located at r = 13.38 Å and the second at r = 17.63 Å. Between these two low substituted systems, a more uniform distribution is observed as the extent of PrA substitution increased from 0.25 to 0.75. No significant changes are apparent in the motion of PrA substituents between initial and final configurations; in particular, there are no PrA moieties within the 10 Å from the COM of the complexes. The most drastic change is observed in the system $\alpha = 1$; the hydrophobic moieties started to migrate into the core region of the complex, indicated by the two sharp peaks located as close to the COM of the complex as 0.38 Å and 1.63 Å. It is clear that a considerable number of PrA moieties are now distributed within the first 10 Å from the COM of the complex, as opposed to being located beyond 10 Å as observed in the $\alpha = 0.25$ and $\alpha = 0.75$ systems. This phenomenon holds true in the system $\alpha = 2$ as well; however, it should be considered that some PrA carbon atoms were already present within 5 Å from the COM of the complex in its initial configuration.

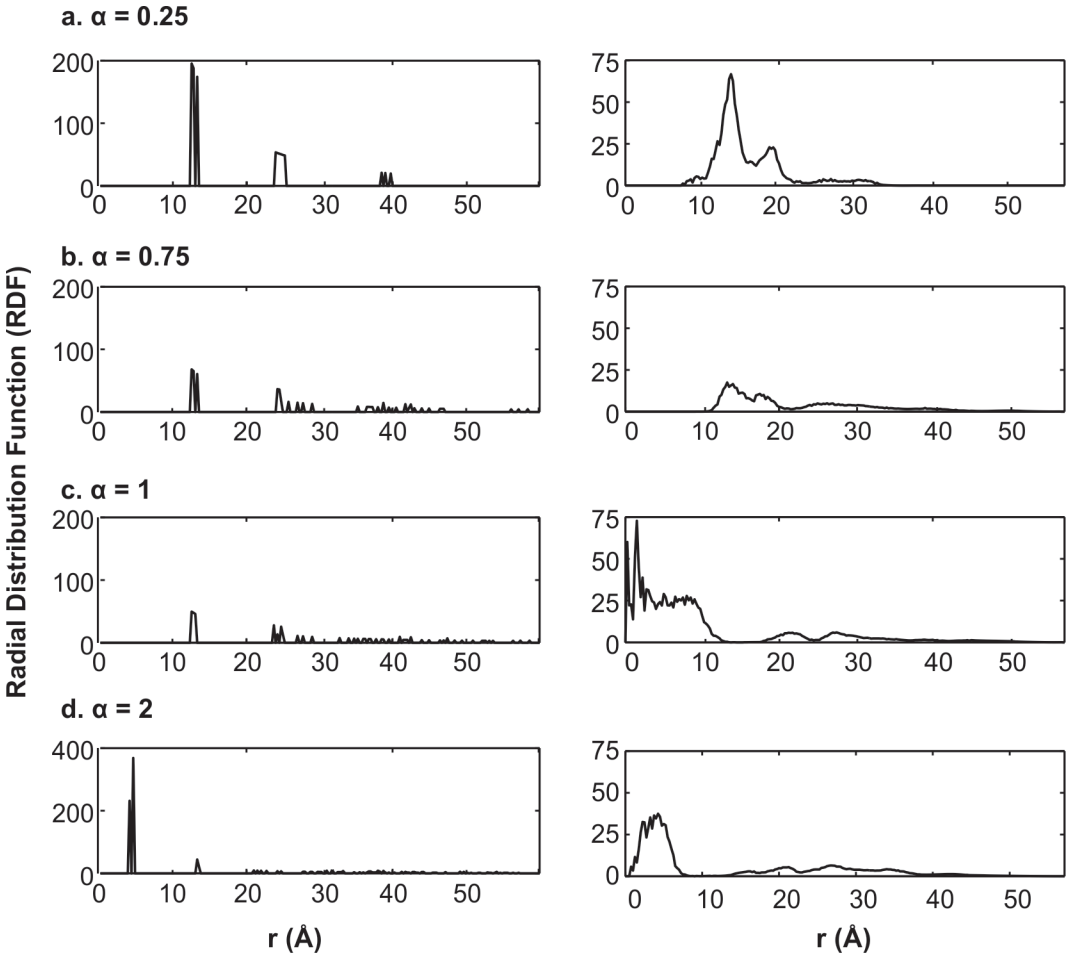

Figure 3.7. Radial distribution function of carbon atoms of hydrophobic PrA moieties as a function of the distance from the center of mass of the complex.
RDF in the initial configuration is given in the left panel, and the average over the last 80 ns of the simulations is given in the right panel, in the systems **(a)** α = 0.25, **(b)** α = 0.75, **(c)** α = 1 and **(d)** α = 2, respectively.

Since surface hydrophobicity might influence the interactions of the complexes with cell membranes (and uptake), the migration of PrA moieties into the core of the complex at high substitution ratios raises the question of the density of PrA groups on particle surfaces. Each complex is anisotropic; hence, in order to define the surface of the complexes, we approximated each complex by a sphere, and calculated the effective radii of the spheres from R_g (details on the calculation is given in Section A.4 of Appendix A). Here, R_g is selected as a geometrical

variable for the definition of the surface of the anisotropic complexes. Other choices of geometrical variable are possible; for instance, in the context of molecular recognition, hydrodynamic radius of the complexes (R_H) could be of more importance, particularly in regards to the hydrodynamic properties of the resulting particles. However, here our aim is to define an effective surface of the complexes, and selecting R_g allows us to perform the mapping from the anisotropic complex to a perfect sphere. Upon determining the surface of each complex, the number of PrA Cs outside the spherical surface is then counted from the number integral over RDF of PrA Cs averaged over the last 80 ns of the simulations (Figure A.6 in Appendix A), and divided by the surface area of the sphere to calculate the surface density of PrA Cs.

The calculated surface density is plotted in Figure 3.8a. A non-monotonic change in the surface PrA density is observed with the increase in the extent of substitution. Lower substitution ratios resulted in lower surface densities. As a consequence of having all the modified PEIs amidst the 4 siRNAs, there are no PrA moieties on the surface in the system $\alpha = 0.25$. In the system $\alpha = 0.75$, however, all the modified PEIs were placed homogenously to surround the 4 siRNAs, hence there is a slight increase in the surface density of PrAs. Apart from the differences in the number of PrA moieties, the initial configurations of the systems $\alpha = 1$ and $\alpha = 2$ are similar to that of $\alpha = 0.75$. The highest surface density is observed in system $\alpha = 1$ among all systems; however, further increasing the substitution extent to $\alpha = 2$ lowered the surface groups. This could be explained in the context of hydrophobic interactions that minimize the number of PrA moieties exposed to water via the migration to the core (Figure 3.7c, d), as observed above. However, if the hydrophobic interactions are not strong enough to drive the PrAs to the core, considerable number of PrAs still remains on the surface, as in the case of the system $\alpha = 1$. Increasing the substitution extent to a higher level ($\alpha = 2$) provided

enough hydrophobic driving force, hence lowered the surface density. The proportions of the PrA moieties inside the complexes are in fact 100%, 91%, 82% and 92% for the systems α = 0.25, α = 0.75, α = 1 and α = 2, respectively. Considering the number of PrA Cs in the system α = 2 (= 96), it is evident that it has the most hydrophobic core among all systems.

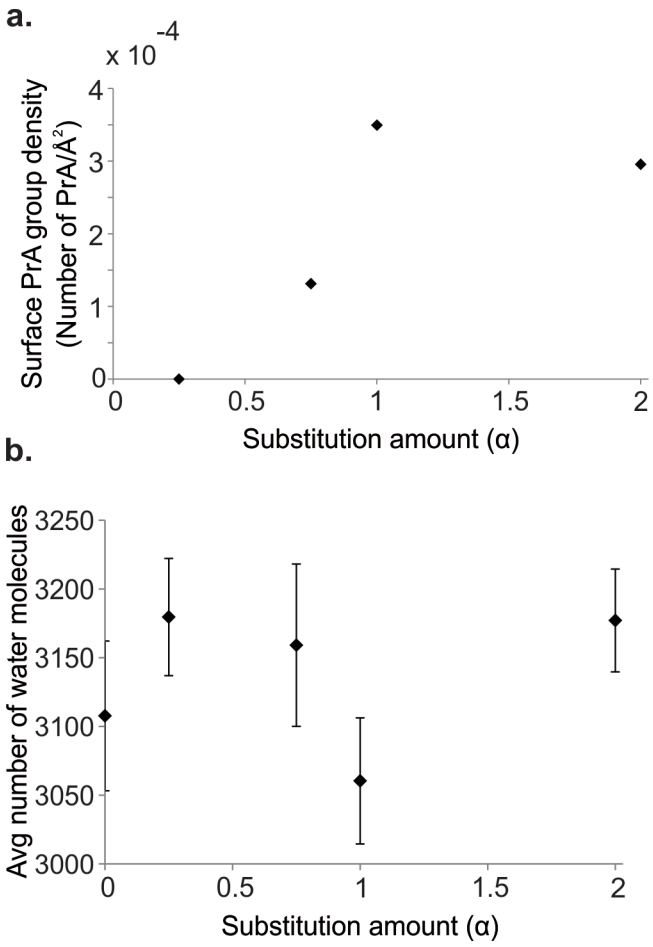

Figure 3.8. Effect of PrA substitution on surface hydrophobicity and surface hydration of the complexes.
(a) Surface density of the PrA moieties, **(b)** number of water molecules in the hydration shell of siRNAs/PEIs, as a function of the substitution amount (α).

The variation in the surface density of the PrA moieties made us wonder about the change in the surface hydration of the complexes. Hydration of the surfaces with hydrophobic domains

plays a major role in biomolecular recognition [33, 34]; hence to explore the level of hydration of the complexes in a quantitative manner, we calculated the number of water molecules in the hydration shell of siRNAs and PEIs. Here we define the hydration shell to be 3 Å from any siRNA/PEI atom. As the complexes are formed, water molecules are expelled from their interior locations to the periphery (Section A.5 in Appendix A). The average number of water molecules in the hydration shell upon reaching dynamic equilibrium is plotted in Figure 3.8b. There exists an inverse correlation between the surface density of PrA groups (Figure 3.8a) and the level of hydration. As a consequence of the lower PrA surface density of the systems $\alpha = 0.25$, $\alpha = 0.75$ and $\alpha = 2$, the complexes are more hydrated given by the higher number of water molecules in the hydration shell. Loss of hydration in the system $\alpha = 1$ is due to water molecules being expelled from the periphery as a result of the high PrA surface density, revealing the complex formed at $\alpha = 1$ to be the most hydrophobic one among others.

To explore the effect of substituted PrA moieties on PEI's binding capability to siRNA, we plot the number of PEI Ns in close contact with siRNA N/O atoms (Figure 3.9a). Here we define the close contact distance to be 4 Å from any siRNA N/Os, i.e., the distance at which a direct H-bond could be formed between PEI amines and siRNA N/O atoms [17]. Grafting PrAs into PEIs structure increased the interactions between PEIs and siRNAs in general, given the upward trend in the number of close contacts established with the increase in the substitution extent, with $\alpha = 2$ giving the highest number. The hydrophobic attractions among PrA moieties drive them to the core of the complex, along with their associated PEIs. Clustering in the core area, then, increases the number of PEI Ns in close contact with siRNAs, evident from the higher number of close contacts established in systems $\alpha = 1$ and $\alpha = 2$ in comparison with the lower substituted systems.

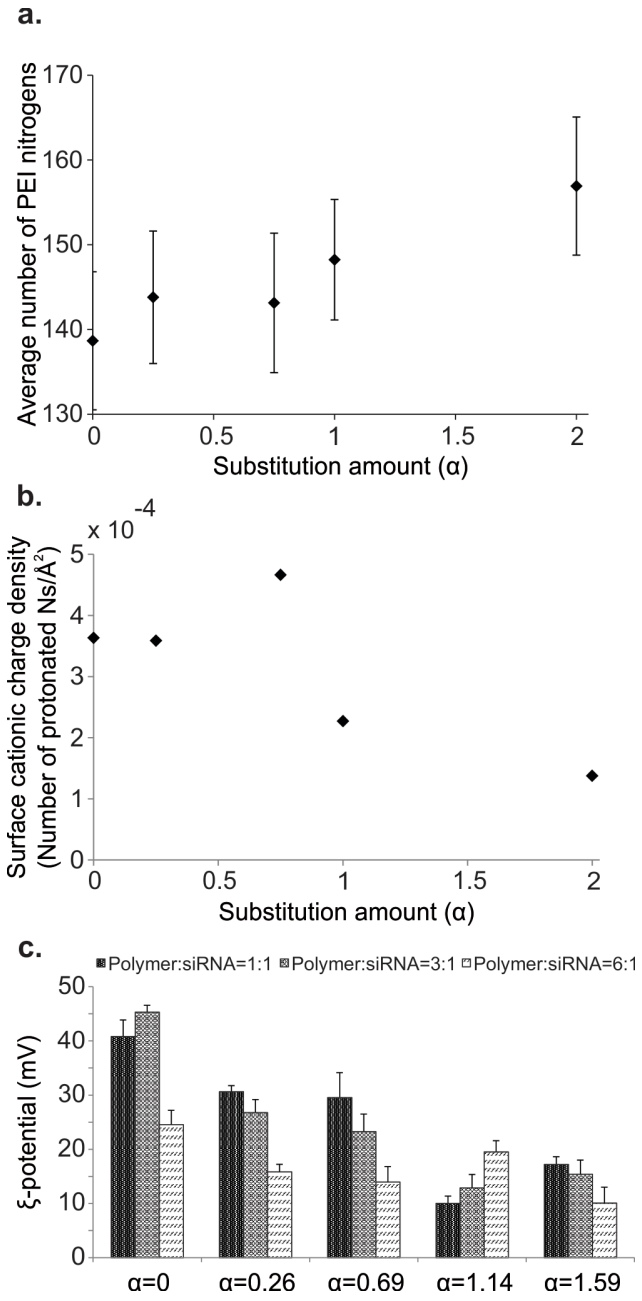

Figure 3.9. Effect of PrA substitution on PEI's binding capability to siRNA and cationic surface charge of the complexes.

(a) Average number of PEI N atoms in close contact with siRNAs, **(b)** surface cationic charge density, as a function of the substitution amount (α). **(c)** ζ-potential of the complexes of different substitution amounts, prepared at polymer:siRNA weight ratios of 1:1, 3:1 and 6:1.

The higher number of contacts established between siRNAs and PEIs in high substitution amounts due to PrA migration into the core could possibly affect the assembly of cationic amine groups on the complex surfaces, hence might have an impact on their cellular uptake. In order to monitor the change in the cationic surface charge of complexes with PrA substitution amounts, we explored the density of protonated PEI Ns on the surface of the complexes by following the procedure described previously for the definition of the spherical complex surfaces. The number of protonated PEI Ns outside the spherical surface is then counted from the number integral over the RDF of protonated PEI Ns averaged over the last 80 ns of the simulations (Figure A.9b in Appendix A) and divided by the surface area of the sphere (details are given in Section A.6 of Appendix A). The resulting surface cationic charge density is plotted in Figure 3.9b. Moderate enhancements in the hydrophobicity of the complexes gave rise to a higher cationic surface charge in comparison with the unmodified system ($\alpha = 0$); $\alpha = 0.75$ had the highest cationic surface charge among all systems. However, further increasing the substitution extent significantly reduced the number of cationic groups on the surface. In fact, system $\alpha = 1$ and $\alpha = 2$ have substantially lower cationic surface charge than the unmodified system, $\alpha = 0$, with $\alpha = 2$ giving the lowest surface charge. It is evident that the new assembly mechanism brought about by the high amount of PrA moieties affected the complexation between siRNAs and PEIs and caused the PEIs to be dragged to the core; which in turn resulted in a deleterious effect on the cationic surface charge of the complexes. Surface charge (ζ-potential) of the particles was also investigated to explore the effect of PrA substitution experimentally (Figure 3.9c). Complexes were prepared at different polymer:siRNA ratios (1:1, 3:1 and 6:1). We observed slightly more positively charged particles (higher ζ-potential) for $\alpha = 0$, 0.26 and 0.69 in polymer:siRNA weight ratios of 1:1 and 3:1 than the highest ratio tested,

6:1. A decreasing trend in ζ-potential with the increase in PrA substitution amount was apparent irrespective of the polymer:siRNA weight ratio studied; however it was more pronounced at the lower polymer:siRNA weight ratios, 1:1 and 3:1. Along the lines of the surface charge of complexes from the simulation trajectories, here we report the adverse effect of excess PrA substitution on the surface charge of the complexes again, with more than 2-fold decrease from $\alpha = 0$ to $\alpha = 1.59$ in all the polymer:siRNA weight ratios tested.

Non-bonded interactions with PEIs might cause changes in siRNA's structure. H-bonding is critical in maintaining the structure of nucleic acids via Watson-Crick base pairing; therefore, we examined the H-bonding pattern between the two strands of siRNAs during complex formation. The downward trend within the first ~100 ns of the simulations indicates the loss of siRNAs' structure as a result of complexation (Figure A.10a in Appendix A). For a quantitative analysis of structural changes, the total number of H-bonds is averaged upon reaching dynamic equilibrium (Figure 3.10a). In comparison with the unmodified system ($\alpha = 0$), PrA substitution altered the structure of siRNAs given by the loss of H-bonding in systems $\alpha = 0.25$, $\alpha = 0.75$ and $\alpha = 2$. Considering the majority of the PrA moieties are located inside of the complexes at these substitution ratios, alterations in siRNA's structure are expected as a result of the steric effect introduced by PrA moieties. Consistent with its highest surface PrA density, the most stable siRNA structure is achieved in the system $\alpha = 1$.

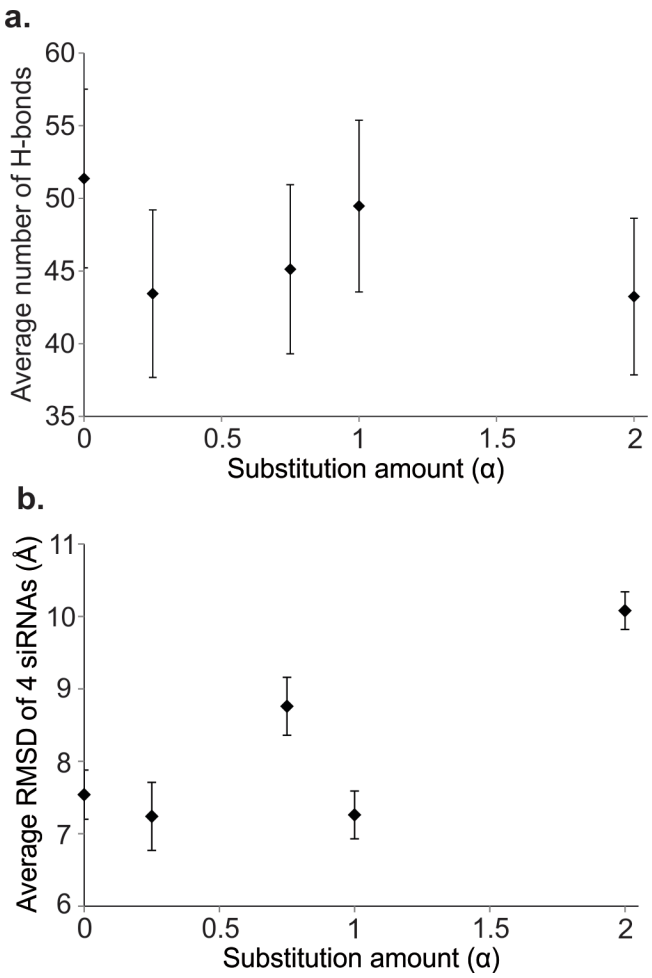

Figure 3.10. Effect of PrA substitution on the structural stability of the siRNAs in the resulting complexes.
(a) Total number of siRNA H-bonds. Each system has 4 siRNA molecules; the H-bonds established between the two strands of each siRNA is summed over the 4 siRNA molecules, and then averaged over the last 80 ns. **(b)** RMSD values of the 4 siRNAs with respect to their initial configurations as a function of the substitution amount (α).

The structural changes in siRNA upon complexation can be further confirmed by examining the root mean square deviation (RMSD) of the 4 siRNAs with respect to their initial configurations (Figure 3.10b). The time evolutions of the RMSD for the four systems are given in Figure A.10b. The upward trend within the first ~120 ns is due to the profound deviations caused by complex formation. The systems $\alpha = 0$, $\alpha = 0.25$ and $\alpha = 1$ displayed very similar

RMSD trends throughout the simulations. The relatively higher deviation in the system α = 0.75 could be attributed to its kinetics of complexation, i.e. two PrA substituted PEIs were observed to be fully solvated within the first ~110 ns, and they established contacts with the complex around ~110 and ~140 ns, respectively, causing siRNAs to be more deviated as a result of having more polymers in contact. Among all the other system, the highest deviation is observed with the system α = 2. Supporting the previous discussion on the migration of PrA moieties to the core of the complex, having more contacts built with PEIs and losing siRNA structure at the highest substitution, the highest deviation is observed at α = 2.

3.3.3. Discussion

PrA modifications investigated in this chapter were aimed to increase the performance of less cytotoxic albeit non-functional LMW PEI. Enhancements in PEI's gene delivery capability and resulting gene silencing capacity of siRNA were observed at low substitution amounts, whereas a significant reduction in PEI's performance was detected as the extent of PrA substitution, hence the hydrophobicity of PEI, increased further. This interesting observation suggests that a certain balance between hydrophobicity and hydrophilicity is needed to achieve the optimal transfection efficiency and silencing capability. This was not the case with moderately longer chain aliphatic lipid substituents (8C substitution), where a gradual increase in transfection efficiency was obtained in proportion with substitution amounts. However, a similar phenomenon was reported previously by others with shorter hydrophobes. Conjugation of varying lengths of alkyl chains, ethyl, octyl and deodecyl, into 1.8 kDa PEI showed that shorter hydrophobic substituent ethyl was capable of inducing higher transfection efficiencies than their longer counterparts, octyl and deodecyl. Moreover, extending the conjugation degree of ethyl resulted in higher transfection at the intermediate conjugation levels, while at the highest

substitution (i.e. when 100% of the amines were conjugated) transfection efficiency of PEI was drastically decreased [14]. A different study explored the effect of hydrophobic/hydrophilic balance of 25 kDa PEI on its performance by grafting amino acids, one with a short side chain, alanine (Ala, 1C), and one with a longer side chain, leucine (Leu, 4C). They reported that moderate enhancements on the hydrophobicity of 25 kDa PEI via conjugation of Ala resulted in higher transfection efficiencies than the engraftment of Leu [35]. Although these experimental studies revealed the importance of hydrophobic/hydrophilic balance of carrier vectors for an optimal performance, no mechanistic findings were reported to explain the deleterious effects of increasing hydrophobicity. It was proposed that hydrophobic groups cluster together and possibly affect PEI's protonation ratio [35], but no evidence was provided to validate this hypothesis.

Experiments accompanied by MD simulations on caprylic (8C) and linoleic acid (18C) substituted 2 kDa PEI revealed one possible mechanism for non-monotonic relationship between substitution level and cellular uptake. Increasing the substitution extent of caprylic acid was reported to improve siRNA delivery monotonically from *in vitro* experiments. In line with experimental observations, MD simulations indicated higher stability of the complexes in the presence of more caprylic acid substituents, due to the stabilizing effect of enhanced lipid-lipid association among different PEI molecules. Increasing the substitution extent of linoleic acid, on the other hand, did not always lead to an increase in PEI's performance. MD trajectories showed self-association of the aliphatic lipid tails located on the same PEI molecule, which gave rise to steric hindrance and adversely influenced siRNA complexation [17]. In the work presented in this chapter, due to PrA's short nature, association of PrA groups was not observed. However, gradual increase in the extent of PrA substitution gave rise to an interesting

phenomenon, namely migration of hydrophobic PrA groups into the core of the complex to minimize the interactions with the aqueous phase. Clustering in the complex core in the highest substitution caused a reduction in the surface density of PrA groups, and hence the surface hydrophobicity. Peripheral hydrophobic moieties may facilitate the interactions of the complexes with the plasma membrane and expedite the cellular uptake of the complexes. Absence of surface hydrophobicity might possibly impede and/or abolish the uptake, especially if the surface cationic charge is not sufficient to protect and translocate the siRNA cargo along the delivery path. We reported that, although all the simulated native and modified PEIs carried the same cationic charge, intermediate PrA substitution amounts gave rise to a higher cationic charge on the complex surface compared to the unmodified and low substituted systems, whereas surface cationic charge of the complexes was drastically decreased as the extent of substitution was increased. The hydrophobic force driving the PrA moieties into the core dragged the associated PEIs; that was evident from the highest number of PEI Ns in close contact with siRNAs at the highest amount of PrA substitution. This, in turn, reduced the amount of PEI's protonated amine groups on the complex surface. A relationship with the cationic surface charge and the assembly mechanism of carrier vectors was previously reported by Posocco and coworkers [36]. The analysis carried out from the mesoscale simulation trajectories revealed that different self-assembly mechanisms brought by cholesterol modified generation 1 and 2 spermine dendrimers controlled the cationic surface charge density of the aggregates. Less effective dendrimer assembly led to a reduction in cationic surface charge which affected their DNA packing capability as a consequence [36]. In line with their argument, here we reported that the new complexation mechanism induced by the presence of the abundant PrA moieties has a profound effect on the cationic surface charge of the complexes. This phenomenon was

further validated with experimental ζ-potential measurements, where we reported more than 2-fold decrease in the surface charge at the highest PrA substitution amount in comparison with the unmodified polymer. Moreover, cationic surface charge of the nanoparticles has known to possibly induce membrane damage, hence cytotoxicity [37]. MTT assay showed polymers with low/moderate PrA substitution amounts to be more toxic than their high substituted counterparts at high polymer concentrations. This is, again, another indicative of the loss of the cationic charge in the presence of abundant PrA modifications. Coupled with the loss of surface hydrophobicity at the highest substitution, it resulted in loss of cellular uptake and gene silencing capability of siRNA, as is evident from the *in vitro* experiments.

The structural stability of siRNA is also affected by the clustering of PrA moieties at the core of the complex. Both the H-bonding and RMSD data provided such evidence; i.e. at the highest substitution amount, siRNAs deviated the most with respect to their initial configurations while displaying a reduced amount of H-bonding compared to that of unmodified PEI. Loss of siRNA's structural stability is worrisome as it could most likely affect the overall activity of the siRNA, and hence the desired pharmaceutical effect. Coupling the changes in the surface hydrophobicity and cationic charge density of the complexes with the observed structural instabilities, siRNAs might become more vulnerable to degrading nucleases in the presence of high PrA modifications on PEIs, which consequently might cause the loss siRNA's biological activity.

3.4. Conclusions

LMW (1.2 kDa) PEI was hydrophobically modified with varying amounts of PrA moieties. Cellular uptake and silencing activity of the complexes was enhanced at low/moderate substitution amounts, while further increase in PrA substitution abolished siRNA uptake and

hence the silencing activity. All-atom MD simulations revealed a new siRNA-PEI assembly mechanism in the high presence of PrA substituents: PrA moieties were observed to migrate into the core region of the complex under the hydrophobic driving force for minimizing their exposure to the aqueous phase. This new assembly mechanism led to: (*i*) higher surface hydrophobicity and (*ii*) higher surface charge density at intermediate substitution amount; while increasing the substitution extent further caused detrimental changes on surface hydrophobicity and cationic charge density, as well as siRNA stability. The molecular details obtained from the simulation trajectories elucidated possible mechanistic details on the effect of hydrophobic/hydrophilic balance of the carrier vectors in complex assembly and the resulting structure – function relationships, and they should provide valuable insights in the design of novel hydrophobic substituents.

3.5. Acknowledgements

Compute Canada and high performance computing facility at National Institute for Nanotechnology, Edmonton, Canada were gratefully acknowledged for providing computing resources and technical support. This work is funded by Natural Sciences and Engineering Research Council of Canada, Canadian Institutes of Health Research, an NSERC CREATE Scholarship (H. Uludağ; NCPRM from University of Laval), Alberta Innovates-Technology Futures, and Canada Foundation for Innovation. We thank Dr. Afsaneh Lavasanifar (Faculty of Pharmacy & Pharmaceutical Sciences, University of Alberta) for access to the Zetasizer.

3.6. References

1. Liu Z, Zhang Z, Zhou C, & Jiao Y (2010) Hydrophobic Modifications of Cationic Polymers for Gene Delivery. *Prog. Polym. Sci.* 35:1144–1162.
2. Fire A, Xu S, Montgomery MK, Kostas SA, Driver SE, & Mello CC (1998) Potent and Specific Genetic Interference by Double-stranded RNA in Caenorhabditis Elegans. *Nature* 391(6669):806-811.
3. Boussif O, Lezoualc'h F, Zanta MA, Mergny MD, Scherman D, Demeneix B, & Behr JP (1995) A Versatile Vector for Gene and Oligonucleotide Transfer into Cells in Culture and In Vivo: Polyethylenimine. *Proc. Natl. Acad. Sci. U.S.A.* 92(16):7297-7301.
4. Demeneix B & Behr JP (2005) Polyethylenimine (PEI). *Adv. Genet.* 53:217-230.
5. Aliabadi HM, Landry B, Sun C, Tang T, & Uludag H (2012) Supramolecular Assemblies in Functional siRNA Delivery: Where Do We Stand? *Biomaterials* 33(8):2546-2569.
6. Godbey WT, Wu KK, & Mikos AG (1999) Size Matters: Molecular Weight Affects the Efficiency of Poly(ethylenimine) as a Gene Delivery Vehicle. *J. Biomed. Mater. Res.* 45(3):268-275.
7. Fischer D, Bieber T, Li Y, Elsasser HP, & Kissel T (1999) A Novel Non-Viral Vector for DNA Delivery Based on Low Molecular Weight, Branched Polyethylenimine: Effect of Molecular Weight on Transfection Efficiency and Cytotoxicity. *Pharm. Res.* 16(8):1273-1279.
8. Fischer D, Li Y, Ahlemeyer B, Krieglstein J, & Kissel T (2003) In Vitro Cytotoxicity Testing of Polycations: Influence of Polymer Structure on Cell Viability and Hemolysis. *Biomaterials* 24(7):1121-1131.
9. Neamnark A, Suwantong O, Bahadur RK, Hsu CY, Supaphol P, & Uludag H (2009) Aliphatic Lipid Substitution on 2 kDa Polyethylenimine Improves Plasmid Delivery and Transgene Expression. *Mol. Pharmaceutics* 6(6):1798-1815.
10. Incani V, Lavasanifar A, & Uludag H (2010) Lipid and Hydrophobic Modification of Cationic Carriers on Route to Superior Gene Vectors. *Soft Matter* 6:2124-2138.
11. Han S, Mahato RI, & Kim SW (2001) Water-Soluble Lipopolymer for Gene Delivery. *Bioconjugate Chem.* 12(3):337-345.
12. Furgeson DY, Cohen RN, Mahato RI, & Kim SW (2002) Novel Water Insoluble Lipoparticulates for Gene Delivery. *Pharm. Res.* 19(4):382-390.
13. Bajaj A, Kondaiah P, & Bhattacharya S (2008) Synthesis and Gene Transfection Efficacies of PEI-Cholesterol-based Lipopolymers. *Bioconjugate Chem.* 19(8):1640-1651.
14. Teo PY, Yang C, Hedrick JL, Engler AC, Coady DJ, Ghaem-Maghami S, George AJ, & Yang YY (2013) Hydrophobic Modification of Low Molecular Weight Polyethylenimine for Improved Gene Transfection. *Biomaterials* 34(32):7971-7979.

15. Pettersen EF, Goddard TD, Huang CC, Couch GS, Greenblatt DM, Meng EC, & Ferrin TE (2004) UCSF Chimera - A Visualization System for Exploratory Research and Analysis. *J. Comput. Chem.* 25(13):1605-1612.

16. Utsuno K & Uludag H (2010) Thermodynamics of Polyethlyenimine-DNA Binding and DNA Condensation. *Biophys. J.* 99(1):201-207.

17. Sun C, Tang T, & Uludag H (2013) A Molecular Dynamics Simulation Study on the Effect of Lipid Substitution on Polyethylenimine Mediated siRNA Complexation. *Biomaterials* 34(11):2822-2833.

18. Schrödinger Release 2014-2: Maestro V, Schrödinger, LLC, New York, NY, 2014.

19. Humphrey W, Dalke A, & Schulten K (1996) VMD: Visual Molecular Dynamics. *J. Mol. Graphics* 14(1):33-38.

20. Phillips JC, Braun R, Wang W, Gumbart J, Tajkhorshid E, Villa E, Chipot C, Skeel RD, Kale L, & Schulten K (2005) Scalable Molecular Dynamics with NAMD. *J. Comput. Chem.* 26(16):1781-1802.

21. Jorgensen WL, Chandrasekhar J, Madura JD, Impey RW, Klein ML (1983) Comparison of Simple Potential Functions for Simulating Liquid Water. J. Chem. Phys. 79: 926-935.

22. Sun C, Tang T, Uludag H, & Cuervo JE (2011) Molecular Dynamics Simulations of DNA/PEI Complexes: Effect of PEI Branching and Protonation State. *Biophys. J.* 100(11):2754-2763.

23. Vanommeslaeghe K, Hatcher E, Acharya C, Kundu S, Zhong S, Shim J, Darian E, Guvench O, Lopes P, Vorobyov I, & Mackerell AD, Jr. (2010) CHARMM General Force Field: A Force Field for Drug-like Molecules Compatible with the CHARMM All-atom Additive Biological Force Fields. *J. Comput. Chem.* 31(4):671-690.

24. Berendsen HJC, Postma JPM, von Gunsteren WF, Hermans J (1981) Interaction Models for Water in Relation to Protein Hydration. *Intermolecular Forces*, The Jerusalem Symposia on Quantum Chemistry and Biochemistry, eds Pullman B (Springer, Dordrecht, Holland), Vol 14, pp 331-342.

25. Mahoney MW, Jorgensen WL (2000) A Five-site Model for Liquid Water and the Reproduction of the Density Anomaly by Rigid, Nonpolarizable Potential Functions. *J. Chem. Phys.* 112: 8910-8922.

26. Nutt DR, Smith JC (2007) Molecular Dynamics Simulations of Proteins: Can the Explicit Water Model Be Varied? *J. Chem. Theory Comput*. 3: 1550-1560.

27. Brooks BR, Bruccoleri RE, Olafson BD, States DJ, Swaminathan S, & Karplus M (1983) Charmm – A Program for Macromolecular Energy, Minimization, and Dynamics Calculations. *J. Comput. Chem.* 4:187–217.

28. MacKerell AD, Brooks B, Brooks CL, Nilsson L, Roux B, Won Y, & Karplus M (1998) CHARMM: The Energy Function and Its Parameterization with an Overview of the Program. *The Encyclopedia of Computational Chemistry*, (John Wiley & Sons, Chichester), pp 271-277.

29. Foloppe N & MacKerell J, A.D. (2000) All-Atom Empirical Force Field for Nucleic Acids: I. Parameter Optimization Based on Small Molecule and Condensed Phase Macromolecular Target Data. *J. Comput. Chem.* 21:86-104.

30. MacKerell AD & Banavali NK (2000) All-atom Empirical Force Field for Nucleic Acids: II. Application to Molecular Dynamics Simulations of DNA and RNA in Solution. *J. Comput. Chem.* 21(2):105-120.

31. Darden T, York D, & Pedersen L (1993) Particle Mesh Ewald: An N · log(N) Method for Ewald Sums in Large Systems. *J. Chem. Phys.* 98:10089-10092.

32. Ryckaert JP, Ciccotti G, & Berendsen HJC (1977) Numerical Integration of the Cartesian Equations of Motion of a System with Constraints: Molecular Dynamics of N-alkanes. *J. Comput. Phys.* 23(3):327-341.

33. Blokzijl W & Engberts JBFN (1993) Hydrophobic Effects. Opinion and Facts. *Angew. Chem. Int. Ed. Engl.* 32:1545-1579.

34. Cheng YK & Rossky PJ (1998) Surface Topography Dependence of Biomolecular Hydrophobic Hydration. *Nature* 392(6677):696-699.

35. Thomas M & Klibanov AM (2002) Enhancing Polyethylenimine's Delivery of Plasmid DNA into Mammalian Cells. *Proc. Natl. Acad. Sci. U.S.A.* 99(23):14640-14645.

36. Posocco P, Pricl S, Jones S, Barnard A, & Smith DK (2010) Less Is More – Multiscale Modelling of Self-assembling Multivalency and Its Impact on DNA Binding and Gene Delivery. *Chem. Sci.* 1:393–404.

37. Frohlich E (2012) The Role of Surface Charge in Cellular Uptake and Cytotoxicity of Medical Nanoparticles. *Int. J. Nanomed.* 7:5577-5591.

4. Probing the Effect of miRNA on siRNA – PEI Complexes[X]

[X] A version of this chapter has been published. Adapted with permission from Meneksedag-Erol D, Tang T, & Uludağ H (2015) Probing the Effect of miRNA on siRNA−PEI Polyplexes. *J. Phys. Chem. B* 119: 5475−5486. Copyright (2015) American Chemical Society.

4.1. Introduction

Altering gene expression with the delivery of nucleic acids has been of a great interest to researchers since the discovery of RNA interference (RNAi) [1]. Post transcriptional gene silencing with the delivery of short interfering RNAs (siRNAs) has proven to be a promising approach in the treatment of cancer and various genetic disorders [2]. Challenges encountered in the use of siRNAs have led to a search for efficient delivery systems, and have driven the design of non-viral carrier vectors which assemble siRNAs into nanoscale complexes [3]. Among others, polymeric carriers have proven to be effective due to their capability to be engineered and functionalized at will. Polyethylenimine (PEI) is one of the most promising polycationic carriers bearing certain superior properties such as high buffering capacity (important for endosomal escape) and cellular uptake [4]. In an efficient delivery process, siRNAs get encapsulated by the carrier vectors to form complexes, which are then uptaken via endocytosis, followed by the escape into cytosol and release of siRNAs from their carriers [5]. The guide strand in the siRNA can be recognized by Argonautes to form the core of RNA-induced silencing complex (RISC) [6] only if siRNAs are released from their carriers. Although a large number of systematic studies have been conducted on the intracellular stages of the delivery process (see computational [7-10] and experimental [11, 12] studies as examples), mechanistic details underlying the dissociation of complexes are yet to be explored.

One mechanism proposed for the dissociation of the complexes is based on the proton sponge effect [13] for carriers that possess a high H^+-buffering capacity, such as PEI. This mechanism suggests that PEI is able to resist pH changes within the endocytic vesicles due to having amine groups that can be protonated under the low pH environment of the endosomes [4]. During osmotic swelling and rupture of the vesicles containing PEI complexes, complex

integrity might be affected, and complexes may become prone to dissociation. However, controversial reports exist in the literature on the validity of this mechanism [14, 15]. Irrespective of the proton sponge effect, the dynamic environment along the delivery pathway is likely to affect the integrity of complexes. Over the years, heparan-sulfate glycosaminoglycans (HSGAGs) have been used to test the stability of polynucleotide complexes *in vitro*. HSGAGs are complex polysaccharides located either on the cell membrane or in the extracellular matrix of eukaryotic cells. They are known for their role in cell signaling, tumor angiogenesis and metastasis in a variety of cancer types by modulating cell-cell interactions [16]. Heparin, a highly sulfated member of HSGAG family, has been widely adopted for testing the stability of complexes, and reported as an effective binding agent to cationic carriers [17-20], which competes with siRNA binding and can induce dissociation of the complexes.

Bearing in mind that an efficient transfection requires dissociation of the complex upon endosomal escape, what triggers the release of siRNA from the carriers, and the role of intracellular molecules on the integrity of complexes need to be understood. Since the electrostatic attraction between siRNAs and cationic carriers is the main driving force in the formation of complexes [21], anionic intracellular molecules could be potent to destabilize the complexes. The microRNAs (miRNAs) are relatively short (~22 nucleotides per strand) non-coding RNAs that are highly anionic. They are involved in many cellular processes, such as differentiation, apoptosis, and proliferation, and recently employed in transcriptional and post-transcriptional silencing of target genes [22, 23]. miRNA-21 (miR-21) is one of the first identified mammalian miRNAs [24], known to be aberrantly expressed in several types of cancers, e.g. breast, colon, lung, pancreas, prostate, stomach; and its up-regulation is associated with carcinogenesis and tumor survival [25]. Considering its over-expression in cancers and

anionic nature, miR-21 may have the capability of causing dissociation of delivered siRNA complexes.

In this chapter, we explore the effect of endogenous anionic molecules on the integrity of siRNA-PEI complexes using miR-21 as a representative molecule. Gel electrophoresis mobility shift assays (EMSA), particle size and zeta (ζ)-potential analyses, and a series of all-atom molecular dynamics (MD) simulations were performed in order to elucidate the role of miR-21 on complex dissociation. Our study aims to shed light on the fate of siRNA complexes in cytosol by simulating a more cell-like environment with the introduction of intracellular molecules and testing their effects with experimental approach.

4.2. Materials and Methods

4.2.1. Experimental

2 kDa PEI and heparin sodium from porcine intestinal mucosa (molecular weight of 17-19 kDa) were purchased from Sigma-Aldrich (St. Louis, MO). The polymer was dried by freeze-drying and reconstituted in distilled/deionized water at desired concentrations. Unlabeled and 5′-carboxyfluorescein (FAM)-labeled negative control siRNAs were purchased from Ambion (Austin, TX). The siRNA has the following sequence: sense strand: 5′-CAGAAAGCUUAGUA CCAAATT-3′; antisense strand: 5′-UUUGGUACUAAGCUUUCUGTC-3′ (Figure 4.1a), with the ability of P-glycoprotein silencing [26]. miRNA was purchased from Integrated DNA Technologies (IDT) (Coralville, IA). The sequence of miRNA is given in Figure 4.1b, except the synthesized miRNA comprises A-U Watson-Crick base pairs instead of G-U Wobble base pairs. SYBR Green II RNA gel stain (10,000X concentrate in DMSO) was purchased from Cambrex Bio Science (Rockland, ME).

PEI binding to siRNA and miRNA was investigated with EMSA and SYBR Green II dye exclusion assays. Complexes were prepared with 1 μg control (scrambled) siRNA (in ddH_2O) or 1.5 μg miRNA (in ddH_2O) incubated with various concentrations of 2 kDa PEI in 25 μL of 150 mM KCl for 30 minutes. For EMSA, samples were run on a 2% agarose gel containing 1 μg/mL ethidium bromide (100 V, 1 hour) in duplicates. The gels were visualized under UV. Percentage of binding was calculated based on the intensity of free siRNA or miRNA bands. For SYBR Green II dye exclusion assays, complexes were prepared as described above. 100 μL SYBR Green II solution (1:10000 dilution in 150 mM KCl) was added to the complexes. The fluorescence of the samples was measured using Fluoroskan Ascent Microplate Fluorometer (λ_{ex}:485 nm, λ_{em}: 527 nm). Percentage of binding was calculated based on the fluorescence intensity relative to the siRNA or miRNA alone samples. Assays were run in triplicates, and the binding curves were generated by plotting the percentage of bound RNA versus PEI:RNA weight ratio.

The EMSA was also performed for the assessment of miRNA's effect on the integrity of siRNA-PEI complexes. Complexes were prepared with 0.3 μg FAM-siRNA (in ddH_2O) and incubated with 2 kDa PEI at PEI:siRNA weight ratio = 1 for 30 minutes. Various concentrations of miRNA were added onto the complexes and the mixtures were further incubated for 1 hour. Samples were run on a 2% agarose gel (100 V, 1 hour) in duplicates. As a control, heparin was added to the complexes in the same way and run on the gel. The gels were visualized with Fluoro Image Analyzer using FAM filter. Percentage of dissociation was calculated from the fluorescence intensity of the dissociated bands to that of the free FAM-siRNA bands. Curves were generated by plotting the percentage of unbound FAM-siRNA versus the heparin/miRNA to FAM-siRNA mole ratio.

For the determination of particle size, two different PEI:RNA weight ratios were used for the complex formation: PEI:RNA = 0.3, corresponding to the weight ratio used in binding simulations, and PEI:RNA = 1, corresponding to the highest ratio used in binding experiments as well as in the experiments carried out for investigation of miRNA's effect on the complexes. Complexes were either prepared in ddH_2O or in salt (150 mM KCl) with a final volume of 50 μL, by incubating 2 μg control (scrambled) siRNA (in ddH_2O) or 3 μg miRNA (in ddH_2O) with different concentrations of 2 kDa PEI for 30 minutes. To determine the effect of miRNA on the size of siRNA-PEI complexes, complexes were prepared with 2 μg control (scrambled) siRNA as described above. Various concentrations of miRNA were added to the complexes and the mixtures were further incubated for 1 hour. For the determination of ζ-potential, samples were prepared in the same way as described above, but only in ddH_2O. All the size and ζ-potential measurements were carried out in triplicates using Zetasizer (Nano ZS; Malvern Instruments, UK).

4.2.2. Computational

The simulated siRNA is identical to what was used in experiments, shown in Figure 4.1a. It carries a total charge of –40 on its backbone phosphate groups in the fully deprotonated state. The simulated carrier is native branched PEI (Figure 4.2), which is composed of 43 amine groups, and has a molecular weight of 1874 Da. It possesses 20 protonated amine groups, corresponding to the protonation ratio of 47%, found experimentally at pH=6 [27]. The simulated miRNA is mature miR-21 [24], which has the following sequence: sense strand: 5′-UAGCUUAUCAGACUGAUGUUGA-3′; antisense strand: 5′-CAACACCAGUCGAUGGGC UGU-3′. It bears two G-U wobble base pairs; one bulge and one mismatch, located at A10 and

A16 (Figure 4.1b). Total charge of the miR-21 is –41 in the fully deprotonated state. For the discussion purposes herein, miR-21 will be referred to simply as miRNA.

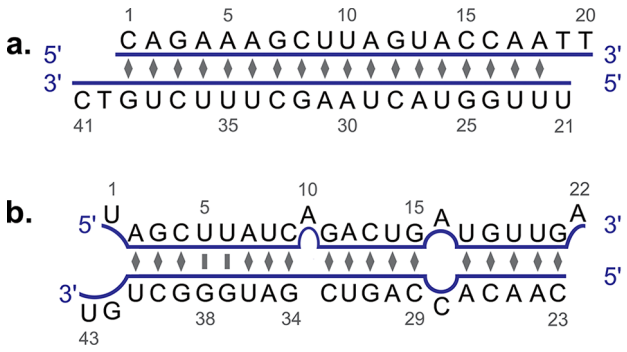

Figure 4.1. Schematic structures of the simulated polynucleotides.
(a) siRNA, **(b)** miRNA. Watson-Crick base pairs are shown with diamonds, while Wobble base pairs are shown with rectangles.

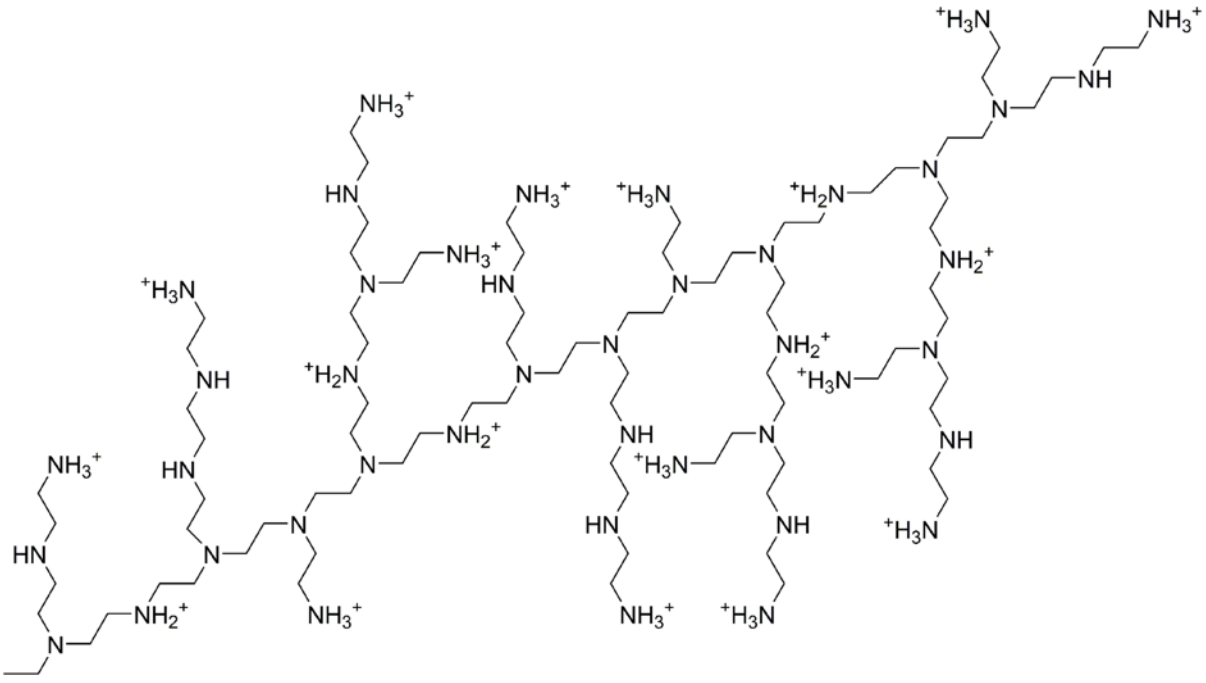

Figure 4.2. Molecular structure and protonation sites of the simulated PEI.

The initial structures (pdbs) of individual siRNA and PEI molecules were adopted from a previous study [28] published by our group. The topology for PEI molecules was developed and validated in a prior work [29] based on CHARMM General Force Field [30], while CHARMM 27 [31-34] force field was used for all other molecules. Pre-equilibration of PEI was carried out earlier [28] in NAMD [35] for 50 ns, upon solvation with TIP3P water [36] and neutralization with proper amount of Cl^- ions. siRNA was built with AMBER NAB tool [37], and used without any pre-equilibration due to its stability in aqueous environments [28]. The initial structure of miRNA was built with make-na server (http://structure.usc.edu/make-na/); and pre-equilibrated for 60 ns in NAMD; upon solvation with TIP3P water and neutralization with proper amount of K^+ ions (see Section B.1 in Appendix B for details).

Two sets of simulations were performed to investigate (*i*) the binding of PEI to siRNA and miRNA, and (*ii*) the effect of miRNA on the integrity of pre-formed siRNA-PEI complexes. For (*i*) binding studies, two simulations were performed with systems containing either two siRNAs (labeled as siRNAs A and B, see Figure 4.3a left panel) or two miRNAs (labeled as miRNA A and B, see Figure 4.3b left panel), and four PEI molecules (labeled as PEI 1, 2, 3 and 4, see Figure 4.3a and b left panel). These two systems will be referred to as 2s-4P and 2m-4P, respectively. Each system was solvated in a cubic box with TIP3P water, and K^+ and Cl^- ions were added to obtain physiological salt conditions of 150 mM. Simulation was performed for 50 ns for each system. For the investigation of (*ii*) miRNA's effect on siRNA-PEI complex, four miRNA molecules (labeled as miRNA A, B, C and D, see Figure 4.3c left panel) were introduced to the final configuration of 2s-4P system at the end of 50 ns dynamics; the system will be referred to as 2s-4P-4m. Same solvation procedure and salt concentration were adopted, and simulation was performed for 100 ns. Table 4.1 lists the details of the three simulated

systems. Initial configurations of the simulated systems are depicted in Figure 4.3 (left and middle panels). Different initial configurations were tested and shown not to affect the overall results (see Section B.2 in Appendix B for details).

All simulations were performed with NAMD [35] with a time step of 2 fs, periodic boundary conditions (PBC), and electrostatics with particle mesh Ewald (PME) [38]. The cut-off for van der Waals and pairwise electrostatic interactions was set to 12 Å, and SHAKE algorithm [39] was used to constrain bonds involving H atoms. Each system was first minimized for 5000 steps, and then heated from 0 K to 300 K with a harmonic restraint (10 kcal/mol·$Å^2$) on non-H atoms of the solute for 20 ps. After minimization and heating, the restraint was kept for 10 ns, and then removed for NPT simulations. Temperature and pressure control was carried out with Langevin dynamics thermostat and Nosé-Hoover Langevin barostat. Thermostat damping coefficient was set to 10 ps^{-1} for all non-H atoms. Barostat damping time scale was chosen to be 100 fs, and oscillation period for Langevin piston was set to 200 fs. The length of unrestrained NPT simulation for each system is given in Table 4.1. Trajectories were visualized and analyzed with VMD [40].

Table 4.1. Information on the three simulated systems.

name	molecules simulated	number of atoms	size of simulation box ($Å^3$)	number of K^+/Cl^-	simulation time restrained + free (ns)
2s-4P	2 siRNA, 4 PEI	123,034	128 x 98 x 103	112/112	10 + 50
2m-4P	2 miRNA, 4PEI	106,427	128 x 98 x 90	98/96	10 + 50
2s-4P-4m	2siRNA, 4PEI, 4 miRNA	220,971	147 x 147 x 108	363/199	10 + 100

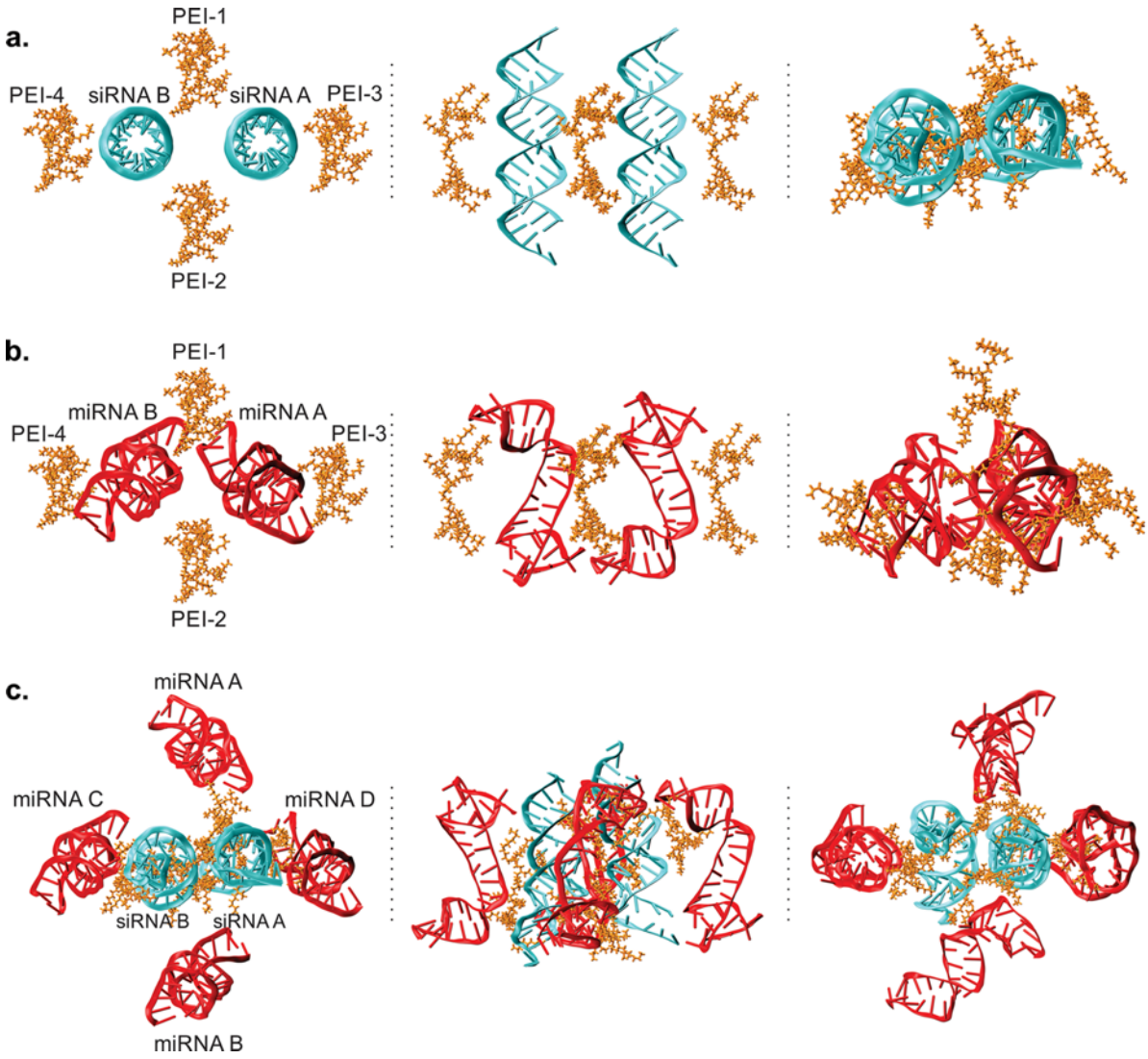

Figure 4.3. Initial and final configurations of the simulated systems.
Initial (left panel: top view, middle panel: side view) and final (right panel: top view) configurations of systems **(a)** 2s-4P, **(b)** 2m-4P, **(c)** 2s-4P-4m. siRNAs are given in cyan, while miRNAs and PEIs are represented in red and orange, respectively. Water and ions are removed for clarity.

4.3. Results and Discussion

4.3.1. PEI binding to siRNA and miRNA

PEI's binding ability to siRNA and miRNA was investigated with EMSA and SYBR Green II dye exclusion assays. Figure 4.4a shows the EMSA images of siRNA and miRNA binding to

PEI (top panel), along with the percentage of bound RNA as a function of PEI:RNA weight ratio (bottom panel), quantified based on the intensity of the siRNA/miRNA bands in the top panel. As the PEI:RNA ratio increased, an increase in the bound siRNA and miRNA fraction was observed as expected, and 100% binding was achieved for both RNAs at approximately 1:1 weight ratio. At lower PEI:RNA weight ratios (< 0.4), percentage of bound miRNA was found to be higher than that of siRNA at a given weight ratio. These observations were further validated with SYBR Green II dye exclusion assays (Figure 4.4b), where the same binding trend was observed. Particularly, at PEI:RNA weight ratios of 0.05 and 0.1, respectively 48% and 76% of the miRNA are bound, while the corresponding data for siRNA are 30% and 57%. Both RNAs reach the same % binding (88%) at PEI:RNA weight ratio of 0.2, and a plateau is observed beyond that point. The plateau value is slightly higher for siRNA, but both plateau lines are within the standard deviations in this region.

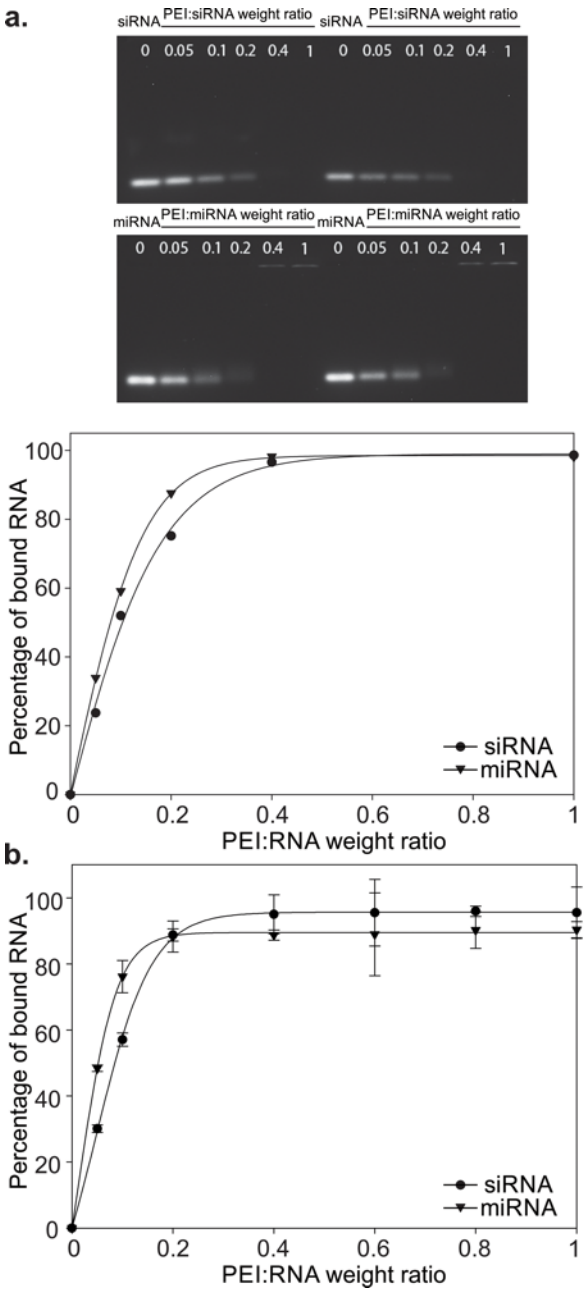

Figure 4.4. Physicochemical studies on PEI binding to siRNA and miRNA.
(a) Top panel: EMSA images of siRNA and miRNA binding to PEI. The first lane corresponds to the free siRNA or miRNA bands (PEI:RNA weight ratio = 0), while PEI:RNA weight ratio was gradually increased in the following lanes. Data from the duplicate assays is given. Bottom panel: Percentage of siRNA or miRNA bound to PEI as a function of PEI:RNA weight ratio, quantified based on the intensity of the free siRNA or miRNA bands. **(b)** Percentage of bound RNA as a function of the PEI:RNA weight ratio from SYBR Green II dye exclusion assays. For PEI:RNA weight ratios of 0, 0.05, 0.1, 0.2, 0.4, 0.6, 0.8 and 1, the corresponding N:P ratios are 0, 0.39, 0.79, 1.58, 3.16, 4.74, 6.32 and 7.90, respectively.

From both EMSA and SYBR Green II dye exclusion assays, it is clear that miRNA shows slightly better binding to PEI at low PEI:RNA weight ratios. In order to investigate the atomistic details of PEI binding to siRNA and miRNA, MD simulations were carried out on siRNA and miRNA complexes. Simulation systems were designed at PEI:RNA weight ratio of ~0.3 in order to be consistent the PEI:RNA weight ratio range tested in the experiments. The corresponding PEI:RNA charge ratio was 1. Figure 4.3a, b (right panels) show the snapshots of final configurations of the complexes formed by PEI binding to siRNAs and miRNAs, respectively. Visual examination of the snapshots revealed similar characteristics of complex formation. Specifically, in both cases, all PEIs were found to bind to and surround centrally sequestered siRNAs or miRNAs. To probe the compactness of the formed complexes, radius of gyration (R_g) of the two siRNAs or miRNAs are plotted as a function of the simulation time (Figure 4.5a). A lower R_g value indicates a more compact RNA arrangement within the complex. Both R_g curves follow a decreasing trend within the first 20 ns of the simulations as a result of the complex formation; while in the range of 20-50 ns, they reach plateau with some fluctuations. The average R_g values for the last 10 ns of the simulations are 23.08 ± 0.23 Å and 21.36 ± 0.20 Å for systems 2s-4P and 2m-4P, respectively, which indicates that system 2m-4P has a slightly more compact RNA arrangement compared to that of 2s-4P. Figure 4.5b shows the center of mass (COM) distances between the RNAs during the complexation. The COM distances start from 35.5 Å, which was the distance between the RNAs set in the initial configuration of 2s-4P and 2m-4P systems. Both curves follow a decreasing trend within the first ~20 ns. Fluctuations appear between 20 and 45 ns, and both curves reach plateau at ~45 ns. The average COM distance values for the last 10 ns of the simulations are 26.96 ± 0.74 Å and 25.45 ± 0.45 Å for systems 2s-4P and 2m-4P, respectively. In agreement with the trend observed for R_g in Figure

4.5a, COM distance of miRNAs in system 2m-4P is slightly lower than the COM distance of siRNAs in system 2s-4P, which confirms the formation of slightly more compact RNA arrangement in 2m-4P system. To investigate the potential reason behind this observation, root mean square deviations (RMSD) of the non-H atoms of the individual RNAs with respect to their initial configurations are plotted as a function of the simulation time (Figure 4.5c). All four RMSD curves follow an increasing trend due to the motion of RNAs during complex formation within the first ~20 ns. The average RMSD values of individual RNAs for the last 10 ns of the simulations are 4.21 ± 0.31 Å for siRNA A and 3.63 ± 0.58 Å for siRNA B in system 2s-4P; 6.73 ± 0.16 for miRNA A and 9.34 ± 0.31 Å for miRNA B in system 2m-4P, respectively.

Larger deviation observed in 2m-4P system indicates larger deformation and structural fluctuation of the miRNA. This observation could be attributed to bulge and mismatch regions in the miRNA, which lead to the loss of H-bonding network between base pairs (See Section B.1 in Appendix B for details). The larger deformation of miRNA accommodated PEI better, so that a more compact miRNA arrangement in the complex was obtained.

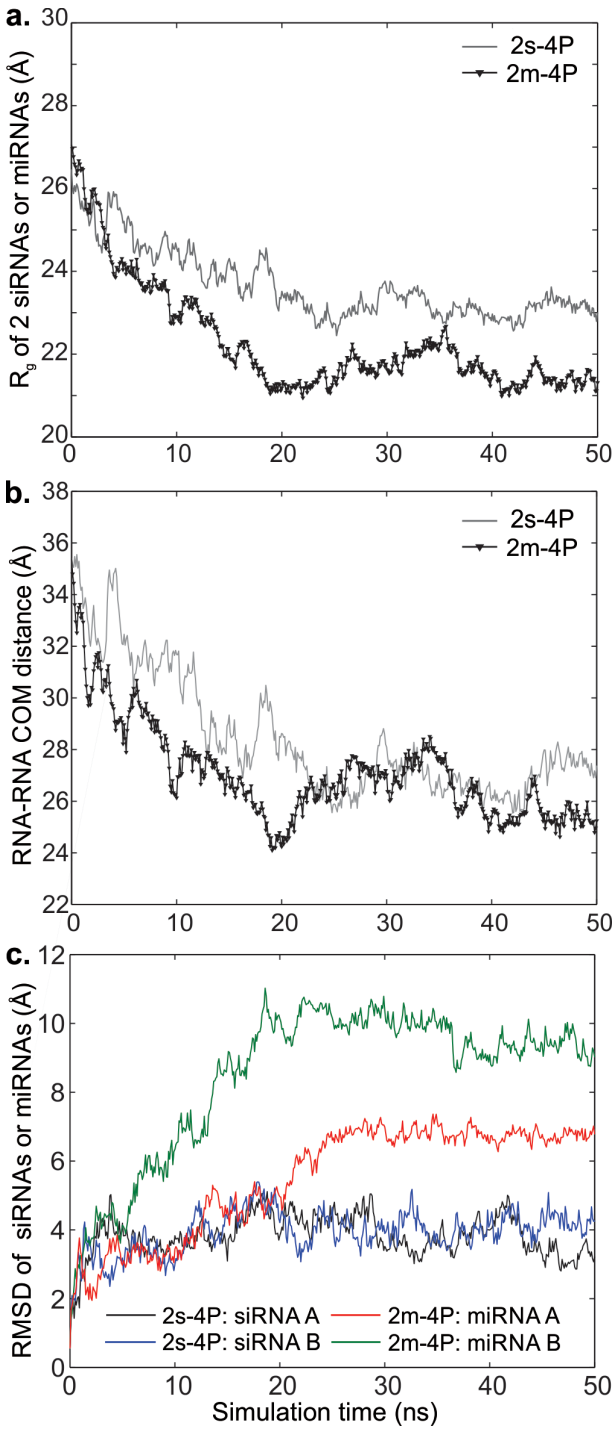

Figure 4.5. Compactness and stability of the siRNA-PEI and miRNA-PEI complexes. **(a)** R_g of two siRNAs and miRNAs; **(b)** RNA-RNA COM distance; **(c)** RMSD of the non-H atoms of individual siRNAs and miRNAs with respect to their initial configurations. Data are plotted as a function of simulation time. In **(a)** and **(b)** each subfigure contains two curves, corresponding to 2s-4P and 2m-4P systems respectively; and in **(c)** there are four curves corresponding to each RNA in 2s-4P and 2m-4P systems.

Previous MD simulations [41] indicated PEI's role in polynucleotide aggregation to be two-fold: (*i*) formation of polyion bridges between different polynucleotide segments, and (*ii*) screening of polynucleotide charges. PEI's role in aggregating siRNA and miRNA was investigated based on these mechanisms. First, to explore polyion bridging, in Figure 4.6 we plot the number of PEI N atoms within 4 Å of any N/O atoms of siRNA or miRNA, as a function of simulation time. The 4 Å limit was chosen as it is the distance for a direct H-bond to be formed between a PEI amine group and a RNA N/O atom [28]. Each subfigure consists of four plots that correspond to the four PEIs in the system (numbered in Figure 4.3a, b, left panel), and each plot contains two curves each representing one RNA (siRNA or miRNA) molecule (labeled in Figure 4.3a, b, left panel). In the initial configurations, PEI-1 and PEI-2 are located in the region between two RNA molecules, while PEI-3 and PEI-4 are on the right and left hand sides of the RNAs, respectively. To quantify polyion bridging, a PEI N is said to be in close contact with a RNA if it is within 4 Å of an siRNA or miRNA N/O atom. A PEI is said to be bound to a RNA if it has at least one N atom in close contact with the RNA. A polyion bridge is said to be formed if one PEI is simultaneously bound to more than one RNA molecules. From Figure 4.6, it can be seen that after 20 ns, the binding of PEIs to both RNAs shows very similar pattern. Specifically, PEI-1 and PEI-2 are found to bridge the two RNA molecules, whereas PEI-3 and PEI-4 are only bound to one of the RNAs: PEI-3 to siRNA A or miRNA A, and PEI-4 to siRNA B or miRNA B. Quantitatively, the number of PEI Ns in close contact with an RNA are also comparable in the two cases. The observation on the interactions of PEI-3 and PEI-4 only with their nearest RNA is the consequence of initial placement of PEIs. No apparent difference was found between siRNA and miRNA complexes in PEI binding dynamics, indicating that polyion

bridging is not affected by the type of the RNA, given similar size, charge density and initial configuration of the RNAs.

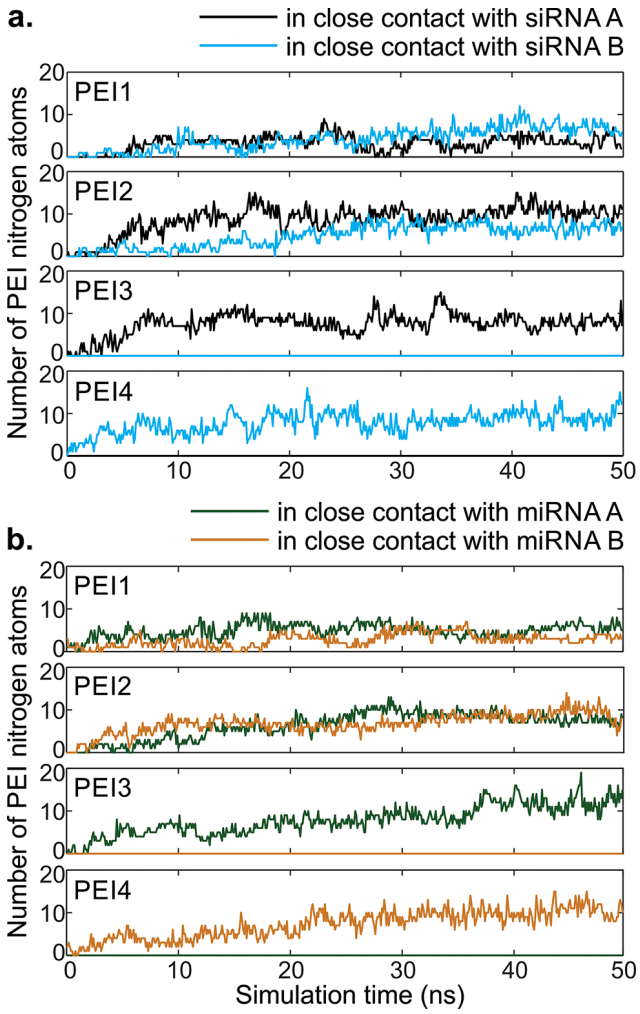

Figure 4.6. Dynamics of PEI binding to RNA in siRNA-PEI and miRNA-PEI systems. Number of N atoms for each PEI within 4 Å of any **(a)** siRNA, and **(b)** miRNA N/O atoms as a function of simulation time. Four plots in each subfigure correspond to four PEIs and two curves in each plot correspond to two siRNAs or miRNAs.

In order to probe the electrostatic screening of RNA charges, cumulative distributions of PEI N^+, K^+ and Cl^- atoms as well as their total net charge are plotted as a function of the distance from any siRNA (Figure 4.7a) or miRNA (Figure 4.7b) C1′ atoms, averaged over the last 10 ns of the simulations. In each subfigure, the black dashed line indicates the negative charge coming

from the two siRNAs (80 in Figure 4.7a) or from the two miRNAs (82 in Figure 4.7b). The blue solid curve stands for the total net charge coming from all the charged entities in the system, except the RNAs, within the given range. Intersection of the black dashed line and the blue solid curve indicates the point of 100% neutralization of RNA charges. For system 2s-4P, 100% neutralization occurs at a distance of 15.99 Å (Figure 4.7a), while for system 2m-4P, it occurs at a shorter distance of 13.88 Å (Figure 4.7b). RNAs are over-neutralized if the total charge coming from PEI N^+ atoms and K^+ and Cl^- ions exceed the total charge of RNAs, i.e., when the blue solid curve becomes above the black dashed line. It can be seen that for both systems over-neutralization occurs, reaching a maximum at 24.25 Å for 2s-4P (Figure 4.7a) and at 18.75 Å for 2m-4P (Figure 4.7b) systems. Although the characteristics of neutralization are similar for the two systems, slight differences exist in the number of individual types of atoms. At short distances (< 7 Å) number of PEI N^+s are higher in 2m-4P system than in 2s-4P. In contrast, in the range of 7 Å < r < 14 Å , number of PEI N^+s become higher in 2s-4P than in 2m-4P, and at large distances (14 to 40 Å) they are similar to each other. Number of K^+ ions is higher in 2m-4P than in 2s-4P till 28 Å, while the trend changes to 2s-4P > 2m-4P in the range of 28 Å to 40 Å. Number of Cl^- ions follow a similar trend in both systems up to 28 Å, while they become higher in 2s-4P than 2m-4P afterwards. Irrespective of the differences in the number of individual types of atoms, net charge of PEI and ions (blue solid curve) determines the point of 100% neutralization of RNA charges. Neutralization of miRNA charges at a shorter distance shows slightly better screening capability of PEI and ions in the 2m-4P system in comparison to the 2s-4P system.

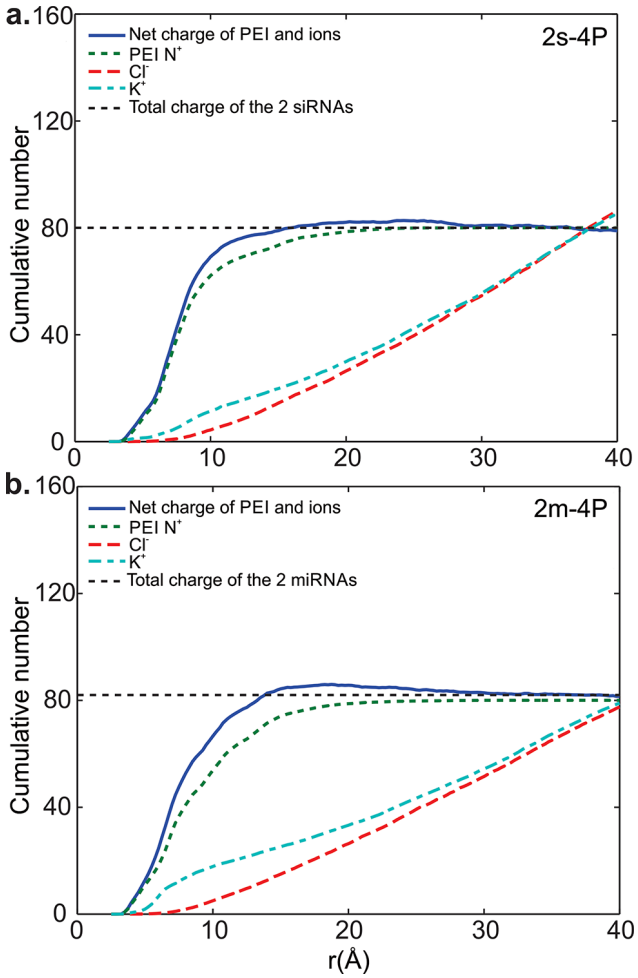

Figure 4.7. Electrostatic screening of the RNA charges.
Cumulative numbers of PEI N^+, K^+ and Cl^- atoms, and the total net charge of PEI and ions as a function of the distance from any **(a)** siRNA or **(b)** miRNA C1′ atoms, averaged over the last 10 ns of the simulations. Total charge of –80 of the two siRNAs **(a)** and –82 of the two miRNAs **(b)** are plotted by black dashed lines as reference.

Computational observations on the slightly better binding of miRNA to PEI as compared to siRNA binding to PEI are in agreement with experiments. These results led us to ask the question: can miRNAs attract PEIs in a pre-formed siRNA-PEI complex and cause dissociation? This hypothesis was investigated via experiments and simulations below.

4.3.2. Effect of miRNA on siRNA-PEI complex integrity

In order to examine the effect of miRNA on the integrity of siRNA-PEI complexes experimentally, EMSA was performed with the addition of miRNA into pre-formed FAM-siRNA-PEI complexes. Heparin was used as a reference, due to its well-known capability of dissociating the complexes. The concentration of miRNA or heparin added onto the pre-formed complexes was gradually increased; and the intensity of the fluorescence signal was quantified to calculate the amount of unbound FAM-siRNA (Figure 4.8). At heparin:FAM-siRNA and miRNA:FAM-siRNA mole ratios of 1.55 and 2.05, respectively, we have observed 56% of FAM-siRNA dissociated by heparin; while no FAM-siRNA release is apparent with miRNA. Further increase in the mole ratio (≥ 3) resulted in 98-100% of FAM-siRNA to be released by heparin; however, miRNA addition only resulted in 5% FAM-siRNA release, even at the highest ratio (= 8.2). In addition, starting from miRNA:FAM-siRNA mole ratio of 4.2, some miRNAs were observed to float freely in solution (data not shown) instead of participating in binding to or dissociating the pre-formed FAM-siRNA complex.

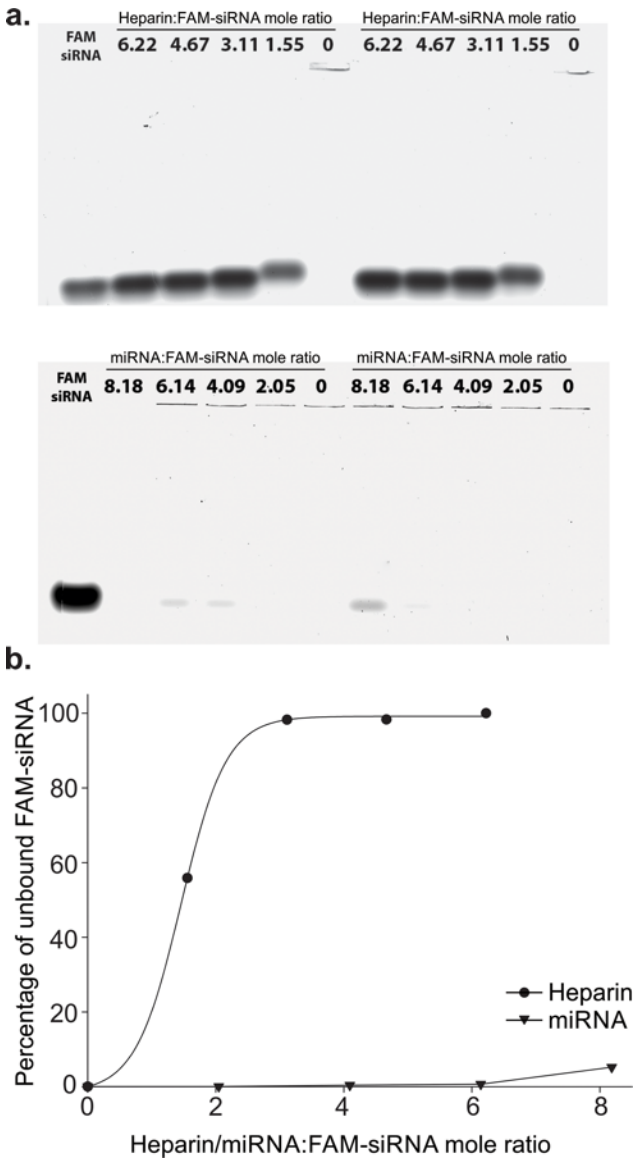

Figure 4.8. Physicochemical studies exploring the effect of heparin or miRNA addition on the integrity of pre-formed siRNA-PEI complexes.

(a) EMSA images of FAM-siRNA release from FAM-siRNA-PEI complex by heparin (top panel) and miRNA (bottom panel). Heparin/miRNA:FAM-siRNA mole ratio is gradually increased from right to left, while the leftmost lane corresponds to FAM-siRNA only (no PEI , heparin or miRNA). Data from the duplicate assays is given. **(b)** Analysis of the unbound FAM-siRNA (%) as a function of heparin/miRNA:FAM-siRNA weight ratio, quantified based on the intensity of free FAM-siRNA bands provided in **(a)**. The mole ratios were calculated by assuming molecular weights of 18 kDa and 13.7 kDa for heparin and miRNA, respectively, and molecular weight of 14 kDa for siRNA.

We further investigated the effect of miRNA addition on the size and ζ-potential of the siRNA-PEI complexes. First, siRNA-PEI and miRNA-PEI complexes were prepared at two different PEI:RNA weight ratios, 0.3 and 1, corresponding to the ratio used in binding simulations and the maximum ratio used in experiments, respectively, and measurements were conducted in 150 mM KCl and ddH_2O. In 150 mM KCl, the particles were 350-500 nm for siRNA-PEI, and 600-750 nm for miRNA-PEI systems (Figure 4.9a). Increasing PEI:RNA weight ratio resulted in no significant changes in size. As the environment changes from 150 mM KCl to ddH_2O, we observed a decrease in particle sizes, except for PEI:siRNA = 1 (Figure 4.9b). Electrostatic screening in the presence of ions might have resulted in larger particles. When miRNAs were gradually introduced into siRNA-PEI complexes, particles remained intact (Figure 4.9c). It has to be noted that size fluctuations were observed, particularly in the complexes prepared at PEI:siRNA weight ratio = 1. However, no significant change was detected in the hydrodynamic diameter of the complexes which would be indicative of dissociation. With the gradual addition of miRNA, the ζ-potential decreased for complexes prepared at both PEI:siRNA weight ratios, reaching the final charge of –27 and –29.6 for PEI:siRNA weight ratio = 0.3 and 1, respectively (Figure 4.9d). These observations show that miRNAs do not trigger the dissociation of the complexes, but rather possibly lead to the formation of an outer layer surrounding the siRNA-PEI complex.

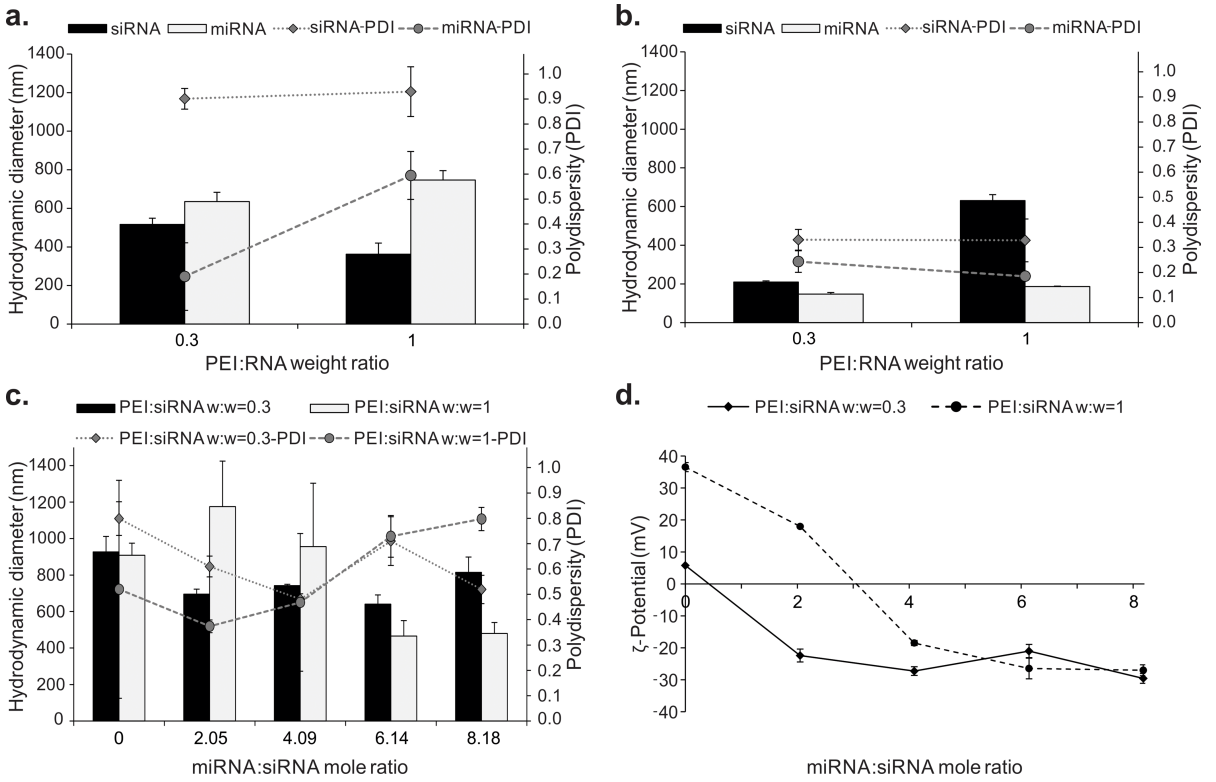

Figure 4.9. Effect of miRNA addition on the size and ζ-potential of the siRNA-PEI complexes.

Hydrodynamic diameter of the complexes prepared at PEI:RNA weight ratios of 0.3 and 1, as measured in **(a)** 150 mM KCl, and **(b)** ddH_2O. **(c)** Hydrodynamic diameters of the siRNA-PEI complexes (PEI:siRNA weight ratio = 0.3 and 1) with the gradual addition of miRNA, as measured in 150 mM KCl. **(d)** The ζ-potential of the siRNA-PEI complexes with the gradual addition of miRNA. For PEI:RNA weight ratios of 0.3 and 1, the corresponding N:P ratios are 2.37 and 7.90, respectively.

In order to test our hypothesis on the formation of ternary siRNA-PEI-miRNA structures, a simulation was performed by introducing four miRNA molecules into the final configuration of 2s-4P system, so as to surround the pre-formed siRNA-PEI complex symmetrically (Figure 4.3c, left and middle panels) and form the 2s-4P-4m system. The 2s-4P-4m system was simulated for 100 ns and visual examination of the complex structure at the end (Figure 4.3c,

right panel) revealed that although contacts were formed between miRNAs and PEIs, the siRNA complex remained intact and no apparent loosening of the complex was visible.

To quantify the compactness of siRNA arrangement upon miRNA introduction, R_g of the two siRNAs in 2s-4P-4m system is plotted as a function of the simulation time (Figure 4.10). At the beginning of the simulation (after the minimization and restrained dynamics), R_g is found to be 22.83 Å, which is almost the same as the final R_g of 2s-4P system, 22.90 Å. Although fluctuations are apparent during the entire simulation, a plateau is reached in the last 20 ns. The average R_g for the last 20 ns is 22.21 ± 0.12 Å, which is very close to the initial value. Therefore, although our earlier simulations showed slightly better binding of miRNA to PEI, their addition into pre-formed siRNA-PEI complex did not loosen the compact arrangement of the siRNAs.

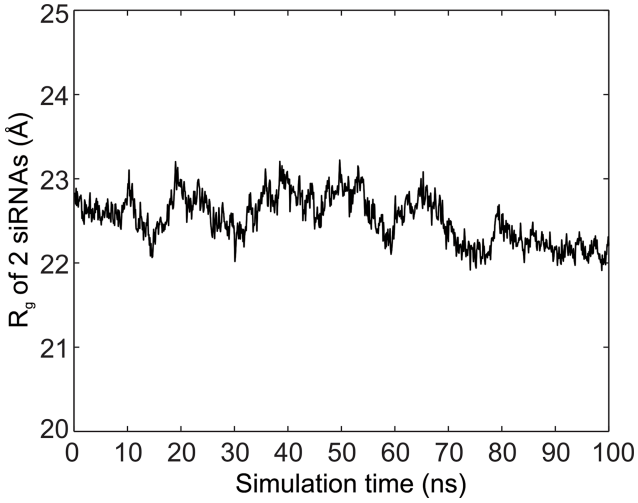

Figure 4.10. R_g of the two siRNAs in 2s-4P-4m system as a function of simulation time.

On the other hand, Figure 4.3c (right panel) revealed the formation of contacts between miRNAs and PEIs, and attachment of miRNAs to the periphery of the complex. Dynamics of PEI binding to both RNAs was probed for system 2s-4P-4m (Figure 4.11), with the same procedure described in Section 4.3.1. The four plots in each subfigure again correspond to the

four PEIs in the system, while six curves are present in each plot, representing the six RNA molecules, two siRNAs and four miRNAs. Previously in system 2s-4P, PEI-1 and PEI-2 were found to bridge siRNA A and B (Figure 4.6a). In Figure 4.11, it is clear that these two PEIs continue to bridge the two siRNAs, and the numbers of PEI Ns in close contact with the siRNAs have not decreased after miRNA contact. In fact, for PEI-1, the numbers of Ns in close contact with the siRNAs, averaged over the last 20 ns, are respectively 9 and 10 for siRNA A and B. These numbers are even slightly larger than the average numbers (over the last 10 ns) found for system 2s-4P before the introduction of miRNAs, which are 4 and 7. As in system 2s-4P, PEI-3 and PEI-4 do not participate in polyion bridging and are only bound to one siRNA. In addition to maintaining the same binding pattern with siRNA, new contacts are established between PEIs and miRNAs. In particular, PEI-1 is bound to miRNA A, thereby simultaneously bridging three RNAs, two siRNAs and one miRNA. PEI-2 bridges the two siRNAs as well as miRNA B. PEI-3 started to bridge siRNA A and miRNA D; additionally, short term transient bridges with miRNA A are observed (between 50-60 ns, 70-80 ns and after 90 ns). Similarly, PEI-4 bridges siRNA B and miRNA C, and forms short term transient bridges with miRNA B (between 80-90 ns). These results show that introduction of miRNA not only conserved the overall binding pattern of PEI to siRNA, but also allowed the formation of new polyion bridges between siRNA and miRNA molecules, which clearly demonstrate the ability of PEI to accommodate additional RNAs.

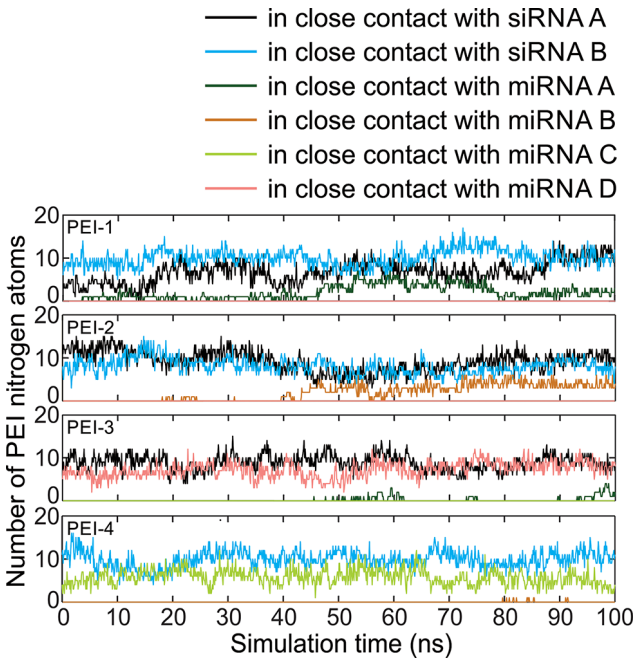

Figure 4.11. PEI binding dynamics upon miRNA introduction into pre-formed siRNA-PEI complex.
Number of Ns for each PEI within 4 Å of each siRNA and miRNA N/O atoms as a function of simulation time. Four plots in each subfigure correspond to four PEIs and six curves in each plot correspond to two siRNAs and four miRNAs in 2s-4P-4m system.

To examine the change in the screening of siRNA charges upon miRNA introduction, cumulative distributions of PEI N^+, K^+, Cl^- and miRNA P^- atoms as well as their total net charge are plotted as a function of the distance from any siRNA C1′ atom, averaged over the last 20 ns of the simulation (Figure 4.12). Black solid line indicates the cumulative number of miRNA P^-s as a function of distance from siRNA C1′s; while the rest of the curves are represented in the same way as in Figure 4.7a. miRNA charges follow an increasing trend; and at large distances, 49-50 Å, they reach up to their total charge of –164. No considerable change is observed in the number of PEI N^+s upon miRNA introduction, while the K^+ charges increase more rapidly to accommodate the excessive negative charge coming from miRNA P^-s. 100% neutralization of siRNA charges occur at 15.98 Å, which is almost identical to that reported in

2s-4P system (15.99 Å). On the other hand, the over-neutralization seen in 2s-4P system is no longer observed. Excessive negative charge of miRNA led to the formation of an overall negatively charged complex structure, indicated by the fact the solid blue curve decreases beyond the neutralization distance and is never above the black dashed line.

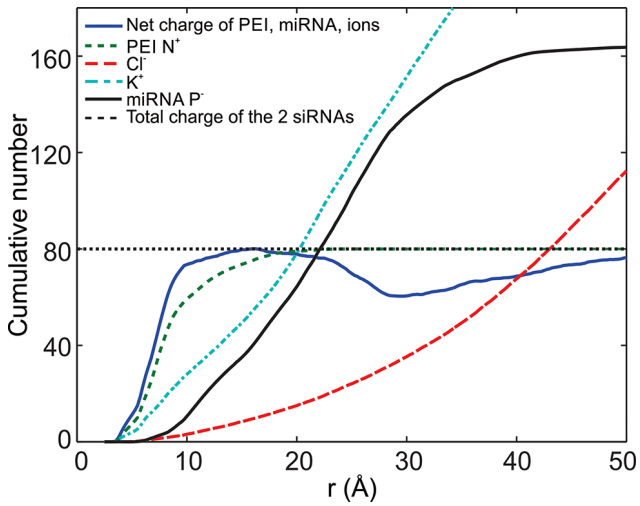

Figure 4.12. Effect of miRNA introduction on the electrostatic screening of the siRNA charges.
Cumulative numbers of PEI N^+, K^+, Cl^- and miRNA P^- atoms, and the total net charge of PEI, miRNA and ions as a function of the distance from any siRNA C1′ atoms, averaged over the last 20 ns of the 2s-4P-4m simulation. Total charge of –80 of the two siRNAs is plotted by a black dashed line as a reference.

To summarize, for the simulated system where the miRNA:siRNA mole ratio is set to 2 and within the simulation time of 100 ns, the miRNAs were not observed to affect the integrity of the siRNA-PEI complex. This is in agreement with the experimental data presented earlier. In contrast to our initial speculation that the stronger binding between miRNA and PEI might lead to dissociation of siRNA complexes in the presence of miRNAs, our experimental and computational results showed that PEIs are capable of bridging the miRNAs to the siRNA-PEI complex and forming an additional miRNA layer.

4.3.3. Limitations

In this work, size characterization of the nanoparticles have shown hydrodynamic diameters of 517 ± 32 nm for siRNA-PEI, and 635 ± 48 nm for miRNA-PEI systems at PEI:RNA weight ratio of 0.3 (Figure 4.9a), while the corresponding particle sizes reported from our simulations were 5-6 nm. With the current computational capabilities, it is not practical to simulate a system which is hundreds of nanometers in size. Despite the smaller size of our systems, we believe that our simulations should capture the fundamental complexation mechanism at the atomistic level. In terms of time, in reality, the formation and dissociation of siRNA complexes occur on the scale of minutes (< 1 hour), while current computational capabilities allow simulations up to μs in the atomistic scale. Our binding simulations in this work were performed for 50 ns, which are longer than most of the all-atom simulations reported on the binding of biomolecules; e.g. typically 4 – 26 ns for polycation binding to siRNA [42-49] and 12 – 20 ns to DNA [50, 51]. To our knowledge, there have not been any all-atom MD simulations probing the dissociation of siRNA complexes and/or the effect of anionic endogenous molecules on the integrity of siRNA complexes. Unlike binding, our simulations inspecting the effect of miRNA on the integrity of siRNA-PEI complex are longer (100 ns), but it is possible that they might still be too short to capture the most probable configuration of the siRNA complex upon the addition of miRNA, if the simulated system is trapped in a potential energy well. However, it should be emphasized that the conclusion made on the effect of miRNA (i.e., absence of dissociation and formation of a siRNA-PEI-miRNA ternary complex) is not solely based on the simulations. Our EMSA and ζ-potential analysis provided direct evidence for such phenomena, while MD simulation validated the experimental observations giving atomistic details on the interaction of miRNA with the siRNA-PEI complex. Given the current computational

limitations, it is encouraging to see that our simulations provided a good agreement with the experimental observations.

In our simulations, we adopted two initial configurations of the siRNA-PEI complex (one presented in Figure 4.3a (left and middle panels), and the other in Figure B.2 in Appendix B (left and middle panels)), for the simulations on complex formation as well as for probing the effect of miRNA on the complex integrity. Although these initial configurations led to slightly different quantitative results, e.g. 0.87 Å difference in R_g of the siRNA-PEI complex, the qualitative outcomes are similar. Practically, it is not possible to examine all initial configurations with MD simulations; therefore, the structures observed at the end of our simulations are only some of the possible configurations that can be formed by these molecules. However, the good agreement found between simulations and experimental ζ-potential measurements, i.e. positively charged particles formed by siRNA and/or miRNA with PEI, and negatively charged particles formed upon gradual miRNA addition onto siRNA-PEI complexes, indicate these final structures are highly probable configurations.

4.4. Conclusions

We performed experimental binding studies and a series of all-atom MD simulations to study PEI binding to siRNA and miRNA, and the effect of miRNA addition on the integrity of siRNA-PEI complexes. EMSA and SYBR Green II dye exclusion assays along with individual complexation simulations with miRNA and siRNA revealed PEI's slightly better binding to miRNA. Despite the observed better binding, from EMSA and SYBR Green II dye exclusion assays, we found that miRNA introduction into pre-formed siRNA-PEI complex failed to break the pre-formed interactions between the siRNA and PEI. This is confirmed by MD simulations where additional miRNA was observed to bind to the pre-formed siRNA complex through the

electrostatic interactions with the accessible PEI, and formed an additional surrounding layer without weakening the interactions already formed between siRNA and PEI. The resulting structure observed from MD simulation, an overall negatively charged ternary complex comprising a core of siRNA-PEI complex and an outer layer of miRNA, is consistent with the experimental finding that ζ-potential of the particle decreases upon gradual addition of miRNA.

4.5. Acknowledgements

Computing resources and technical support from Compute Canada and the high performance computing facility at National Institute for Nanotechnology, Edmonton, Canada were gratefully acknowledged. This work is funded by Natural Sciences and Engineering Research Council of Canada, Canadian Institutes of Health Research, Alberta Innovates Health Solutions, Alberta Innovates-Technology Futures, and Canada Foundation for Innovation. We thank Dr. Afsaneh Lavasanifar (Faculty of Pharmacy & Pharmaceutical Sciences) for access to the Zetasizer.

4.6. References

1. Fire A, Xu S, Montgomery MK, Kostas SA, Driver SE, & Mello CC (1998) Potent and Specific Genetic Interference by Double-stranded RNA in Caenorhabditis Elegans. *Nature* 391(6669):806-811.
2. Davidson BL & McCray PB, Jr. (2011) Current Prospects for RNA Interference-based Therapies. *Nat. Rev. Genet.* 12(5):329-340.
3. Zhang S, Zhao B, Jiang H, Wang B, & Ma B (2007) Cationic Lipids and Polymers Mediated Vectors for Delivery of siRNA. *J. Control. Release* 123(1):1-10.
4. Boussif O, Lezoualc'h F, Zanta MA, Mergny MD, Scherman D, Demeneix B, & Behr JP (1995) A Versatile Vector for Gene and Oligonucleotide Transfer into Cells in Culture and In vivo: Polyethylenimine. *Proc. Natl. Acad. Sci. U.S.A.* 92(16):7297-7301.
5. Dominska M & Dykxhoorn DM (2010) Breaking Down the Barriers: siRNA Delivery and Endosome Escape. *J. Cell. Sci.* 123:1183-1189.
6. Czech B & Hannon GJ (2011) Small RNA Sorting: Matchmaking for Argonautes. *Nat. Rev. Genet.* 12(1):19-31.

7. Ding HM & Ma YQ (2012) Role of Physicochemical Properties of Coating Ligands in Receptor-mediated Endocytosis of Nanoparticles. *Biomaterials* 33(23):5798-5802.

8. Ding HM & Ma YQ (2013) Design Maps for Cellular Uptake of Gene Nanovectors by Computer Simulation. *Biomaterials* 34(33):8401-8407.

9. Ding HM & Ma YQ (2013) Controlling Cellular Uptake of Nanoparticles with pH-sensitive Polymers. *Sci. Rep.* 3:2804.

10. Dinh AT, Pangarkar C, Theofanous T, & Mitragotri S (2007) Understanding Intracellular Transport Processes Pertinent to Synthetic Gene Delivery via Stochastic Simulations and Sensitivity Analyses. *Biophys. J.* 92(3):831-846.

11. Gilleron J, Querbes W, Zeigerer A, Borodovsky A, Marsico G, Schubert U, Manygoats K, Seifert S, Andree C, Stoter M, Epstein-Barash H, Zhang L, Koteliansky V, Fitzgerald K, Fava E, Bickle M, Kalaidzidis Y, Akinc A, Maier M, & Zerial M (2013) Image-based Analysis of Lipid Nanoparticle-mediated siRNA Delivery, Intracellular Trafficking and Endosomal Escape. *Nat. Biotechnol.* 31(7):638-646.

12. Sahay G, Querbes W, Alabi C, Eltoukhy A, Sarkar S, Zurenko C, Karagiannis E, Love K, Chen DL, Zoncu R, Buganim Y, Schroeder A, Langer R, & Anderson DG (2013) Efficiency of siRNA Delivery by Lipid Nanoparticles is Limited by Endocytic Recycling. *Nat. Biotechnol.* 31(7):653-658.

13. Behr JP (1997) The Proton Sponge: A Trick to Enter Cells the Viruses Did Not Exploit. *Chimia* 51(1-2):34-36.

14. Benjaminsen RV, Mattebjerg MA, Henriksen JR, Moghimi SM, & Andresen TL (2013) The Possible "Proton Sponge " Effect of Polyethylenimine (PEI) Does Not Include Change in Lysosomal pH. *Mol. Ther.* 21(1):149-157.

15. Won YY, Sharma R, & Konieczny SF (2009) Missing Pieces in Understanding the Intracellular Trafficking of Polycation/DNA Complexes. *J. Control. Release* 139(2):88-93.

16. Sasisekharan R, Shriver Z, Venkataraman G, & Narayanasami U (2002) Roles of Heparan-Sulphate Glycosaminoglycans in Cancer. *Nat. Rev. Cancer* 2:521-528.

17. Xu YH & Szoka FC (1996) Mechanism of DNA Release from Cationic Liposome/DNA Complexes Used in Cell Transfection. *Biochemistry* 35(18):5616-5623.

18. Ruponen M, Yla-Herttuala S, & Urtti A (1999) Interactions of Polymeric and Liposomal Gene Delivery Systems with Extracellular Glycosaminoglycans: Physicochemical and Transfection Studies. *Biochim. Biophys. Acta* 1415(2):331-341.

19. Moret I, Esteban Peris J, Guillem VM, Benet M, Revert F, Dasi F, Crespo A, & Alino SF (2001) Stability of PEI-DNA and DOTAP-DNA Complexes: Effect of Alkaline pH, Heparin and Serum. *J. Control. Release* 76(1-2):169-181.

20. Ruponen M, Honkakoski P, Ronkko S, Pelkonen J, Tammi M, & Urtti A (2003) Extracellular and Intracellular Barriers in Non-viral Gene Delivery. *J. Control. Release* 93(2):213-217.

21. Aliabadi HM, Landry B, Sun C, Tang T, & Uludag H (2012) Supramolecular Assemblies in Functional siRNA Delivery: Where Do We Stand? *Biomaterials* 33(8):2546-2569.

22. Calin GA & Croce CM (2006) MicroRNA Signatures in Human Cancers. *Nat. Rev. Cancer* 6(11):857-866.

23. Esquela-Kerscher A & Slack FJ (2006) Oncomirs - MicroRNAs with a Role in Cancer. *Nat. Rev. Cancer* 6(4):259-269.

24. Lagos-Quintana M, Rauhut R, Lendeckel W, & Tuschl T (2001) Identification of Novel Genes Coding for Small Expressed RNAs. *Science* 294(5543):853-858.

25. Krichevsky AM & Gabriely G (2009) miR-21: A Small Multi-faceted RNA. *J. Cell. Mol. Med.* 13(1):39-53.

26. Abbasi M, Lavasanifar A, Berthiaume LG, Weinfeld M, & Uludag H (2010) Cationic Polymer-mediated Small Interfering RNA Delivery for P-glycoprotein Down-regulation in Tumor Cells. *Cancer* 116(23):5544-5554.

27. Utsuno K & Uludag H (2010) Thermodynamics of Polyethlyenimine-DNA Binding and DNA Condensation. *Biophys. J.* 99(1):201-207.

28. Sun C, Tang T, & Uludag H (2013) A Molecular Dynamics Simulation Study on the Effect of Lipid Substitution on Polyethylenimine Mediated siRNA Complexation. *Biomaterials* 34(11):2822-2833.

29. Sun C, Tang T, Uludag H, & Cuervo JE (2011) Molecular Dynamics Simulations of DNA/PEI Complexes: Effect of PEI Branching and Protonation State. *Biophys. J.* 100(11):2754-2763.

30. Vanommeslaeghe K, Hatcher E, Acharya C, Kundu S, Zhong S, Shim J, Darian E, Guvench O, Lopes P, Vorobyov I, & Mackerell AD, Jr. (2010) CHARMM General Force Field: A Force Field for Drug-like Molecules Compatible with the CHARMM All-atom Additive Biological Force Fields. *J. Comput. Chem.* 31(4):671-690.

31. Brooks BR, Bruccoleri RE, Olafson BD, States DJ, Swaminathan S, & Karplus M (1983) Charmm – A Program for Macromolecular Energy, Minimization, and Dynamics Calculations. *J. Comput. Chem.* 4:187–217.

32. MacKerell AD, Brooks B, Brooks CL, Nilsson L, Roux B, Won Y, & Karplus M (1998) CHARMM: The Energy Function and Its Parameterization with an Overview of the Program. *The Encyclopedia of Computational Chemistry*, (John Wiley & Sons, Chichester), pp 271-277.

33. Foloppe N & MacKerell J, A.D. (2000) All-Atom Empirical Force Field for Nucleic Acids: I. Parameter Optimization Based on Small Molecule and Condensed Phase Macromolecular Target Data. *J. Comput. Chem.* 21:86-104.

34. MacKerell AD & Banavali NK (2000) All-atom Empirical Force Field for Nucleic Acids: II. Application to Molecular Dynamics Simulations of DNA and RNA in Solution. *J. Comput. Chem.* 21(2):105-120.

35. Phillips JC, Braun R, Wang W, Gumbart J, Tajkhorshid E, Villa E, Chipot C, Skeel RD, Kale L, & Schulten K (2005) Scalable Molecular Dynamics with NAMD. *J. Comput. Chem.* 26(16):1781-1802.

36. Jorgensen WL (1981) Quantum and Statistical Mechanical Studies of Liquids .10. Transferable Intermolecular Potential Functions for Water, Alcohols, and Ethers - Application to Liquid Water. *J. Am. Chem. Soc.* 103(2):335-340.

37. Balasubramanian C, Ojha RP, Maiti S, & Desideri A (2010) Sampling the Structure of the Noncanonical lin-4:lin-14 microRNA:mRNA Complex by Molecular Dynamics Simulations. *J. Phys. Chem. B* 114(49):16443-16449.

38. Darden T, York D, & Pedersen L (1993) Particle Mesh Ewald: An N · log(N) Method for Ewald Sums in Large Systems. *J. Chem. Phys.* 98:10089-10092.

39. Ryckaert JP, Ciccotti G, & Berendsen HJC (1977) Numerical Integration of the Cartesian Equations of Motion of a System with Constraints: Molecular Dynamics of N-alkanes. *J. Comput. Phys.* 23(3):327-341.

40. Humphrey W, Dalke A, & Schulten K (1996) VMD: Visual Molecular Dynamics. *J. Mol. Graphics* 14(1):33-38.

41. Sun C, Tang T, & Uludag H (2011) Molecular Dynamics Simulations of PEI Mediated DNA Aggregation. *Biomacromolecules* 12(10):3698-3707.

42. Ouyang D, Zhang H, Parekh HS, & Smith SC (2011) The Effect of pH on PAMAM Dendrimer-siRNA Complexation: Endosomal Considerations as Determined by Molecular Dynamics Simulation. *Biophys. Chem.* 158(2-3):126-133.

43. Karatasos K, Posocco P, Laurini E, & Pricl S (2012) Poly(amidoamine)-based Dendrimer/siRNA Complexation Studied by Computer Simulations: Effects of pH and Generation on Dendrimer Structure and siRNA Binding. *Macromol. Biosci.* 12(2):225-240.

44. Pavan GM, Albertazzi L, & Danani A (2010) Ability to Adapt: Different Generations of PAMAM Dendrimers Show Different Behaviors in Binding siRNA. *J. Phys. Chem. B.* 114(8):2667-2675.

45. Pavan GM, Kostiainen MA, & Danani A (2010) Computational Approach for Understanding the Interactions of UV-degradable Dendrons with DNA and siRNA. *J. Phys. Chem. B.* 114(17):5686-5693.

46. Jensen LB, Mortensen K, Pavan GM, Kasimova MR, Jensen DK, Gadzhyeva V, Nielsen HM, & Foged C (2010) Molecular Characterization of the Interaction between siRNA and PAMAM G7 Dendrimers by SAXS, ITC, and Molecular Dynamics Simulations. *Biomacromolecules* 11(12):3571-3577.

47. Ouyang D, Zhang H, Parekh HS, & Smith SC (2010) Structure and Dynamics of Multiple Cationic Vectors-siRNA Complexation by All-atomic Molecular Dynamics Simulations. *J. Phys. Chem. B.* 114(28):9231-9237.

48. Ouyang D, Zhang H, Herten DP, Parekh HS, & Smith SC (2010) Structure, Dynamics, and Energetics of siRNA-Cationic Vector Complexation: A Molecular Dynamics Study. *J. Phys. Chem. B.* 114(28):9220-9230.

49. Vasumathi V & Maiti PK (2010) Complexation of siRNA with Dendrimer: A Molecular Modeling Approach. *Macromolecules* 43:8264–8274.

50. Ziebarth J & Wang Y (2009) Molecular Dynamics Simulations of DNA-Polycation Complex Formation. *Biophys. J.* 97(7):1971-1983.

51. Elder RM, Emrick T, & Jayaraman A (2011) Understanding the Effect of Polylysine Architecture on DNA Binding Using Molecular Dynamics Simulations. *Biomacromolecules* 12(11):3870-3879.

5. Development of A Molecular Model for Heparin[X]

[X]A portion of this chapter will be submitted for publication as Supporting Information to the manuscript: Meneksedag-Erol D, Tang T, & Uludağ H, Mechanistic Insights into the Role of Glycosaminoglycans in Delivery of Polymeric Nucleic Acid Nanoparticles by Molecular Dynamics Simulations.

5.1. Introduction

Heparin and heparan sulfate (HS) are linear anionic polysaccharides that belong to the glycosaminoglycan (GAG) family of complex carbohydrates [1]. Heparin is synthesized in the form of proteoglycan (PG, a glycosaminoglycan covalently connected to a protein core) mostly by connective tissue-type mast cells [2], and stored in the mast cell secretory granules; whereas HS (as PG) is present either on the plasma membrane and/or in the extracellular matrix of eukaryotic cells [1, 3-5]. Structurally, both heparin and HS share the same building units, namely iduronic acid (α-L-iduronic acid, IdoA, or β-D-glucuronic acid, GlcA) and D-glucosamine (GlcN); however the composition and sequence of these units vary between the two molecules [1]. Moreover, both building units are open to different N- and O-sulfation modifications at different positions, which gives rise to a great diversity among heparin and HS GAG structures. The HS is generally less sulfated than heparin [4, 6].

Heparin/ HS GAGs are associated with important biological functions (reviewed in [4]) such as cell growth [7], angiogenesis [8, 9], and blood coagulation [10] processes. Clinical use of heparin is mainly based on its anticoagulant properties; it is administered to prevent blood clotting in a variety of bleeding disorders or during surgical procedures [11]. Given the abundance of functional roles heparin/HS GAGs undertake, they have been actively studied in a variety of biological contexts. Molecular modeling studies with GROMACS and AMBER based force fields have been carried out to study the dynamics of the heparin molecule in solution [12, 13], and binding of heparin to proteins [14], growth factors [15], and of particular interest to polynucleotide-based therapeutics, to polymeric carriers [16]. Motivated by the findings of Chapter 4 where heparin disassembled siRNA-polyethylenimine (PEI) complexes in a concentration dependent manner (observed by physicochemical studies) while micro RNA,

miRNA, was found adsorbed onto the siRNA-PEI complex without disrupting its integrity (physicochemical studies and MD simulations with CHARMM force field), our ultimate goal is to perform MD simulations to investigate the mechanism of action of heparin on polynucleotide complexes with CHARMM force field. Although the topology and parameters of the heparin's main building blocks are available in CHARMM36 carbohydrate force field [17, 18], given the structural diversity of the heparin/HS GAGs, further parameterization is needed depending on the particular heparin structure of interest. In this chapter, we present CHARMM force field based topology development and parameterization of the nuclear magnetic resonance (NMR) solution structure of a heparin fragment (PDB code: 1HPN [19]).

5.2. Building the Force Field for Heparin

5.2.1. Initial Structures and Nomenclature

The NMR solution structure of a heparin fragment (PDB code: 1HPN [19]) is composed of six N,O6-disulfo-glucosamine (GlcNS(6S)) – 2-O-sulfo-alpha-L-idopyranuronic acid (IdoA2S) disaccharide units. The chemical structures of GlcNS(6S) and IdoA2S are given in Figure 5.1. Adopting the initial atomic coordinates of the GlcNS(6S) – IdoA2S disaccharide from the NMR structure of heparin (PDB code: 1HPN, Model 1 [19]), we investigated two heparin molecules having different chain lengths, 12 residues and 21 residues, respectively. Hereafter, we will refer to these molecules, respectively, as 12-mer and 21-mer heparin. The chemical structures of the two heparins studied are given in Figure 5.2. For the construction of the initial structure of the 12-mer heparin, the atomic coordinates were directly adopted from the PDB code: 1HPN, Model 1 [19]; then two ends of the molecule were saturated with H atoms as these saturation sites are missing in the original crystal structure. Specifically, the 12-mer heparin molecule starts with a GlcNS(6S), saturated with H at the O1 position; continues with five repeating units of the

IdoA2S – GlcNS(6S) disaccharide; and ends with IdoA2S, saturated with H at the O4 position (Figure 5.2a). Similarly, for the construction of the initial structure of the 21-mer heparin, the initial atomic coordinates were adopted from the PDB code: 1HPN, Model 1 [19]. In order to extend the length of the heparin chain, the number of repeating units of the IdoA2S – GlcNS(6S) disaccharide (n) was increased from n = 5 to n = 9, using Schrödinger's Maestro software [20]. Specifically, the molecule starts with a GlcNS(6S), saturated with H at the O1 position; continues with nine repeating units of the IdoA2S – GlcNS(6S) disaccharide; followed by an IdoA2S residue; and ends with a GlcNS(6S), saturated with H at the O4 position (Figure 5.2b). In both heparin molecules studied, all the residues are linked together via the 1 → 4 glycosidic linkage. The saturation sites at both ends of the heparin molecule, as well as one of the 1 → 4 glycosidic linkages as an example are highlighted in red in Figure 5.2.

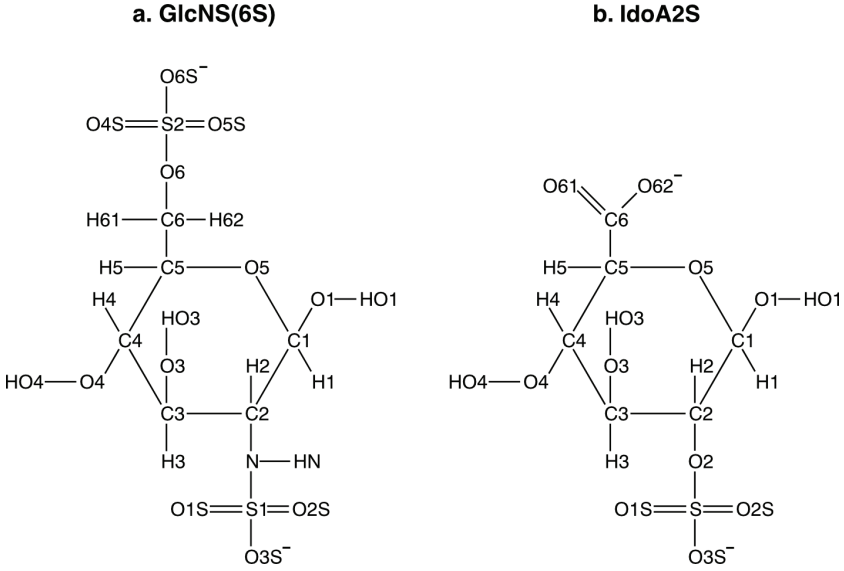

Figure 5.1. Planar representations of the building blocks of heparin.
(a) N,O6-disulfo-glucosamine (GlcNS(6S)), **(b)** 2-O-sulfo-alpha-L-idopyranuronic acid (IdoA2S). The numbering of the atoms is included to provide clarity to some of the discussed structural features, and it is as follows: the carbons: C1, C2, C3, C4, C5, C6; the hydrogens: H1, H2, H3, H4, H5, H61, H62, HO1, HO3, HO4, HN; the oxygens: O1, O2, O3, O4, O5, O6, O61, O62, O1S, O2S, O3S, O4S, O5S, O6S; the nitrogen: N; and the sulfurs: S, S1, S2.

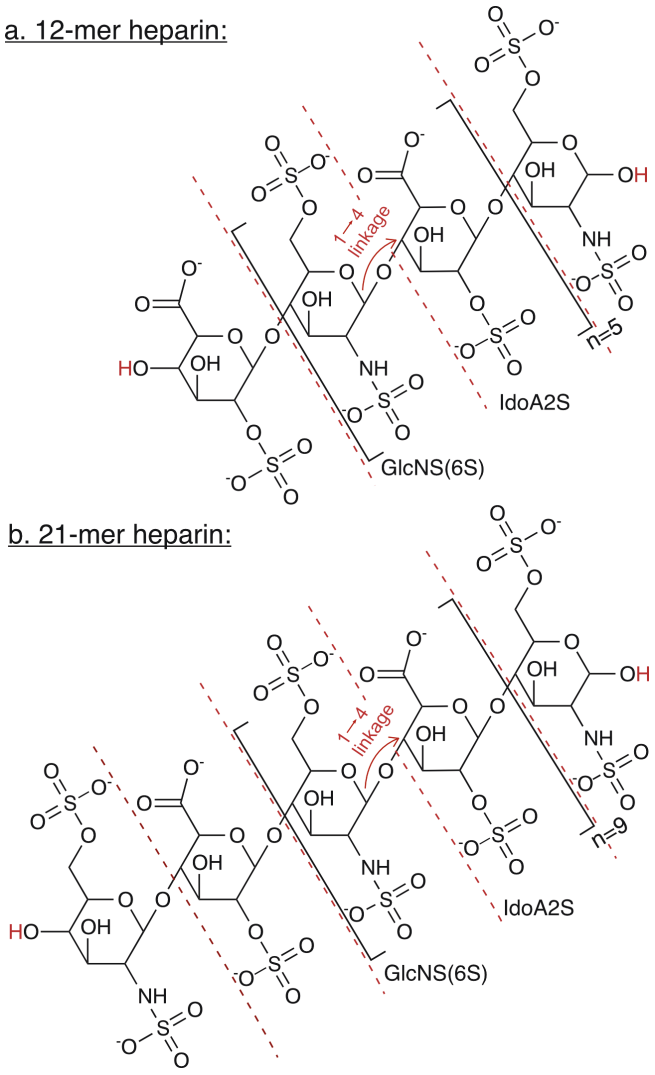

Figure 5.2. Planar structures of the heparin molecules studied.
(a) 12-mer, and **(b)** 21-mer heparin molecule. The number of repeating units of the IdoA2S – GlcNS(6S) disaccharide is denoted with n. The boundaries of each residue are indicated with red dashed lines. The saturation sites and one of the 1 → 4 glycosidic linkages are highlighted in red.

5.2.2. Topology Development and Parameterization

Topology of the building blocks of heparin are available in CHARMM36 additive all-atom carbohydrate force field [17] except for the sulfamate group ($NHSO_3^-$) in GlcNS(6S), which is adopted from an extended CHARMM36 general force field (CGENFF36) of sulfonyl-

containing compounds [21]. All the atom types were assigned by analogy to their parent compounds. The analogous residue (the parent compound) to GlcNS(6S) in CHARMM36 additive all-atom carbohydrate force field is "AGLCNA", which is α-N-acetylglucosamine (GlcNAc). This parent compound consists of a hexopyranose ring, a C2 N-acetylamine and a C6 hydroxyl group. The chemical structure of AGLCNA, and the process of building the GlcNS(6S) from AGLCNA and other identified compounds in CHARMM36 additive all-atom carbohydrate force field and CHARMM36 general force field (CGENFF36) are schematically shown in Figure 5.3. Firstly, a sulfate patch to C6 position (PRES SHOM) was applied from the model compounds in CHARMM additive force field developed for phosphate and sulfate groups linked to carbohydrates [18] in order to have the O-sulfate group at C6. Initial atomic partial charges of the hexopyranose ring as well as the O-sulfate group linked to C6 position were assigned from the parent compounds by analogy. The sulfamate group in GlcNS(6S) was built based on the analogy to residues "MMSM, N-Methylmethanesulfonamide", and "EESM, N-ethyl-ethanesulfonamide" in the extended CGENFF36 for sulfonyl-containing compounds [21]. These two residues were selected among the other sulfonyl-containing compounds as they both contain an identical $–NHSO_2–$ group that better resembles the sulfamate group of the GlcNS(6S) in terms of chemical structure and neighbouring bonds. The atom types of the $–NHSO_2–$ group was directly adopted from the aforementioned two parent compounds. Since GlcNS(6S) comprises a $NHSO_3^-$ group instead of $NHSO_2$, an extra oxygen atom having the same atom type as the other oxygens in the SO_2 group was added to the structure, as to follow a similar methodology to CHARMM's in creating negatively charged sulfate patches comprising three identical oxygens bound to a sulfur atom [18]. Although the atom types of the sulfamate group were directly assigned from the parent compounds by analogy, the partial atomic charges were

not transferred, as the charge distribution is expected to differ when the sulfamate group is bound to the hexapyranose ring. For a more accurate determination of the atomic charges of the sulfamate group and its neighboring atoms, C2 and H2, quantum mechanical (QM) calculations were carried out. Single-point energy calculations were performed on a single GlcNS(6S) molecule, saturated with H at both ends (at O1 and O4 positions) (Figure 5.1a), at HF/6-31G(d) level using Gaussian 09 [22]. AmberTools [23] was then used to obtain the restrained electrostatic potential (Resp) charges that render a good fit to the calculated electrostatic potential. The charge calculation was carried out for the whole molecule, and the resulting Resp charges along with their comparison to the partial atomic charges adopted from CHARMM36 additive all-atom carbohydrate force field are given in Table 5.1. The reported decimal points in the calculated Resp charges was adjusted to be consistent with the CHARMM36 charges. Note that the CHARMM force field divides the molecules into charge groups where the sum of the partial atomic charges evaluates to an integer value. The charge groups of GlcNS(6S) are shown in Table 5.1, and for consistency, the same group representation is followed for the Resp charges. Only the partial atomic charges of the sulfamate group and its neighboring atoms (Group 2 in Table 5.1) were adopted from the QM calculations (shown in italic in Table 5.1); as the rest of the charge assignment was done by analogy to the parent compounds in CHARMM36 additive all-atom carbohydrate force field. The expected total charge of the individual GlcNS(6S) molecule is –2; –1 charge being localized to the sulfamate group (Group 2 in Table 5.1) and the remaining –1 charge localized to the O-sulfate group at C6 position (Group 5 in Table 5.1). The distribution of the charges, however, is slightly different between CHARMM36 additive all-atom carbohydrate force field and Resp charges calculated at QM level amongst the charge groups. Adopting only the charges of the Group 2 from the QM level

calculations (–0.981), hence, introduced a small error to the expected charge of the Group 2 (–1). The error of –0.019 was equally distributed (–0.0063 each) to the three oxygens (O1S, O2S, O3S) bound to the S1 atom of the sulfamate group (details of the atom numbering can be found in Figure 5.1a), yielding –0.720 per sulfate oxygen and –1 for the total charge of Group 2.

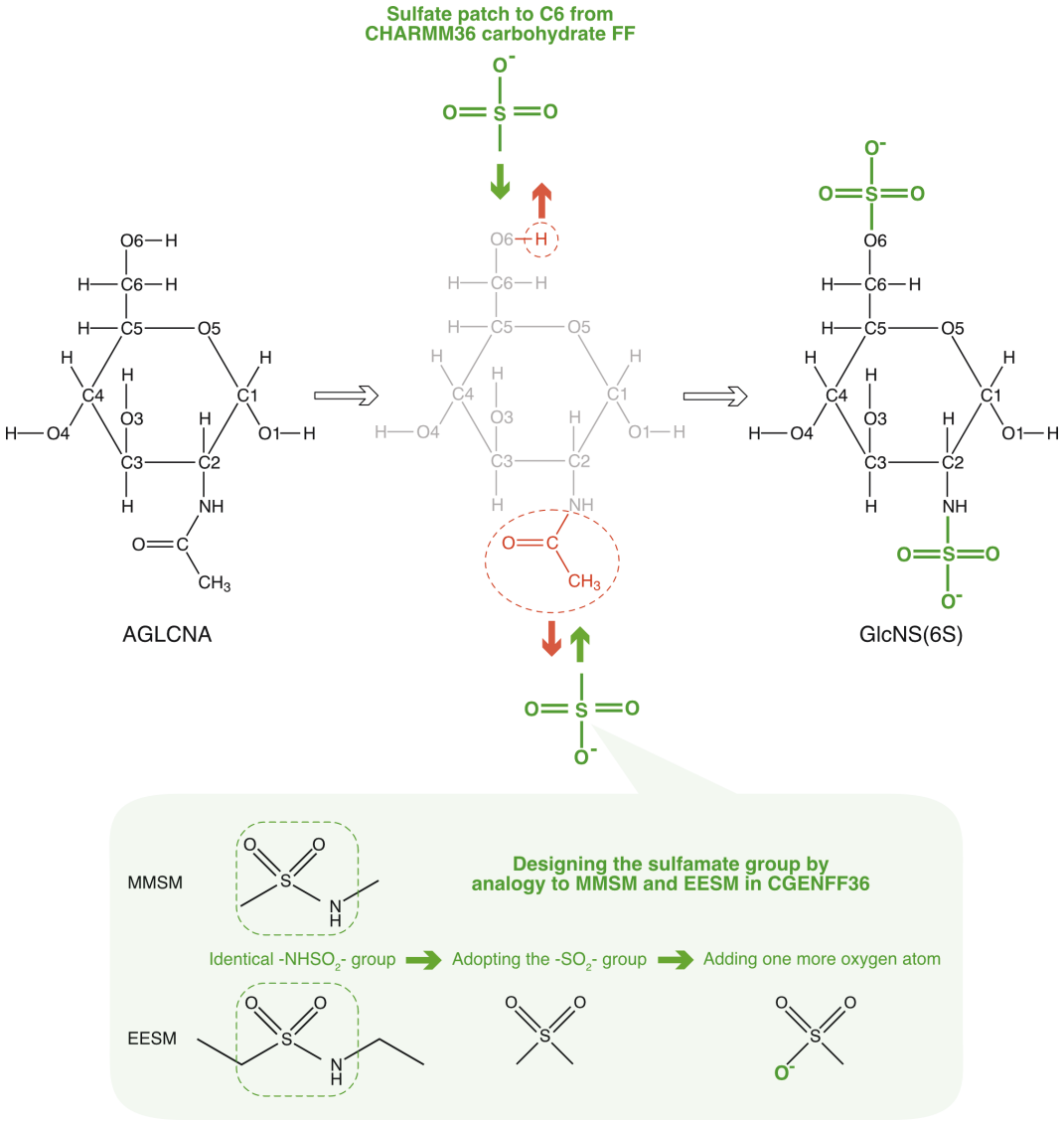

Figure 5.3. The flowchart of building the topology of GlcNS(6S) from the analogous molecules in CHARMM36 additive all-atom carbohydrate force field and CHARMM36 general force field (CGENFF36).
The planar representations of the molecules are given, and only the numbering of the atoms of interest is shown for clarity.

Table 5.1. Comparison of the partial atomic charges of an individual GlcNS(6S) molecule. Charges are retrieved from (*i*) the charge assignment by analogy to the parent molecules in CHARMM36 additive all-atom carbohydrate force field and (*ii*) quantum mechanical calculations at HF/6-31G(d) level. Only the charges shown in italic are adopted from the restrained electrostatic potential charges, with the adjustment to the charges of O1S, O2S and O3S as explained above. The details of the atom numbering of GlcNS(6S) can be found in Figure 5.1a.

	Atom	Charges adopted from CHARMM36 all-atom carbohydrate force field	Restrained electrostatic potential (Resp) charges from QM calculations
GROUP #1	C1	0.340	0.116
	H1	0.090	0.202
	O1	-0.650	-0.667
	HO1	0.420	0.451
	C5	0.110	0.029
	H5	0.090	0.091
	O5	-0.400	-0.383
Total charge of the group 1:		**0**	**-0.161**
GROUP #2	C2	0.070	*0.057*
	H2	0.090	*0.136*
	N	-0.470	*-0.680*
	HN	0.310	*0.314*
	S1	Not available	*1.334*
	O1S	Not available	*-0.714*
	O2S	Not available	*-0.714*
	O3S	Not available	*-0.714*
Total charge of the group 2:		**Not available***	**-0.981**
GROUP #3	C3	0.140	0.255
	H3	0.090	0.098
	O3	-0.650	-0.672
	HO3	0.420	0.425
Total charge of the group 3:		**0**	**0.106**
GROUP #4	C4	0.140	0.146
	H4	0.090	0.144
	O4	-0.650	-0.716
	HO4	0.420	0.465
Total charge of the group 4:		**0**	**0.039**
GROUP #5	C6	-0.280	0.007
	H61	0.090	0.120
	H62	0.090	0.047
	O6	-0.280	-0.367
	S2	1.330	1.240
	O4S	-0.650	-0.683
	O5S	-0.650	-0.683
	O6S	-0.650	-0.683
Total charge of the group 5:		**-1**	**-1.002**
Total charge of the molecule		**Not available***	**-1.999**

*: The atomic partial charges of the sulfamate group are not directly available in CHARMM36 additive all-atom force field. However, the expected charge of the Group 2 is -1, with total charge of the molecule being -2.

The analogous residue to IdoA2S in CHARMM36 additive all-atom force field is "AIDOA", which is α-L-iduronic acid. This parent compound consists of a hexopyranose ring, a C2 hydroxyl group, a carboxylate anion at C5. The chemical structure of AIDOA, and the process of building IdoA2S from AIDOA and the other identified compounds in CHARMM36 additive all-atom carbohydrate force field are schematically shown in Figure 5.4. In order to build IdoA2S from the parent compound, a sulfate patch to C2 (PRES CHSHB) was applied from model compounds in CHARMM additive force field developed for phosphate and sulfate groups linked to carbohydrates [18] in order to have the O-sulfate group at C2 position. Initial partial charges of all the atoms were assigned from the parent compounds by analogy. The total charge of the individual IdoA2S molecule is –2; each –1 being carried by the carboxylate and the O-sulfate groups linked at C5 and C2 positions, respectively.

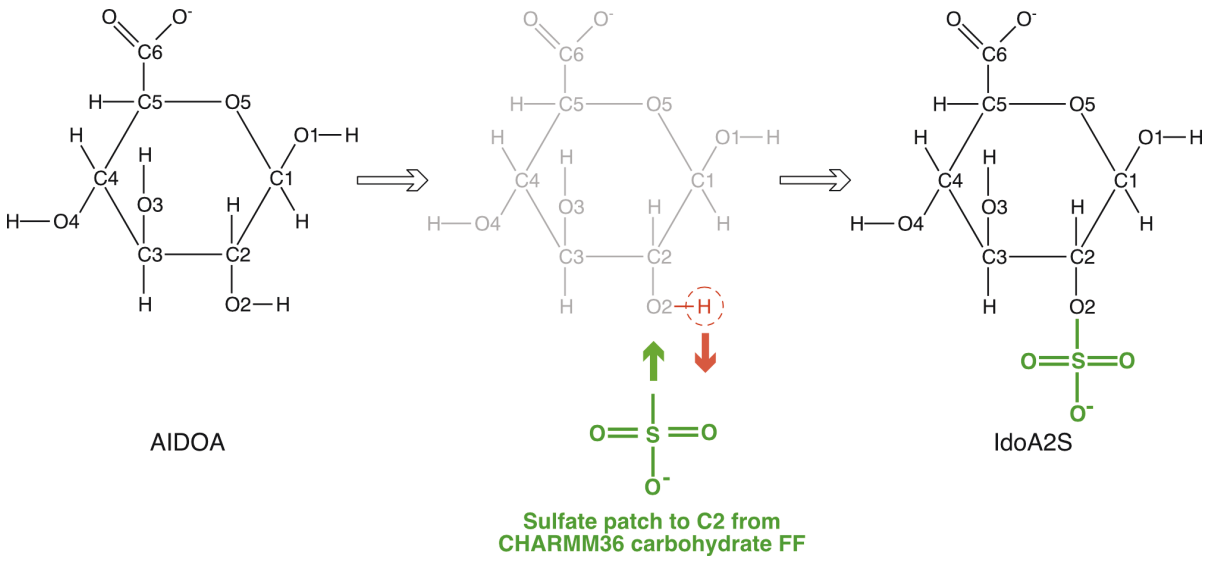

Figure 5.4. The flowchart of building the topology of IdoA2S from the analogous molecules in CHARMM36 additive all-atom carbohydrate force field.
The planar representations of the molecules are given, and only the numbering of the atoms of interest are shown for clarity.

Upon building the topology of the GlcNS(6S) and IdoA2S, the individual building blocks were linked together via 1→4 glycosidic linkage. The process we followed while linking the residues of heparin is given in Figure 5.5. We adopted a similar procedure to the equatorial – axial 1→4 linkage (PRES 14ba) patch in CHARMM36 additive all-atom carbohydrate force field [24]. In the case of two residues to be linked together, the patch PRES 14ba deletes the HO4 of the first residue, and the O1 and HO1 of the second, hence assigns O4 as the linkage oxygen; while in the original pdb (PDB code: 1HPN [19]), the O1 atom was kept as the linkage oxygen. To follow the same numbering of the linkage atoms in the original PDB for consistency, we removed the O4 and HO4 of the first and the HO1 of the second residue, keeping O1 of the second residue and assigning it as the linkage oxygen (Figure 5.5). Despite the slight differences in the two procedures, both result in the same 1 → 4 glycosidic linkage: C1 – O (O1 or O4 depending on the atomic numbering and/or which atoms are removed during the linkage) – C4. The partial charges of the linkage atoms were assigned accordingly from the patch PRES 14ba.

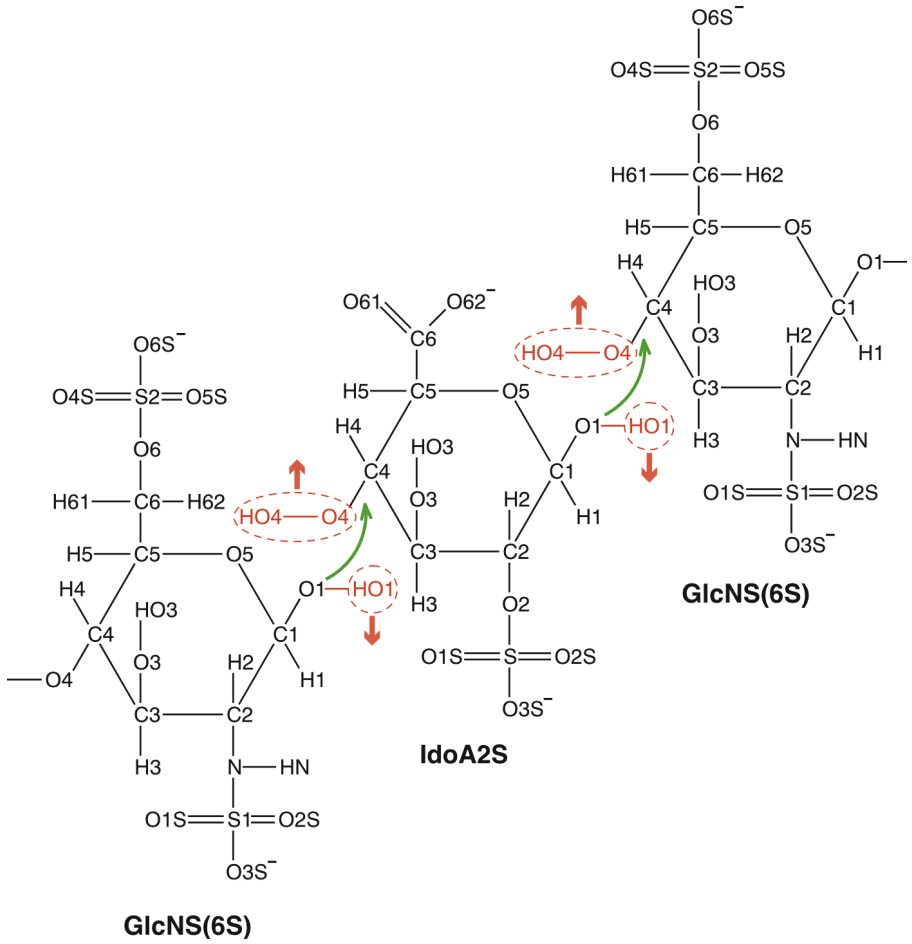

Figure 5.5. The schematic representation of the process of linking the building blocks of heparin together.

The planar representations of the building blocks, GlcNS(6S) and IdoA2S, are given (see Figure 5.1 for the details on the atom numbering), and the linkage of three residues is shown as an example. The atoms to be removed during the linking process are shown in red, and highlighted with dashed circles and red arrows. The 1→4 glycosidic linkages to be formed between the residues are pointed with a green arrow.

Bond, angle, torsion, and van der Waals parameters were adopted from the existing parameters of the analogous compounds selected from CHARMM36 additive all-atom carbohydrate force field [17] and CGENFF36 [21]. The missing parameters were assigned by following the methodology outlined in CGENFF [25].

5.3. Validation of the Force Field

For the equilibration of the initial structures of 12-mer and 21-mer heparin; each individual molecule was solvated in a TIP3P water box, with a 15 Å margin from all the sides; and neutralized with the addition of a proper amount of K^+ ions. Simulations were then performed with MD package of NAMD [26] with a time step of 2 fs and periodic boundary conditions (PBC), particle mesh Ewald (PME) [27] for full electrostatics, a cut-off of 12 Å for van der Waals and pairwise interactions, and SHAKE algorithm [28] to constrain the bonds involving H atoms. Systems were first minimized for 10 ps, then were gradually heated to 300 K within a 20 ps period, with a harmonic restraint (10 kcal/mol·$Å^2$) on non-H atoms of the solute. This restraint was kept for another 10 ns, and then removed; and NPT simulations were further performed for 10 ns. Later the validation of the force field will be carried out by comparison to a previously published simulation study in literature [12] where a decasaccharide heparin fragment was simulated for 3ns; therefore 10 ns was chosen as the simulation time to be closer to the simulation length of the adopted reference study for fair comparison. Temperature control was achieved with Langevin dynamics thermostat with a thermostat damping coefficient of 10 ps^{-1} for all the non-H atoms. Nosé−Hoover−Langevin barostat, with the damping time scale of 100 fs and Langevin piston oscillation period of 200 fs, was used for pressure control. The initial and final (at the end of 10 ns restrained + 10 ns free MD simulation) structures of the two heparin molecules simulated are given in Figure 5.6. Some changes were observed in the conformation of the hexopyranose rings over the course of the simulations (final structures in Figure 5.6). The internal iduronic acid residues are known to have an equilibrium ring conformation between chair, $^1C_4$, and skew boat, $^2S_0$ conformers [29]. The NMR solution structure of heparin (PDB code: 1HPN [19]) comprises two models, Model 1 and 2; where hexopyranose rings of the

IdoA2S residues have the $^{2}S_{0}$ and $^{1}C_{4}$ conformations, respectively. In this study, we adopted the initial coordinates from the Model 1, and did not implement any constraints on the hexopyranose rings to keep their initial ring puckering states; therefore, they are free to transition between any favored ring conformer over the course of the simulations. From the final structures given in Figure 5.6, it could be seen that the ring conformations in both heparins show some tendency of deviation from their initial configurations; however, investigation of the degree of transition in the ring puckering states is out of the scope of this study.

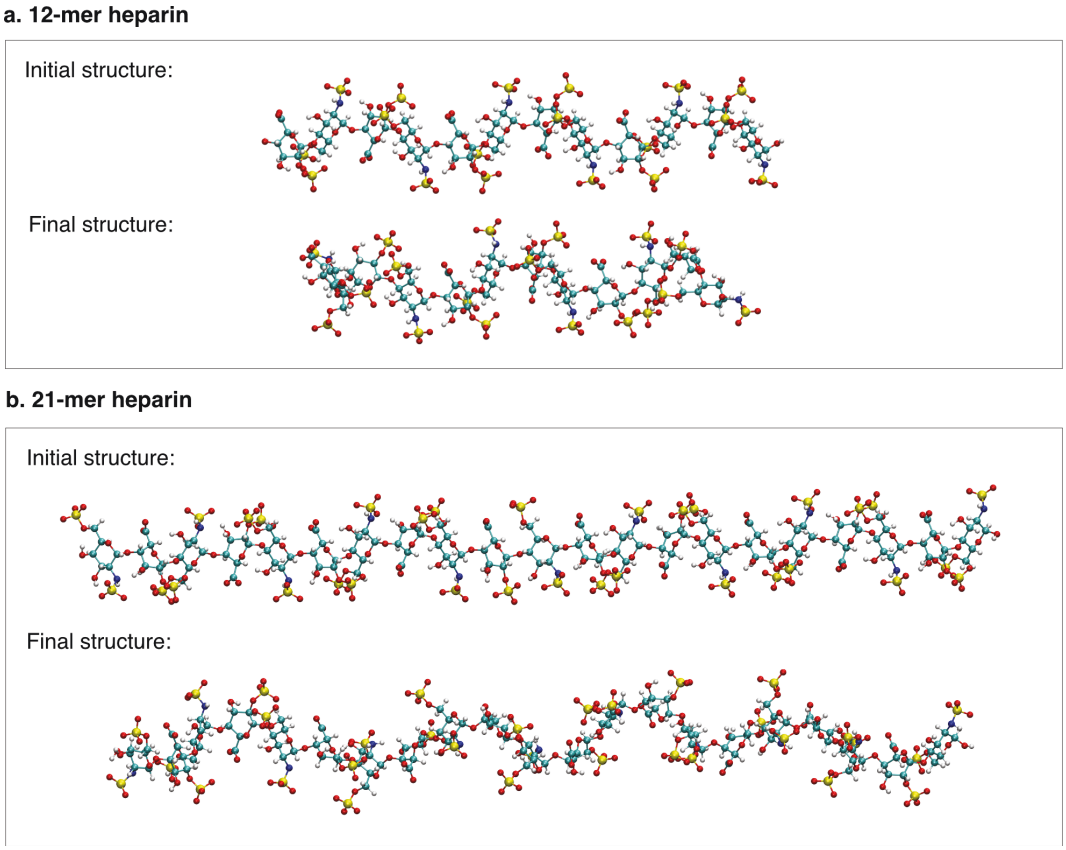

Figure 5.6. The initial and final (at the end of 10 ns restrained + 10 ns free MD simulation) structures of the heparin molecules studied.
(a) 12-mer, and **(b)** 21-mer heparin. The color coding of the atoms is as follows: cyan, C; red, O; yellow, S; blue, N; white, H.

The validation of the developed force field for heparin was carried out by monitoring the two torsional angles of the glycosidic linkages of the 12-mer heparin molecule (Figure 5.7c) over the course of the simulations, and comparing the resulting trends with the previously published data in Ref. 12. In Ref. 12, a decasaccharide fragment of heparin was simulated upon adopting the initial coordinates of the heparin building blocks from PDB code: 1HPN. Ref. 12 studies both Models 1 and 2; however, for the purpose of this work, we will only compare our results with their published data on Model 1. Ref. 12 uses a PRODRG [30] based topology, with some refinements on the partial atomic charges by adopting the Lowdin charges from QM calculations. Improper dihedral angles to constrain the $^2S_0$ conformational state of the IdoA2S residues as in PDB code: 1HPN, Model 1 [19] were also implemented in Ref. 12; whereas in our work no additional constraints on the IdoA2S residues were used. 3 ns MD simulations on a single heparin decasacchharide were carried out in Ref. 12 using GROMACS MD package and force field.

Figure 5.7 shows the heparin molecules simulated in Ref. 12 and in this work, as well as the detailed definition of the torsional angles. It should be noted that there are some differences in the residue numbering between this work and Ref. 12. We followed the residue numbering in the original PDB file (PDB code: 1HPN [19]), where the structure consists of 12 residues which are numbered in ascending order from right to left (Figure 5.7b). The structure simulated in Ref. 12 however, has 10 residues which are labeled with letters in ascending order from left to right (Figure 5.7a).

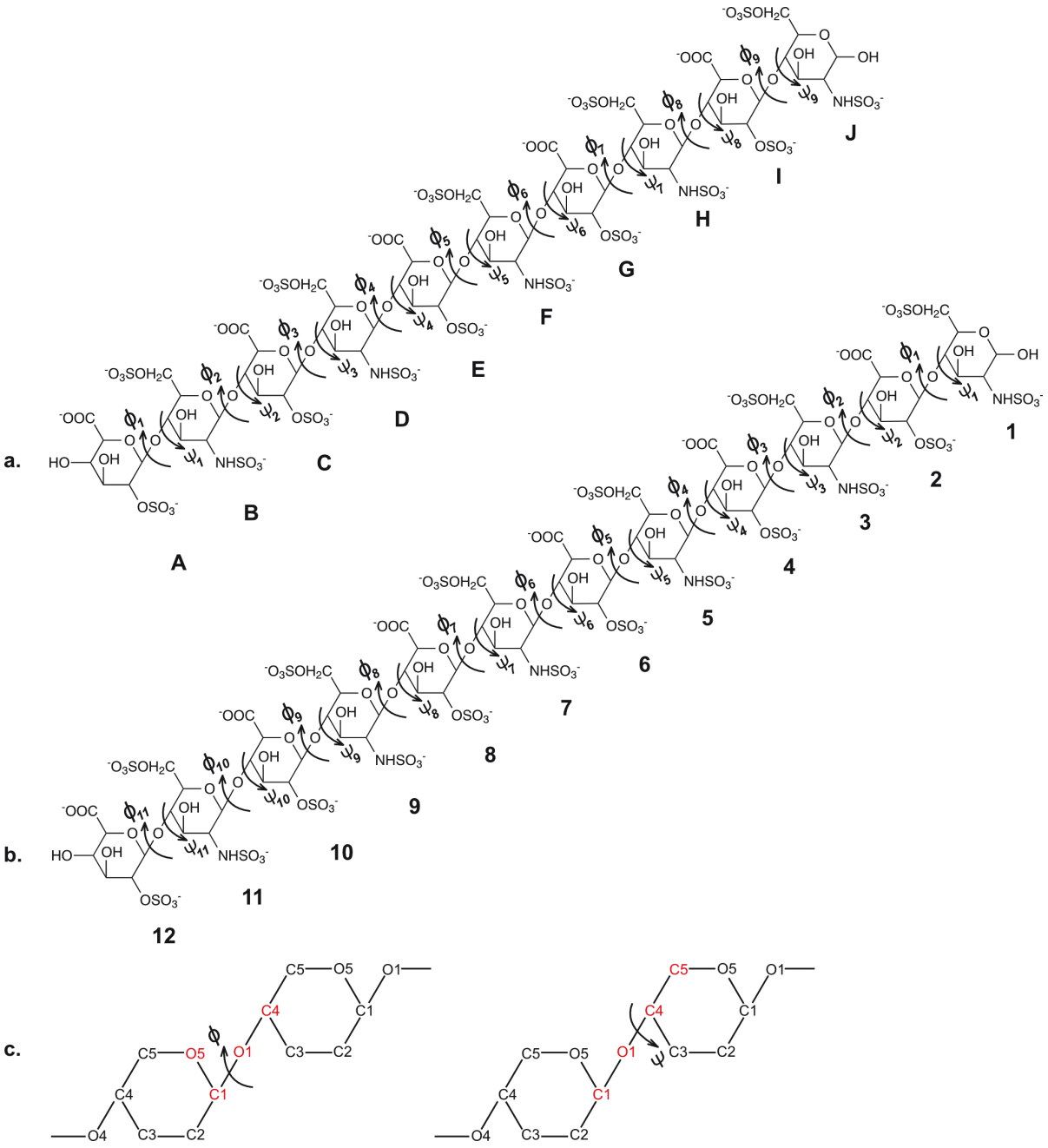

Figure 5.7. Planar representations, residue numbering, and glycosidic torsional angles of the heparin molecules.

(a) Simulated in Ref. 12, and **(b)** simulated in this study. The torsional angles, ϕ and ψ, are also shown, of which the detailed definition is given in **(c)**, with the atoms constituting the torsional angles being highlighted in red.

There are two types of 1→4 linkages, one from IdoA2S to GlcNS(6S), which will be denoted as IdoA2S→GlcNS(6S); and one from GlcNS(6S) to IdoA2S which will be denoted as GlcNS(6S)→IdoA2S. In the 12-mer heparin molecule, this definition generates six IdoA2S→GlcNS(6S) linkages, where the corresponding torsion angles will be odd-numbered; and five GlcNS(6S)→IdoA2S linkages, where the corresponding torsion angles will be even-numbered (Figure 5.7b). The difference in residue numbering between this work and Ref. 12 leads to some differences in the numbering of the torsional angles; e.g. the ϕ_1 in this study corresponds to ϕ_9 in Ref. 12 (Figure 5.7a, b).

We monitored the torsional angles over the 10 ns NPT simulations, and plotted these angles as a function of simulation time in Figure 5.8a. The reference data retrieved from Ref. 12 is also given in Figure 5.8b for comparison. We were able to regenerate the distribution of all the torsional angles reported in Ref. 12. It must be noted that a slightly larger data scattering is observed for the torsional angles of the GlcNS(6S)→IdoA2S linkage.

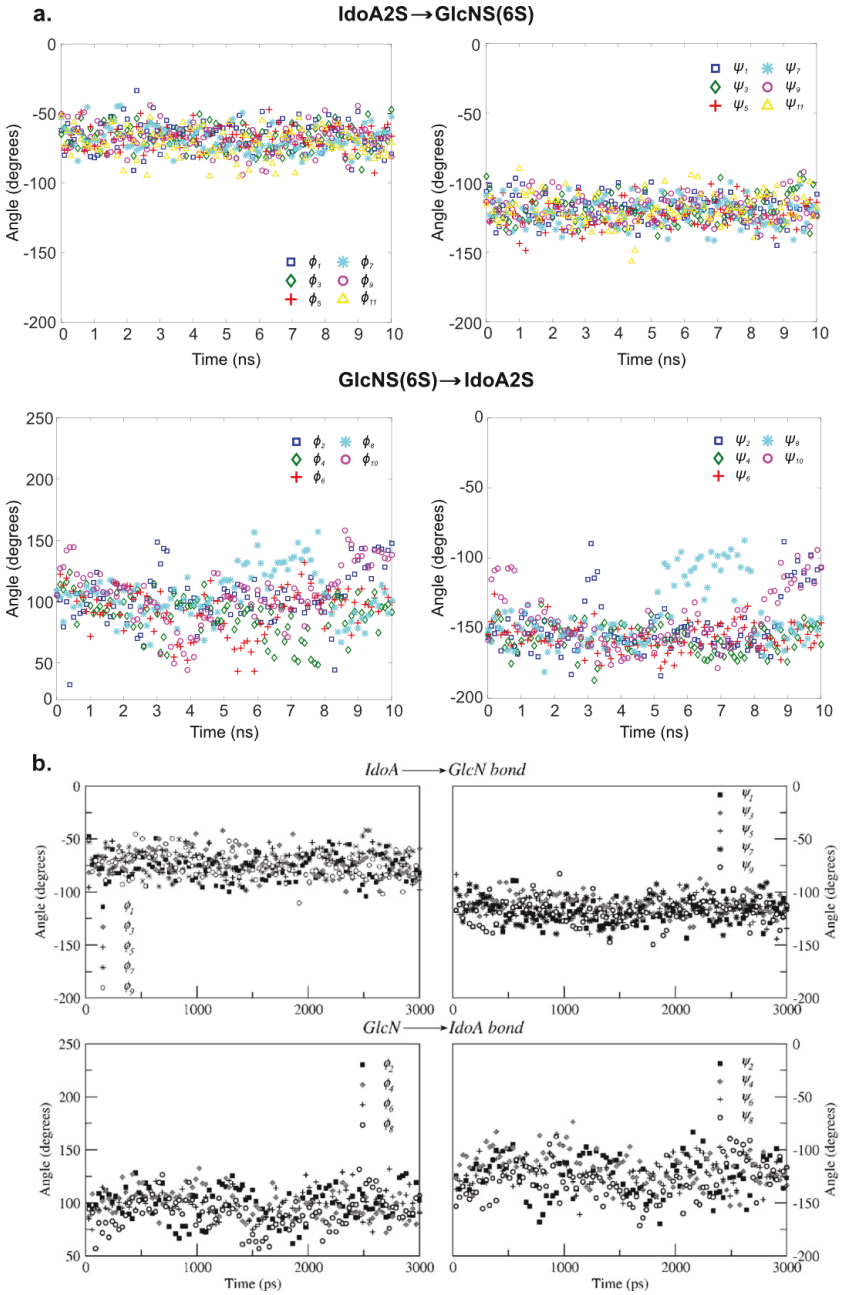

Figure 5.8. Glycosidic torsional angles as a function of the simulation time.
(a) From the analysis of the simulations performed in this study. **(b)** Results reported in Ref. 12; reprinted from Verli H & Guimarães JA (2004) Molecular dynamics simulation of a decasaccharide fragment of heparin in aqueous solution. *Carbohydr Res* 339(2):281-290, Copyright 2004, with permission from Elsevier. Each subfigure consists of four plots corresponding to ϕ and ψ of the two types of 1→4 linkages, IdoA2S→GlcNS(6S) and GlcNS(6S)→IdoA2S. IdoA2S and GlcNS(6S) are denoted as IdoA and GlcN, respectively, in Ref. 12.

For a more quantitative comparison, we also investigated the average values of the torsional angles over the simulation period (Table 5.2). Our developed CHARMM force field for heparin was able to generate IdoA2S → GlcNS(6S) ϕ and GlcNS(6S) → IdoA2S ψ angles closer to the NMR reference data than the force field used in Ref. 12. Other angles, IdoA2S→GlcNS(6S) ψ and GlcNS(6S)→IdoA2S ϕ, were close to the data reported in Ref. 12 with a slightly higher standard deviation in GlcNS(6S)→IdoA2S ϕ due to the slightly larger data scattering discussed above.

Table 5.2. Average values of the glycosidic torsional angles.
The data averaged over the simulated time of this study, and the reported average angles in Ref. 12 (Figure 5.8b) are given. The reference data obtained from the NMR solution structure of heparin (PDB code: 1HPN, Model 1 [19]) is also provided for comparison.

Torsional angles (°)		PDB Code: 1HPN, Model 1	Ref. 12 Model 1	This study
IdoA2S → GlcNS(6S)	ϕ	-55.4	-75.0 ± 10.7	-68.2 ± 9.6
	ψ	-107.4	-116.6 ± 10.6	-119.8 ± 9.9
GlcNS(6S) → IdoA2S	ϕ	108.6	96.6 ± 14.1	99.8 ± 21.1
	ψ	-157.5	-125.0 ± 15.1	-149.5 ± 18.7

In addition to the glycosidic linkage torsional angles, we monitored the intramolecular H-bonds between the carboxylate/sulfamate moieties and the hydroxyl groups of the heparin residues. Ref. 12 investigated three H-bonds (illustrated in Figure 5.9) that could form between (*i*) the hydroxyl group of GlcNS(6S) and carboxylate of IdoA2S (labeled as A in Figure 5.9), (*ii*) hydroxyl and sulfamate groups of GlcNS(6S) (labeled as B in Figure 5.9), and (*iii*) hydroxyl group of IdoA2S and sulfamate of GlcNS(6S) (labeled as C in Figure 5.9). The distance between the O atoms of the tagged pairs was reported as representative of each H-bond.

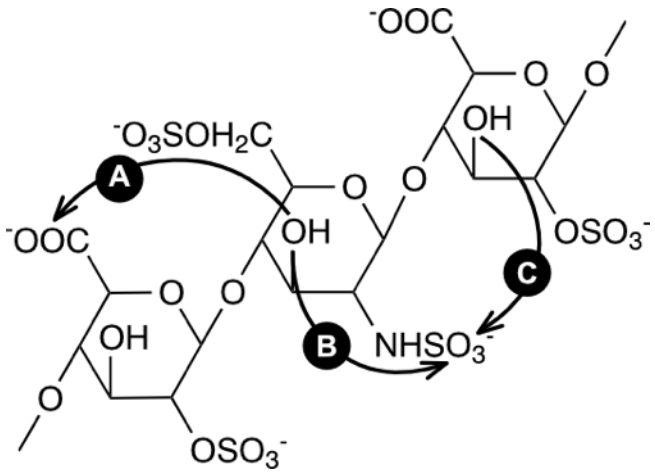

Figure 5.9. Representation of the intramolecular H-bonds of the heparin chain.
A schematic is given for the intramolecular H-bonds reported in Ref. 12 that could form between (A) the hydroxyl group of GlcNS(6S) and the carboxylate of IdoA2S, (B) the hydroxyl and sulfamate groups of GlcNS(6S), (C) the hydroxyl group of IdoA2S and sulfamate of GlcNS(6S).

As the carboxylate and sulfamate moieties contain multiple O atoms that can act as proton acceptors, two or three O – O distances can be measured, respectively, for the tagged pairs. Ref. 12 reported the minimum value of the distance measured among these two or three possibilities; therefore, for consistency, we followed the same approach and reported the average value of the lowest distance measured throughout the time trajectory (Table 5.3). We compared our results with the reference values calculated from the NMR solution structure of heparin, and the data reported in Ref. 12, which are given in the first two columns of Table 5.3, respectively. Despite the absence of improper dihedrals to constrain the $^2S_0$ conformational state of the IdoA2S residues in this work in comparison with the constrained structure in Ref. 12, the O – O distances of the tagged pairs measured from our trajectories were closer to the NMR reference data. In this study, the deviation from the NMR reference data in the O – O distances were found to be 0.2 Å, 0 Å, and 0.5 Å for the A, B, and C pairs, respectively; whereas a larger deviation was reported in all the O – O distances in Ref. 12 (0.4 Å, 0.2 Å, and 0.9 Å, for A, B, and C,

respectively). These results indicate that 12-mer heparin in our study did not experience significant conformational changes, thus mostly conserved its intramolecular H-bonding network. This also explains the linkage dihedrals we reported in Table 5.2 being closer to NMR reference data than those of Ref. 12. Moreover, the large data scattering observed in the GlcNS(6S) → IdoA2S angles (Figure 5.8) could be due to the deviation of 0.5 Å from NMR reference data in the interaction between the hydroxyl group of IdoA2S and sulfamate of GlcNS(6S) (labeled as C in Figure 5.9), affecting the torsional angle between the two residues.

Table 5.3. The O – O distance (Å) of the tagged pairs depicted in Figure 5.9.
The minimum distance amongst the two or three possibilities was chosen as outlined in Ref. 12, and the data reported in this study is the average of the minimum distances over the 10 ns simulation time.

Distance between the oxygen atoms of the tagged pair (Å)	PDB Code: 1HPN, Model 1	Ref. 12 Model 1	This study
A	3.4	3.8	3.6
B	3.7	3.5	3.7
C	2.8	3.7	3.3

5.4. Conclusions

We presented the topology development and parameterization of the NMR solution structure of a 12-mer heparin, and an extended 21-mer heparin chain, based on the available CHARMM36 carbohydrate force field. We ran 10 ns, unrestrained MD simulation on the 12-mer heparin fragment, and monitored the glycosidic torsional angles and the intramolecular H-bonds for the validation of our model. We performed a comparison with Verli and Guimarães' study [12] where a PRODRG based topology with charge refinements and GROMACS force field were used. We obtained similar results to the outcomes reported by Verli and Guimarães, which demonstrates the reliability of our model. The 12-mer heparin molecule simulated in this study

did not experience significant conformational changes and mostly conserved its starting intramolecular H-bonding network and glycosidic torsional angles, and yielded closer values to the NMR reference data. The constructed molecular model and force field for heparin will be used in the MD simulations in Chapter 6 to investigate the roles of heparin on the delivery of polynucleotide-based therapeutics with polymeric carriers.

5.5. Acknowledgements

Compute Canada and WestGrid are gratefully acknowledged for providing the computing resources and technical support. We thank Dr. Morteza Chehel Amirani for the determination of the restrained electrostatic potential charges of a heparin residue from quantum mechanical calculations. Research funding for this work was provided by Natural Sciences and Engineering Research Council of Canada (NSERC), NSERC Collaborative Research and Training Experience Program for Regenerative Medicine (NCPRM), Canadian Institutes of Health Research (CIHR), Alberta Innovates Technology Futures (AITF), and Canada Foundation for Innovation (CFI).

5.6. References

1. Rabenstein DL (2002) Heparin and Heparan Sulfate: Structure and Function. *Nat. Prod. Rep.* 19(3):312-331.
2. Kreuger J, Spillmann D, Li JP, & Lindahl U (2006) Interactions Between Heparan Sulfate and Proteins: The Concept of Specificity. *J. Cell. Biol.* 174(3):323-327.
3. Gandhi NS & Mancera RL (2008) The Structure of Glycosaminoglycans and Their Interactions with Proteins. *Chem. Biol. Drug Des.* 72(6):455-482.
4. Sasisekharan R & Venkataraman G (2000) Heparin and Heparan Sulfate: Biosynthesis, Structure and Function. *Curr. Opin. Chem. Biol.* 4(6):626-631.
5. Sasisekharan R, Shriver Z, Venkataraman G, & Narayanasami U (2002) Roles of Heparan-sulphate Glycosaminoglycans in Cancer. *Nat. Rev. Cancer* 2(7):521-528.
6. Lamari FN, Militsopoulou M, Mitropoulou TN, Hjerpe A, & Karamanos NK (2002) Analysis of Glycosaminoglycan-derived Disaccharides in Biologic Samples by

Capillary Electrophoresis and Protocol for Sequencing Glycosaminoglycans. *Biomed. Chromatogr.* 16(2):95-102.

7. Perrimon N & Bernfield M (2000) Specificities of Heparan Sulphate Proteoglycans in Developmental Processes. *Nature* 404(6779):725-728.

8. Iozzo RV & San Antonio JD (2001) Heparan Sulfate Proteoglycans: Heavy Hitters in the Angiogenesis Arena. *J. Clin. Invest.* 108(3):349-355.

9. Sasisekharan R, Ernst S, & Venkataraman G (1997) On the Regulation of Fibroblast Growth Factor Activity by Heparin-like Glycosaminoglycans. *Angiogenesis* 1(1):45-54.

10. Machovich R (1975) Mechanism of Action of Heparin Through Thrombin on Blood Coagulation. *Biochim. Biophys. Acta* 412(1):13-17.

11. Jaques LB (1979) Heparin: An Old Drug with a New Paradigm. *Science* 206(4418):528-533.

12. Verli H & Guimarães JA (2004) Molecular Dynamics Simulation of a Decasaccharide Fragment of Heparin in Aqueous Solution. *Carbohydr. Res.* 339(2):281-290.

13. Munoz-Garcia JC, Corzana F, de Paz JL, Angulo J, & Nieto PM (2013) Conformations of the Iduronate Ring in Short Heparin Fragments Described by Time-averaged Distance Restrained Molecular Dynamics. *Glycobiology* 23(11):1220-1229.

14. Verli H & Guimarães JA (2005) Insights into the Induced Fit Mechanism in Antithrombin-Heparin Interaction Using Molecular Dynamics Simulations. *J. Mol. Graph. Model.* 24(3):203-212.

15. Canales A, Lozano R, Lopez-Mendez B, Angulo J, Ojeda R, Nieto PM, Martin-Lomas M, Gimenez-Gallego G, & Jimenez-Barbero J (2006) Solution NMR Structure of a Human FGF-1 Monomer, Activated by a Hexasaccharide Heparin-analogue. *FEBS J.* 273(20):4716-4727.

16. Barnard A, Posocco P, Pricl S, Calderon M, Haag R, Hwang ME, Shum VW, Pack DW, & Smith DK (2011) Degradable Self-assembling Dendrons for Gene Delivery: Experimental and Theoretical Insights into the Barriers to Cellular Uptake. *J. Am. Chem. Soc.* 133(50):20288-20300.

17. Guvench O, Mallajosyula SS, Raman EP, Hatcher E, Vanommeslaeghe K, Foster TJ, Jamison FW, 2nd, & Mackerell AD, Jr. (2011) CHARMM Additive All-atom Force Field for Carbohydrate Derivatives and Its Utility in Polysaccharide and Carbohydrate-Protein Modeling. *J. Chem. Theory Comput.* 7(10):3162-3180.

18. Mallajosyula SS, Guvench O, Hatcher E, & MacKerell AD (2012) CHARMM Additive All-Atom Force Field for Phosphate and Sulfate Linked to Carbohydrates. *J. Chem. Theory Comput.* 8(2):759-776.

19. Mulloy B, Forster MJ, Jones C, & Davies DB (1993) N.M.R. and Molecular-modelling Studies of the Solution Conformation of Heparin. *Biochem. J.* 293 (Pt 3):849-858.

20. Schrödinger Release 2015-4: Maestro, Schrödinger, LLC, New York, NY, 2015.

21. Yu WB, He XB, Vanommeslaeghe K, & MacKerell AD (2012) Extension of the CHARMM General Force Field to Sulfonyl-containing Compounds and Its Utility in Biomolecular Simulations. *J. Comput. Chem.* 33(31):2451-2468.

22. Frisch MJT, G. W.; Schlegel, H. B.; Scuseria, G. E.; Robb, M. A.; Cheeseman, J. R.; Scalmani, G.; Barone, V.; Mennucci, B.; Petersson, G. A.; Nakatsuji, H.; Caricato, M.; Li, X.; Hratchian, H. P.; Izmaylov, A. F.; Bloino, J.; Zheng, G.; Sonnenberg, J. L.; Hada, M.; Ehara, M.; Toyota, K.; Fukuda, R.; Hasegawa, J.; Ishida, M.; Nakajima, T.; Honda, Y.; Kitao, O.; Nakai, H.; Vreven, T.; Montgomery, Jr., J. A.; Peralta, J. E.; Ogliaro, F.; Bearpark, M.; Heyd, J. J.; Brothers, E.; Kudin, K. N.; Staroverov, V. N.; Kobayashi, R.; Normand, J.; Raghavachari, K.; Rendell, A.; Burant, J. C.; Iyengar, S. S.; Tomasi, J.; Cossi, M.; Rega, N.; Millam, J. M.; Klene, M.; Knox, J. E.; Cross, J. B.; Bakken, V.; Adamo, C.; Jaramillo, J.; Gomperts, R.; Stratmann, R. E.; Yazyev, O.; Austin, A. J.; Cammi, R.; Pomelli, C.; Ochterski, J. W.; Martin, R. L.; Morokuma, K.; Zakrzewski, V. G.; Voth, G. A.; Salvador, P.; Dannenberg, J. J.; Dapprich, S.; Daniels, A. D.; Farkas, Ö.; Foresman, J. B.; Ortiz, J. V.; Cioslowski, J.; Fox, D. J. (2009) Gaussian 09 (Gaussian Inc. , Wallingford, CT), Revision A.1.

23. Case DA, Darden TA, Cheatham TE, III , Simmerling CL, Wang J, Duke RE, Luo R, Walker RC, Zhang W, Merz KM, Roberts B, Hayik S, Roitberg A, Seabra G, Swails J, Götz AW, Kolossváry I, Wong KF, Paesani F, Vanicek J, Wolf RM, Liu J, Wu X, Brozell SR, Steinbrecher T, Gohlke H, Cai Q, Ye X, Wang J, Hsieh M-J, Cui G, Roe DR, Mathews DH, Seetin MG, Salomon-Ferrer R, Sagui C, Babin V, Luchko T, Gusarov S, Kovalenko A, & Kollman PA (2012) AmberTools 13 (University of California, San Francisco).

24. Guvench O, Hatcher E, Venable RM, Pastor RW, & MacKerell AD (2009) CHARMM Additive All-Atom Force Field for Glycosidic Linkages between Hexopyranoses. *J. Chem. Theory Comput.* 5(9):2353-2370.

25. Vanommeslaeghe K, Hatcher E, Acharya C, Kundu S, Zhong S, Shim J, Darian E, Guvench O, Lopes P, Vorobyov I, & MacKerell AD (2010) CHARMM General Force Field: A Force Field for Drug-Like Molecules Compatible with the CHARMM All-Atom Additive Biological Force Fields. *J. Comput. Chem.* 31(4):671-690.

26. Phillips JC, Braun R, Wang W, Gumbart J, Tajkhorshid E, Villa E, Chipot C, Skeel RD, Kale L, & Schulten K (2005) Scalable Molecular Dynamics with NAMD. *J. Comput. Chem.* 26(16):1781-1802.

27. Darden T, York D, & Pedersen L (1993) Particle Mesh Ewald - an N.Log(N) Method for Ewald Sums in Large Systems. *J. Chem. Phys.* 98(12):10089-10092.

28. Ryckaert JP, Ciccotti G, & Berendsen HJC (1977) Numerical-Integration of Cartesian Equations of Motion of a System with Constraints - Molecular-Dynamics of N-Alkanes. *J. Comput. Phys.* 23(3):327-341.

29. Sanderson PN, Huckerby TN, & Nieduszynski IA (1987) Conformational Equilibria of Alpha-L-iduronate Residues in Disaccharides Derived from Heparin. *Biochem. J.* 243(1):175-181.

30. van Aalten DM, Bywater R, Findlay JB, Hendlich M, Hooft RW, & Vriend G (1996) PRODRG, A Program for Generating Molecular Topologies and Unique Molecular Descriptors from Coordinates of Small Molecules. *J. Comput. Aided Mol. Des.* 10(3):255-262.

6. Mechanistic Insights into the Role of Glycosaminoglycans in Polymeric Nanoparticle Delivery by Molecular Dynamics Simulations[X]

[X] A version of this chapter will be submitted for publication as: Meneksedag-Erol D, Tang T, & Uludağ H, Mechanistic Insights into the Role of Glycosaminoglycans in Delivery of Polymeric Nucleic Acid Nanoparticles by Molecular Dynamics Simulations.

6.1. Introduction

Gene therapy with polynucleotide-based therapeutic agents holds considerable promise in a range of genetic and acquired diseases, including cancer. For functional delivery, polynucleotides are formulated into nanoparticulate structures by drug carriers for the protection of the polynucleotide cargo while facilitating its translocation through the plasma membrane. Owing to their safety and versatility, synthetic cationic polymers are the most utilized carriers. For a therapeutic benefit, either locally or systemically administered polynucleotides must be internalized by the targeted cells, remain intact in endocytic compartments, and disassemble from the polymeric carriers to be transported to the appropriate sub-cellular compartment. Extracellular matrix components and cell membrane molecules have been recognized to be involved in the process of polynucleotide delivery, as the cellular uptake of the polynucleotide complexes is influenced by their interaction with the membrane milieu. Glycosaminoglycans (GAGs) located on the cell surface and in extracellular matrix, are a class of structurally heterogeneous complex polysaccharides (10-100 kDa [1]), having a high anionic charge density due to the presence of carboxyl and sulfate groups [2, 3]. The most common GAGs are heparin/heparan sulfate (HS), chondroitin/dermatan sulfate (CS/DS), keratan sulfate (KS), and hyaluronic acid (HA) [4-6].

The role of the GAGs on polynucleotide complexes has been controversial and long debated. Previous studies have reported widely different and seemingly contradictory conclusions on the involvement of GAGs in the polynucleotide delivery pathway. On one hand, sulfated GAGs have been attributed beneficial effects in the delivery of polynucleotide complexes. It was suggested that GAGs can act as “receptors”, upon the observation of a significant reduction in the transfection efficiency of complexes *in vitro* [7] and *in vivo* [8] after

alteration of cell surface GAGs by either treatment with chlorate that decreases the sulfation of GAGs [9] or by enzymatic removal of the GAGs with GAG lysases. Moreover, chlorate treated cells were shown to display increased levels of cationic lipid associated cytotoxicity while addition of exogenous sulfated GAGs to the medium could reverse this toxic effect, suggesting that GAGs can reduce the complex cytotoxicity by shielding the high cationic charge of the complexes [2]. On the other hand, exogenous GAGs were reported to decrease *in vitro* transfection efficiency of the complexes [7, 8, 10]. The delivery agents that are the most susceptible to the deleterious effects of GAGs were identified as the polycationic carriers with buffering capability, such as polyamidoamine dendrimers, polyethylenimine (PEI), and dioctadecylamidoglycylspermine; while fusogenic lipids such as 1,2-dioleyl-3-phosphatidylethanolamine (DOPE) were observed to resist better the GAG associated inhibitory events [10]. The inhibitory effects of the GAGs were attributed to their capability to alter or disrupt the integrity of complexes. Many physicochemical studies carried out in this context [10-13] have reported partial relaxation of the complexes or complete release of polynucleotide cargo depending on GAG concentration and the physical properties of the GAG. In addition, binding of free GAGs to complexes was suggested to sequester the cationic charge of complexes, preventing them from establishing electrostatic interactions with the cell membrane or "GAG receptors" on the cell surface, hence blocking the cellular entry [8]. GAGs could also affect intracellular trafficking/dissociation of the polynucleotide complexes. Confocal microscopy studies have shown that exogenous GAGs could be internalized by the cells in complex with the carriers [3] and polynucleotide complexes [14], and the complex-bound GAGs may direct the complexes into unfavorable endosomes for functional translation [15, 16].

Accordingly, these reported dual roles of GAGs in polynucleotide-based therapeutics creates a discrepancy in our understanding of GAGs in polynucleotide delivery.

The molecular details of the interactions between the GAGs and polynucleotide complexes are obscure. The factors governing the extent of their interaction and the subsequent effects of these interactions on the functional performance are not well defined. The lack of a mechanistic understanding on the conditions leading to the change in biological performance hinders the development of functional polynucleotide delivery systems that could make use of the beneficial aspects of the GAGs, while withstanding their inhibitory effects. MD simulations can provide atomic resolution information on the dynamic evolution of the biological systems, which could not be readily attainable with most experimental tools. In this study, we performed a series of all-atom molecular dynamics (MD) simulations on model polynucleotide complex – GAG systems. We used a short interfering RNA (siRNA) as a representative polynucleotide and PEI as a prototypical polymeric carrier, while heparin served as a prototypical GAG. The simulation systems were designed based on the experimental literature with the aim of creating a series of scenarios in which the siRNA/PEI/heparin ternary systems might exist. At the all-atom level, Barnard and coworkers developed an approach to estimate a carrier's ability to release a polynucleotide cargo by comparing the carrier's binding affinity to DNA and to heparin sulfate from individual one-on-one binding simulations [17], without addressing the complex disassembly question directly. While this approach is useful to make comparative analysis among different carriers without running the three partite simulations, it does not provide any mechanistic details on complex disassembly and the behavior of the complexes in the presence of heparin. To the best of our knowledge, our study is the first attempt to simulate the interactions of heparin with polynucleotide complexes using all-atom MD simulations. We aim

to shed light on the ambiguity in the experimental literature through detailed analysis of heparin interactions with the siRNA-PEI complexes and heparin-mediated changes on the conformational states of the complexes, and correlating them with the current experimental data.

6.2. Methods

6.2.1. Simulated Systems

The specific siRNA simulated is designed for P-glycoprotein mRNA silencing [18]: sense: 5′-CAGAAAGCUUAGUACCAAATT-3′; antisense: 5′-UUUGGUACUAAGCUUUCUGTC-3′. It carries a total charge of –40 in the fully deprotonated state. The initial structure of the siRNA is adopted from our previous study [19]. We studied two PEIs differing in molecular weight (MW): 568 Da and 1874 Da (Figure 6.1a and b). 568 Da PEI consists of 13 amine groups, of which 6 are protonated; 1874 Da PEI has 43 amine groups and 20 of them are protonated (indicated in Figure 6.1a, b). The protonation ratio is fixed to 46%, which corresponds to the experimentally determined protonation state at pH = 6 [20]. The initial structures of the PEIs are adopted from our previous studies [21, 22], where the pre-equilibration of the structures was performed for 6 ns for the 568 Da PEI [21], and 50 ns for the 1874 Da PEI [22] with MD package of NAMD [23]. We investigated two heparin molecules differing in length: a dodecasaccharide (12-mer), and a henicosasaccharide (21-mer). The structures of heparin (Figure 6.1c and d) consist of alternating units of N,O6-disulfo-glucosamine (GlcNS(6S)) and 2-O-sulfo-alpha-L-idopyranuronic acid (IdoA2S) residues. The charge of the heparin molecule is dependent on its length; the 12-mer heparin carries a total charge of –24, whereas the 21-mer heparin molecule carries a total charge of –42. Details of the development of initial structures of the heparin fragments can be found in Chapter 5.

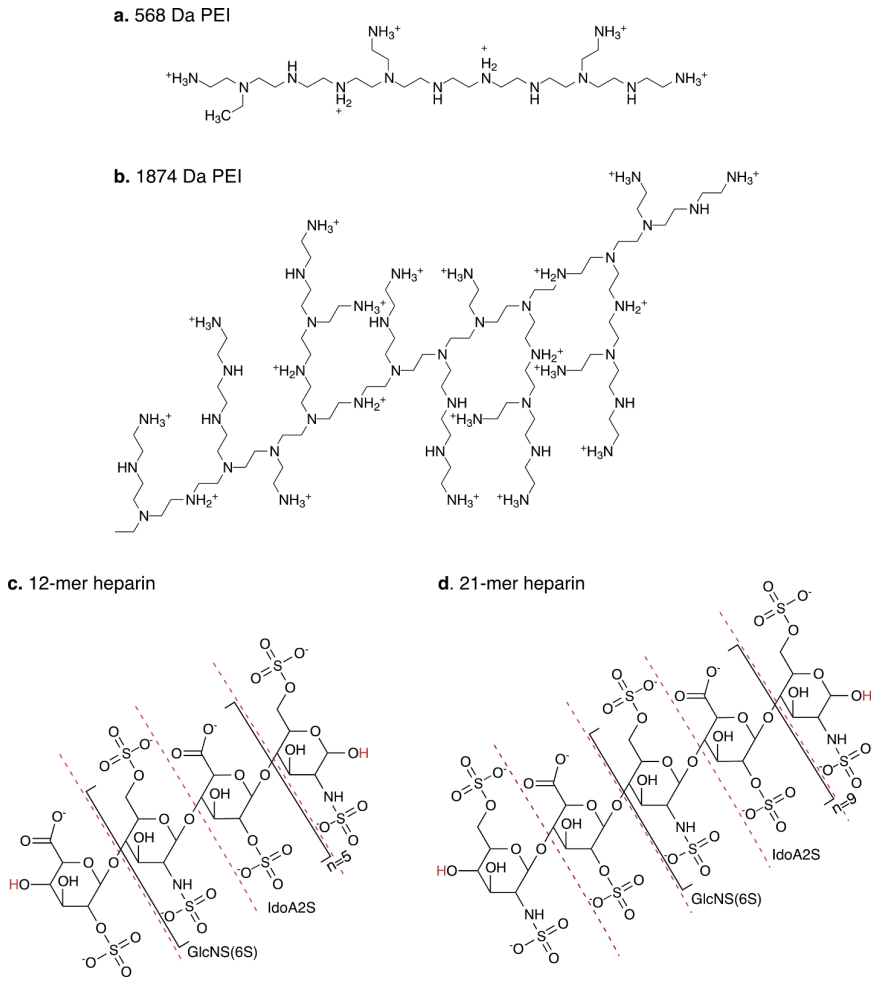

Figure 6.1. Chemical structures of the simulated molecules.
(a) 568 Da PEI, **(b)** 1874 Da PEI, **(c)** 12-mer heparin, and **(d)** 21-mer heparin. Protonation sites of the PEIs are indicated with (+) in **(a)** and **(b)**. The saturation sites in the heparin molecules are highlighted in red, and the number of the repeating IdoA2S – GlcNS(6S) disaccharide is denoted with n in **(c)** and **(d)**.

We investigated two groups of siRNA–PEI complexes with different polymer/siRNA charge ratios: one group with polymer/siRNA charge ratio >=1, and the other with polymer/siRNA charge ratio < 1. Changing the polymer/siRNA charge ratio (Table 6.1) was achieved by changing the MW of the PEI and/or the number of PEI molecules in the complexes. Complex 1 (C1) consisted of 2 siRNA and 14 PEI (568 Da) molecules. In the initial configuration of C1 (Figure 6.2a, left and middle panels), 2 siRNA molecules were placed at a

center of mass (COM) distance of 17.7 Å. Two PEIs were then placed amidst the 2 siRNAs, and the remaining 12 PEIs were placed symmetrically to surround the siRNAs. Upon solvation with TIP3P water and adding a proper amount of K^+ and Cl^- ions to achieve 150 mM salt concentration, the system was simulated for 10 ns (restrained) + 50 ns (free) for the complexation to occur. From the final configuration of C1 at the end of the simulation (Figure 6.2a, right panel), the initial structure of the system Complex 2 (C2) was generated (Figure 6.2b, left and middle panels). This was done by removing the 12 PEI molecules in the periphery of the C1's final structure, along with all the water molecules and ions, while keeping the 2 PEI molecules bridging the 2 siRNAs. Upon re-solvation and re-ionization (150 mM KCl), C2 was simulated for 10 ns (restrained) + 10 ns (free). Complex 3 (C3) consists of 2 siRNA and 4 PEI (1874 Da) molecules. In the initial configuration of C3 (Figure 6.2c, left and middle panels), 2 siRNA molecules were placed at COM distance of 17.7 Å. Two PEIs were then positioned amidst the 2 siRNAs, and the remaining 2 PEIs were placed symmetrically to the periphery of the siRNAs. The system was solvated, ionized with 150 mM KCl and simulated for 10 ns (restrained) + 50 ns (free). The final configuration of C3 is given in Figure 6.2c, right panel. By removing the 2 peripheral PEIs along with all the water molecules and ions and keeping the 2 PEIs bridging the two siRNAs, the initial structure of Complex 4 (C4) was built (Figure 6.2d, left and middle panels). System C4 was re-solvated and re-ionized, and then simulated for 10 ns (restrained) + 10 ns (free). The final configurations of systems C1, C2, C3 and C4 (right panel of Figure 6.2a–d, respectively) were then adopted as input structures to further simulations with heparins.

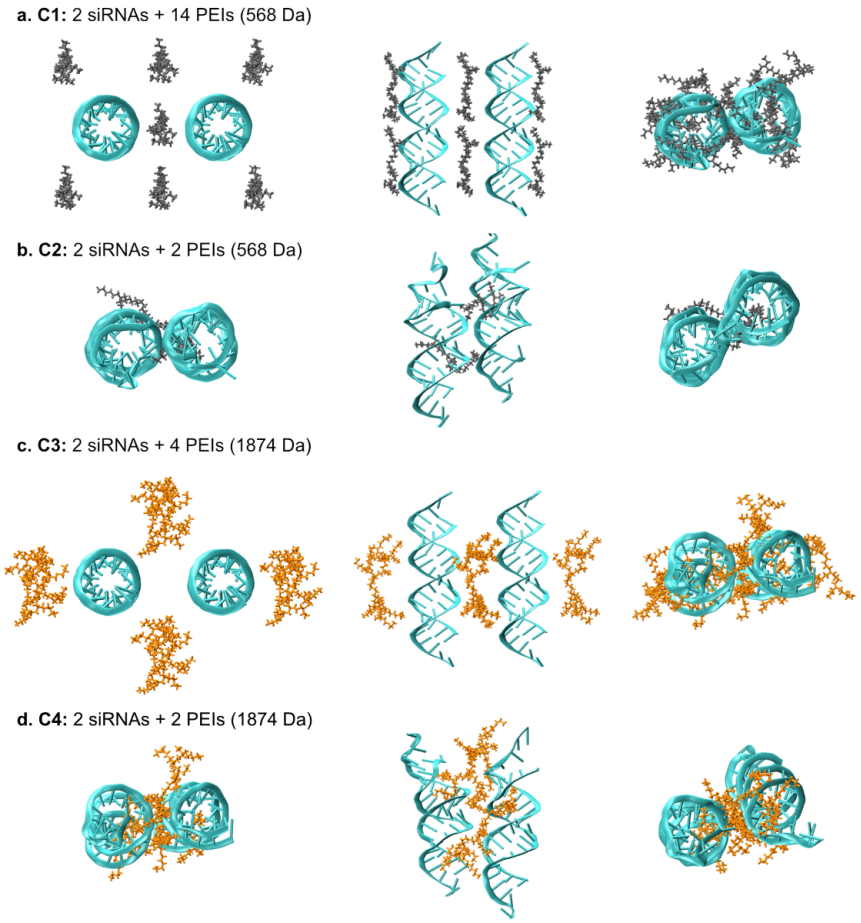

Figure 6.2. Initial and final configurations of the simulated siRNA-PEI complexes. Initial (left: top view; and middle: side view) and final (right: top view). **(a)** C1, **(b)** C2, **(c)** C3, and **(d)** C4. siRNAs are given in cyan, 568 Da PEIs are in gray, and 1874 Da PEIs are in orange. Water and ions are removed for clarity.

To explore heparin's effects on the complexes, seven simulation systems were designed to contain different numbers of heparin molecules (Table 6.1). All the siRNA-PEI-heparin ternary systems possess a net negative charge; the charge ratio of the heparin to PEI molecules in each system is given in the last column of Table 6.1. To design the initial structures of the siRNA-PEI-heparin ternary systems (Figure 6.3a, c–f, h, i; left panel), a desired number of heparin molecules was added to the pre-formed siRNA-PEI complexes, which corresponded to the final configurations of systems C1, C2, C3 and C4 simulated. To facilitate the discussion herein, the

simulation systems are labeled to include the complex identifier, the number of heparins, and the length of the heparin molecule, respectively. For this purpose, 12-mer heparin is represented with lower case letters “sh (short heparin)” and 21-mer heparin with lower case letters “lh (long heparin)”, both appended to the number of heparins in the system name. To explore the influence of the MW of the PEIs, the simulated systems are divided into two main groups that contain PEIs of 568 Da and 1874 Da. The first group consists of systems bearing the 568 Da PEI: C1-7sh, C2-2sh, C2-5sh and C2-2lh; and the second group has the 1874 Da PEI as the carrier: C3-7sh, C4-5sh, C4-2lh. Within the first group, C2-2sh and C2-5sh differ only by the number of heparin molecules, which allows us to investigate the influence of heparin amount on the proposed roles of heparin. Systems C2-2sh and C2-2lh differ only by the length of the heparin molecule, which allows the exploration of possible consequences of heparin chain length (or MW) variation on the properties/dynamics of the complexes. To systematically explore the effect of the PEI MW, comparisons will be made in three pairs of systems: C1-7sh vs. C3-7sh, C2-5sh vs. C4-5sh, and C2-2lh vs. C4-2lh, as the two systems in each pair consist of the same number of heparins of the same chain length. All the heparin containing systems were simulated for 10 ns (restrained) + 250 ns (free), upon solvation in a rectangular box of TIP3P water with a margin of 15 Å from all sides, and ionization with 150 mM KCl.

Two additional simulations were performed in the absence of heparins to serve as a “control”. Specifically, from the final structure of the C2 (Figure 6.2b, right panel), the starting structure of Complex 2 control (C2 ctl) was constructed by removing all the water molecules and ions (Figure 6.3b, left panel). Upon re-solvation and re-ionization (150 mM KCl), system C2 ctl was simulated for 10 ns (restrained) + 250 ns (free). Complex 4 control (C4 ctl, Figure 6.3g, left panel) is constructed from C4, and simulated in a similar way. These systems will be

compared to their heparin bearing counterparts; i.e., system C2 ctl serves as a control to C2-2sh, C2-5sh and C2-2lh, and system C4 ctl is the control to C4-5sh and C4-2lh.

Table 6.1. Information on the siRNA – PEI – heparin ternary systems simulated in this study.

System	PEI MW (Da)	PEI/siRNA charge ratio	Heparin length	Number of heparins	Simulation box volume (nm^3)	Heparin Concentration (mM)	Heparin/PEI charge ratio
C1-7sh	568	1.05	12-mer	7	1129.5	10.3	2.0
C2-2sh	568	0.15	12-mer	2	793.8	4.2	4.0
C2-5sh	568	0.15	12-mer	5	762.3	10.9	10.0
C2-2lh	568	0.15	21-mer	2	981.2	3.4	7.0
C3-7sh	1874	1.00	12-mer	7	1761.0	6.6	2.1
C4-5sh	1874	0.50	12-mer	5	968.2	8.6	3.0
C4-2lh	1874	0.50	21-mer	2	876.4	3.8	2.1

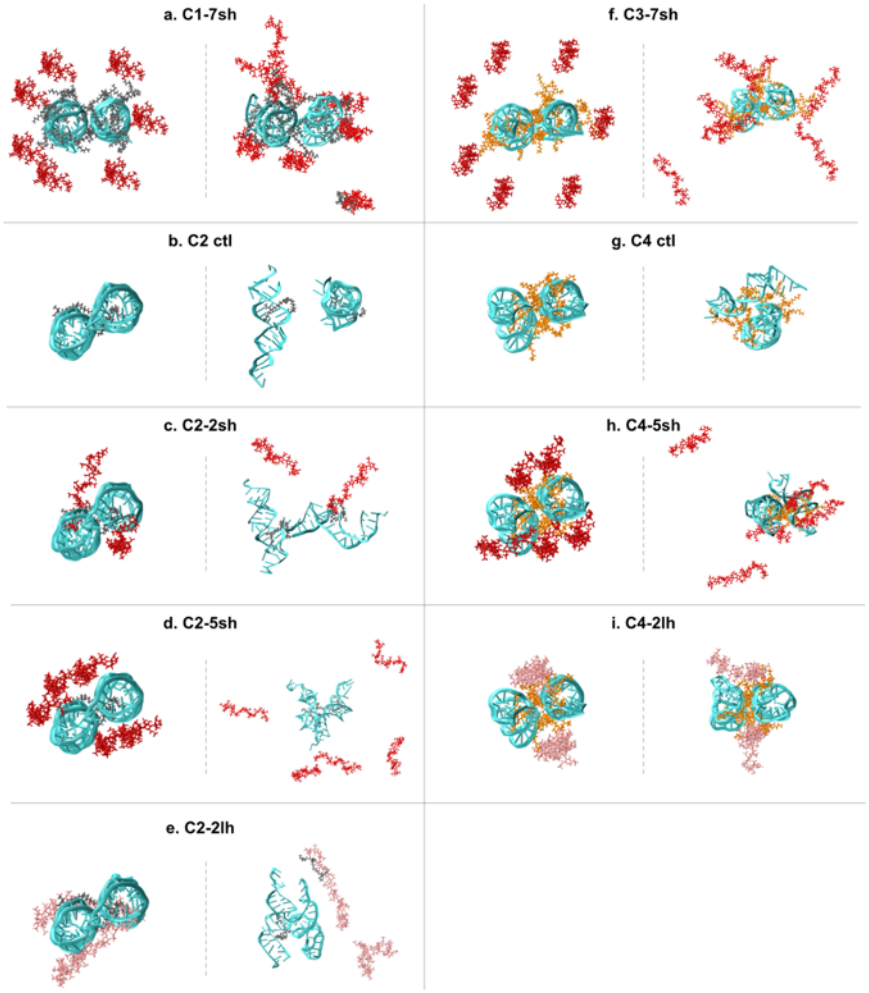

Figure 6.3. The initial and final configurations of the simulated siRNA-PEI-heparin ternary systems and their controls.
Initial (left), final (right) configurations of systems **(a)** C1-7sh, **(b)** C2 ctl, **(c)** C2-2sh, **(d)** C2-5sh, **(e)** C2-2lh, **(f)** C3-7sh, **(g)** C4 ctl, **(h)** C4-5sh, and **(i)** C4-2lh. The color coding of the molecules is as follows: cyan, siRNA; gray, 568 Da PEI; orange, 1874 Da PEI; red, 12-mer heparin; pink, 21-mer heparin. Water and ions are removed for clarity.

6.2.2. Simulation Details.

The force field for the PEI molecules was adopted from a CHARMM format force field which was generated and validated with *ab initio* calculations in our previous works [21, 22, 24]. The force field for the heparin molecule was devised by following the CHARMM General Force

Field (CGENFF) methodology [25]. The procedure we followed for the development and validation of heparin's force field is given in detail in Chapter 5.

All simulations were performed with MD package of NAMD [23]. A time step of 2 fs, periodic boundary conditions (PBC), particle mesh Ewald (PME) [26] for full electrostatics, a cut-off of 12 Å for van der Waals and pairwise interactions, and SHAKE algorithm [27] to constrain the bonds involving H atoms were used in all simulations. All systems were first minimized for 5000 steps, and then gradually heated from 0 K to 300 K within 20 ps, with a harmonic restraint of 10 kcal/mol·Å^2 on non-H atoms of the solute. Systems were further simulated for 10 ns while keeping the restraint on solute's non-H atoms. The restraint was then removed, and NPT simulations were performed for 50 ns for complexes C1 and C3, 10 ns for complexes C2 and C4, and 250 ns for all the siRNA-PEI-heparin ternary systems as well as their controls. Temperature control was achieved with Langevin dynamics thermostat with thermostat damping coefficient of 10 ps^{-1} for all the non-H atoms. Nosé−Hoover−Langevin barostat with damping time scale of 100 fs and Langevin piston oscillation period of 200 fs was used for pressure control. VMD [28] was used for the visualization and analysis of the simulation trajectories.

6.3. Results and Discussion

The final configurations of the siRNA-PEI-heparin ternary systems as well as their controls are shown in the right panel of Figure 6.3. The conformational states of the ternary systems were vastly varied depending on: (*i*) the physical properties of siRNA-PEI complexes, namely PEI/siRNA charge ratio and PEI MW, and (*ii*) heparin properties, namely the length of the heparin chain and the number of heparin molecules. We investigated the effect of heparin on the dynamics of the complexes, as well as the atomistic details of the interactions formed

between the PEI and heparin to elucidate the mechanism of heparin mediated changes on the siRNA complexes.

6.3.1. Dynamics of siRNA Complexes in the Presence of Heparin

6.3.1.1. siRNA Dynamics

The integrity of siRNA complexes en-route to cells is a critical parameter affecting the desired therapeutic outcome. To assess the compactness of the complexes in the absence and presence of heparin molecules, we first monitored the time course of the center of mass (COM) distance between the two siRNAs. In Figure 6.4a, we plotted the COM distance as a function of the simulation time, along with the average COM distance over the last 50 ns of the simulations in Figure 6.4b. It can be seen from Figure 6.4a that five out of seven simulated systems display COM distances that are fluctuating from 25 Å to 35 Å throughout the simulations; whereas two systems, C2 ctl and C2-2sh, exhibited COM separation beyond 35 Å. The latter two systems share the same complex composition (C2) comprising a low MW PEI, and possess a PEI/siRNA charge ratio below unity. For quantification purposes, we defined the time for siRNA separation when the COM distance between the two siRNA molecules reaches 35 Å and shows an overall increasing trend beyond this value. Following this definition, the control system C2 ctl was observed to experience siRNA separation with a sudden jump in the COM distance above 40 Å at around 100 ns, after which an increasing trend with fluctuations was observed reaching to 54.37 ± 5.45 Å on average over the last 50 ns. In comparison, system C2-2sh experienced less separation (with an average value of 40.05 ± 2.38 Å for the last 50 ns) starting at ~170 ns. Increasing the number of heparin molecules from low to moderate (C2-5sh), or the length of the heparin molecule from 12-mer to 21-mer (C2-2lh) prevented the separation of the siRNAs. Compared with C2 ctl (no heparin), the presence of heparin molecules did not expedite (C2-

2sh), or cause (C2-5sh, C2-2lh) siRNA separation; however, these observations could be attributed to MD-related limitations such as finite simulation box size and the use of PBC. PBC are used to introduce the bulk properties of the solution, where the primitive simulation cell is replicated in all directions to create infinite images of the simulation box [29]. As our simulations consist of complex disordered many-body systems, PBC use may bring in an "artificial periodicity" [30]. Our simulation boxes are quite spacious (15 Å water layer from all edges of the box), but the presence of free heparin molecules close to the edges increases the chances of heparins interacting with their own images. This interaction might impose a repulsive force on the primitive cell, confining the contents of the simulation box to a limited space and hindering the necessary particle motions needed for siRNA separation in C2-5sh.

Among the low MW PEI systems, increasing the PEI/siRNA charge ratio above unity (C1-7sh) increased the stability of complexes, so that no separation was evident. No separation was also seen for high MW (1874 Da) PEI systems, namely C3-7sh, C4 ctl, C4-5sh, and C4-2lh, that displayed fairly stable COM separation through the simulations.

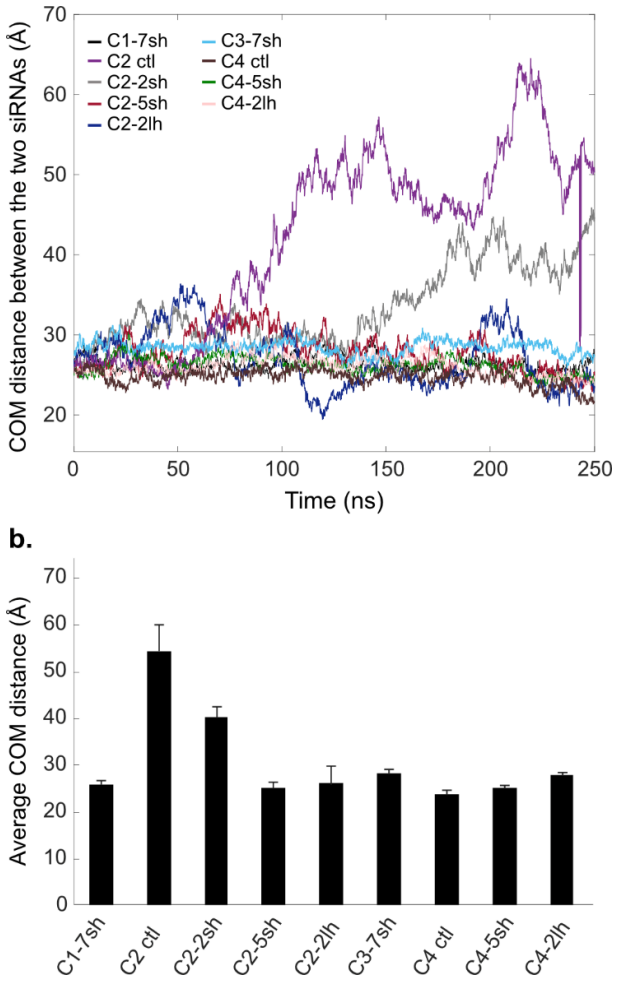

Figure 6.4. COM distance between the two siRNA molecules in siRNA-PEI-heparin ternary systems and their controls.
(a) Time evolution, and **(b)** average values over the final 50 ns of the simulations.

Visual examination of our simulation trajectories revealed an interesting mechanism involving the torsional motion of the siRNAs, i.e., change in relative orientation of the principal axes of the two siRNAs, accompanying siRNA separation. The torsional motion may impose a negative impact on the complex stability arising from (*i*) the weakening of the polyion bridging among multiple nucleic acids, and (*ii*) the generation of an accessible area between the siRNAs for binding of heparin molecules to exposed PEIs. Thus, the relative orientation of the siRNAs was monitored based on the cosine of the angle θ (cos θ) between the two siRNA molecules. To

do so, we defined a vector in each siRNA molecule by connecting two atoms at the opposite ends of the siRNA's two strands (C1′ of the 18th residue in each strand). We then measured the angle θ between the two vectors as a function of the simulation time. θ = 0° (cos θ = 1) represents the configuration of two parallel siRNA molecules, whereas θ = 90° (cos θ = 0) corresponds to the two siRNAs being perpendicular to each other. Figure 6.5 shows the time evolution of cos θ in the simulated systems. All systems consist of two siRNA molecules which are initially aligned parallel (cos θ = 1). We defined the transition from parallel to perpendicular orientation when cos θ is reduced to 0.7, and shows an overall decreasing trend beyond. Such a transition indicates the complexes being "partially relaxed". Partial relaxation was seen in systems C2 ctl, C2-2sh, C2-5sh, and C4 ctl. Among these four systems, separation of the siRNAs took place at ~100 ns and ~170 ns in C2 ctl and C2-2sh, respectively. The time of transition from parallel to perpendicular siRNA orientation is at ~140 ns in both systems, revealing that the torsional motion of the siRNAs could either accompany or follow the siRNA separation, or could be a preceding mechanism to complex disassembly via the partial relaxation of the complex. System C2-5sh displayed a very early transition (at ~50 ns) in siRNA torsional motion in comparison with others, although siRNA separation was not present within the simulated time frame. The onset of partial relaxation was detected at ~230 ns in system C4 ctl, which comprises 1874 Da PEI as the carrier and PEI/siRNA charge ratio below unity. Compared with C2 ctl (both systems are in the absence of heparin), increasing the PEI MW from 568 Da to 1874 Da increased the overall stability of the complex. However, complex relaxation is still seen to some extent in this system given that PEI/siRNA charge ratio is below unity.

Among the remaining systems, C3-7sh displayed the least amount of torsion, followed by C4-2lh and C4-5sh, all consisting of 1874 Da PEI. The systems with 568 Da PEI, C1-7sh and

C2-2lh, did not elicit the signs of partial relaxation, although the periods of high fluctuation in C2-2lh should be noted. These observations thereby highlighted the two distinct influences on the siRNA torsional motion. First, the course of relaxation was highly dependent on PEI MW as well as PEI/siRNA charge ratio. Second, increasing the heparin length in the 568 Da PEI systems impeded the partial relaxation of the complexes (C2-2sh vs. C2-2lh).

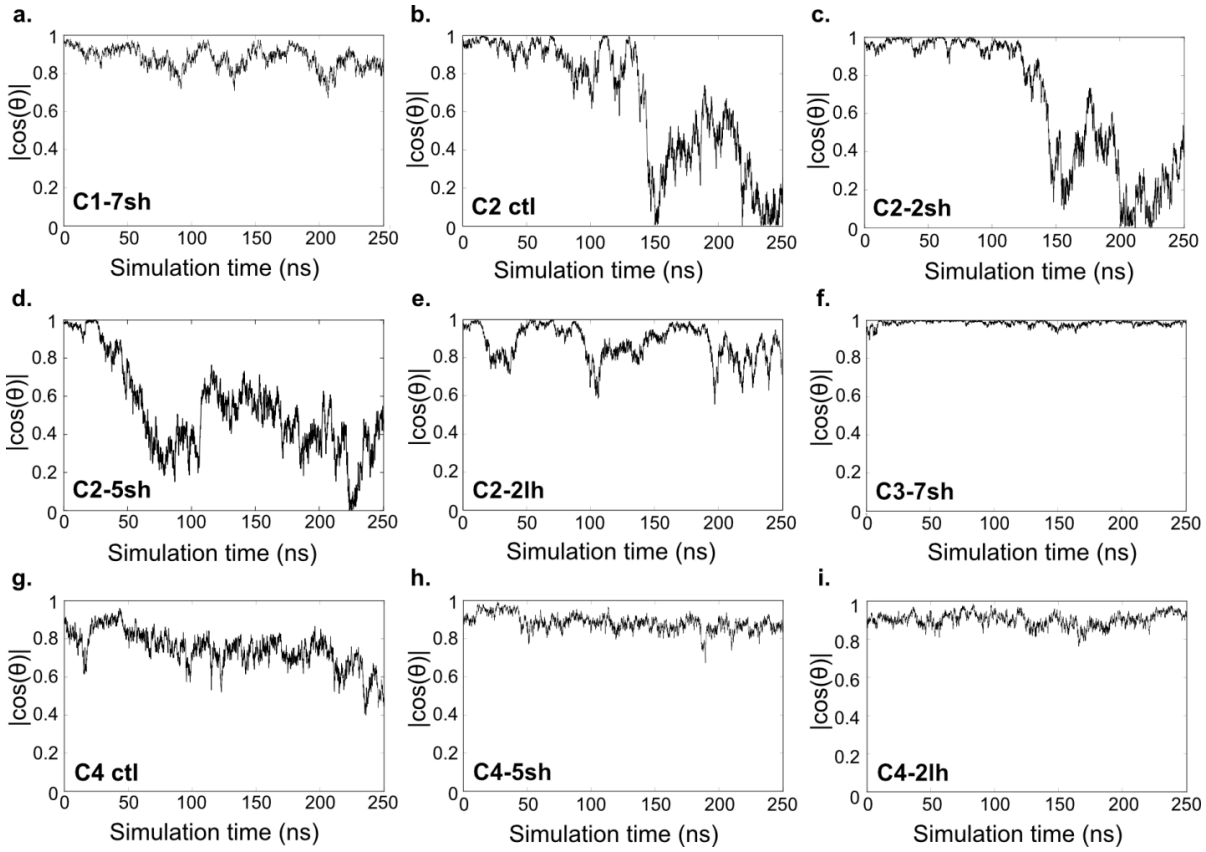

Figure 6.5. Absolute value of cos θ between the two siRNA molecules as a function of the simulation time in siRNA-PEI-heparin ternary systems and their controls.
(a) C1-7sh, **(b)** C2 ctl, **(c)** C2-2sh, **(d)** C2-5sh, **(e)** C2-2lh, **(f)** C3-7sh, **(g)** C4 ctl, **(h)** C4-5sh, and **(i)** C4-2lh.

6.3.1.2. PEI Dynamics

To investigate the PEI dynamics accompanying separation or partial relaxation of the siRNAs, we examined polyion bridging in C2 ctl, C2-2sh, C2-5sh, and C4 ctl, where the complexes displayed signs of instability. The polyion bridging pattern in the remaining systems can be found in Figures C.1 and C.2 in Appendix C. Figure 6.6 shows the number of PEI N atoms within 4 Å of any N/O atoms of siRNA or heparin, as a function of the simulation time. Here, 4 Å represents the distance in which a direct H-bond between PEI amines and siRNA and/or heparin N/O could be formed [31]. Each subfigure contains two plots corresponding to the two PEIs in each system (labeled as PEI-1 and PEI-2 respectively). In these systems, we intentionally kept the two PEI molecules amidst the two siRNAs to serve as a bridge while constructing the initial configurations. Each plot has a different number of curves representing the two siRNA, and two or more of the heparin molecules (each heparin is labeled with a number, for example, heparin-1). To quantify polyion bridging, the following definitions have been made: (*i*) a PEI is defined as bound to an siRNA (or heparin) if it has at least one N atom within 4 Å of any of the N/O of the siRNA (or heparin); (*ii*) a polyion bridge forms when one PEI molecule is bound to two siRNA molecules simultaneously.

In system C2 ctl (Figure 6.6a), PEI-1 and PEI-2 were found to bridge the two siRNA molecules up until 76 ns and 87 ns, respectively. Subsequently, each PEI maintained their interactions with their closest siRNA, losing their interaction with the other siRNA. As discussed above, C2 ctl showed siRNA COM separation at around 100 ns, followed by torsional motion of the siRNAs starting at ~140 ns. The loss of polyion bridging thus preceded both siRNA COM separation and the torsional motion, and may indicate the reason for siRNA separation. The presence of two heparin molecules in system C2-2sh (Figure 6.6b) slightly

extended the bridging brought by the PEI-1 (from 76 ns to 110 ns). PEI-1 was bound to heparin-1 since the beginning of the simulation and this interaction was further strengthened upon the loss of PEI-1's contact with siRNA-1. PEI-1 maintained its bound state to siRNA-2 and heparin-1 past 110 ns. Similar to system C2 ctl, decrease in polyion bridging preceded both the COM separation of the siRNAs as well as siRNA torsional motion, which took place at ~170 ns and 140 ns, respectively. Presence of heparin did not break the polyion bridge formed by PEI-2. However, the strength of this bridge was substantially weakened, fluctuating around 1 or 2 bound Ns (out of 13 N atoms in total) to siRNA-2 past 166 ns. Increasing the number of heparin molecules, on the other hand (C2-5sh, Figure 6.6c), did not lead to the loss of the bridges formed by the PEIs, except in PEI-2 during the early stages of the simulation. The bridging performance of PEI-2 is again significantly weakened, in fact non-existent between 40 and 100 ns, and fluctuating around 1 or 2 N atoms bound to siRNA-2 past 100 ns. In addition, neither of the PEIs are bound to any heparin molecule in system C2-5sh despite the higher number of heparin molecules than that of C2-2sh. Although showing the onset of partial relaxation towards the end of the simulation, system C4 ctl (Figure 6.6d) displayed a strong and consistent polyion bridging throughout the simulation. This system contains 1874 Da PEI which forms stronger contacts with the siRNAs, regardless of the PEI/siRNA charge ratio being below unity.

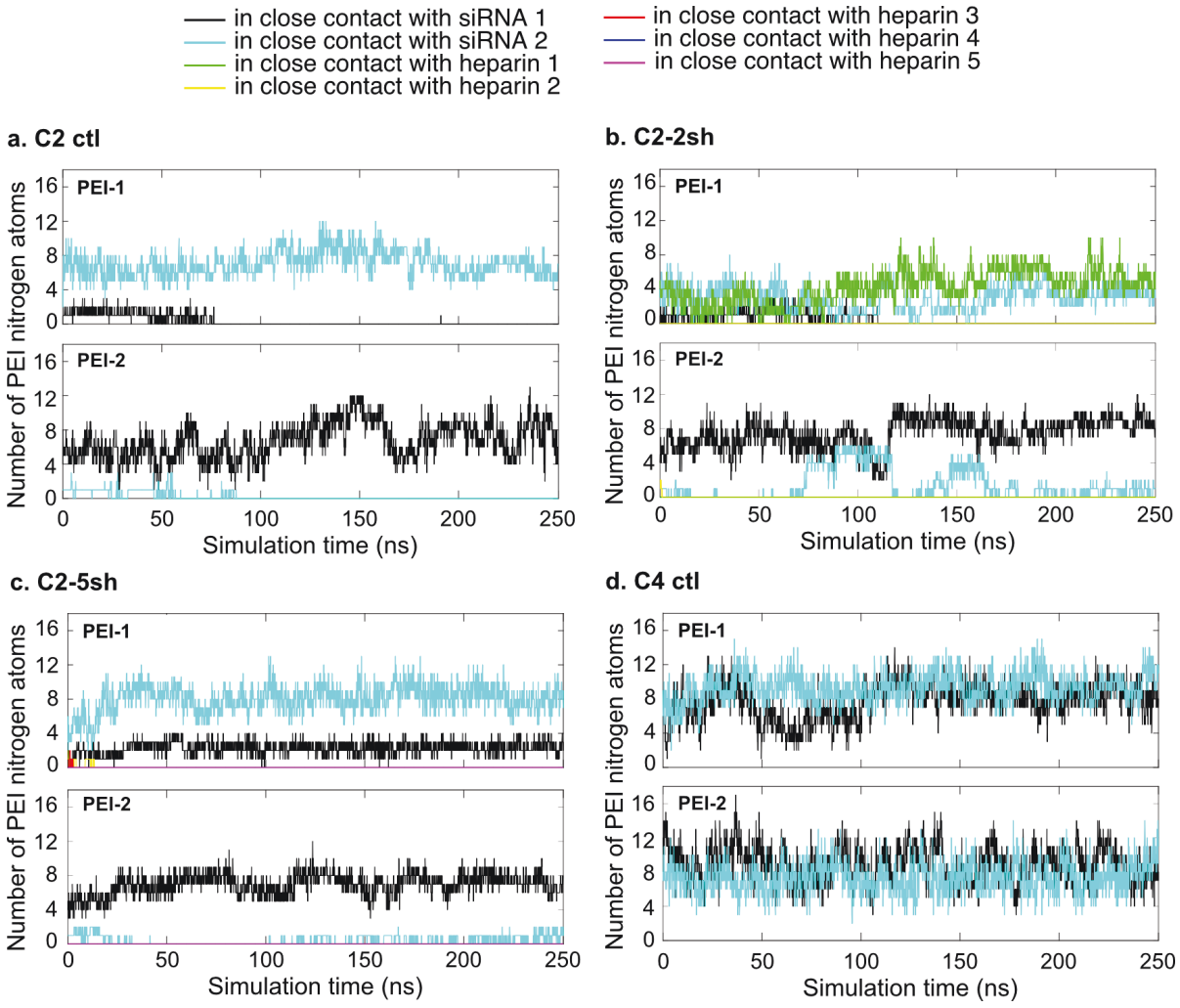

Figure 6.6. PEI binding dynamics in the systems which displayed signs of instability. Number of PEI N atoms within 4 Å of any siRNA and/or heparin N/O atoms as a function of simulation time in systems **(a)** C2 ctl, **(b)** C2-2sh, **(c)** C2-5sh, **(d)** C4 ctl. Two plots in each subfigure represent two separate PEIs (black and cyan curves corresponding to two separate siRNA molecules). The two and five heparin molecules in systems C2-2sh and C2-5sh, respectively, are presented with green, yellow, red, blue and purple curves.

6.3.2. Interactions of PEI with Heparin and siRNAs

The siRNA and heparin are both anionic in nature, capable of forming electrostatic interactions with the cationic PEI. The physicochemical characteristics of each molecule, however, are distinctly different from each other. The type of the anionic group (phosphate groups of siRNA

vs. sulfate and carboxylate groups of heparin), the spacing between the charged groups, as well as the molecule charge density are the key differences [32]. To investigate PEI binding to these polyanions, we followed the same definition of bound PEI Ns as in Section 6.3.1, and used the percentage of bound Ns (out of the total PEI N atoms, Table C.1) to quantify PEI-siRNA and PEI-heparin binding in Figure 6.7a. There was an inverse correlation between PEI's binding to siRNA and heparin; that is, if PEI binding to heparin is stronger, its binding to siRNA is weaker.

Among the systems with 568 Da PEI, maximal PEI binding to heparin is observed in C2-2lh with the average value of ~37%. Analysis of the PEI dynamics has shown that one of the 21-mer heparins is detaching one of the bridging PEIs at ~190 ns, and remains solely bound to this PEI afterwards (Figure C.2a). This also explains the lowest PEI-siRNA binding observed in this system as one of the PEIs completely loses its contact with both siRNAs for about 60 ns (out of 250 ns simulation time in total). Decreasing the length of the heparin molecule from 21-mer to 12-mer (C2-2sh) decreased heparin's binding to PEI by 10%, and this resulted in a subsequent increase in PEI-siRNA binding. On the other hand, increasing the number of the short (12-mer) heparin molecules from low to moderate (C2-2sh vs. C2-5sh) completely hindered PEI-heparin binding, possibly due to MD related artifacts as discussed above. The lack of PEI-heparin binding was reflected in the strong PEI-siRNA binding; the comparison between systems C2-2sh and C2-5sh shows about 15% increase in PEI-siRNA binding in system C2-5sh.

Among the systems with 568 Da PEI, C1-7sh possesses the highest number of PEI molecules to achieve PEI/siRNA ratio >1. The abundance of PEI in the periphery of the complex results in a limited amount of space for each PEI to interact with the siRNAs. This gives rise to the surface PEIs being loosely bound to the siRNAs, as opposed to the PEIs amidst the two

siRNAs establishing strong contacts with siRNAs (bridging PEIs). Close monitoring of the PEI dynamics in system C1-7sh (Figure C.1) has revealed one of the surface PEIs (PEI-1) being detached from the complex by two heparins (heparin-5 and heparin-6) almost immediately after the simulation began (~10 ns). The interaction between heparin-6 and PEI-1 was maintained from the moment of their initial binding, whilst the binding between heparin-5 and PEI-1 was unstable. It appears that the length of the heparin is an important contributor to its binding strength to PEI, while 21-mer heparin was capable of detaching a strongly bound, bridging PEI (C2-2lh), under the same conditions, 12-mer heparin was unable to do so (C2-2sh). However, when 12-mer heparin interacted with loosely bound surface PEIs (C1-7sh), it was able to disengage the PEI from the complex surface. PEIs at different locations in the complex possess different binding strength to siRNA, which is another major factor impacting PEI binding affinity/strength toward heparin.

All the systems containing 1874 Da PEI displayed similar levels of PEI-siRNA and PEI-heparin binding. The ability of heparin to detach PEI was not evident on the 1874 Da PEI (Figure C.2b-d). This suggests that MW of the PEI is critical for the heparin's destabilizing effect on siRNA complexes.

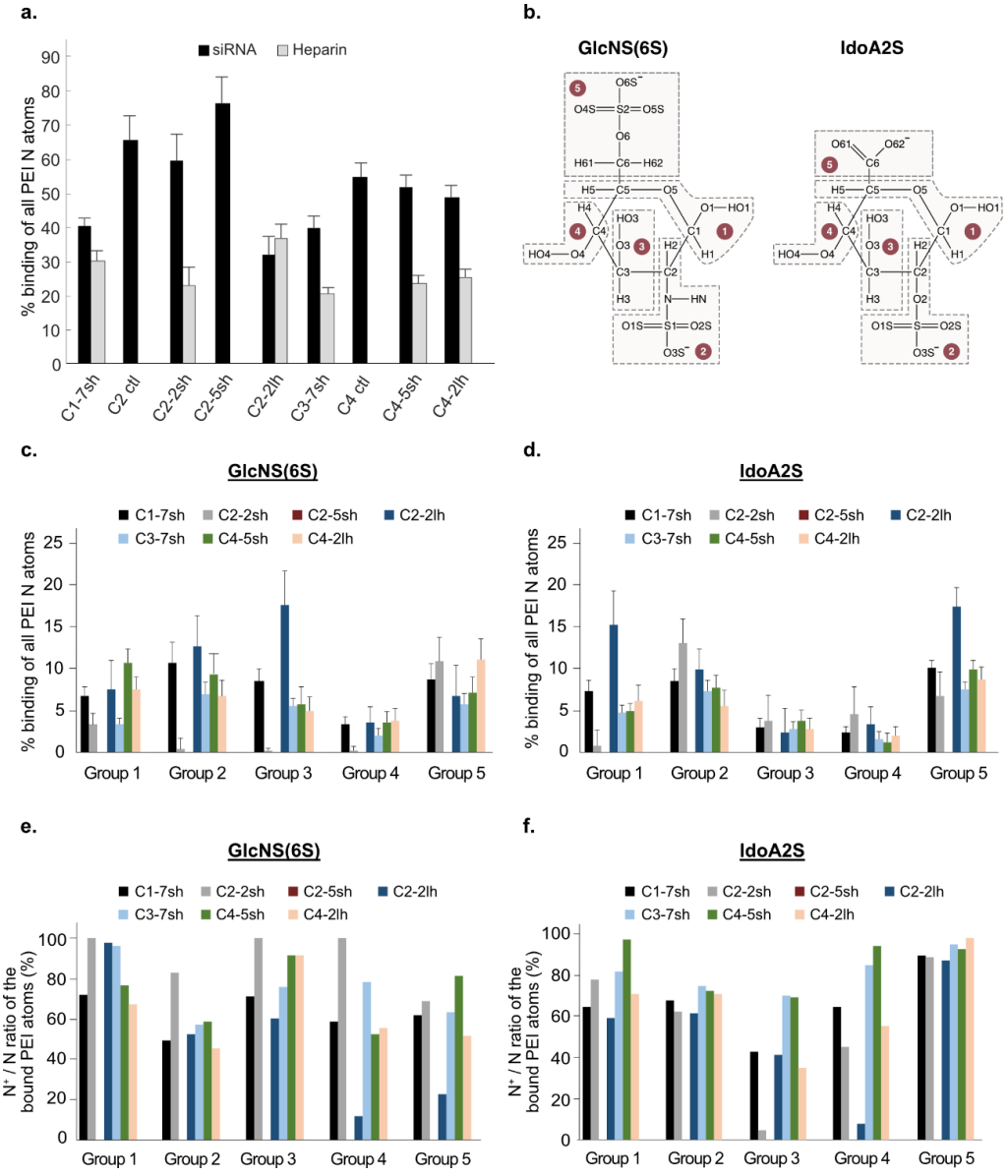

Figure 6.7. Quantitative analysis of PEI binding to siRNA and heparin.
(a) Percent binding of all PEI Ns to siRNA and heparin. Due to the higher number of PEI molecules in the systems with PEI/siRNA charge ratio ≥1 (thus higher number of PEI N atoms), the percentage of PEI binding to siRNA was found to be lower than that of the systems having PEI/siRNA charge ratio <1 (except for C2-2lh where PEI-siRNA binding is comparable), despite the presence of a higher number of Ns in bound state. **(b)** The groups of GlcNS(6S) and IdoA2S, where the summation of the atomic partial charges yields an integer group charge. Percent binding of all PEI N atoms to individual groups of heparin's building blocks **(c)** GlcNS(6S), and **(d)** IdoA2S. Percent contribution of the protonated PEI N atoms to overall PEI-heparin binding in **(e)** GlcNS(6S), and **(f)** IdoA2S. All the presented data in **(a)**, **(c)**, **(d)**, **(e)**, and **(f)** are average values over the final 50 ns of the simulations.

Next, we examined the binding between the individual groups of heparin and PEI to assess the contribution of each group in binding. To do so, we first divided each heparin residue, GlcNS(6S) or IdoA2S, into five groups, where the summation of the atomic partial charges yields an integer group charge (Figure 6.7b). Group 2 and Group 5 are the anionic groups, each carrying an overall charge of –1. Group 2 comprises a sulfamate moiety in GlcNS(6S), and a sulfate moiety in IdoA2S; whereas Group 5 contains a sulfate moiety in GlcNS(6S), and a carboxylate in IdoA2S. Group 3 has an overall neutral charge. Groups 1 and 4 are the connection points between the two residues in the heparin molecule, i.e., 1 → 4 linkage, their overall charge can differ depending on whether they undertake a linking role (–0.18 for Group 1 and 0.18 for Group 4) or remain as isolated residues at the two ends of the molecule (neutral). In Figure 6.7c,d, we plotted the %binding of all the PEI Ns to designated groups in GlcNS(6S) and IdoA2S, respectively (see Table C.1 in Appendix C for the actual number of PEI Ns bound to each group). Based on the analysis in Figure 6.7c, d, Group 4 is the least contributing group to PEI binding, given that it is a small group residing in the 1→4 linkage. Group 1 exhibited considerable PEI binding levels in both GlcNS(6S) and IdoA2S residues, whereas Group 3 binding was more complex, its contribution was considerable in GlcNS(6S) but very little in IdoA2S. The anionic Group 2 and Group 5 were substantial contributors to PEI binding.

The strong binding demonstrated by the anionic groups brings up the question whether this behavior is a result of the electrostatic interactions between the anionic sulfate, sulfamate, or carboxylate moieties of heparin and the protonated Ns in PEI. In Figure 6.7e, f, we plotted the percent contribution of the protonated PEI Ns to overall PEI-heparin binding (the actual number of PEI protonated Ns bound to the heparin groups is given in Table C.1 in Appendix C, along with the their % binding in Figure C.3a, b). Protonated Ns of PEI are expected to form

electrostatic interactions with the anionic groups of heparin, as well as with the heparin atoms carrying negative partial charges. It could be seen from Figure 6.7e, f that heparin's two building blocks, GlcNS(6S) and IdoA2S, display marked differences in their ability to establish electrostatic interactions with the protonated PEI Ns despite their equal anionic charge. Starting with the Group 2 of IdoA2S (a sulfate moiety), it was observed that 60 to 75% of the PEI-Group 2 binding comes from direct contacts with the protonated Ns of PEI (Figure 6.7f). Having a sulfamate moiety in position 2 in GlcNS(6S), however, slightly hinders Group 2's ability to form electrostatic interactions, and reduces the electrostatic contribution to PEI-Group 2 binding to 45-60%, except for system C2-2sh (Figure 6.7e). PEI-Group 5 binding displays even more marked differences between GlcNS(6S) and IdoA2S; the carboxylate moiety of IdoA2S is responsible of 87 to 98% of the overall PEI-Group 5 binding, as opposed to the GlcNS(6S)'s sulfate moiety where the corresponding contribution fluctuates from 23 to 81%, mostly localizing around 60%. The pattern observed in the electrostatic interactions was reflected in the H-bonds formed between the heparin's groups and the PEI Ns (Figure C.3c, d in Appendix C). Groups 2 and 5 displayed the highest number of H-bonds per PEI Ns, while the number of H-bonds formed by Groups 1 and 3 were significantly less, but comparable to each other. Group 4 was identified as the least contributor. The carboxylate of IdoA2S was again the most prominent group leading the H-bond interactions.

The anionic moieties of heparin possess acid dissociation constants (pKa) in the range of 0.5 and 1.5 for the sulfate groups, and 2.0 – 4.0 for the carboxylates [33]. Given that the carboxylates are inherently weaker acids than the sulfates [34], one might expect sulfate containing groups dominating the binding of heparin to other biomolecules [1]. On the other hand, different moieties of heparin other than the sulfates could be essential for heparin binding

[35]. We have observed that the carboxylate moiety of the iduronic acid is a major contributor to PEI binding. However, given the abundancy of sulfated groups in heparin (three sulfate moieties in the repeating disaccharide), the contribution to overall PEI binding from all the sulfated groups combined could be more than that of the carboxylate. The mechanism for the difference between the binding of sulfate and the carboxylate moieties remains to be explored. It is possible that the conformational flexibility of the internal iduronic acid pyranose rings [36, 37] may lead to the positioning of the carboxylates that is favorable for PEI binding, or the steric hindrance brought by the bulky sulfates might be hindering their interactions.

6.3.3. Mechanistic Insights into Heparin Mediated Complex Disassembly

Our simulation trajectories revealed that siRNA-PEI complexes display different responses to the presence of heparin in their periphery. We evaluated the response of each system by monitoring the motion of the siRNAs and the heparin's mode of action. The motion of the siRNAs was examined to see if the siRNAs remain complexed, or become partially relaxed or separated, whereas the heparin's action was determined from its binding to PEI, its PEI detachment activity, or its free floating motion in the bulk solution. These key observations are summarized in Table 6.2. There exists a clear distinction for the systems with different PEI MW; systems containing 568 Da PEI were found to be more vulnerable to the destabilizing effects of heparin, displaying a variety of different siRNA motions contingent on the heparin-related variables, whereas in 1874 Da PEI systems, the siRNAs remained in complex regardless of the heparin length or number of heparin molecules. Along the same lines, heparin's PEI detachment action can be seen in the 568 Da PEI systems, whilst PEI disengagement from the 1874 Da PEI bearing complexes was not possible. This puts great emphasis on the size of the carrier to resist heparin mediated destabilization. In support of this observation, Danielsen and coworkers

previously reported easier dissociation of DNA – low degree of polymerized chitosan complexes by heparin than the complexes from longer chitosan [38]. It also should be noted that polymers are polydisperse in nature; hence, the variation in polymer MW among the polymer samples and the resulting complexes could potentially affect the response of the complexes to the destabilizing effects of heparin.

Among the 568 Da PEI systems, it could be seen that the change in the complex integrity is related to PEI/siRNA charge ratio and heparin length. Having the PEI/siRNA charge ratio > 1 delivered a more stable complex, where shorter heparins were observed to disengage the loosely bound surface PEIs, but not the PEIs undertaking siRNA bridging role. The loss of a surface PEI did not induce any significant change in the complex stability, as there were still plenty of PEIs maintaining the overall integrity. Decreasing the number of PEIs (i.e. lowering the PEI/siRNA charge ratio below unity), led to more exposure of the siRNAs and the bridging PEIs to the heparin molecules, thus induced complex instability. The separation of the siRNAs was dependent on the amount of heparin as well as the length of the heparin chain. 12-mer heparin triggered the separation of the siRNAs when the number of heparin molecules in the system is low, whereas having excess heparin in the periphery did not allow for the full separation of the siRNAs, only permitting the partial relaxation. Owing to its longer chain length, hence higher negative charge, at the same amount of heparin molecules in the system, 21-mer heparin displayed stronger destabilizing action than its 12-mer counterpart by disengaging a bridging PEI from the complex.

Table 6.2. Summary of the behavioral patterns observed in the siRNA-PEI-heparin ternary systems.
The orange icons represent the state of siRNAs, whereas the blue icons demonstrate the heparin's mode of action.

	PEI/siRNA charge ratio	PEI M.W.	Heparin length	Heparin conc.	Observed phenomena
C1-7sh	1.05	568 Da	12-mer	High	■ ▲ ●
C2-2sh	0.15	568 Da	12-mer	Low	★ ▲ ⬟
C2-5sh	0.15	568 Da	12-mer	Moderate	◆ ⬟
C2-2lh	0.15	568 Da	21-mer	Low	■ ▲ ● ⬟
C3-7sh	1.00	1874 Da	12-mer	High	■ ▲ ⬟
C4-5sh	0.50	1874 Da	12-mer	Moderate	■ ▲ ⬟
C4-2lh	0.50	1874 Da	21-mer	Low	■ ▲

In the light of the different behavioral patterns demonstrated by our simulation systems, we propose the following five-stage mechanism for heparin-mediated disassembly of the siRNA-PEI complexes: (*i*) heparin binding to complex, (*ii*) detachment of surface PEIs, (*iii*) disengagement of bridging PEIs, (*iv*) change in siRNA torsional motion and partial relaxation of the complexes, and (*v*) separation of siRNAs (Figure 6.8). It is important to note that the sequence of some of the proposed events does not necessarily have to be in this particular order; e.g. stages (*iv*) and (*v*) may happen simultaneously or one after the other; and some of the proposed stages may not be readily observed such as the detachment of the bridging PEIs.

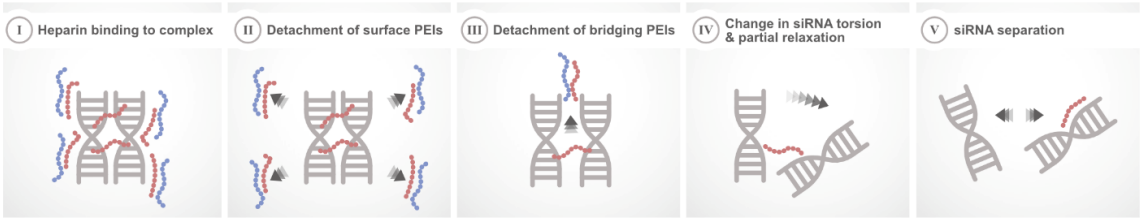

Figure 6.8. Proposed mechanism for the heparin-mediated siRNA-PEI complex disassembly.
The representative siRNAs are given in gray, and representative PEIs and heparins are given in red and blue, respectively.

6.3.4. Implications

Our methodology in varying the preparation variables has led to the sampling of different conformational states at the atomistic level. In Figure 6.9, we schematically illustrate the proposed free energy landscape of siRNA-PEI-heparin ternary systems in explicit water. From the analysis of many atomistic trajectories, we observed three main metastable conformational states; namely (*i*) heparin coated stable siRNA-PEI complex, (*ii*) stable siRNA-PEI complex with partially removed PEIs (surface bound and/or bridging), and (*iii*) relaxed or disassembled complex. As these states are derived from the simulation trajectories of different compositions, we are unable to decide which one of the metastable states is thermodynamically more stable than the others. Therefore, we present all the observed states as if they possess the same level of thermodynamic stability; however, in reality, the resultant conformational states may not have the same energy, e.g. some conformations might be more favorable than the others.

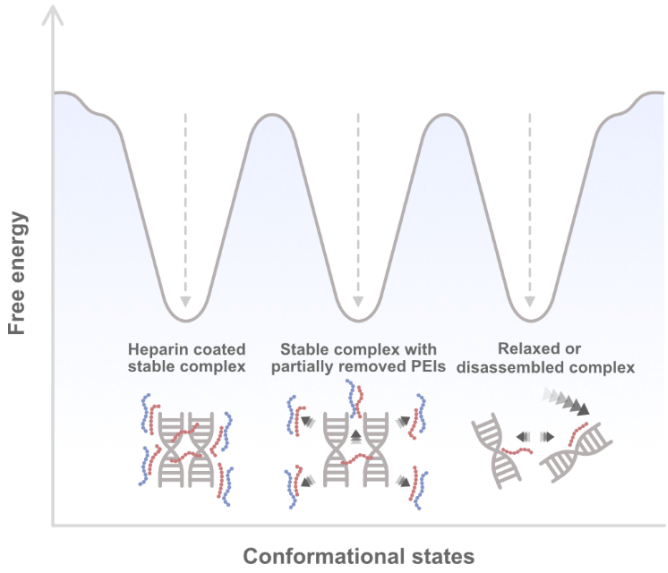

Figure 6.9. Proposed conformational states of the siRNA-PEI-heparin ternary systems in explicit water.
The representative siRNAs are given in gray, and representative PEIs and heparins are given in red and blue, respectively.

The atomistic details of the ternary systems acquired from our MD simulations have shown that siRNA-PEI complexes experience a variety of heparin-mediated changes in their conformational states. Due to complex effects of GAGs on the complexes, previously conducted experimental studies have assigned contradictory roles to GAGs in the context of polynucleotide-based therapeutics. Our simulations have shown that heparins bind to siRNA-PEI complexes through electrostatic interactions and H-bonding with PEIs. The surface of the complexes becomes coated with heparin molecules in the presence of abundant peripheral PEIs, therefore the positive surface charge of the complex is sequestered by the heparins. This could be beneficial to reduce the cytotoxicity of the complexes, as the cationic charge of the PEI is mainly responsible for inducing damage to cell membranes and endocytic compartments [39]. If the complexes remain stable and coated with heparin (one of the proposed metastable states

depicted in Figure 6.9) prior to binding to the membrane milieu, heparins adsorbed on complex surfaces may explain the effects related to reduced cytotoxicities [2].

When heparin is present on cell surfaces in the form of heparin sulfate proteoglycans (HSPG), the attractive forces between highly anionic HS chains and the cationic complexes could facilitate the cellular uptake of the complexes [40]; GAGs may act as "receptors" in this case [7, 8]. Cells and tissues display a great variety in their GAG size and content [41], and our simulations revealed the importance of heparin physical properties determining the extent of its effect on the cationic polynucleotide complexes. Therefore, the number of heparins/HSPGs present on the cell surface and the length of heparin/HS GAG chains may critically influence the strength of the interactions and the resulting cellular uptake efficiency of complexes, as also previously suggested by Ruponen and coworkers [15]. On the other hand, cell surface GAGs may also disrupt the integrity of the complexes, by detaching the surface and bridging PEIs; the extent of this effect is dependent on GAG chain length, as well as the MW of the carrier and the cationic charge of the complex.

Binding of heparin to the polynucleotide complexes may also affect the subsequent intracellular trafficking events [14-16]. Shielding of the PEI cationic charges may adversely affect endosomal escape ability of PEI, and can eventually trap the complexes in the endocyctic compartments. Complexes may experience heparin mediated partial relaxation and/or disassembly as shown by our MD simulations, which will make them more susceptible to the destabilizing effects of the pH changes in endosomes, hence they may be prematurely degraded. On the other hand, if the partially relaxed complexes could manage to escape from the endosomes, their disassembly in the cytosol, a key rate-limiting step to polynucleotide delivery, may have been facilitated by the relaxation that is already initiated by heparin.

6.4. Conclusions

The effect of heparin on siRNA-PEI complexes has been elucidated from a series of all-atom MD simulations. We developed an approach to study the transitional states of the siRNA-PEI-heparin ternary complexes to reveal a picture of the heparin-mediated changes in complex conformation. We found that heparin binds to siRNA-PEI complex through electrostatic interactions and H-bonding with PEI Ns. These interactions with PEI were mainly governed by the anionic $–N/O-SO_3^-$ and $–COO^-$ groups of heparin. The $–COO^-$ moiety of the iduronic acid residues was a major contributor to PEI binding. The MW of PEI and PEI/siRNA charge ratio in complexes were found to regulate the response to heparin. The chain length of heparin and the number of heparin molecules present in the system were critical. From these findings, we propose the following multi-step mechanism for heparin mediated disassembly of the siRNA-PEI complexes: (*i*) heparin binding to complex, (*ii*) detachment of surface PEIs, (*iii*) disengagement of bridging PEIs, (*iv*) change in siRNA torsional motion and partial relaxation of the complexes, and (*v*) separation of siRNAs. We further propose three metastable states in the energy landscape of the ternary systems in explicit water, which are (*i*) heparin coated stable siRNA-PEI complex, (*ii*) stable siRNA-PEI complex with partially removed PEIs (surface and/or bridging), and (*iii*) relaxed or disassembled complex. These mechanistic observations should further facilitate design of new carriers for gene medicines and help to better understand the behavior of polynucleotide complexes in the physiological milieu.

6.5. Acknowledgements

Compute Canada and WestGrid are gratefully acknowledged for providing the computing resources and technical support. This work is funded by Natural Sciences and Engineering Research Council of Canada (NSERC), NSERC Collaborative Research and Training

Experience Program for Regenerative Medicine (NCPRM), Canadian Institutes of Health Research (CIHR), Alberta Innovates Technology Futures (AITF), and Canada Foundation for Innovation (CFI).

6.6. References

1. Gandhi NS & Mancera RL (2008) The Structure of Glycosaminoglycans and Their Interactions with Proteins. *Chem. Biol. Drug. Des.* 72(6):455-482.
2. Belting M & Petersson P (1999) Protective Role for Proteoglycans Against Cationic Lipid Cytotoxicity Allowing Optimal Transfection Efficiency In Vitro. *Biochem. J.* 342 (Pt 2):281-286.
3. Belting M & Petersson P (1999) Intracellular Accumulation of Secreted Proteoglycans Inhibits Cationic Lipid-mediated Gene Transfer. Co-transfer of Glycosaminoglycans to the Nucleus. *J. Biol. Chem.* 274(27):19375-19382.
4. Gallagher JT, Lyon M, & Steward WP (1986) Structure and Function of Heparan Sulphate Proteoglycans. *Biochem. J.* 236(2):313-325.
5. Kjellen L & Lindahl U (1991) Proteoglycans: Structures and Interactions. *Annu. Rev. Biochem.* 60:443-475.
6. Raman R, Sasisekharan V, & Sasisekharan R (2005) Structural Insights into Biological Roles of Protein-Glycosaminoglycan Interactions. *Chem. Biol.* 12(3):267-277.
7. Mislick KA & Baldeschwieler JD (1996) Evidence for the Role of Proteoglycans in Cation-mediated Gene Transfer. *Proc. Natl. Acad. Sci. U.S.A.* 93(22):12349-12354.
8. Mounkes LC, Zhong W, Cipres-Palacin G, Heath TD, & Debs RJ (1998) Proteoglycans Mediate Cationic Liposome-DNA Complex-based Gene delivery In Vitro and In Vivo. *J. Biol. Chem.* 273(40):26164-26170.
9. Humphries DE & Silbert JE (1988) Chlorate: A Reversible Inhibitor of Proteoglycan Sulfation. *Biochem. Biophys. Res. Commun.* 154(1):365-371.
10. Ruponen M, Yla-Herttuala S, & Urtti A (1999) Interactions of Polymeric and Liposomal Gene Delivery Systems with Extracellular Glycosaminoglycans: Physicochemical and Transfection Studies. *Biochim. Biophys. Acta* 1415(2):331-341.
11. Xu Y & Szoka FC, Jr. (1996) Mechanism of DNA Release from Cationic Liposome/DNA Complexes Used in Cell Transfection. *Biochemistry* 35(18):5616-5623.
12. Wiethoff CM, Smith JG, Koe GS, & Middaugh CR (2001) The Potential Role of Proteoglycans in Cationic Lipid-mediated Gene Delivery. Studies of the Interaction of Cationic Lipid-DNA Complexes with Model Glycosaminoglycans. *J. Biol. Chem.* 276(35):32806-32813.
13. Liu Y & Reineke TM (2006) Poly(glycoamidoamine)s for Gene Delivery: Stability of Polyplexes and Efficacy with Cardiomyoblast Cells. *Bioconjug. Chem.* 17(1):101-108.

14. Ruponen M, Ronkko S, Honkakoski P, Pelkonen J, Tammi M, & Urtti A (2001) Extracellular Glycosaminoglycans Modify Cellular Trafficking of Lipoplexes and Polyplexes. *J. Biol. Chem.* 276(36):33875-33880.

15. Ruponen M, Honkakoski P, Tammi M, & Urtti A (2004) Cell-surface Glycosaminoglycans Inhibit Cation-mediated Gene Transfer. *J. Gene Med.* 6(4):405-414.

16. Nomani A, Hyvonen Z, Pulkkinen E, Hiekkala M, & Ruponen M (2014) Intracellular Gene Delivery is Dependent on the Type of Non-viral Carrier and Defined by the Cell Surface Glycosaminoglycans. *J. Control. Release* 187:59-65.

17. Barnard A, Posocco P, Pricl S, Calderon M, Haag R, Hwang ME, Shum VW, Pack DW, & Smith DK (2011) Degradable Self-assembling Dendrons for Gene Delivery: Experimental and Theoretical Insights into the Barriers to Cellular Uptake. *J. Am. Chem. Soc.* 133(50):20288-20300.

18. Abbasi M, Lavasanifar A, Berthiaume LG, Weinfeld M, & Uludag H (2010) Cationic Polymer-mediated Small Interfering RNA Delivery for P-glycoprotein Down-regulation in Tumor Cells. *Cancer* 116(23):5544-5554.

19. Meneksedag-Erol D, Tang T, & Uludag H (2015) Probing the Effect of miRNA on siRNA-PEI Polyplexes. *J. Phys. Chem. B* 119(17):5475-5486.

20. Utsuno K & Uludag H (2010) Thermodynamics of Polyethylenimine-DNA Binding and DNA Condensation. *Biophys. J.* 99(1):201-207.

21. Sun C, Tang T, & Uludag H (2011) Molecular Dynamics Simulations of PEI Mediated DNA Aggregation. *Biomacromolecules* 12(10):3698-3707.

22. Sun C, Tang T, & Uludag H (2012) Molecular Dynamics Simulations for Complexation of DNA with 2 kDa PEI Reveal Profound Effect of PEI Architecture on Complexation. *J. Phys. Chem. B* 116(8):2405-2413.

23. Phillips JC, Braun R, Wang W, Gumbart J, Tajkhorshid E, Villa E, Chipot C, Skeel RD, Kale L, & Schulten K (2005) Scalable Molecular Dynamics with NAMD. *J. Comput. Chem.* 26(16):1781-1802.

24. Sun C, Tang T, Uludag H, & Cuervo JE (2011) Molecular Dynamics Simulations of DNA/PEI Complexes: Effect of PEI Branching and Protonation State. *Biophys. J.* 100(11):2754-2763.

25. Vanommeslaeghe K, Hatcher E, Acharya C, Kundu S, Zhong S, Shim J, Darian E, Guvench O, Lopes P, Vorobyov I, & MacKerell AD (2010) CHARMM General Force Field: A Force Field for Drug-Like Molecules Compatible with the CHARMM All-Atom Additive Biological Force Fields. *J. Comput. Chem.* 31(4):671-690.

26. Darden T, York D, & Pedersen L (1993) Particle Mesh Ewald - an N.Log(N) Method for Ewald Sums in Large Systems. *J. Chem. Phys.* 98(12):10089-10092.

27. Ryckaert JP, Ciccotti G, & Berendsen HJC (1977) Numerical-Integration of Cartesian Equations of Motion of a System with Constraints - Molecular-Dynamics of N-Alkanes. *J. Comput. Phys.* 23(3):327-341.

28. Humphrey W, Dalke A, & Schulten K (1996) VMD: Visual Molecular Dynamics. *J. Mol. Graph.* 14(1):33-38, 27-38.

29. Schlick T (2010) Chapter 10: Nonbonded Computations. *Molecular Modeling and Simulation: An Interdisciplinary Guide* (Springer, New York, USA), pp 311-312.

30. González MA (2011) Force Fields and Molecular Dynamics Simulations. *Collection SFN* 12:169–200.

31. Sun C, Tang T, & Uludag H (2013) A Molecular Dynamics Simulation Study on the Effect of Lipid Substitution on Polyethylenimine Mediated siRNA Complexation. *Biomaterials* 34(11):2822-2833.

32. Smith SA, Choi SH, Collins JN, Travers RJ, Cooley BC, & Morrissey JH (2012) Inhibition of Polyphosphate as a Novel Strategy for Preventing Thrombosis and Inflammation. *Blood* 120(26):5103-5110.

33. Wang HM, Loganathan D, & Linhardt RJ (1991) Determination of the pKa of Glucuronic Acid and the Carboxy Groups of Heparin by ^{13}C-Nuclear-Magnetic-Resonance Spectroscopy. *Biochem. J.* 278 (Pt 3):689-695.

34. Park JW & Chakrabarti B (1978) Optical Characteristics of Carboxyl Group in Relation to the Circular Dichroic Properties and Dissociation Constants of Glycosaminoglycans. *Biochim. Biophys. Acta* 544(3):667-675.

35. Chevalier F, Lucas R, Angulo J, Martin-Lomas M, & Nieto PM (2004) The Heparin-Ca(2^+) Interaction: The Influence of the O-sulfation Pattern on Binding. *Carbohydr. Res.* 339(5):975-983.

36. Ferro DR, Provasoli A, Ragazzi M, Casu B, Torri G, Bossennec V, Perly B, Sinay P, Petitou M, & Choay J (1990) Conformer Populations of L-iduronic Acid Residues in Glycosaminoglycan Sequences. *Carbohydr. Res.* 195(2):157-167.

37. Mulloy B & Forster MJ (2000) Conformation and Dynamics of Heparin and Heparan Sulfate. *Glycobiology* 10(11):1147-1156.

38. Danielsen S, Strand S, de Lange Davies C, & Stokke BT (2005) Glycosaminoglycan Destabilization of DNA-Chitosan Polyplexes for Gene Delivery Depends on Chitosan Chain Length and GAG Properties. *Biochim. Biophys. Acta* 1721(1-3):44-54.

39. Nel AE, Madler L, Velegol D, Xia T, Hoek EM, Somasundaran P, Klaessig F, Castranova V, & Thompson M (2009) Understanding Biophysicochemical Interactions at the Nano-bio Interface. *Nat. Mater.* 8(7):543-557.

40. Kopatz I, Remy JS, & Behr JP (2004) A Model for Non-viral Gene Delivery: Through Syndecan Adhesion Molecules and Powered by Actin. *J. Gene Med.* 6(7):769-776.

41. Esko JD, Kimata K, & Lindahl U (2009) Chapter 16: Proteoglycans and Sulfated Glycosaminoglycans. *Essentials of Glycobiology*, eds Varki A, Cummings RD, Esko JD, Freeze HH, Stanley P, Bertozzi CR, Hart GW, & Etzler ME (Cold Spring Harbor Laboratory Press, Cold Spring Harbor (NY)), 2nd Ed.

7. Molecular Dynamics Simulations on Nucleic Acid Binding Polymers to Arrest Thrombosis

7.1. Introduction

Thrombosis, pathologic formation of an occlusive blood clot, is a serious complication of malignancy [1, 2]. Malignancy associated hypercoagulability (i.e., tendency of blood to clot excessively) affects the majority of cancer patients in the form of several serious thrombotic disorders such as deep vein thrombosis (DVT) and pulmonary embolism (PE), or venous thromboembolism (VTE) in general, disseminated intravascular coagulation (DIC), and stroke [3]. Some aggressive cancer types, such as brain, pancreas, ovarian and lung cancers, are associated with a higher risk of VTE [4-8]. Aggressive treatments like chemotherapy may increase the risk for thrombotic episodes up to six-fold higher than the baseline for each cancer type [9]. Moreover, patients with cancer are at four-times higher risk of developing recurrent episodes of VTE, as well as anticoagulant-induced hemorrhagic complications, than the patients without malignancy [10, 11].

Conventional anticoagulant drugs target key proteases of the coagulation cascade, therefore impose high bleeding risks. The bleeding and recurrence risks associated with the presence of malignancy makes thrombosis management in cancer patients further challenging [11]. There is an urgent need for the development of safer alternatives to current clinical anticoagulants. Recent studies revealed that some indigenous molecules play important roles in thrombosis, while their deficiency does not lead to clinically important hemostatic anomalies [12], and have paved the way for the development of more targeted and safer strategies in antithrombotic therapy. This chapter will investigate polymeric structures designed to arrest thrombosis. First, we will give a brief overview of hemostasis, then discuss malignancy associated hypercoagulable states and recent advances in the treatment options in Section 7.2 below.

7.2. Background Information and Literature Review

7.2.1. Overview of Hemostasis

Hemostasis is a series of interconnected physiological events that take place to prevent blood loss following injury to blood vessels, by means of sealing up the injury site via forming a blood clot [13, 14]. This is achieved in two main stages: primary and secondary hemostasis. Primary hemostasis aims at forming a primary hemostatic plug at the vascular injury site. This primary plug can seal up the damaged blood vessel temporarily; however, it is highly fragile and unstable, and can easily be disengaged [15]. In secondary hemostasis, a series of enzymatic reactions known as the coagulation cascade forms a more durable plug [14]. Coagulation cascade is regulated by coagulation factors, that usually exist as inactive proenzymes in the blood stream [14, 16]. Roman numeral nomenclature is used for the representation of the coagulation factors; and the Roman numerals are further labeled with letter "a" if the coagulation factors are in their activated form; e.g. fXII for the inactive proenzyme, and fXIIa for the active form [16]. Once the cascade is initiated, the activation of the coagulation factors is achieved through a proteolytic reaction between the substrate, the inactive proenzyme itself, and the enzyme which is the activated coagulation factor (a serine protease) preceding the substrate [14, 16].

Coagulation cascade comprises three pathways: extrinsic, intrinsic, and common [14, 17]. Detailed representation of these pathways of the coagulation cascade are given in Figure 7.1. The extrinsic pathway is triggered upon tissue injury, through the exposure of tissue factor (TF) to blood [12, 16, 18]. Following the TF exposure, the TF:fVIIa complex is formed either through binding of TF to fVII and activating it to fVIIa, or binding of TF directly to the active factor,

fVIIa. TF:fVIIa complex then activates its substrates, fIX and fX [16]. FIX can also be activated into fIXa by fXIa of the intrinsic pathway [14, 19], which will be discussed in detail below.

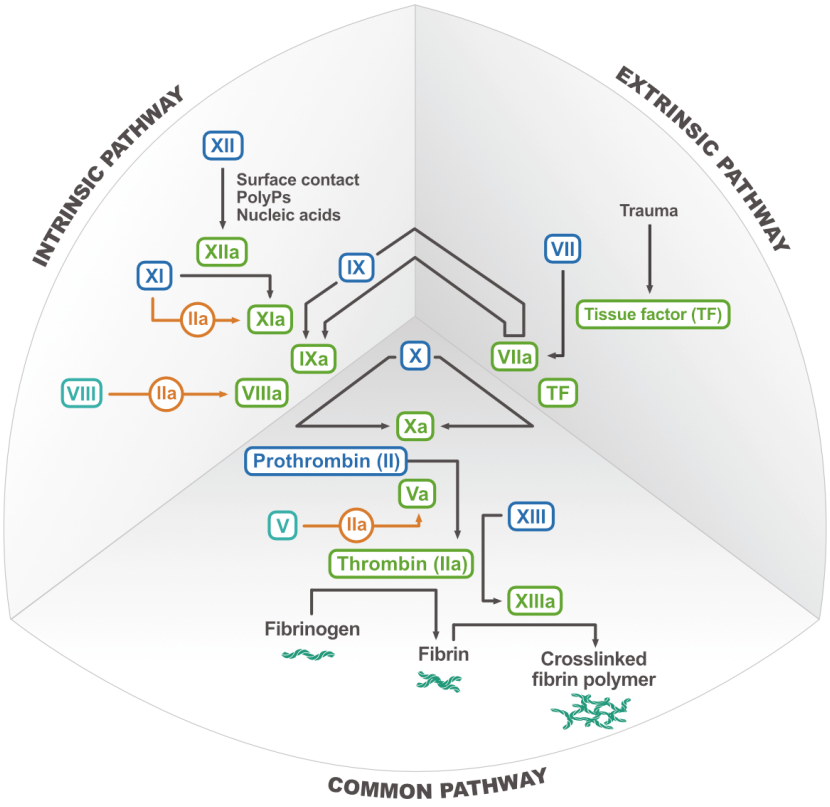

Figure 7.1. The coagulation cascade.
The traditional classification of the coagulation cascade into intrinsic, extrinsic and common pathways are depicted. Inactive coagulation factors are shown in blue, their activated forms are shown in green. Thrombin undertaking a positive feedback role is represented in orange.

The coagulation factors fXII, fXI, fIX, cofactor fVIII, and their activated forms constitute the intrinsic pathway of the coagulation cascade [12]. The intrinsic pathway is initiated through the activation of fXII to fXIIa. The *ex vivo* activation of fXII involves the contact of blood with artificial, negatively charged surfaces, e.g. glass, clay minerals such as kaolin [12, 20]. A conformational change in fXII occurs as a result of this surface contact, which subsequently triggers its activation into fXIIa [16]. Blood plasma proteins proenzyme prekallikrein, serine

protease kallikrein, and high molecular weight kininogen (HMWK) are a part of the *in vitro* coagulation reactions that are induced upon surface contact [19]. It has to be noted that the contact activation of the coagulation cascade could possibly be triggered *in vivo* when blood encounters foreign body surfaces such as implanted cardiac devices or medical devices used in blood dialysis [18], or when blood comes into contact with subendothelial collagen [21]. Produced upon surface contact, fXIIa activates prekallikrein into kallikrein; then a virtuous cycle begins where the produced kallikrein activates fXII to fXIIa, while fXIIa further activates prekallikrein to kallikrein [16, 20, 22]. HMWK acts as a cofactor in the activation reactions [20, 22, 23]. The *in vivo* activators of fXII have long been investigated [12], and the proposed candidates include inorganic polyphosphates (polyPs) [24], and extracellular circulating nucleic acids (NAs) [25, 26]. Once fXII is activated to fXIIa, it then triggers the activation of fXI to fXIa, followed by fXIa mediated activation of fIX into fIXa. Facilitated by the cofactor fVIIIa, fIXa activates fX [16].

Either through the extrinsic or the intrinsic pathway, the activation of fX to fXa initiates the final common pathway of the coagulation cascade. By recruiting the cofactor fVa, fXa assembles into a complex structure (also known as prothrombinase), which activates the downstream substrate prothrombin (fII) into thrombin (fIIa). Thrombin, then, turns the fibrinogen into fibrin monomers, and subsequent polymerization of the fibrin monomers forms the fibrin polymer. FXIIIa – the active form of fXIII, activated by thrombin positive feedback loop – catalyzes the crosslinking reaction of the fibrin polymer for the generation of the end product of the coagulation cascade: the crosslinked fibrin clot [14, 16, 27].

7.2.2. Regulation of Hemostasis

In order to limit the formation of the hemostatic plug to the site of damaged vasculature, as well as to control the size of the hemostatic plug to prevent it from completely occluding the blood vessels, hemostasis is regulated through the physiologic anticoagulant system occurring in balance with the procoagulant reactions [14, 28]. Natural anticoagulant system comprises many mechanisms that take place synergistically. Regarding the regulation of the platelet response, endothelial cells produce prostacyclin that inhibits platelet activation and aggregation [14, 29]. The activated coagulation factors are then inactivated by a number of systems. Thrombin and other essential coagulation factors, fIXa, fXa, fXIa, and fXIIa, are inactivated by a serine protease inhibitor, antithrombin. Antithrombin binds to these coagulation factors and prevents their further interactions with the downstream substrates, which in turn hinders the subsequent reactions in the coagulation cascade [14, 30]. The catalytic activity of antithrombin can be enhanced by heparin and heparin-like endogenous molecules. Under physiological conditions, glycosaminoglycans (GAGs) that are found on the cell membrane milieu of the intact endothelial cells such as endogenous heparin-like molecules (e.g. heparan sulfate) bind to antithrombin, and induce a change in its conformation. This conformational change facilitates subsequent binding to the aforementioned coagulation factors to stop them contributing to the cascade reactions. From a pharmacological standpoint, this is achieved via exogenous heparin, one of the most clinically used antithrombotic drugs [14, 30]. Thrombin can also be inactivated by heparin cofactor II (HCII) [31].

Other members of the natural anticoagulant system are protein C, capable of inactivating the coagulation factors, fVa and fVIIIa [28, 31, 32]; and tissue factor pathway inhibitor (TFPI) administering the extrinsic pathway of the coagulation cascade [14, 31]. Moreover, the

fibrinolytic system regulates the size of the clot, or removes the clot from the site of the injury once hemostasis is attained, by breaking down the fibrin clot into smaller fragments [17, 33, 34].

7.2.3. Pathogenesis of Thrombosis and Hypercoagulability in Malignancy

A lack of balance between the hemostatic systems may lead to serious thrombotic complications [35]. When the hemostatic balance is disrupted in favor of the procoagulation pathway either by immoderate activation of the coagulation system or loss of activity in natural anticoagulant and fibrinolytic system, blood tends to clot excessively. This pathologic condition of undesirable clotting is known as the "hypercoagulable state"; and the pathologic blood clot is referred to as "thrombus" [32, 36].

In malignancy, several interrelated processes could lead to thrombotic complications; thus, the cause of cancer-associated hypercoagulability is proposed to be multifactorial in origin [37]. Moreover; the type of cancer, the choice of treatment, as well as patient characteristics are major risk determining factors for thrombogenic events [38]. Multiple mechanisms have been proposed to contribute to hypercoagulability in cancer patients, and one of these processes relies on TF expression by the malignant cells, and initiation of the extrinsic pathway in the absence of trauma [37]. Other procoagulant substances generated by the malignant cells include cysteine proteases [39] and sialic acid [40] which can activate fX to fXa either proteolytically (cysteine protease) or nonenzymatically (sialic acid). Tumor cells also can cause the secretion of proinflammatory cytokines such as interleukin-1 and tumor necrosis factor, which induce damage to the endothelium leading to subsequent activation of coagulation factors fXII, fX, or fVII via TF [41]. The interaction of the tumor cells directly with the leukocytes – white blood

cells – and platelets is another mechanism contributing to the activation of coagulation in malignancy [42].

The procoagulant and prothrombotic nature of cell free nucleic acids (cfNAs) have been the subject of numerous experimental studies. Moreover, there exists a strong connection between the cfNAs in circulation and malignancy. Elevated levels of cfNAs in the blood stream is strongly related to the presence of an underlying malignant condition. An early study by Leon *et al.* reported the mean value of cell free DNA (cfDNA) concentration in the serum of 55 healthy individuals to be 13 ± 3 ng/ml; whereas approximately ten-fold increase was observed in serum cfDNA levels of 173 cancer patients, with an average of 180 ± 38 ng/ml. Among the cancer patients, metastasis was shown to elevate the serum cfDNA levels by two-fold [43]. Benign lesions may also raise the levels of circulating cfNAs [44]. Shapiro *et al.* quantified the amount of circulating cfDNA in the serum of 386 patients with benign and malignant diseases in the gastrointestinal tract. The mean value of the serum cfDNA in patients with benign disease was measured at 118 ± 14 ng/ml, while a four-fold increase was observed in the presence of malignancy (with a mean value of 412 ± 63 ng/ml) [45]. In an early small study, Kopreski et al. reported the detection of tyrosinase mRNA in the serum of 4 (out of 6) malignant melanoma patients, while none of the tested healthy subjects (0 out of 20) showed detectable amounts [46]. Similarly, significantly higher levels of GAPDH mRNA were reported in the plasmas of patients with hepatocellular carcinoma in comparison to the healthy individuals [47]. As the presence of cfNAs in circulation could be strongly indicative of cancer presence, cfNAs are even identified as potential “biomarkers” in the diagnosis and monitoring of cancer [44].

Multiple mechanisms could be responsible of cfNA release into blood in malignancy. CfNAs could get into the circulation throughout tumor progression, or could be released from

the apoptotic and necrotic tumor cells [44]. Moreover, some aggressive cancer therapies such as chemotherapy may trigger the release of cfNAs into the blood stream [41]. Doxorubicin and epirubicin used in breast cancer chemotherapy were reported to increase plasma cfDNA levels approximately three-fold in ~73% of the patients, 24 h post chemotherapy in the first cycle of treatment [48]. The release of neutrophil extracellular traps (NETs) – network structures comprising DNA and histones, released from immune cells neutrophils [49] – from the dying cells was proposed as the mechanism underlying the chemotherapy-induced cfDNA release into the circulation [48].

The thrombotic risk of the cfNAs arise from their capability of triggering the intrinsic pathway of coagulation. Recent studies have shown that extracellular NAs could be the *in vivo* activators of fXII due to their anionic nature [50]. Kannemeier *et al.* compared the procoagulant activities of cfNAs (cellular RNA or genomic DNA from Chinese hamster ovary (CHO) cells) with that of kaolin in human blood plasma; and reported accelerated clotting time in a concentration dependent manner with both NAs and kaolin, proposing that cfNAs are the "natural analogue of kaolin" in the activation of the intrinsic pathway. Furthermore, the cfNAs were shown to activate the contact phase proteins – fXII, fXI and kallikrein – comparably to kaolin. RNA was shown to specifically bind to fXII and fXI (and weaker binding to prekallikrein and kininogen), but not to other coagulation factors. Mice arterial thrombosis models revealed the presence of cfRNA in the formed thrombi, and the treatment of mice with RNase significantly delayed the arterial blockage time [26]. Chemotherapy-released cfDNAs were shown to activate the intrinsic pathway of coagulation *in vitro*. Swystun *et al*. collected venous whole blood samples from healthy individuals and further incubated them with various concentrations of chemotherapeutic agent epirubicin for 24 h to trigger the cfDNA release into

blood. The released cfDNA was then isolated from the blood and added to recalcified plasma at various concentrations for the monitoring of thrombin generation. It was shown that increasing concentrations of cfDNA elevated thrombin generation in a concentration-dependent fashion. Enhanced coagulation in the presence of cfDNA was further shown to be the result of the activation of the intrinsic pathway as the addition of fXII inhibitor diminished thrombin formation, as well as using fXII and fXI deficient plasma [48]. In addition to the NAs serving as natural anionic surfaces for the activation of fXII, Gansler *et al.* proposed that NA oligomers comprising hairpin structures can trigger activation of prekallikrein to kallikrein, and fXI to fXIa, through their binding to kininogen [51].

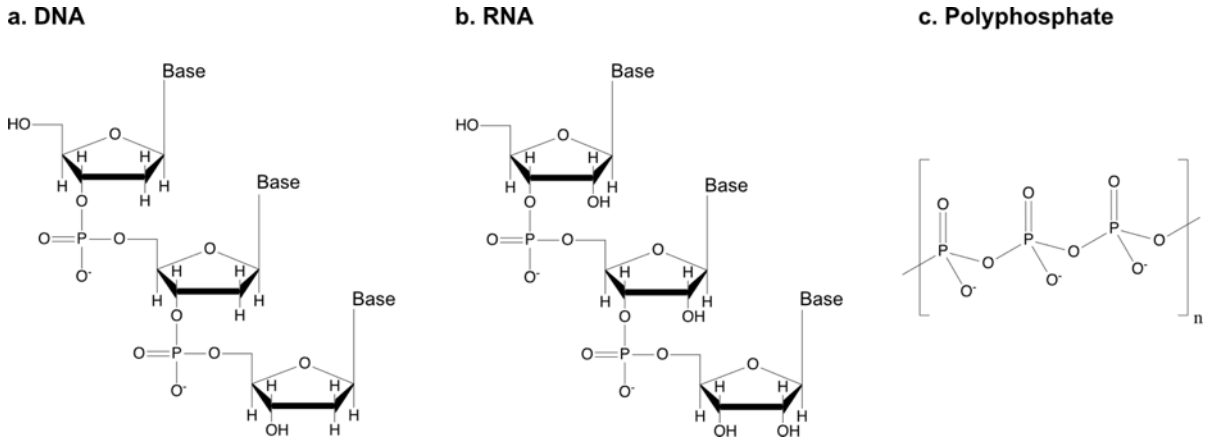

Figure 7.2. Chemical structures of the in vivo activators of the intrinsic pathway of coagulation.
(a) DNA backbone, **(b)** RNA backbone, and **(c)** polyP. For simplicity, three repeating units are shown in each molecule.

In addition to the phosphate-containing biomolecules DNA and RNA, inorganic polyphosphates (polyPs) are also known to display procoagulant and prothrombotic activities. The structural differences between DNA, RNA, and polyP are shown in Figure 7.2. Dense granules of human platelets were shown to store short-chain polyPs (~70-75 phosphate units per

chain) in large amounts [52]. These polyPs can be secreted upon thrombin stimulation/activation of the platelets, and play a part in a variety of processes in the coagulation cascade [53]. Via *in vitro* plasma clotting assays, Muller *et al.* reported the activation of the intrinsic pathway by short-chain polyPs (~60-100 phosphate units per chain) derived from human platelets, through their direct binding to fXII, and the activation of fXII to fXIIa. Furthermore, intravenous injection of a high dose of polyP (300 μg/g body weight) induced formation of a lethal PE in mouse models; and the mice defective in fXII were significantly protected from the fatal effects of the polyP-induced PE [24]. The extent of polyP's procoagulant activity was shown to significantly correlate with its chain length. While the polyPs having ~60-100 phosphate units per chain were five times more effective than the clay mineral kaolin in initiating the intrinsic pathway of coagulation; longer polyPs (more than 500 phosphate units per chain, such as the microbial polyPs) were found to be three orders of magnitude more powerful [54]. In addition to participation in the activation of the intrinsic pathway, polyPs may have other roles in the coagulation cascade [53], such as facilitating the activation of fV [56], and fXI by thrombin [56], and contributing to the stability of the fibrin clot [57]. The role of polyP in cancer-associated thrombosis was recently reported by Nickel and coworkers [58]. Their findings highlighted that prostate cancer cells and prostasomes, i.e., extracellular vesicles secreted from the prostate epithelial cells [59], possess long-chain polyPs (200 to >1000 phosphate units per chain) on their plasma membranes, triggering the activation of the intrinsic pathway of coagulation via fXII activation, thus contributing greatly to hypercoagulable states in prostate cancer.

7.2.4. Targeted Inhibition of the Cell Free Nucleic Acid and Polyphosphate Procoagulant Activity

Current treatment options for cancer-associated thrombosis mostly comprise heparin derived anticoagulants such as unfractionated heparin (UFH), low molecular weight heparin (LMWH), and the synthetic heparin antithrombin-binding pentasaccharide analog, fondaparinux [60]. These heparin derivatives mainly differ in their MWs; i.e. UFH (standard heparin), MW: 5 – 30 kDa; LMWH, MW: 1 – 5 kDa [14]; fondaparinux, MW: 1728 Da [61]. The structural differences among the heparin derivatives are responsible for the variation in their anticoagulant activities, half-lives, dosing requirements, and clearance pathways [61]. Heparin acts as an anticoagulant via binding to antithrombin and mediating a conformational change in its structure. This structural change amplifies antithrombin's catalytic activity at least 1000-fold by increasing the accessibility of antithrombin's reactive region to the active proteases thrombin and fXa. Once these active proteases assemble into a complex structure with heparin and antithrombin, their ability to act freely in the coagulation cascade is hindered, which inevitably impedes the formation of the fibrin clot [14]. Depending on the type of the heparin derivative, the inhibitory activity may differ; i.e. UFH and LMWH are capable of inhibiting thrombin (the latter being a poor inhibitor) and fXa, while fondaparinux inhibits fXa, but not thrombin [14, 62]. Despite their effectiveness, heparin derived antithrombotic drugs possess serious bleeding risks as they target the key members in the common pathway of the coagulation cascade (thrombin, fXa). Cancer patients are already at a higher risk of developing thrombotic disorders; moreover, they have a higher risk of anticoagulant-induced bleeding than the patients without malignancy [63]. There is an urgent need for the development of safe anticoagulants effective in arresting thrombosis without increasing the hemorrhagic complications.

Recent studies have shown the importance of the intrinsic pathway in *in vivo* thrombus formation. FXII was reported to play an essential role in thrombi formation and stabilization in mice [64-66], and nonhuman primate models [67], while deficiency of fXII is not associated with bleeding anomalies of clinical relevance [50]. Targeted inhibition of the *in vivo* activators of the intrinsic pathway thus may constitute a potentially safer alternative to conventional anticoagulants. In this context, NA and polyP binding polymers have been sought for thrombosis prevention. Jain and coworkers investigated the *in vitro* and *in vivo* anticoagulant activity of a generation 3 (G3) polyamidoamine (PAMAM) dendrimer comprising 32 surface amine groups. PAMAM G3 was shown to bind to inorganic polyphosphate (60 phosphate units per chain) and double stranded (ds) DNA with similar binding affinities which are higher than that of single stranded (ss) DNA and dsRNA. PAMAM G3 successfully inhibited the coagulation started by a kaolin surface, also extended the blood clot formation time in whole human blood significantly (~3-fold). *In vivo* mice models of carotid artery injury and pulmonary thromboembolism showed that mice treated with PAMAM G3 (20 mg/kg) had prolonged times of vessel occlusion or survival, without a significant increase in blood loss in comparison to the saline treated group [68]. Smith *et al.* screened a library of cationic molecules, polymers and proteins for their inhibitory performance against polyP's prothrombotic activity *in vitro*, and identified potent inhibitors that include low and high molecular weight (MW) PEI, spermine, and generation 1 (G1) PAMAM dendrimer. In *in vivo* mouse models, G1 PAMAM dendrimer caused a decrease in the size of the thrombus as well as its associated fibrin content [53].

Recently Travers *et al*. [69] screened a library of universal heparin reversal agents (UHRAs) to explore their performance in inhibiting polyP's prothrombotic activity. UHRAs are a family of dendritic polymers that serve as synthetic heparin antidotes, developed by

Kizhakkedathu and coworkers [70]. Their structure comprises a dendritic polymer core functionalized with cationic heparin binding groups, which then is shielded by the engraftment of short polyethylene glycol (PEG) chains. The heparin binding groups comprise tertiary amines which can be protonated at physiological pH, and are structurally similar to other amine containing cationic polynucleotide binding polymers such as PEI. Travers *et al.* studied four UHRA compounds possessing a trivalent polyP-binding group (R, also known as heparin binding group), and the number of R groups were varied from 7 to 24. These UHRA compounds were shown to induce a two-fold increase in *in vitro* polyP- and RNA-initiated plasma clotting times at nM and μM concentration range, respectively. Moreover, they displayed less toxic side effects, such as less platelet activation (10-15%) and no fibrinogen aggregation, than protamine and PEI. Moreover, UHRA compounds displayed less bleeding side effects compared to heparin based anticoagulants; i.e., tail bleeding times in mice treated with 200 mg/kg UHRA were found to be significantly shorter than the mice treated with 1000 U/kg UFH [69]. Taken together, these studies employing cationic polymers as antithrombotic agents against the activators of the intrinsic pathway suggest that targeted inhibition of the procoagulant activity of NAs/polyPs is a promising approach for the generation of safer anticoagulant medications.

In this chapter, we investigated NA binding performance of polymers that are composed of a PEG chain attached to a cationic R group, with molecular dynamics (MD) simulations. We explored the influence of PEG chain length as well as size and charge of the R group on binding performance of the polymers. DNA was chosen as a representative NA, but we articulate that the binding behavior of the polymers should be applicable to RNAs and polyPs of similar size (see Figure 7.2 for structural comparison). Our aim is to identify the molecular mechanisms governing polymer – NA binding, and the optimal structural features of the polymers for a better

NA binding performance. This level of information is crucial for the design of polymeric structures displaying the highest NA binding performance, which could be further put through *in vitro* and *in vivo* studies to assess their ability to arrest thrombosis.

7.3. Methods

7.3.1. Simulated Systems

The DNA simulated in this chapter is Drew-Dickerson dodecamer, a prototypical 24 nucleotide B-DNA duplex with the sequence of $d(CGCGAATTCGCG)_2$. It carries a total charge of –22 in the fully deprotonated state. The initial structure of the DNA is adopted from our previous study [71]. The polymer chains explored in this chapter are composed of a PEG tail, and a cationic head group (R) comprising tertiary amine groups. Two different tail lengths were studied, which will be referred to as short and long tails hereafter, where the number of repeating PEG monomer units (n) are 11 and 22, respectively (Figure 7.3a). We investigated three different head groups, R1, R2, and R3, comprising 3, 4, and 7 tertiary amine groups, respectively (Figure 7.3b). R2 corresponds to the R group of the UHRA compounds previously studied by Travers and coworkers [69]. The total charge of the head groups under physiological conditions is +3, +3, and +7, respectively, for R1, R2, and R3. For the discussion herein, the polymers are named with the tail identifier, "s" for short tail and "l" for long tail, appended to "PEG", followed with the name of the head group. For example, polymer PEGs-R1 is composed of a short PEG tail and the head group R1. The initial structures of the polymers are given in Figure 7.4.

For the equilibration of the polymers, their initial structures were placed in a TIP3P water box, and neutralized with the addition of a proper amount of Cl^- ions; and two independent, 10 ns (restrained) + 100 ns (free) long simulations were carried out. During the simulation course, the polymers were observed to visit and exchange between two distinct conformational states:

one where the polymer head is in an extended form with no tail in close proximity (extended configuration), and the other where the polymer tail is wrapped around the head group (shielded configuration). To capture the potential influences of these two different configurations, the simulation trajectories were visually examined to choose one extended and one shielded configurations for each polymer. The final structures of the polymers are given in Figure 7.5. The naming of the polymers was updated to include the polymer configuration identifier; "e" for extended and "s" for shielded, appended to the previously assigned names of the polymers.

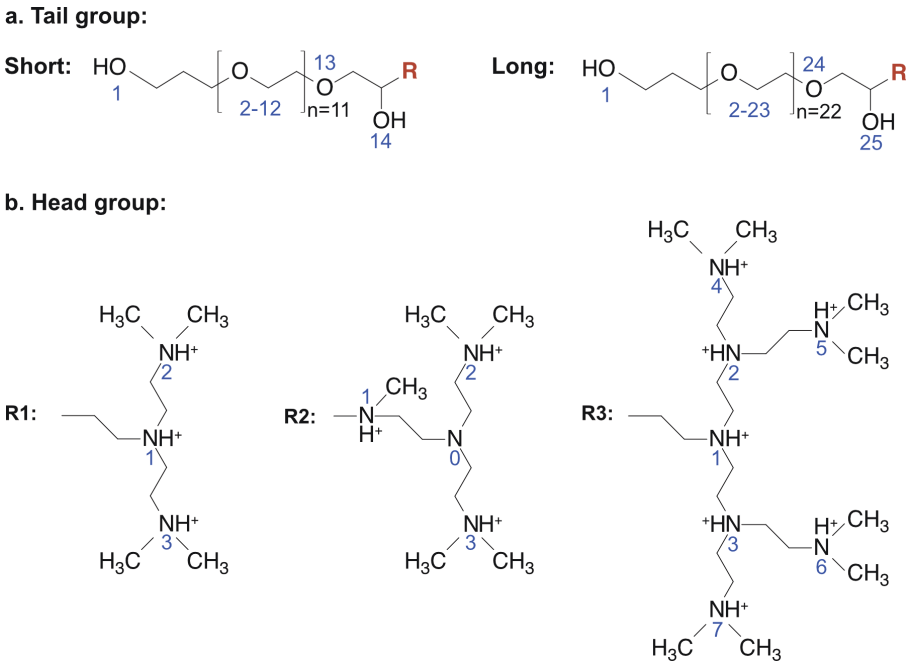

Figure 7.3. Chemical structures of the simulated polymers.
(a) The length of the polymer tail is varied by changing the number of repeating PEG monomer units (n). The short tail (n = 11) will be referred to as PEGs, and the long tail (n = 22) will be referred to as PEGl. **(b)** The head groups consist of a different number (3, 4, and 7 for R1, R2, and R3, respectively) of tertiary amines groups. The protonation sites at physiological pH are marked with "+".

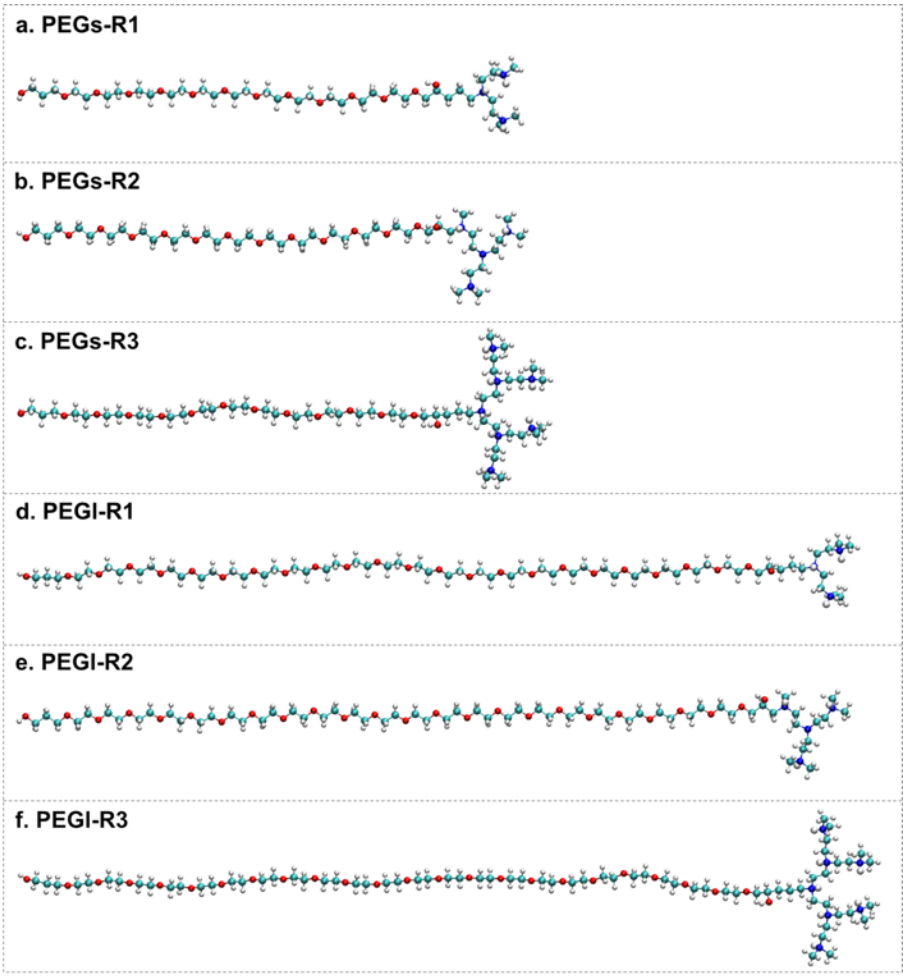

Figure 7.4. Initial configurations of the simulated polymers.
The color coding of the atoms is as follows: cyan, C; red, O; blue, N; white, H.

The final structures of the polymers were adopted as input to simulations with DNA. The polymers are oriented in a way to position their head groups to face DNA; and placed at a center of mass (COM) distance of 17 Å, on the DNA major groove side. The initial configurations of the simulation systems are shown in Figure 7.6. The simulation systems were named with the name of the polymer followed by "DNA" to distinguish between the single polymer simulations and polymer – DNA systems. For example, system PEGs-R1e–DNA is composed of a polymer with short tail and the head group R1 in extended configuration, and one DNA molecule. All polymer – DNA systems were solvated in a TIP3P water box with a margin of 15 Å from all

sides, and ionization with the addition of 150 mM NaCl to mimic the physiological conditions. Systems were then simulated for 10 ns (restrained) + 150 ns (free).

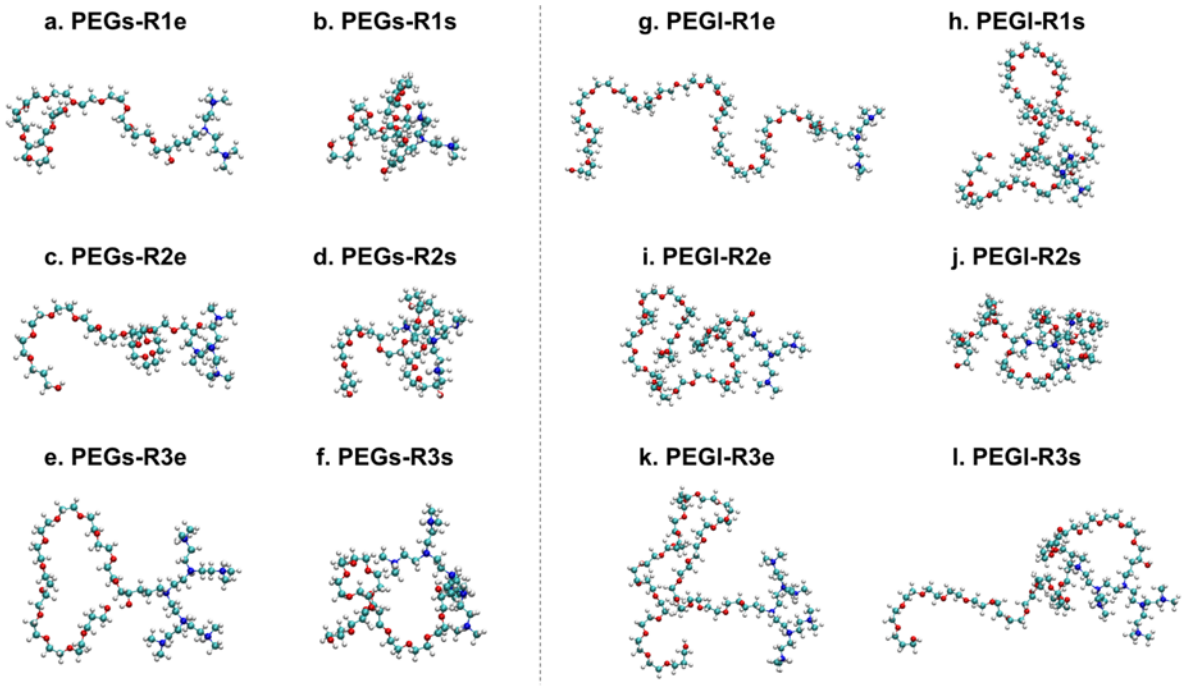

Figure 7.5. Final configurations of the simulated polymers.
For clarity, water and ions are not shown. The color coding of the atoms is as follows: cyan, C; red, O; blue, N; white, H. Each configuration is selected from an independent simulation of the polymer in explicit water.

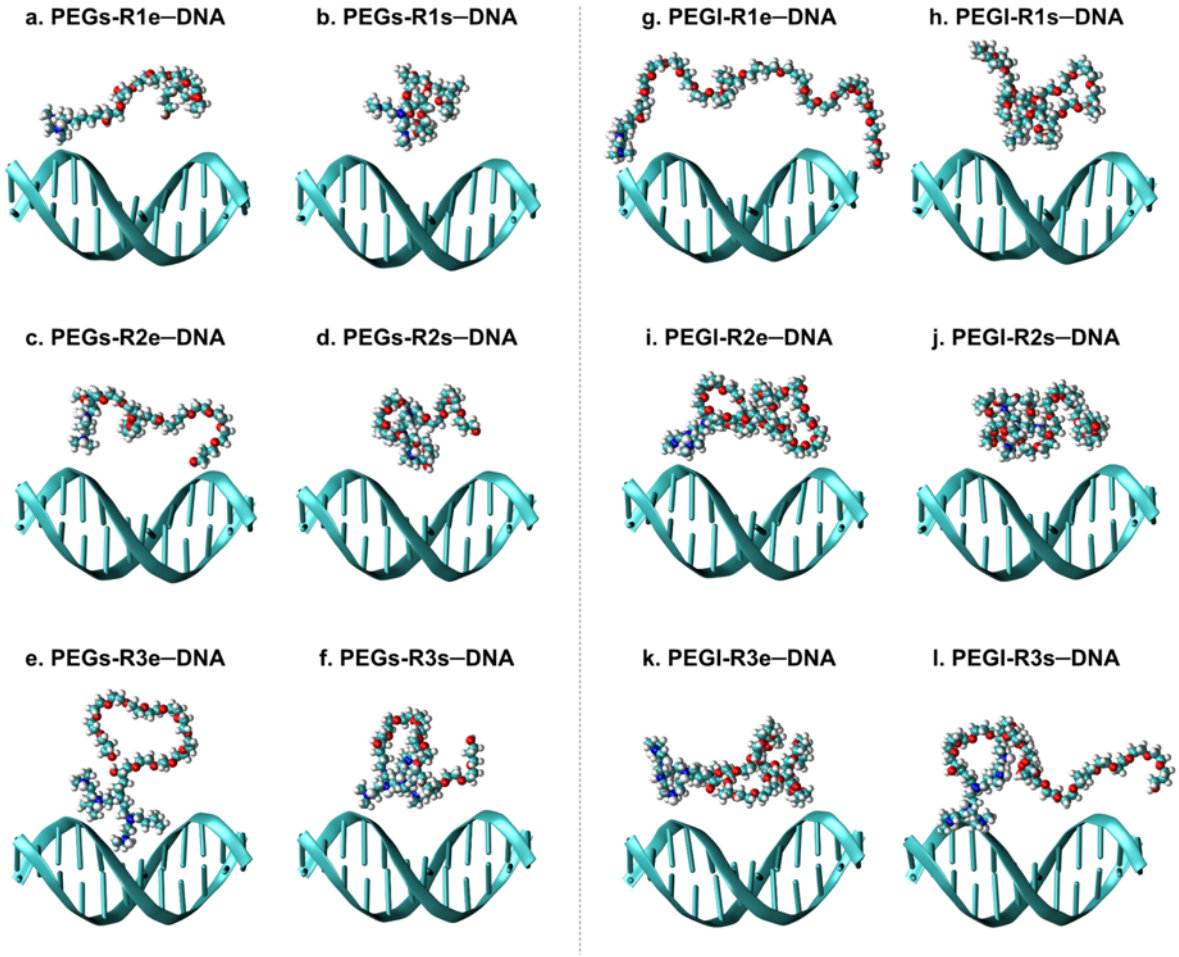

Figure 7.6. Initial configurations of the polymer-DNA simulation systems.
(a) PEGs-R1e–DNA, **(b)** PEGs-R1s–DNA, **(c)** PEGs-R2e–DNA, **(d)** PEGs-R2s–DNA, **(e)** PEGs-R3e–DNA, **(f)** PEGs-R3s–DNA, **(g)** PEGl-R1e–DNA, **(h)** PEGl-R1s–DNA, **(i)** PEGl-R2e–DNA, **(j)** PEGl-R2s–DNA, **(k)** PEGl-R3e–DNA, and **(l)** PEGl-R3s–DNA. DNA duplex is shown in cyan. The color coding of the polymer atoms is as follows: cyan, C; red, O; blue, N; white, H. Water and ions are not shown for clarity.

7.3.2. Force Field for the Studied Molecules

The parameterization of the polymers was carried out by following CHARMM general force field (CGENFF) methodology [72]. The topology of the building blocks of the polymer tail are available in CHARMM36 general force field (CGENFF36) [72]. The residue names of the adopted parent molecules from CGENFF36 are as follows: “ETOH” for the OH-CH_2-CH_2– group at the left end of the polymer tail, “PEGM” for the repeating –CH_2-O-CH_2– groups,

"PRO2" for the CH-OH group preceding the polymer head group. The topology of the building blocks of the head groups are adopted from CGENFF36, and a CHARMM format force field which was built for PEI molecules and validated with ab initio calculations in our previous works [71, 73, 74]. The residue names of the parent compounds adopted from CGENFF36 are as follows: "BUTA" for the –CH2-CH2– spacer preceding the tertiary amine groups in R1 and R3, and "PIP1" for the protonated tertiary amine groups. The topology of the unprotonated tertiary amine group in head group R2 is adopted from our force field devised and validated for PEI molecules [71, 73, 74].

Bond, angle, torsion, and van der Waals parameters were adopted from the existing parameters of the parent compounds adopted from CGENFF36, and the missing parameters were assigned by following CGENFF methodology [72]. CHARMM36 all-atom force field for NAs was used for DNA [75].

7.3.3. Simulation Details

All simulations were performed with MD package of NAMD [76], with a time step of 2 fs, periodic boundary conditions (PBC), particle mesh Ewald (PME) [77] for full electrostatics, a cut-off of 12 Å for van der Waals and pairwise interactions, and SHAKE algorithm [78] to constrain the bonds involving H atoms. First, each system was minimized for 5000 steps, followed by the gradual heating from 0 K to 300 K within 20 ps, with a harmonic restraint of 10 kcal/mol·$Å^2$ on solute non-H atoms. Keeping the restraint on non-H atoms of the solute, the system was further simulated for 10 ns. The restraint was then removed, and NPT simulation was performed for 150 ns. Langevin dynamics thermostat with thermostat damping coefficient of 10 ps^{-1} for all the non-H atoms was used for temperature control. Pressure control was achieved with Nosé−Hoover−Langevin barostat with damping time scale of 100 fs and

Langevin piston oscillation period of 200 fs. Simulation trajectories were visualized and analyzed with VMD [79].

7.4. Results

The final structures of the simulated systems are given in Figure 7.7. Visual examination of the simulation trajectories has shown that polymers bind to DNA mainly through interactions with the DNA major groove. In addition to the major groove, some polymers, namely PEGs-R2e, PEGl-R1s, PEGl-R2s, PEGl-R3e, and PEGl-R3s, formed interactions with the DNA minor groove. Moreover, polymers with R3 showed prolonged periods of DNA contact in comparison to the polymers with lower cationic charge head groups, R1 and R2, highlighting the role of the head group cationic charge in binding to DNA. Another interesting observation was that three out of four systems comprising the R2 head group (Figure 7.7c, d, i, j) exhibited poor binding to DNA, as evident by the separation from DNA, even though R2 carries the same cationic charge (+3) as R1. This suggests that, in addition to the cationic charge of the polymers, the structure of the head group plays an important role in determining the binding performance of the polymers. To investigate these observations, in the following sections, we quantify the binding of different polymer head and tail groups to DNA, and explore the mechanisms affecting the binding performance of the polymers.

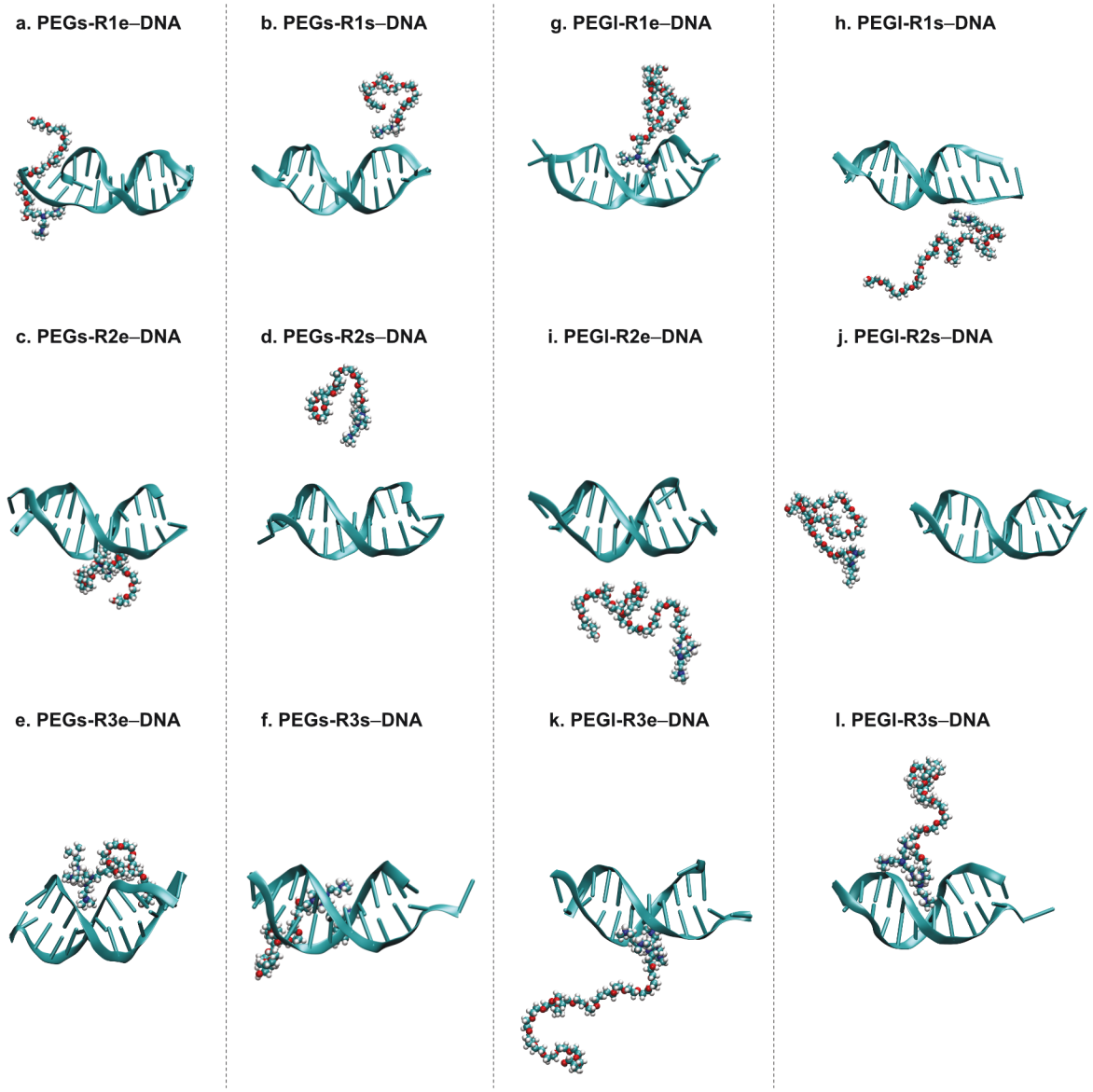

Figure 7.7. Final configurations of the polymer-DNA simulation systems.
(a) PEGs-R1e–DNA, **(b)** PEGs-R1s–DNA, **(c)** PEGs-R2e–DNA, **(d)** PEGs-R2s–DNA, **(e)** PEGs-R3e–DNA, **(f)** PEGs-R3s–DNA, **(g)** PEGl-R1e–DNA, **(h)** PEGl-R1s–DNA, **(i)** PEGl-R2e–DNA, **(j)** PEGl-R2s–DNA, **(k)** PEGl-R3e–DNA, and **(l)** PEGl-R3s–DNA. DNA duplex is shown in cyan. The color coding of the polymer atoms is as follows: cyan, C; red, O; blue, N; white, H. Water and ions are not shown for clarity.

7.4.1. Polymer – DNA Binding

We investigated polymer – DNA binding by monitoring the interactions of the polymers' head and tail with the DNA. To do so, we defined a cut-off distance of 4 Å for a close contact to be formed between polymer head/tail and the DNA. We previously reported 4 Å as the distance in which a direct H-bond can be formed between DNA and the amine groups of PEI [71]. As the polymer head groups investigated in this study comprise amine groups similar to PEI, we adopted the 4 Å cut-off value again as the distance where a direct H-bond can be formed between the polymer head amines and the electronegative atoms (N/O) of the DNA. For consistency, we followed the same definition for the quantification of the polymer tail – DNA interactions where we defined the Os of the tail group to be in close contact with the DNA if they reside within 4 Å of any DNA N/O, representative of the H-bonds that can form between O-bearing groups of the polymer tail and the DNA electronegative atoms. The time course of the number of close contact Ns is given in Figure D.1 (Appendix D). For a more quantitative comparison, in Figure 7.8a, we plot the number of head group Ns in close contact with DNA N/O vs. the total number of Ns in the head group, averaged over the final 50 ns of the simulations. The number of Ns establishing close contacts with DNA increased proportionally with the increase in the number of head group Ns from 3 to 7 (systems bearing R1 and R3), irrespective of the polymer initial conformation or tail length.

R2 containing systems, on the other hand, responded differently to the initial conformation of the polymer contingent on the length of the polymer tail. Among the polymers with short tail, the shielded initial configuration of the polymer head resulted in substantially weakened contacts with DNA in comparison to the extended head configuration. In the R2 bearing polymers with long tail, extended configuration exhibited no contacts with DNA, whereas

shielded configuration slightly increased the number contacts. In three out of four systems with R2, PEGs-R2s, PEGl-R2e, and PEGl-R2s, the number of head group Ns in close contact was found to be less than those of the R1 bearing systems, despite the increase in the total number of tertiary amine group of the head group. Visual examination of the simulation trajectories (Figure 7.7d, i, j) showed separation from the DNA in these three systems; and the time of separation identified from Figure D.1b,e for these systems were 108, 45 and 132 ns, respectively. It is evident that the binding of R2 with DNA is not as stable and strong as those of R1 and R3, despite its equal charge to R1.

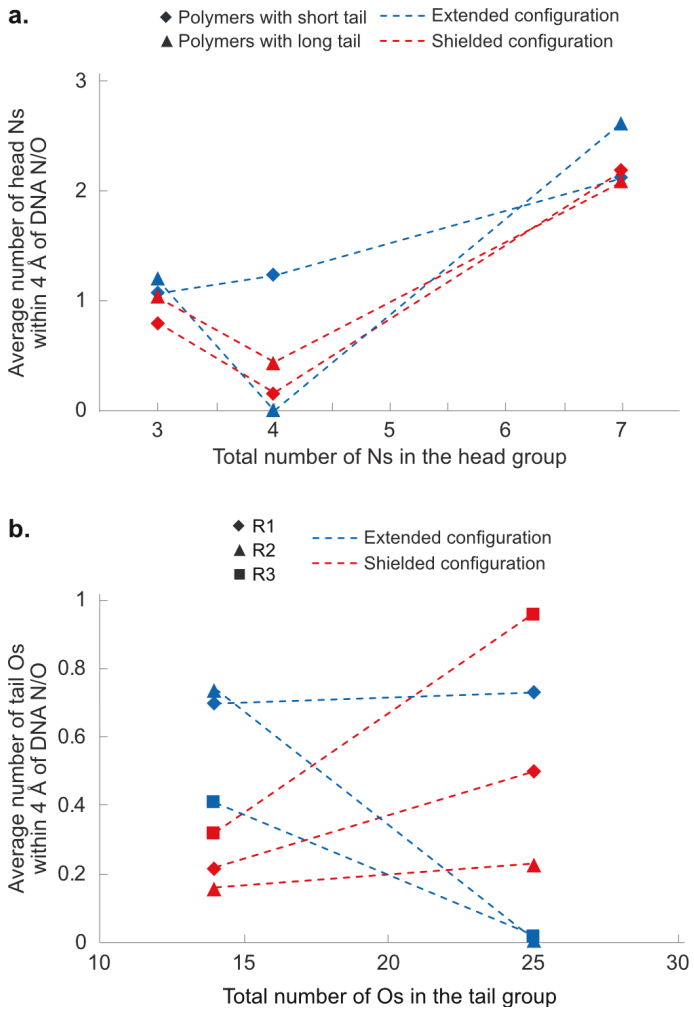

Figure 7.8. Polymer head and tail group binding to DNA.
Average number of **(a)** head group Ns within 4 Å of DNA N/O as a function of the total number of Ns in the head, and **(b)** tail group Os within 4 Å of DNA N/O as a function of the total number of Os in the tail group. The extended and shielded polymer initial configurations are given in blue and red, respectively.

We further investigated whether the polymer tail participates in DNA binding. The number of tail Os in close contact is plotted as a function of the simulation time in Figure D.2 (Appendix D). It could be seen that the polymer tail forms transient interactions with DNA and the strength of interactions between DNA and the polymer tail is weak; for most of the simulation time the number of tail Os interacting with DNA is below 15% of the total number of Os. Moreover, the

interactions weaken or phase out within the final 50 ns of the simulations. One interesting observation from Figure D.2 is the elevated levels of interactions between DNA and both the short and long tail of the polymers with R2 when the polymer head in the initial configuration is shielded, within the first 100 ns of the simulations (Figure D.2b, e). This might indicate that the structure of the initial shielded head conformation of the polymers is preserved throughout the simulation. This could give rise to the slightly increased interactions of the polymer tail group with DNA, given the polymer tail is more exposed to DNA than the head group. These interactions discontinue in the final stages of the simulations. To investigate the contribution of polymer tail to DNA binding in a more quantitative manner, in Figure 7.8b, we plot the average number of in close contact Os (within 4 Å) as a function of the total number of the tail Os. Overall, the average number of close contact Os is below 1 for the final 50 ns of the simulations, further stating that the polymer – DNA interactions are driven by the cationic head group, and participation by the tail is almost negligible. Increasing the length of the polymer tail resulted in a different trend, dependent on the initial configuration. For all the simulation systems, having a long polymer tail increased the interactions with DNA in the shielded polymer configurations. However, the opposite of this effect is seen in the extended polymer configurations where increasing the tail length impedes DNA interactions (one exception to this is systems with R1 where the length of does not seem to affect the extent of tail binding to DNA).

As polymer binding to DNA is driven by the cationic head groups, we further investigated the intermolecular contacts between polymer head and DNA. We monitored the number of Ns in close contact with DNA backbone Os – the phosphate Os: O1P and O2P, the phosphate esteric Os: O3′ and O5′, and the sugar ring O: O4′; as well as the base N/O (Figure 7.9). With one exception (PEGs-R2e), binding of polymer head to DNA was driven by the interactions with

DNA backbone phosphate Os, O1P and O2P, consistent with previous reports of DNA binding to oligoamines [80-84] and PEI [71, 74, 85]. Weaker interactions with the phosphate esteric Os, O3′ and O5′, and base N/O was observed in all systems (except for PEGs-R2e where the level of binding among these groups are comparable). The sugar ring O, O4′, was only observed to participate to DNA binding in two systems, PEGs-R2e and PEGl-R3e, in a weak manner.

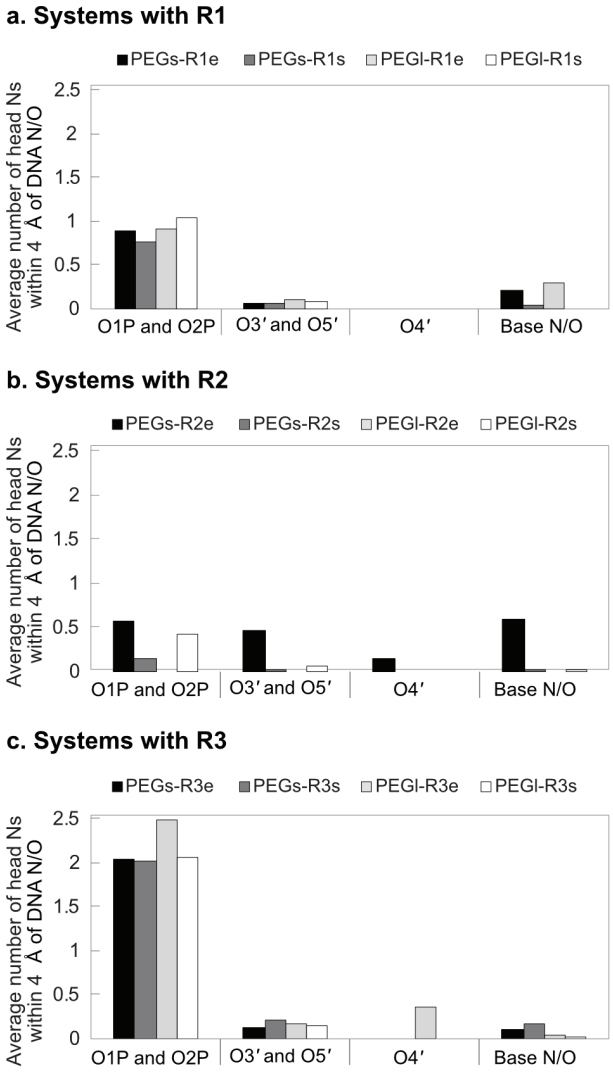

Figure 7.9. Details of intermolecular contacts between polymer head and DNA. Number of head group Ns within 4 Å of DNA backbone Os (O1P and O2P, O3′ and O5′, and O4′) and base N/O, averaged over the final 50 ns of the simulations with the polymers of **(a)** R1, **(b)** R2, and **(c)** R3 head groups.

As the number of tertiary amine groups is gradually increased from R1 to R3 (3, 4, and 7 for R1, R2, and R3, respectively), we investigated how such an increase influences the interactions of the individual amines (see Figure 7.3 for the numbering of the head group Ns) with DNA. In Figure 7.10, we plot the percentage of time in which the Ns of the polymer head reside within 4 Å (in close contact) of DNA N/O over the final 50 ns of the simulations. 100% corresponds to a state where a given N atom is in close contact with at least one DNA N/O atom at all times over the final 50 ns, where 0% represents the case of no interactions (i.e., no contact within 4 Å). In the systems with R1 (Figure 7.10a), N1 forms the highest amount of DNA contact, followed by N2, and N3.

In the R2 bearing systems (Figure 7.10b), the ability of N1 to interact with DNA is significantly impeded. The interactions are mostly shifted towards N2 and N3 in systems PEGs-R2e and PEGl-R2s, while the remaining systems display little or no interactions brought by these two Ns. In all R2 bearing systems, N0 – the unprotonated N – failed to participate in DNA binding. Given the observed difference, it is possible that the R1 head group aligns itself parallel to DNA backbone to make strong contact through N1, while also augmenting the interactions with DNA via N2 and N3. In R2, the lack of a positive charge in the position 0 might dictate the orientation of the head group for binding to DNA, allowing the head group to position itself in a way to maximize the number of protonated Ns in close contact with DNA (two out of three Ns). Despite the positioning of the head group R2 to augment the interactions with DNA, N2 and N3 exhibited very poor binding in three out of four systems (PEGs-R2s, PEGl-R2e, and PEGl-R2s). This suggests R2 bearing polymers might have some other features that are unfavorable for DNA binding. We will explore such features in Section 7.4.2.

In the R3 containing systems (Figure 7.10c), for the discussion herein, we will investigate the head group in three parts: N2, N4, and N5 constitute one end of the head group; N3, N6, and N7 form the other end; and N1 is the connection between the two ends. Starting with PEGs-R3e, N3 displayed the highest amount of DNA contact time with an average value of 65%, followed by N4 with 49%. The contribution by N2, N5, and N6 was comparable (~20%), and N1 and N7 exhibited the least amount of interactions (15% and 6%, respectively). This indicates that the interactions with DNA are made mainly through the two ends, while N1 – the connection between the two ends – acts as the hinge point regulating the orientation of the two ends. In PEGs-R3s, the % contact time of individual Ns differed from those of PEGs-R3e, however, the overall binding pattern was conserved. The time of DNA contact was comparable among N5, N2, and N3 with an average value of ~40%, followed by N6 and N4 with ~30%. Again, N7 and N1 were the least contributing Ns with 18% and 8%.

Increasing the length of the polymer tail of R3 bearing polymers gave rise to a different mode of DNA binding, contingent on the polymer initial configuration. In PEGl-R3e, unlike the previous observations, DNA binding became mainly localized to three Ns: N2 and N3, which are in close contact with DNA at all times, followed by N6 with 49% occupancy. N1 showed no interactions at all, thus remained as the hinge point. Changing the initial configuration of the polymer head from extended to shielded (PEGl-R3s) significantly affected the role of N1. In this system, N1 was found to be in close contact with DNA for 97% of the final 50 ns. N4 and N7, located at the edges of the two ends of the head group, followed N1 with 34% and 22%. The remaining Ns showed similar levels of interactions in the range of 10% to 20%. The reduced interaction of N2, N5, N3 and N6 with DNA might be due to the polymer tail shielding the portions of the head group in the initial configurations of the polymers, which might have been

conserved in DNA binding simulations, hindering the interactions of these Ns with DNA, and further causing the head group to maximize its interactions through the remaining Ns: N1, N4, and N7.

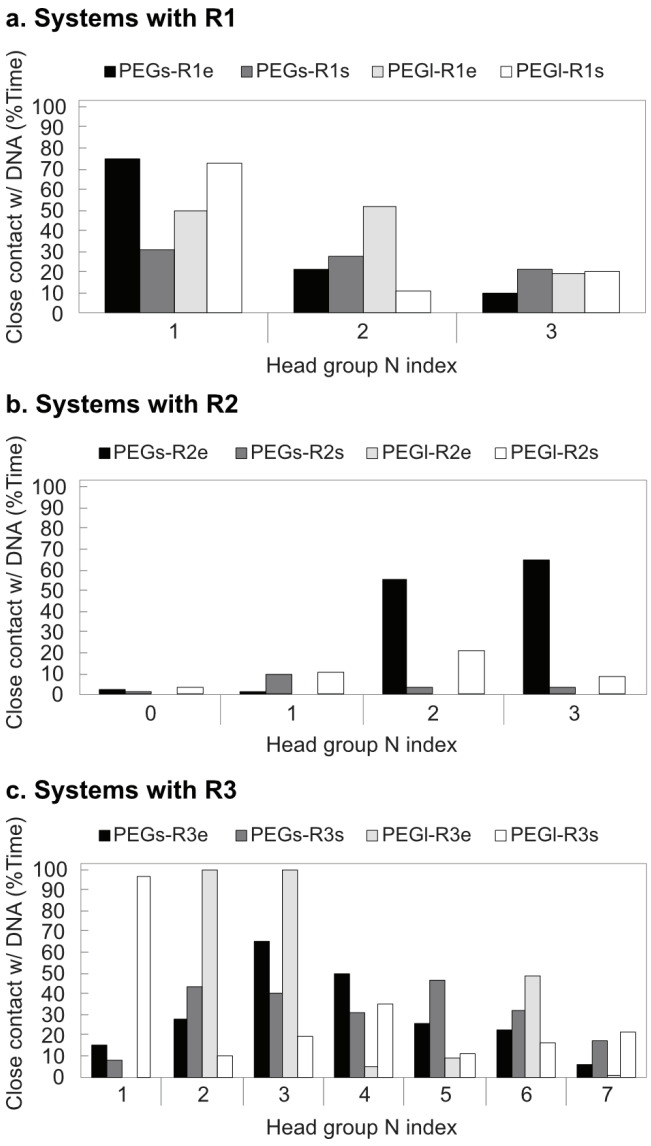

Figure 7.10. Percentage of time in which head group Ns are in close contact with DNA N/O (both backbone and base) in the final 50 ns of the simulations.
The data is presented for the systems with **(a)** R1, **(b)** R2, and **(c)** R3. The numbering of the head group Ns is given in Figure 7.3b.

It is evident from previous observations that the interactions with DNA are through charged groups of the polymer head. Interestingly, when the number of tertiary amine groups in the head group is increased without changing the head group cationic charge (R1 vs. R2 systems), polymer – DNA binding is significantly altered. The mechanism behind this drastic change in the binding performance is not clear from the previous analysis, which motivated us to study the conformational states of the polymers in simulations with DNA in more detail.

7.4.2. Mechanisms Governing DNA Binding Performance of the Polymers

As R2 containing systems are identified as the systems most sensitive to the initial configuration of the polymers (extended vs. shielded) in terms of DNA binding, we hypothesize that there might exist strong intramolecular interactions in R2 bearing polymers between the polymer head and tail groups, possibly leading to a collapsed state of the polymer where the tail partially covers the head group. This in turn might hinder interactions with DNA. To test this hypothesis, we adopted the 4 Å cut-off again as the distance of close contact where amine groups of the head group can form direct H-bonds with the tail Os, and monitored the number of head group Ns in close contact with the tail Os throughout the simulations (Figure 7.11). Irrespective of the polymer initial configuration or length of the polymer tail, systems with R1 and R3 demonstrated weak transient intrachain associations, which can be deemed as negligible. Systems with R2, however, displayed elevated levels of intramolecular interactions over the course of the simulations (except for PEGl-R2e where the intramolecular interactions are observed in a transient fashion); the intrachain associations are even more pronounced in the shielded polymer head initial configurations.

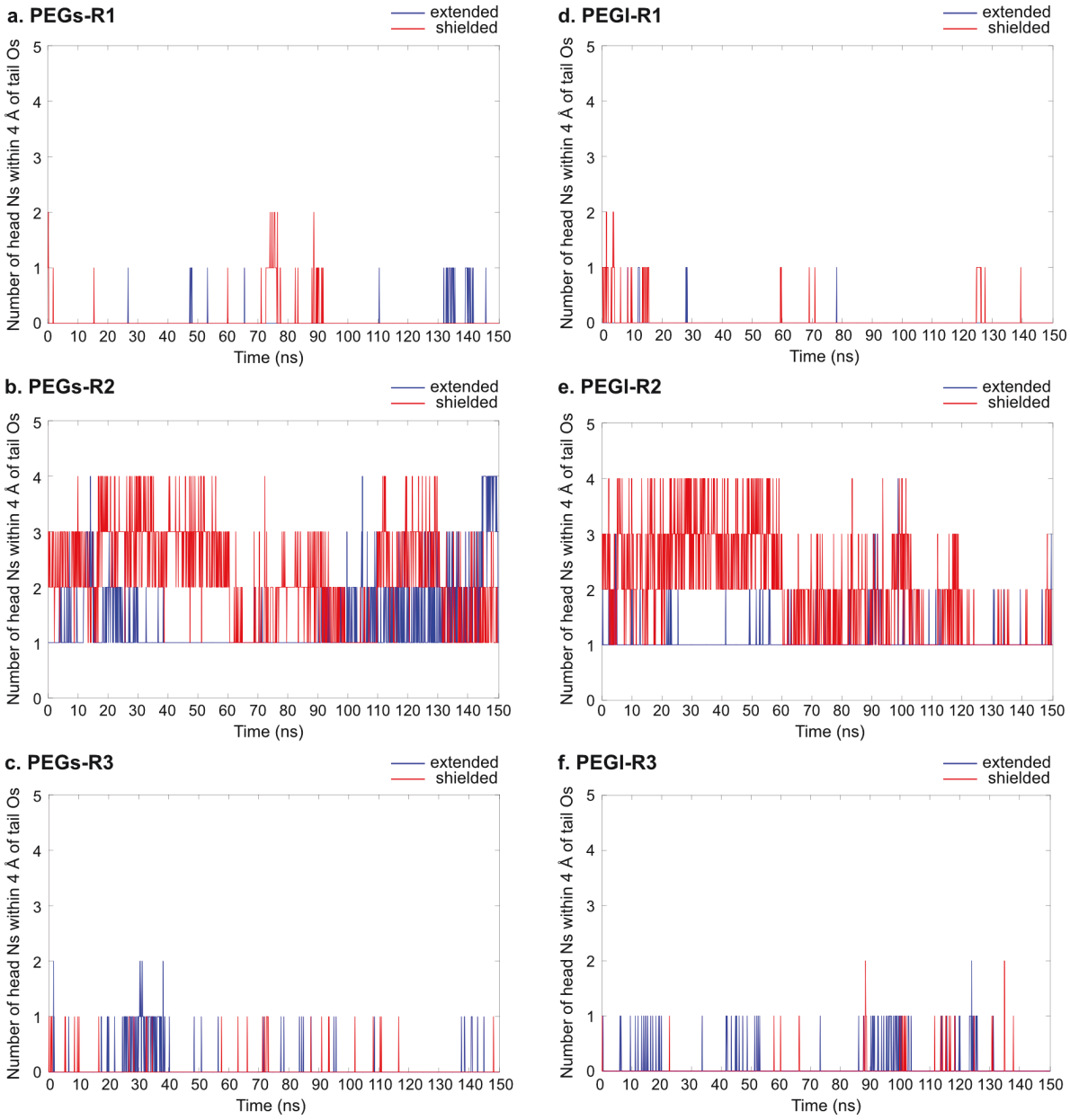

Figure 7.11. Number of head group Ns within 4 Å of tail Os as a function of simulation time.
The data is presented for the systems with DNA and **(a)** PEGs-R1, **(b)** PEGs-R2, **(c)** PEGs-R3, **(d)** PEGl-R1, **(e)** PEGl-R2, and **(f)** PEGl-R3. The two curves in each plot represents the two initial polymer configurations, extended (blue) and shielded (red).

Another interesting observation from Figure 7.11b and Figure 7.11e is that there is always one head group N in close contact with DNA. To identify which of the head group Ns is making

this permanent contact with the polymer tail, we examined the contacts made by the individual Ns by tracking the percentage of time over the final 50 ns of the simulations in which the head group Ns are interacting with the tail Os (Figure 7.12). The head group Ns in R1 and R3 systems are observed to be in close contact with tail Os for at most 7% of the time (in the final 50 ns), further confirming that polymer intrachain associations in these systems are negligible. In the systems with R2, the individual N atom making the permanent contact with the tail is found to be N1. Following N1 are N0, N3, and N2, ordered from the most to least interacting.

In parallel to Figure 7.12, we also explored the distribution of the tail Os around head Ns. This is presented in Figure 7.13, by the RDF of tail Os around head group. Firstly, the initial configuration of the polymers did not significantly affect the trend of the tail O distribution around head Ns; i.e., given a type of polymer, the RDF peak positions are very similar between the two polymer initial configurations. There exist some differences in the height of the RDF peaks between the two polymer conformations; i.e., in DNA systems with PEGs-R1 and PEGs-R2, extended initial polymer configurations demonstrated higher RDF peaks than the shielded, suggesting that initial configuration of the polymer can influence the probability of finding a tail O within neighbour distances. Secondly, increasing the length of the polymer tail decreases the probability of finding a tail O around head N, as is evident from the reduced RDF peak height in the polymers with long tail compared to those of the shorter tail polymers. This effect is most significant for the R2 system.

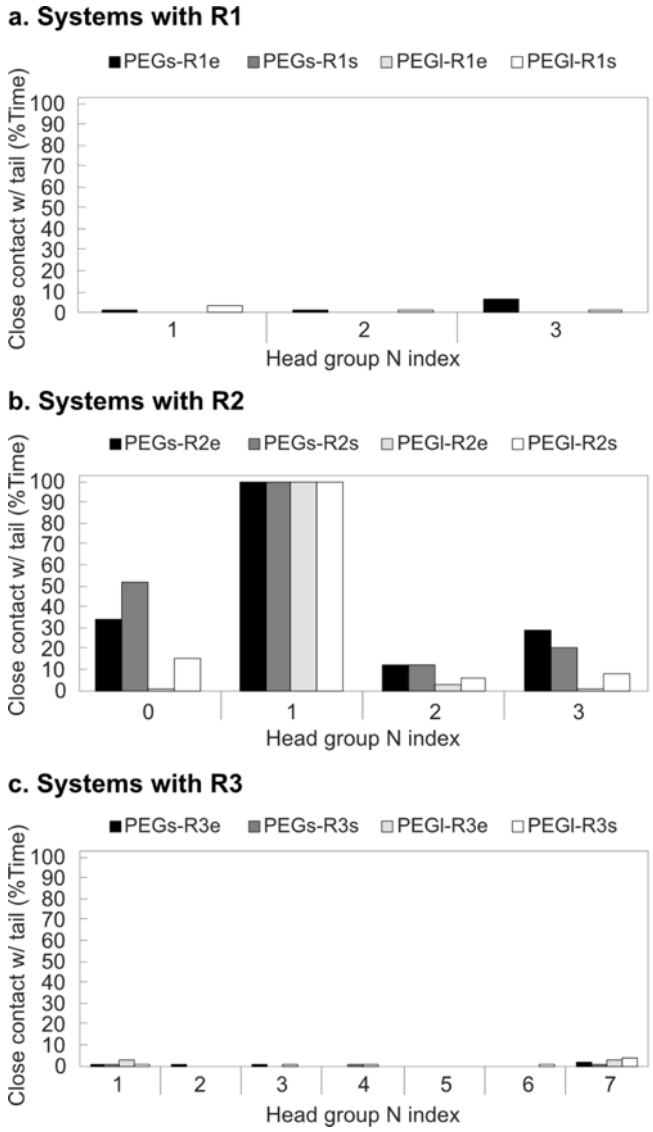

Figure 7.12. Percentage of time in which head group Ns are in close contact with tail Os in the final 50 ns of the simulations.

The data is presented for the systems with DNA and polymers bearing the head groups **(a)** R1, **(b)** R2, and **(c)** R3. The numbering of the head group Ns is given in Figure 7.3b.

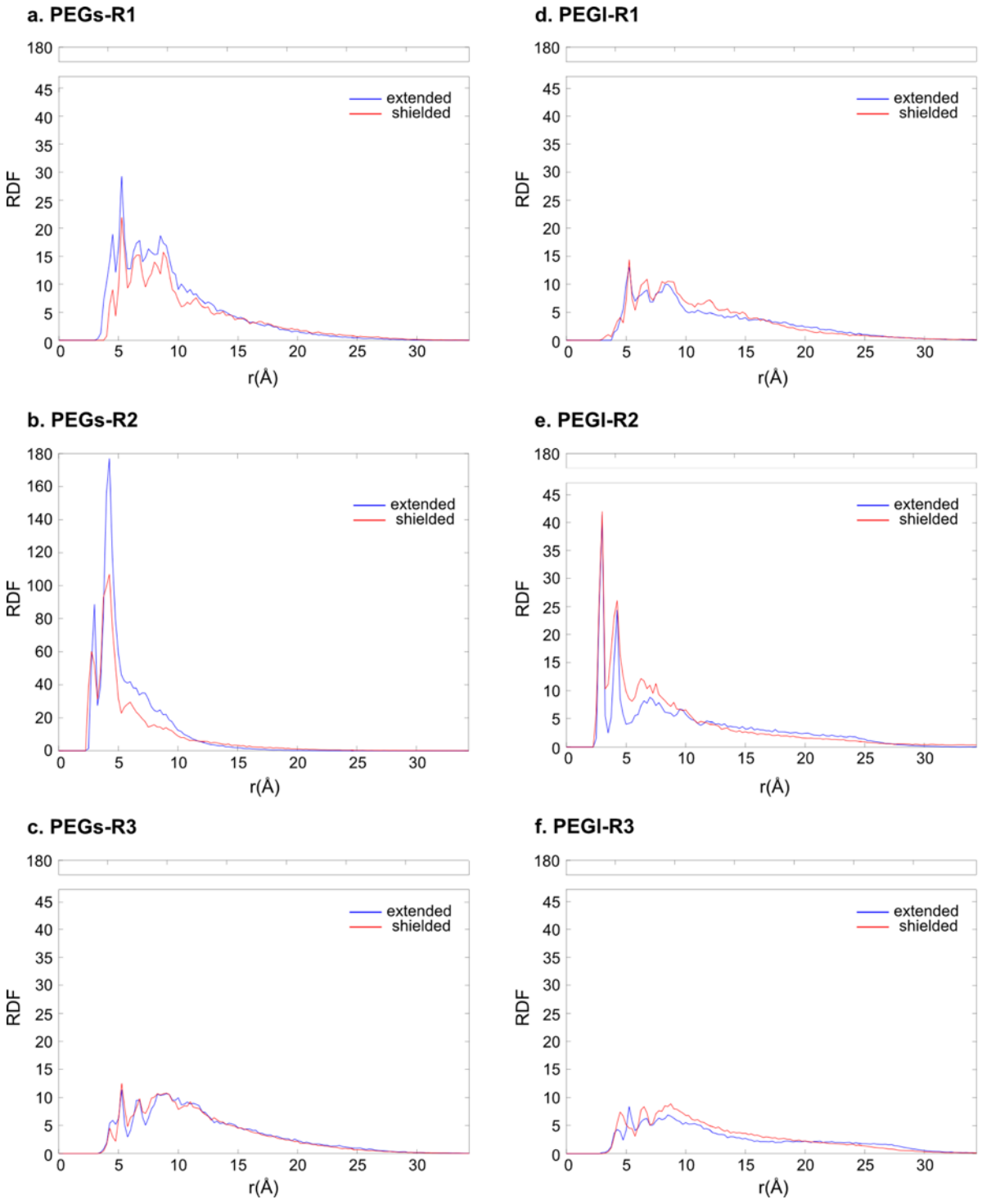

Figure 7.13. RDF of polymer tail Os around head group Ns for the final 50 ns of the simulations.

The data is presented for the systems with DNA and polymers **(a)** PEGs-R1, **(b)** PEGs-R2, **(c)** PEGs-R3, **(d)** PEGl-R1, **(e)** PEGl-R2, and **(f)** PEGl-R3. The two curves in each plot represents the two initial polymer configurations, extended (blue) and shielded (red).

To identify the tail Os that form close contacts with the head group, the first two RDF peaks are compared among the studied systems. For the polymers with short tail, both in the systems with R1 and R3, the first two RDF peaks are located at ~4.5 Å and 5.25 Å, respectively. In the systems with R2, however, these two peaks are located at closer distances, ~3 Å and 4.25 Å, respectively. The same pattern can be seen among the polymers with long tail. Another interesting observation from Figure 7.13 is the significant increase in peak heights in the systems with R2, especially in the polymers with short tail. This indicates more probable presence of tail O around head N, thus higher intrachain associations in the R2 polymers.

The existence of strong short range intramolecular interactions in R2 systems made us further investigate the individual tail Os that are responsible of the intrachain associations. In Figure 7.14, we plot the percentage of time during which the tail Os are in close contact (within 4 Å) with head group Ns in the systems comprising the R2 head group. In both short and long tail polymers, the tail O closest to the head group – O14 in the polymers with short tail and O25 in the polymers with long tail (numbering of the tail Os can be found in Figure 7.3a) – is in close contact with at least one head group N at all times during the final 50 ns of the simulations. Previous analysis has shown that N1 of the head group is making a permanent contact with the tail within the last 50 ns period (Figure 7.12b), indicating that the H-bond interaction of the N1 – O14/ O25 pair is mainly responsible of the intrachain associations seen in R2 systems. Another observation from Figure 7.14 is that the length of the tail group determines the pattern of the intrachain associations. In both short and long tail bearing systems, the tail Os closest to the head group R2 makes the strongest contacts. The strength of this association is weakened as we move farther away from the head group in the long tail polymers; however, in the short tail systems the middle region of the tail displays elevated levels of interactions.

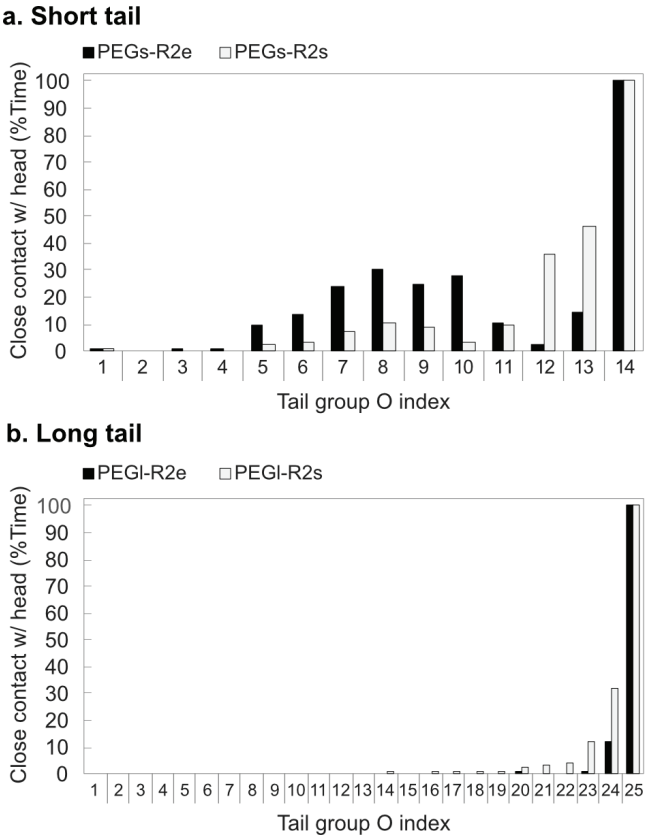

Figure 7.14. Percentage of time in which polymer tail group Os are in close contact with head Ns in the final 50 ns of the simulations.
The data is presented for the systems with DNA, and the polymers bearing the R2 head groups with **(a)** short, and **(b)** long tail. The numbering of the tail group Os is given in Figure 7.3a. O1 represents the farthest O in the tail, whereas O14 / O25 is the closest O to the head group.

7.5. Discussion

Figure 7.15 shows the proposed configurations of the polymer tail around the head group R2 in explicit water. The association between the head and tail groups induces intramolecular collapse of the polymer chain; and the degree of collapse is dependent on the length of the polymer tail; i.e., intrachain associations between the head and tail of polymer chains is higher in the short tail polymers. There exists a permanent contact between the protonated N, N1, of the R2 head group and the closest tail Os, O14/ O25, which creates a local "lock" and impedes N1's ability

to interact with the DNA. This interaction stands for an internal O···H-N H-bond between the O14/ O25 of the tail -OH and H-N1 of the head group. The distance between the O14/ O25 and H-N1 is 2.9 – 3.3 Å on average (over the final 50 ns of the simulations, depicted in Figure 7.16b), allowing for such a connection to be formed. Although this distance falls within the broad range category for bond length of normal/weak H-bonds, presence of cations in the H-bonds may increase their strength [86]. Due to the cationic charge of the tertiary amine, the -OH is proposed to act as the proton acceptor in this interaction, and H-N1 serves as the donor. It is known that -OH groups tend to act as H-bonding donors [87], however it is possible for them to serve as proton acceptors when faced with proton donors [88, 89]. This intramolecular H-bond interaction is absent in the systems containing other head groups, R1 and R3. The distance between the O14/ O25 and N1 ranges from 4.9 to 5.7 Å on average (based on final 50 ns, depicted in Figure 7.16a, c) in R1 and R3 systems, which falls beyond the 3 – 4 Å cut-off for an H-bond to form between a donor-acceptor pair. The $–CH_2$-$CH_2–$ spacer preceding the first tertiary amine of the head groups R1 and R3 places the N1 farther away from O14/ O25, thus eliminates the head-tail associations.

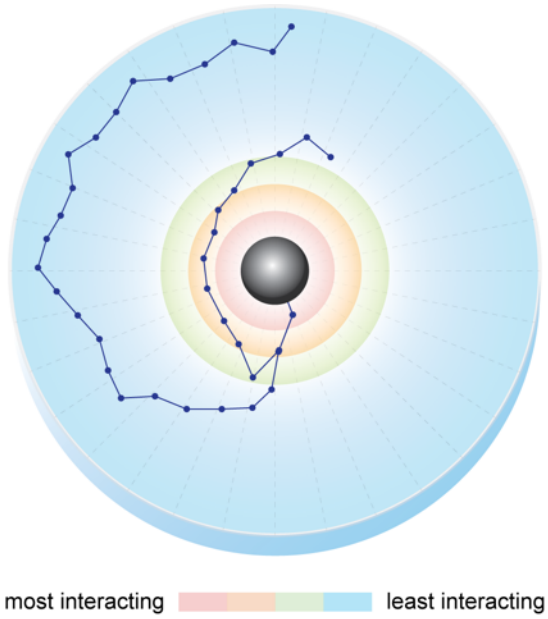

Figure 7.15. Proposed conformations polymer tails around the head group R2 in explicit water.
The R2 head group is represented as a grey sphere, and the tail groups are shown with dark blue lines. The circle markers in the tail groups represent the Os. The surroundings of the R2 head group is divided into four zones, where the innermost layer (light red) shows the most interacting region of the polymer tail, and the outermost layer (light blue) shows the no interaction zone.

It is evident that the polymer intramolecular interactions and intermolecular attractive forces are the two competing forces in polymer-DNA binding; and in the R2 bearing systems, the intrachain associations dominates the latter. This results in a significant decrease in DNA binding performance of the polymers, leading to their separation from the DNA. The inherent assumption in polymeric structures employed to arrest thrombosis is that polymers with strong DNA binding capability minimize blood clotting events. Thus, our simulations can give insights into the antithrombotic activity of the polymers. The R2 head group simulated in this chapter is identical to the R group explored with *in vitro* and *in vivo* experiments by Travers *et al.* [69], where a number of identical R groups are grafted to a dendritic polymer core. Travers and coworkers reported the requirement of at least 5 or more R groups within the UHRA for an

efficient inhibition of thrombin – polyP binding. Moreover, they observed UHRAs possessing lower cationic charge (7 R groups) being less effective than their higher charge counterparts (11 R groups) in terms of their *in vivo* antithrombotic activity, indicating that cationic charge of the polymers is associated with their antithrombotic activity to some extent. Our simulations revealed that polymers interact with DNA mainly through their charged groups, and increasing the number of protonated tertiary amines in the head group strengthens polymer-DNA binding. We articulate that this observation from our simulations correlates well with the reported experimental outcomes, and suggests that stronger electrostatic attraction between polymer and DNA may account for enhanced antithrombotic activity of the polymer.

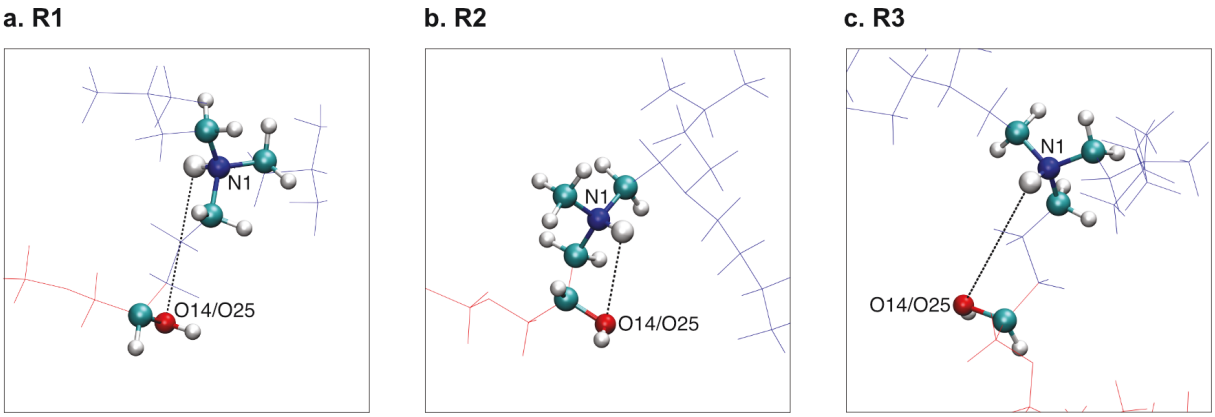

Figure 7.16. The O···H-N H-bond that could form between the acceptor O14/ O25 of the tail and donor H-N1 of the head groups.
Representation for the systems with **(a)** R1, **(b)** R2, and **(c)** R3. The -OH group of the tail and the tertiary amine of the head group comprising N1 are shown as spheres, while the remainder of the tail and head are shown as red and blue lines, respectively. The color coding of the sphere representation of the atoms is as follows: cyan, C; red, O; blue, N; white, H.

What remains to be explored (from MD simulation perspective) is the behavior of the R2 head group when grafted to a dendritic polymer core shielded with PEG chains, as in the UHRA compounds. The binding of polyPs or NAs with R2-containing polymers is expected to differ

when R2 is connected to a single PEG chain vs. a more rigid and bulky dendritic structure. From isothermal titration calorimetry experiments, Shenoi *et al.* reported that dendritic UHRAs exhibit a few orders of magnitude higher binding affinity to UFH than that of the methoxy PEG-R chain [70]. When R2 is attached to a dendritic core, the "locking" of the head group via the intrachain associations could still take place if the short distance between tail O and protonated tertiary amine of the head group is preserved. However, this interaction may not dominate the attractive forces to polyP/NA anymore, as UHRA structures bear multiple R groups ranging from 1 to 33 [69, 70] which might be sufficient to drive polymer-DNA binding, as opposed to only one R in the structures simulated in this chapter. It will be useful to design UHRA like structures containing different R groups varying in size and cationic charge, and test their polyP/NA binding performance and antithrombotic activity for better comparison, which cannot be predicted from the MD simulations described here.

7.6. Conclusions

In this chapter, we performed all-atom MD simulations to explore DNA duplex binding of polymers bearing three different cationic head groups with different tail lengths, and two distinct initial configurations. We found that polymers bind to DNA mainly through interactions of the cationic polymer head group with DNA backbone phosphate Os, and the contribution of the polymer tail to DNA binding was negligible. Increasing the number of protonated tertiary amine groups of the head group increased the interactions with DNA. When the number of tertiary amine groups was increased while keeping the same cationic charge (partially protonated system), binding to DNA was decreased disproportionately. Further analysis of this system has shown significantly higher levels of polymer intrachain associations, which dominated polymer-DNA intermolecular attractions in this case, resulted in very poor binding to or separation from

DNA. Other polymers exhibited little to no intramolecular interactions within the polymers. Such difference was attributed to the absence of a $–CH_2-CH_2–$ spacer in the partially protonated system, resulting in a local conformational constraint that positions the polymer tail in the proximity of the head group. Our simulations provided insights into the structural features of the polymers needed for better DNA binding performance, and should facilitate the design of new head group architectures to arrest thrombosis.

7.7. Acknowledgements

Compute Canada and WestGrid are gratefully acknowledged for providing the computing resources and technical support. This work is funded by Natural Sciences and Engineering Research Council of Canada (NSERC), NSERC Collaborative Research and Training Experience Program for Regenerative Medicine (NCPRM), Canadian Institutes of Health Research (CIHR), Alberta Innovates Technology Futures (AITF), and Canada Foundation for Innovation (CFI). This project has been carried out in collaboration with Dr. Jayachandran N. Kizhakkedathu (Department of Chemistry, Center for Blood Research and Department of Pathology and Laboratory Medicine, University of British Columbia).

7.8. References

1. Rickles FR & Edwards RL (1983) Activation of Blood coagulation in Cancer: Trousseau's Syndrome Revisited. *Blood* 62(1):14-31.
2. Francis JL, Biggerstaff J, & Amirkhosravi A (1998) Hemostasis and Malignancy. *Semin Thromb. Hemost.* 24(2):93-109.
3. Kvolik S, Jukic M, Matijevic M, Marjanovic K, & Glavas-Obrovac L (2010) An Overview of Coagulation Disorders in Cancer Patients. *Surg. Oncol.* 19(1):e33-46.
4. Anderson JA & Weitz JI (2013) Chapter 142: Hypercoagulable States, Part XII: Hemostasis and Thrombosis. *Hematology: Basic Principles and Practice*, eds Hoffman

R, Benz Jr. EJ, Silberstein LE, Heslop H, Weitz JI, & Anastasi J (Elsevier Saunders Philadelphia, United States), 6th Ed., pp 2013-2024.

5. Cronin-Fenton DP, Sondergaard F, Pedersen LA, Fryzek JP, Cetin K, Acquavella J, Baron JA, & Sorensen HT (2010) Hospitalisation for Venous Thromboembolism in Cancer Patients and the General Population: A Population-based Cohort Study in Denmark, 1997-2006. *Br. J. Cancer* 103(7):947-953.

6. Walker AJ, Card TR, West J, Crooks C, & Grainge MJ (2013) Incidence of Venous Thromboembolism in Patients with Cancer - A Cohort Study Using Linked United Kingdom Databases. *Eur. J. Cancer* 49(6):1404-1413.

7. Horsted F, West J, & Grainge MJ (2012) Risk of Venous Thromboembolism in Patients with Cancer: A Systematic Review and Meta-analysis. *PLoS Med* 9(7):e1001275.

8. Timp JF, Braekkan SK, Versteeg HH, & Cannegieter SC (2013) Epidemiology of Cancer-associated Venous Thrombosis. *Blood* 122(10):1712-1723.

9. Heit JA (2003) Risk Factors for Venous Thromboembolism. *Clin. Chest. Med.* 24(1):1-12.

10. Prandoni P, Lensing AW, Piccioli A, Bernardi E, Simioni P, Girolami B, Marchiori A, Sabbion P, Prins MH, Noventa F, & Girolami A (2002) Recurrent Venous Thromboembolism and Bleeding Complications During Anticoagulant Treatment in Patients with Cancer and Venous Thrombosis. *Blood* 100(10):3484-3488.

11. Schafer AI, Levine MN, Konkle BA, & Kearon C (2003) Thrombotic Disorders: Diagnosis and Treatment. *Hematology Am. Soc. Hematol. Educ. Program*:520-539.

12. Geddings JE & Mackman N (2014) New Players in Haemostasis and Thrombosis. *Thromb. Haemost.* 111(4):570-574.

13. Van Dam-Mieras MCE & Muller AD (1986) Blood Coagulation as A Part of the Haemostatic System. *New Compherensive Biochemistry,* Blood Coagulation, eds Neuberger A & Van Deenen LLM (Elsevier Science Publisher B. V. (Biomedical Division)), Vol 13, pp 1-13.

14. Armstrong AW & Golan DE (2008) Chapter 22: Pharmacology of Hemostasis and Thrombosis. *Principles of Pharmacology: The Pathophysiologic Basis of Drug Therapy*, eds Golan DE, Tashjian J, A. H. , Armstrong EJ, & Armstrong AW (Lippincott Williams & Wilkins, U. S. A.), 2nd Ed., pp 387-416.

15. Gawaz M (2001) Chapter 1: Physiology of Hemostasis. *Blood Platelets: Physiology, Pathophysiology, Membrane Receptors, Antiplatelet Principles, and Therapy for Atherothrombotic Diseases* (Thieme, Stuttgart, New York), pp 1-3.

16. Smith SA, Travers RJ, & Morrissey JH (2015) How It All Starts: Initiation of the Clotting Cascade. *Crit. Rev. Biochem. Mol. Biol.* 50(4):326-336.

17. Ondrush J & Junker C (2007) Disseminated Intravascular Coagulation. *Trauma: Critical Care*, eds Wilson WC, Grande CM, & Hoyt DB (CRC Press), pp 1039-1055.

18. Davie EW, Fujikawa K, & Kisiel W (1991) The Coagulation Cascade: Initiation, Maintenance, and Regulation. *Biochemistry* 30(43):10363-10370.

19. Bhagavan NV & Ha C-E (2015) Chapter 34: Biochemistry of Hemostasis. *Essentials of Medical Biochemistry with Clinical Cases* (Academic Press) 2nd Ed., pp 637-660.

20. Heimark RL, Kurachi K, Fujikawa K, & Davie EW (1980) Surface Activation of Blood Coagulation, Fibrinolysis and Kinin Formation. *Nature* 286(5772):456-460.

21. Moore GW, Knight G, & Blann AD (2016) Chapter 14: Bleeding Disorders and Their Laboratory Investigation. *Haematology (Fundamentals of Biomedical Science)* (Oxford University Press) 2nd Ed., pp 461-506.

22. Burger D, Schleuning WD, & Schapira M (1986) Human Plasma Prekallikrein. Immunoaffinity Purification and Activation to Alpha- and Beta-kallikrein. *J. Biol. Chem.* 261(1):324-327.

23. Schmaier AH (2012) Overview of Hemostasis. *Concise Guide to Hematology*, eds Schmaier AH & Lazarus HM (Wiley-Blackwell), pp 91-102.

24. Muller F, Mutch NJ, Schenk WA, Smith SA, Esterl L, Spronk HM, Schmidbauer S, Gahl WA, Morrissey JH, & Renne T (2009) Platelet Polyphosphates are Proinflammatory and Procoagulant Mediators In Vivo. *Cell* 139(6):1143-1156.

25. Danese E, Montagnana M, Fava C, & Guidi GC (2014) Circulating Nucleic Acids and Hemostasis: Biological Basis Behind Their Relationship and Technical Issues in Assessment. *Semin. Thromb. Hemost.* 40(7):766-773.

26. Kannemeier C, Shibamiya A, Nakazawa F, Trusheim H, Ruppert C, Markart P, Song Y, Tzima E, Kennerknecht E, Niepmann M, von Bruehl ML, Sedding D, Massberg S, Gunther A, Engelmann B, & Preissner KT (2007) Extracellular RNA Constitutes a Natural Procoagulant Cofactor in Blood Coagulation. *Proc. Natl. Acad. Sci. U.S.A.* 104(15):6388-6393.

27. DeSancho MT & Rand JH (2003) Physiology of Normal Hemostasis. *Holland-Frei Cancer Medicine*, eds Kufe DW, Pollock RE, Weichselbaum RR, Bast Jr. RC, & Gansler TS (BC Decker Inc., Hamilton, Ontario, Canada), 6th Ed., Vol 2.

28. Brandt JT (2002) Overview of Hemostasis. *Clinical Laboratory Medicine*, ed McClatchey KD (Lippincott Williams & Wilkins), 2nd Ed, pp 987-1009.

29. Rodak BF, Fritsma GA, & Doig K (2007) Part IX: Hemostasis and Thrombosis, Chapter 40: Normal Hemostasis and Coagulation. *Hematology: Clinical Principles and Applications* (Saunders) 3rd Ed., pp 571-587.

30. Matthey F (2016) Anticoagulation and Transfusion. *Oxford Desk Reference: Acute Medicine*, eds Leach R, Bell D, & Moore K (Oxford University Press), pp 532-558.

31. Fareed J & Iqbal O (2016) Physiology of Hemostasis. *Anticoagulation and Hemostasis in Neurosurgery*, ed Loftus CM, (Springer International Publishing, Switzerland), pp 3-16.

32. Hallett JW, Brewster DC, & Rasmussen TE (2001) Chapter 25:Coagulation Disorders. *Handbook of Patient Care in Vascular Diseases* (Lippincott Williams & Wilkins) 4th Ed., pp 295-300.

33. Palta S, Saroa R, & Palta A (2014) Overview of the Coagulation System. *Indian J. Anaesth.* 58(5):515-523.

34. Rogers HJ, Bakdash S, Nakashima MO, & Kottke-Marchant K (2014) Laboratory Analysis of Coagulation. *The Coagulation Consult: A Case-Based Guide*, eds Lichtin A & Bartholomew J (Springer), pp 1-38.

35. Rosendaal FR (2009) Chapter 1: Causes of Venous Thrombosis. *Deep Vein Thrombosis and Pulmonary Embolism*, eds Van Beek EJR, Buller HR, & Oudkerk M (Wiley-Blackwell), pp 3-26.

36. Marlar RA (2003) The Hypercoagulable State. *Hematology/Oncology Secrets*, eds Wood ME & Philips GK (Hanley & Belfus), 3rd Ed, pp 89-95.

37. Furie B & Furie BC (2006) Cancer-associated Thrombosis. *Blood Cells Mol. Dis.* 36(2):177-181.

38. Hisada Y, Geddings JE, Ay C, & Mackman N (2015) Venous Thrombosis and Cancer: From Mouse Models to Clinical Trials. *J. Thromb. Haemost.* 13(8):1372-1382.

39. Gordon SG & Cross BA (1981) A Factor X-Activating Cysteine Protease from Malignant Tissue. *J. Clin. Invest.* 67(6):1665-1671.

40. Pieno GF, Brain MC, Gallus AS, Hirsh J, Hatton MWC, & Regoeczi E (1974) Tumors, Mucus Production, and Hypercoagulability. *Ann. N. Y. Acad. Sci.* 230:262-270.

41. Bick RL (2003) Cancer-associated Thrombosis. *N. Engl. J. Med.* 349(2):109-111.

42. Noble S & Pasi J (2010) Epidemiology and Pathophysiology of Cancer-associated Thrombosis. *Br. J. Cancer* 102 Suppl 1:S2-9.

43. Leon SA, Shapiro B, Sklaroff DM, & Yaros MJ (1977) Free DNA in the Serum of Cancer Patients and the Effect of Therapy. *Cancer Res.* 37(3):646-650.

44. Schwarzenbach H, Hoon DS, & Pantel K (2011) Cell-free Nucleic Acids as Biomarkers in Cancer Patients. *Nat. Rev. Cancer* 11(6):426-437.

45. Shapiro B, Chakrabarty M, Cohn EM, & Leon SA (1983) Determination of Circulating DNA Levels in Patients with Benign or Malignant Gastrointestinal Disease. *Cancer* 51(11):2116-2120.

46. Kopreski MS, Benko FA, Kwak LW, & Gocke CD (1999) Detection of Tumor Messenger RNA in the Serum of Patients with Malignant Melanoma. *Clin. Cancer Res.* 5(8):1961-1965.

47. Ng EK, Tsui NB, Lam NY, Chiu RW, Yu SC, Wong SC, Lo ES, Rainer TH, Johnson PJ, & Lo YM (2002) Presence of Filterable and Nonfilterable mRNA in the Plasma of Cancer Patients and Healthy Individuals. *Clin. Chem.* 48(8):1212-1217.

48. Swystun LL, Mukherjee S, & Liaw PC (2011) Breast Cancer Chemotherapy Induces the Release of Cell-free DNA, a Novel Procoagulant Stimulus. *J. Thromb. Haemost.* 9(11):2313-2321.

49. Amulic B & Hayes G (2011) Neutrophil Extracellular Traps. *Curr. Biol.* 21(9):R297-298.

50. Renne T, Schmaier AH, Nickel KF, Blomback M, & Maas C (2012) In Vivo Roles of Factor XII. *Blood* 120(22):4296-4303.

51. Gansler J, Jaax M, Leiting S, Appel B, Greinacher A, Fischer S, & Preissner KT (2012) Structural Requirements for the Procoagulant Activity of Nucleic Acids. *PLoS One* 7(11):e50399.

52. Ruiz FA, Lea CR, Oldfield E, & Docampo R (2004) Human Platelet Dense Granules Contain Polyphosphate and are Similar to Acidocalcisomes of Bacteria and Unicellular Eukaryotes. *J. Biol. Chem.* 279(43):44250-44257.

53. Smith SA, Choi SH, Collins JN, Travers RJ, Cooley BC, & Morrissey JH (2012) Inhibition of Polyphosphate as a Novel Strategy for Preventing Thrombosis and Inflammation. *Blood* 120(26):5103-5110.

54. Smith SA, Choi SH, Davis-Harrison R, Huyck J, Boettcher J, Rienstra CM, & Morrissey JH (2010) Polyphosphate Exerts Differential Effects on Blood Clotting, Depending on Polymer Size. *Blood* 116(20):4353-4359.

55. Smith SA, Mutch NJ, Baskar D, Rohloff P, Docampo R, & Morrissey JH (2006) Polyphosphate Modulates Blood Coagulation and Fibrinolysis. *Proc. Natl. Acad. Sci. U.S.A.* 103(4):903-908.

56. Choi SH, Smith SA, & Morrissey JH (2011) Polyphosphate is a Cofactor for the Activation of Factor XI by Thrombin. *Blood* 118(26):6963-6970.

57. Smith SA & Morrissey JH (2008) Polyphosphate Enhances Fibrin Clot Structure. *Blood* 112(7):2810-2816.

58. Nickel KF, Ronquist G, Langer F, Labberton L, Fuchs TA, Bokemeyer C, Sauter G, Graefen M, Mackman N, Stavrou EX, Ronquist G, & Renne T (2015) The Polyphosphate-factor XII Pathway Drives Coagulation in Prostate Cancer-associated Thrombosis. *Blood* 126(11):1379-1389.

59. Aalberts M, Stout TA, & Stoorvogel W (2014) Prostasomes: Extracellular Vesicles from the Prostate. *Reproduction* 147(1):R1-14.

60. Lee AY & Peterson EA (2013) Treatment of Cancer-associated Thrombosis. *Blood* 122(14):2310-2317.

61. Weitz JI (2013) Antithrombotic Drugs. *Hematology: Basic Principles and Practice*, eds Hoffman R, Benz Jr. EJ, Silberstein LE, Heslop H, Weitz JI, & Anastasi J (Elsevier Saunders), 6th Ed, pp 2102-2119.

62. Linhardt RJ & Gunay NS (1999) Production and Chemical Processing of Low Molecular Weight Heparins. *Semin. Thromb. Hemost.* 25 Suppl 3:5-16.

63. Schulman S, Zondag M, Linkins L, Pasca S, Cheung YW, de Sancho M, Gallus A, Lecumberri R, Molnar S, Ageno W, Le Gal G, Falanga A, Hulegardh E, Ranta S, Kamphuisen P, Debourdeau P, Rigamonti V, Ortel TL, & Lee A (2015) Recurrent Venous Thromboembolism in Anticoagulated Patients with Cancer: Management and Short-term Prognosis. *J. Thromb. Haemost.* 13(6):1010-1018.

64. Renne T, Pozgajova M, Gruner S, Schuh K, Pauer HU, Burfeind P, Gailani D, & Nieswandt B (2005) Defective Thrombus Formation in Mice Lacking Coagulation Factor XII. *J. Exp. Med.* 202(2):271-281.

65. Cheng Q, Tucker EI, Pine MS, Sisler I, Matafonov A, Sun MF, White-Adams TC, Smith SA, Hanson SR, McCarty OJ, Renne T, Gruber A, & Gailani D (2010) A Role for Factor XIIa-mediated Factor XI Activation in Thrombus Formation In Vivo. *Blood* 116(19):3981-3989.

66. Kleinschnitz C, Stoll G, Bendszus M, Schuh K, Pauer HU, Burfeind P, Renne C, Gailani D, Nieswandt B, & Renne T (2006) Targeting Coagulation Factor XII Provides Protection from Pathological Thrombosis in Cerebral Ischemia Without Interfering with Hemostasis. *J. Exp. Med.* 203(3):513-518.

67. Matafonov A, Leung PY, Gailani AE, Grach SL, Puy C, Cheng Q, Sun MF, McCarty OJ, Tucker EI, Kataoka H, Renne T, Morrissey JH, Gruber A, & Gailani D (2014) Factor XII Inhibition Reduces Thrombus Formation in a Primate Thrombosis Model. *Blood* 123(11):1739-1746.

68. Jain S, Pitoc GA, Holl EK, Zhang Y, Borst L, Leong KW, Lee J, & Sullenger BA (2012) Nucleic Acid Scavengers Inhibit Thrombosis Without Increasing Bleeding. *Proc. Natl. Acad. Sci. U.S.A.* 109(32):12938-12943.

69. Travers RJ, Shenoi RA, Kalathottukaren MT, Kizhakkedathu JN, & Morrissey JH (2014) Nontoxic Polyphosphate Inhibitors Reduce Thrombosis While Sparing Hemostasis. *Blood* 124(22):3183-3190.

70. Shenoi RA, Kalathottukaren MT, Travers RJ, Lai BF, Creagh AL, Lange D, Yu K, Weinhart M, Chew BH, Du C, Brooks DE, Carter CJ, Morrissey JH, Haynes CA, & Kizhakkedathu JN (2014) Affinity-based Design of a Synthetic Universal Reversal Agent for Heparin Anticoagulants. *Sci. Transl. Med.* 6(260):260ra150.

71. Sun C, Tang T, Uludag H, & Cuervo JE (2011) Molecular Dynamics Simulations of DNA/PEI Complexes: Effect of PEI Branching and Protonation State. *Biophys. J.* 100(11):2754-2763.

72. Vanommeslaeghe K, Hatcher E, Acharya C, Kundu S, Zhong S, Shim J, Darian E, Guvench O, Lopes P, Vorobyov I, & Mackerell AD, Jr. (2010) CHARMM General Force Field: A Force Field for Drug-like Molecules Compatible with the CHARMM All-atom Additive Biological Force Fields. *J. Comput. Chem.* 31(4):671-690.

73. Sun C, Tang T, & Uludag H (2011) Molecular Dynamics Simulations of PEI Mediated DNA Aggregation. *Biomacromolecules* 12(10):3698-3707.

74. Sun C, Tang T, & Uludag H (2012) Molecular Dynamics Simulations for Complexation of DNA with 2 kDa PEI Reveal Profound Effect of PEI Architecture on Complexation. *J. Phys. Chem. B* 116(8):2405-2413.

75. Hart K, Foloppe N, Baker CM, Denning EJ, Nilsson L, & Mackerell AD, Jr. (2012) Optimization of the CHARMM Additive Force Field for DNA: Improved Treatment of the BI/BII Conformational Equilibrium. *J Chem Theory Comput* 8(1):348-362.

76. Phillips JC, Braun R, Wang W, Gumbart J, Tajkhorshid E, Villa E, Chipot C, Skeel RD, Kale L, & Schulten K (2005) Scalable Molecular Dynamics with NAMD. *J. Comput. Chem.* 26(16):1781-1802.

77. Darden T, York D, & Pedersen L (1993) Particle Mesh Ewald - an N.Log(N) Method for Ewald Sums in Large Systems. *J. Chem. Phys.* 98(12):10089-10092.

78. Ryckaert JP, Ciccotti G, & Berendsen HJC (1977) Numerical-Integration of Cartesian Equations of Motion of a System with Constraints - Molecular-Dynamics of N-Alkanes. *J. Comput. Phys.* 23(3):327-341.

79. Humphrey W, Dalke A, & Schulten K (1996) VMD: Visual Molecular Dynamics. *J. Mol. Graph.* 14(1):33-38, 27-38.

80. Korolev N, Lyubartsev AP, Nordenskiold L, & Laaksonen A (2001) Spermine: An "Invisible" Component in the Crystals of B-DNA. A Grand Canonical Monte Carlo and Molecular Dynamics Simulation Study. *J. Mol. Biol.* 308(5):907-917.

81. Korolev N, Lyubartsev AP, Laaksonen A, & Nordenskiold L (2002) On the Competition Between Water, Sodium Ions, and Spermine in Binding to DNA: A Molecular Dynamics Computer Simulation Study. *Biophys. J.* 82(6):2860-2875.

82. Korolev N, Lyubartsev AP, Laaksonen A, & Nordenskiold L (2003) A Molecular Dynamics Simulation Study of Oriented DNA with Polyamine and Sodium Counterions: Diffusion and Averaged Binding of Water and Cations. *Nucleic Acids Res.* 31(20):5971-5981.

83. Korolev N, Lyubartsev AP, Laaksonen A, & Nordenskiold L (2004) A Molecular Dynamics Simulation Study of Polyamine- and Sodium-DNA. Interplay Between Polyamine Binding and DNA Structure. *Eur. Biophys. J.* 33(8):671-682.

84. Korolev N, Lyubartsev AP, Laaksonen A, & Nordenskiold L (2004) Molecular Dynamics Simulation Study of Oriented Polyamine- and Na-DNA: Sequence Specific Interactions and Effects on DNA Structure. *Biopolymers* 73(5):542-555.

85. Ziebarth J & Wang Y (2009) Molecular Dynamics Simulations of DNA-Polycation Complex Formation. *Biophys. J.* 97(7):1971-1983.

86. Jeffrey GA & Saenger W (1994) Chapter 2: Definitions and Concepts. *Hydrogen Bonding in Biological Structures* (Springer-Verlag, Heidelberg, Germany), pp 15-48.

87. Baker EN & Hubbard RE (1984) Hydrogen Bonding in Globular Proteins. *Prog. Biophys. Mol. Biol.* 44(2):97-179.

88. Takeuchi H, Watanabe N, Satoh Y, & Harada I (1989) Effects of Hydrogen Bonding on the Tyrosine Raman Band in the 1300-1150 cm-1 Region. *J.Raman Spectrosc.* 20:233-237.

89. Bohm HJ (1992) LUDI: Rule-based Automatic Design of New Substituents for Enzyme Inhibitor Leads. *J. Comput. Aided Mol. Des.* 6(6):593-606.

8. Overall Conclusions, General Discussion and Future Perspectives[X]

[X] Versions of sections of this chapter have been published. Adapted from Meneksedag-Erol D, Tang T, & Uludağ H (2014) Molecular Modeling of Polynucleotide Complexes. *Biomaterials* 35: 7068-7076, Copyright (2014), with permission from Elsevier.

[X] Versions of sections of this chapter have been published. Adapted with permission from Meneksedag-Erol D, Tang T, & Uludağ H (2015) Probing the Effect of miRNA on siRNA−PEI Polyplexes. *J. Phys. Chem. B* 119: 5475−5486. Copyright (2015) American Chemical Society.

8.1. Overall Conclusions

This dissertation explored polynucleotide binding polymers in therapeutic applications with a major emphasis on computational studies, with some experimental studies. I particularly focused on (*i*) polymeric carrier vectors for siRNA delivery, whose overall goal is to silence aberrantly expressed genes in malignancy, and (*ii*) polymeric structures developed to bind to and arrest prothrombotic activity of nucleic acids. The thesis work started with an extensive review of the molecular modeling studies employed in the delivery of polynucleotide nanoparticles in **Chapter 2**. It was evident that the majority of the modeling studies focused on the design of polymeric carriers, and formation of nanoparticulate structures from their complexation with polynucleotides, while very few studies addressed other aspects of the polynucleotide delivery process, such as nanoparticle integrity in the physiological milieu or disassembly of polynucleotide nanoparticles for functional translation. The knowledge gaps identified in this Chapter motivated the studies carried out in Chapters 3-6.

Chapter 3 investigated a functionalized polymeric carrier, a low molecular weight PEI modified by systematic substitution of a small, three-carbon hydrophobe, PrA, in detail, for siRNA delivery into leukemic cells. PrA modification gave rise to a non-monotonic behavior in the cellular uptake and silencing efficacy of the siRNA complexes, where the highest efficacy was attained at low/moderate substitutions. MD simulations revealed a new assembly mechanism involving the migration of the PrA moieties into the core of the complex due to hydrophobic forces, regulating the key features (surface hydrophobicity, cationic charge) of the complexes needed for functional performance.

Chapters 4, **5**, and **6** focused on addressing the need for a better understanding of the role of endogenous biomolecules on siRNA complexes. There exists a vast variety of biomolecules

on the delivery route of the nucleic acid complexes, which can induce changes to the conformational states of the complexes and possibly affect their functional performance. **Chapter 4** explored the effect of miRNA-21, an overly-expressed microRNA in several cancers, on the integrity of siRNA complexes through physicochemical studies and MD simulations. Addition of miRNA onto a preformed siRNA-PEI complex resulted in a ternary siRNA-PEI-miRNA complex structure facilitated by the electrostatic interactions between miRNA and the peripheral PEIs, where miRNA constitutes the outermost layer, making the surface of the ternary complex negatively charged. Gel electrophoresis assays confirmed the absence of siRNA-PEI complex dissociation by miRNA; meanwhile they showed complex disassembly by heparin, a member of the glycosaminoglycan family present in the cell membrane milieu, at comparable concentrations to miRNA. Why complex disassembly was triggered by heparin but not miRNA couldn't be explained in the absence of atomic level details in the physicochemical experiments. Moreover, the roles attributed to heparin in the context of nucleic acid delivery in the experimental literature was found to be controversial; i.e., binding of exogenous heparin to polynucleotide complexes was reported to disintegrate the complexes in line with our observations; on the other hand, endogenous heparins were assigned beneficial roles such as being a facilitator for cellular uptake or decreasing the complex cytotoxicity. To investigate the molecular mechanisms causing these seemly contradictory roles from an all-atom perspective, in **Chapter 5**, we developed a molecular model for heparin, which was then put to use in **Chapter 6** to perform a series of all-atom MD simulations on tripartite systems comprising heparin in the periphery of siRNA-PEI complexes. Complexes underwent a number of different heparin mediated conformational states contingent on the complex and heparin physical properties. In the light of our observations, we proposed a multi-step mechanism for heparin

mediated disassembly of the siRNA complexes. We articulated that the visited conformational states of the siRNA-PEI complexes may translate into different functional outcomes, which can explain the ambiguity in the experiments. For instance, if the complexes remain stable with complex-bound heparin at the outermost layer, their cytotoxicity could be decreased. Premature complex relaxation or disassembly by heparin on the other hand, could have deleterious consequences on siRNA integrity and cell uptake. The results reported in this dissertation on several aspects of polymer-siRNA nanoparticle delivery contributed to our understanding of the key properties of polymeric siRNA delivery systems for enhanced stability and functional performance.

Finally, **Chapter 7** explored a different application of the nucleic acid binding polymers, namely arresting thrombosis. There exists a well-established connection between cancer and thrombosis, and elevated levels of cell free nucleic acids in the circulation of cancer patients is one of the proposed mechanisms behind this relation. Cationic polynucleotide binding polymers, such as PEI, PAMAM dendrimers, which are mainly employed in polynucleotide delivery, are beginning to be explored in this newly emerged area. We investigated polymers bearing cationic tertiary amine groups of different architectures and PEG tails of different lengths. DNA binding performance of the polymers was found to be dependent on the extent of polymer intrachain associations, that is, binding to DNA is impeded if the polymer collapses due to intramolecular interactions between the cationic tertiary amines and the PEG tail. As interest to this line of application of the cationic polymers is rapidly increasing, the presented results are expected to advance our knowledge of polymer structural features needed for safely and effectively inhibiting polynucleotide prothrombotic activity.

8.2. Discussion and Future Directions for Polymer-siRNA Nanoparticle Delivery

Our ultimate goal is to design non-immunogenic, non-toxic polymeric carriers capable of effectively delivering the polynucleotide cargo into cancerous cells with minimal off-target effects. This requires a thorough understanding of the atomistic details of every step of the polynucleotide delivery. Our research has revealed many areas that remain to be explored, which will be discussed in the following sections.

8.2.1. Effect of Physiological Milieu on Polynucleotide Nanoparticles

In vivo administration of siRNA nanoparticles comes with the risk of non-specific interactions with blood proteins and other extracellular milieu components [1]. Upon endocytosis and endosomal escape, cytosolic proteins and oligonucleotides may also interact with nanoparticles, possibly influencing their intracellular disassembly. Determination of the impact of these biomolecules on siRNA complexes will help greatly for developing effective siRNA delivery systems via strategies to modulate the non-specific interactions and stability of the complexes. In **Chapters 4** and **6**, we investigated the role of two individual endogenous molecules, miRNA and heparin, on the conformational states of the siRNA-PEI complexes. In **Chapter 4**, our MD simulations revealed the adsorption of miRNA on the pre-formed siRNA-PEI complexes. Apart from the overexpression of miRNA in tumors [2], elevated levels of miRNA in circulation has been reported in cancer [3-5]; and in fact, it has been proposed as a diagnostic tool for the detection of underlying malignancy [6]. Given the diversity of miRNA structures (i.e., size, charge and structure) and the variation in their expression profile among cancer types (i.e., concentration or relative abundance of miRNA), the stability of siRNA complexes could be assessed with MD simulations and experiments by using specific miRNAs and scenarios.

Moreover, the outermost miRNA layer decreased the ζ-potential of the complexes to negative values, which could markedly influence the cytotoxicity profile of the complexes as well as their cellular uptake efficiency. Previous experimental studies have shown adsorption of serum albumin, a negatively charged serum protein, onto oligonucleotide [7] and polynucleotide [8] complexes, which led to a decrease in cellular association of the complexes [7], revealing that the change in the complex composition may affect the subsequent cellular attachment and uptake stages. Therefore, future *in vitro* experimental studies might be beneficial to determine the effect of miRNA addition on the functional performance of the complexes.

In **Chapter 6**, we demonstrated that physical properties of heparin are critical in determining its mode of action on siRNA-PEI complexes. We focused on two heparin molecules consisting of the same repeating disaccharide (GlcNS(6S) – IdoA2S), and varied the length of the heparin chains by changing the number of repeating disaccharide units. In reality, however, there exists a great structural diversity among heparin and HS sequences; i.e., the predominant disaccharide units as well as the sulfation pattern may greatly vary amongst heparin/HS molecules [9, 10]. Future MD simulations are needed to assess the impact of heparin structural variation on its role on the siRNA complexes. In addition to heparin, other members of the GAG family, CS/DS, KS, and HA, should also be explored. The variation in structure and negative charge among these molecules are expected to greatly affect their influence on siRNA delivery systems. For example, HA, the only non-sulfated GAG, has been reported to bind to the complexes without triggering disassembly, at the concentrations where heparin disintegrates the nucleic acid complexes [11]. In fact, researchers have made use of this feature to coat the nucleic acid nanoparticles with HA to reduce cytotoxicity and increase transfection efficiency [12, 13]. Therefore, it will be beneficial to map out the differences among different GAGs regarding their

effects on the siRNA complexes with further MD simulations, and explore the applicability of the proposed mechanism for heparin-mediated complex disassembly to other GAGs.

8.2.2. Molecular Details of Polynucleotide Nanoparticle Endocytosis

Endocytosis of polynucleotide complexes has been poorly studied at the all-atom level due to time and size limitations of classical MD approaches; there exists a few atomistic simulations on the uptake of individual carriers [14] and naked polynucleotides [15, 16]. A number of CG studies (reviewed in [17], also see [18-21] for examples) provided general aspects on the nanoparticle endocytosis, e.g., size and shape of nanoparticles, ligand density and rigidity, and membrane surface tension for efficient uptake. In addition, to mimic the effect of pH in the endosomal environment, most studies adopted an approach where the protonation state of the polycationic carriers was specified at a given pH and it remained unchanged during the simulation [22-24]. This approach has its intrinsic limitations. For instance, in systems comprising PEI as the nucleic acid carrier, the integrity of the nanoparticle is proposed to be affected by the endosomal pH changes due to proton sponge effect [25], however this phenomenon cannot be captured if the carrier's protonation state is fixed. A more realistic way is to perform constant pH simulations at pH values corresponding to early and late endosomes, while allowing the protonation state of the carriers to vary. However, most methods to keep pH constant require the solvent to be implicitly treated [26-28], which cannot capture carrier-polynucleotide H-bonding upon complexation. There have been improvements to treat solvent explicitly [29-31]; application of these methods can help us gain insights into the endosomal stages of delivery.

Functionalization of the polymeric carriers with appropriate hydrophobic lipid moieties and/or cell-specific ligands usually help to improve the cellular association of the complexes

and reduce off-target effects. Development of all-atom computational models to study the cell membrane attachment and membrane translocation of siRNA-PEI complexes will provide atomistic details of the membrane-complex interactions, and make screening among different functional groups or ligands possible. Steered MD simulations, the MD technique where an external pulling force is exerted on molecules to facilitate transitions between conformational states, could be useful to carry out such a screening among candidates; and best performing systems can be selected for functional *in vitro* and *in vivo* assays. Such a combined approach can help to design delivery systems capable of incorporating enhanced interactions with cell membrane and specific factors affecting cell selectivity and endocytosis for the development of next generation gene therapeutics.

8.2.3. Use of Advanced Simulation Techniques

MD simulations can provide atomic resolution information on the dynamic evolution of the biological systems, which could not be readily attainable with most experimental tools. The ergodic hypothesis, the equality of time average and ensemble average over infinite periods of time, makes it possible to extract time averages from the simulation trajectories. However, classical all-atom MD is bound by size and time scale limitations, which makes it highly challenging to effectively sample the phase space. As a result of poor sampling, the initial placement of the molecules might have potential consequences on the resulting conformational states; i.e. different initial configurations could possibly lead to the sampling of different conformational states. This possibility has been treated with caution throughout the simulations presented in this dissertation. The dependence of the observed phenomena on the initial configuration, if any, is tested where possible. For example, in **Chapter 4**, it was found that the impact of complex initial configuration was negligible in regards to the complex formation as

well as the complex integrity in the presence of miRNA (Section B.2. in Appendix B). In the studies presented in **Chapter 7**, the individual equilibration simulations of the polymers showed the existence of two polymer configurations transient throughout the trajectories: an extended configuration where the polymer is fully solvated, and a shielded configuration where a portion of the polymer tail is wrapped around the polymer head (depicted in Figure 7.5). Therefore, for fair comparison of the polymers' DNA binding performance, both polymer configurations were adopted as input structures to the simulations with DNA. The existence of dynamic equilibrium was also investigated and the average properties were reported over the dynamic equilibrium; e.g. for the formation of supramolecular assemblies from individual siRNAs and PEIs, R_g of the siRNAs was monitored throughout the simulations (e.g. Figure 3.6), and the region where R_g plateaus was taken as the dynamic equilibrium period.

Concerted efforts have been made for the development of algorithms with the purpose of reaching far beyond the existing size and time range such as replica exchange MD [32], accelerated MD [33], metadynamics [34], simulated annealing [35], or coarse graining (CG) [36] to name a few. For example, under practical conditions, nanoparticles can typically grow up to 100 nm in diameter [37], while largest size of our own atomistic simulation was ~12 nm [38]. CG approaches can accommodate larger sizes; improvement in the accuracies of CG models will therefore allow systems with realistic scales to be simulated. Use of advanced MD approaches in conjunction with all-atom studies will better reveal the complete picture of complex processes of supramolecular assemblies. For example, in **Chapter 6**, we were unable to determine the relative thermodynamic stability of the observed conformational states of the siRNA-PEI-heparin tripartite systems, as they were obtained from independent simulations (i.e., multiple systems of different PEI and heparin compositions). Exceeding the time limitations

with advanced approaches will allow to detect transitions between various nanoparticle conformations within one single trajectory, therefore can advance our understanding on which of the states is energetically more favorable than others.

8.3. Discussion and Future Directions for Polymers in Anticoagulant Therapy

Towards the goal of synthesizing non-toxic polymeric structures capable of inhibiting the thrombotic activity of cell free DNAs and devoid of serious hemorrhagic complications, our research has demonstrated the impact of polymer structure in the regulation of its DNA binding performance. The polymer intrachain associations have found to be detrimental for binding to DNA, therefore, spacer groups of different lengths can be placed to eliminate the possible attractions between the head and tail groups. It remains to be explored how the intrachain association will be affected if all the studied polymers comprised the same spacer between the head and tail groups. Our research involved a model system of a single polymer chain (cationic head and PEG tail), while practically, the polymer head groups are grafted into a dendritic core and shielded with PEG chains [39]. It will be useful to simulate the experimentally determined polymer structures, and explore whether the proposed intrachain associations still exist within a more rigid dendritic structure. The polymers can be further investigated with MD simulations to assess their binding to RNA and polyP, other proposed activators of the intrinsic pathway, for determination of the differences among polynucleotides and polyP, if any, in regard to their interactions with the polymers. The line of research assumes that the DNA binding affinity of the polymers will directly influence thrombogenic events, but this remains to be experimentally validated.

8.4. References

1. Whitehead KA, Langer R, & Anderson DG (2009) Knocking Down Barriers: Advances in siRNA Delivery. *Nat. Rev. Drug Discov.* 8(2):129-138.
2. Croce CM (2009) Causes and Consequences of microRNA Dysregulation in Cancer. *Nat. Rev. Genet.* 10(10):704-714.
3. Mitchell PS, Parkin RK, Kroh EM, Fritz BR, Wyman SK, Pogosova-Agadjanyan EL, Peterson A, Noteboom J, O'Briant KC, Allen A, Lin DW, Urban N, Drescher CW, Knudsen BS, Stirewalt DL, Gentleman R, Vessella RL, Nelson PS, Martin DB, & Tewari M (2008) Circulating microRNAs as Stable Blood-based Markers for Cancer Detection. *Proc. Natl. Acad. Sci. U.S.A.* 105(30):10513-10518.
4. Brase JC, Johannes M, Schlomm T, Falth M, Haese A, Steuber T, Beissbarth T, Kuner R, & Sultmann H (2011) Circulating miRNAs are Correlated with Tumor Progression in Prostate Cancer. *Int. J. Cancer* 128(3):608-616.
5. Corcoran C, Friel AM, Duffy MJ, Crown J, & O'Driscoll L (2011) Intracellular and Extracellular microRNAs in Breast Cancer. *Clin. Chem.* 57(1):18-32.
6. Kosaka N, Iguchi H, & Ochiya T (2010) Circulating microRNA in Body Fluid: A New Potential Biomarker for Cancer Diagnosis and Prognosis. *Cancer Sci.* 101(10):2087-2092.
7. Zelphati O, Uyechi LS, Barron LG, & Szoka FC, Jr. (1998) Effect of Serum Components on the Physico-chemical Properties of Cationic Lipid/Oligonucleotide Complexes and on Their Interactions with Cells. *Biochim. Biophys. Acta* 1390(2):119-133.
8. Oupicky D, Konak C, Dash PR, Seymour LW, & Ulbrich K (1999) Effect of Albumin and Polyanion on the Structure of DNA Complexes with Polycation Containing Hydrophilic Nonionic Block. *Bioconjug. Chem.* 10(5):764-772.
9. Esko JD & Lindahl U (2001) Molecular Diversity of Heparan Sulfate. *J. Clin. Invest.* 108(2):169-173.
10. Turnbull J, Powell A, & Guimond S (2001) Heparan Sulfate: Decoding a Dynamic Multifunctional Cell Regulator. *Trends Cell Biol.* 11(2):75-82.
11. Ruponen M, Yla-Herttuala S, & Urtti A (1999) Interactions of Polymeric and Liposomal Gene Delivery Systems with Extracellular Glycosaminoglycans: Physicochemical and Transfection Studies. *Biochim. Biophys. Acta* 1415(2):331-341.
12. Ito T, Iida-Tanaka N, & Koyama Y (2008) Efficient In Vivo Gene Transfection by Stable DNA/PEI Complexes Coated by Hyaluronic Acid. *J. Drug Target.* 16(4):276-281.
13. He Y, Cheng G, Xie L, Nie Y, He B, & Gu Z (2013) Polyethyleneimine/DNA Polyplexes with Reduction-sensitive Hyaluronic Acid Derivatives Shielding for Targeted Gene Delivery. *Biomaterials* 34(4):1235-1245.
14. Choudhury CK, Kumar A, & Roy S (2013) Characterization of Conformation and Interaction of Gene Delivery Vector Polyethylenimine with Phospholipid Bilayer at Different Protonation State. *Biomacromolecules* 14(10):3759-3768.

15. Tarek M (2005) Membrane Electroporation: A Molecular Dynamics Simulation. *Biophys. J.* 88(6):4045-4053.

16. Breton M, Delemotte L, Silve A, Mir LM, & Tarek M (2012) Transport of siRNA through Lipid Membranes Driven by Nanosecond Electric Pulses: An Experimental and Computational Study. *J. Am. Chem. Soc.* 134(34):13938-13941.

17. Beddoes CM, Case CP, & Briscoe WH (2015) Understanding Nanoparticle Cellular Entry: A Physicochemical Perspective. *Adv. Colloid Interface Sci.* 218:48-68.

18. Voulgarakis NK, Rasmussen KO, & Welch PM (2009) Dendrimers as Synthetic Gene Vectors: Cell Membrane Attachment. *J. Chem. Phys.* 130(15):155101.

19. Ding HM & Ma YQ (2013) Design Maps for Cellular Uptake of Gene Nanovectors by Computer Simulation. *Biomaterials* 34(33):8401-8407.

20. Vacha R, Martinez-Veracoechea FJ, & Frenkel D (2011) Receptor-Mediated Endocytosis of Nanoparticles of Various Shapes. *Nano Lett.* 11(12):5391-5395.

21. Ding HM & Ma YQ (2012) Role of Physicochemical Properties of Coating Ligands in Receptor-mediated Endocytosis of Nanoparticles. *Biomaterials* 33(23):5798-5802.

22. Ouyang D, Zhang H, Parekh HS, & Smith SC (2011) The Effect of pH on PAMAM Dendrimer-siRNA Complexation: Endosomal Considerations as Determined by Molecular Dynamics Simulation. *Biophys. Chem.* 158(2-3):126-133.

23. Pavan GM, Posocco P, Tagliabue A, Maly M, Malek A, Danani A, Ragg E, Catapano CV, & Pricl S (2010) PAMAM Dendrimers for siRNA Delivery: Computational and Experimental Insights. *Chemistry* 16(26):7781-7795.

24. Karatasos K, Posocco P, Laurini E, & Pricl S (2012) Poly(amidoamine)-based Dendrimer/siRNA Complexation Studied by Computer Simulations: Effects of pH and Generation on Dendrimer Structure and siRNA Binding. *Macromol. Biosci.* 12(2):225-240.

25. Boussif O, Lezoualc'h F, Zanta MA, Mergny MD, Scherman D, Demeneix B, & Behr JP (1995) A Versatile Vector for Gene and Oligonucleotide Transfer into Cells in Culture and In vivo: Polyethylenimine. *Proc. Natl. Acad. Sci. U.S.A.* 92(16):7297-7301.

26. Khandogin J & Brooks CL (2005) Constant pH Molecular Dynamics with Proton Tautomerism. *Biophys. J.* 89(1):141-157.

27. Baptista AM, Teixeira VH, & Soares CM (2002) Constant-pH Molecular Dynamics Using Stochastic Titration. *J. Chem. Phys.* 117(9):4184-4200.

28. Mongan J, Case DA, & McCammon JA (2004) Constant pH Molecular Dynamics in Generalized Born Implicit Solvent. *J. Comput. Chem.* 25(16):2038-2048.

29. Wallace JA & Shen JK (2011) Continuous Constant pH Molecular Dynamics in Explicit Solvent with pH-Based Replica Exchange. *J. Chem. Theory Comput.* 7(8):2617-2629.

30. Goh GB, Knight JL, & Brooks CL (2012) Constant pH Molecular Dynamics Simulations of Nucleic Acids in Explicit Solvent. *J. Chem. Theory Comput.* 8(1):36-46.

31. Donnini S, Tegeler F, Groenhof G, & Grubmuller H (2011) Constant pH Molecular Dynamics in Explicit Solvent with lambda-Dynamics. *J. Chem. Theory Comput.* 7(6):1962-1978.

32. Sugita Y & Okamoto Y (1999) Replica-exchange Molecular Dynamics Method for Protein Folding. *Chem. Phys. Lett.* 314(1-2):141-151.

33. Hamelberg D, Mongan J, & McCammon JA (2004) Accelerated Molecular Dynamics: A Promising and Efficient Simulation Method for Biomolecules. *J. Chem. Phys.* 120(24):11919-11929.

34. Laio A & Parrinello M (2002) Escaping Free-energy Minima. *Proc. Natl. Acad. Sci. U.S.A.* 99(20):12562-12566.

35. Tsallis C & Stariolo DA (1996) Generalized Simulated Annealing. *Phys. A Stat. Theor. Phys.* 233:395–406.

36. Levitt M (1976) A Simplified Representation of Protein Conformations for Rapid Simulation of Protein Folding. *J. Mol. Biol.* 104(1):59-107.

37. Goula D, Remy JS, Erbacher P, Wasowicz M, Levi G, Abdallah B, & Demeneix BA (1998) Size, Diffusibility and Transfection Performance of Linear PEI/DNA Complexes in the Mouse Central Nervous System. *Gene Ther.* 5(5):712-717.

38. Sun C, Tang T, & Uludag H (2013) A Molecular Dynamics Simulation Study on the Effect of Lipid Substitution on Polyethylenimine Mediated siRNA Complexation. *Biomaterials* 34(11):2822-2833.

39. Travers RJ, Shenoi RA, Kalathottukaren MT, Kizhakkedathu JN, & Morrissey JH (2014) Nontoxic Polyphosphate Inhibitors Reduce Thrombosis While Sparing Hemostasis. *Blood* 124(22):3183-3190.

Unified Bibliography

1.1. Duncan R (2003) The Dawning Era of Polymer Therapeutics. *Nat. Rev. Drug Discov.* 2(5):347-360.

1.2. Duncan R (2006) Polymer Conjugates as Anticancer Nanomedicines. *Nat. Rev. Cancer* 6(9):688-701.

1.3. Lachelt U & Wagner E (2015) Nucleic Acid Therapeutics Using Polyplexes: A Journey of 50 Years (and Beyond). *Chem. Rev.* 115(19):11043-11078.

1.4. Jain S, Pitoc GA, Holl EK, Zhang Y, Borst L, Leong KW, Lee J, & Sullenger BA (2012) Nucleic Acid Scavengers Inhibit Thrombosis Without Increasing Bleeding. *Proc. Natl. Acad. Sci. U.S.A.* 109(32):12938-12943.

1.5. Smith SA, Choi SH, Collins JN, Travers RJ, Cooley BC, & Morrissey JH (2012) Inhibition of Polyphosphate as a Novel Strategy for Preventing Thrombosis and Inflammation. *Blood* 120(26):5103-5110.

1.6. Travers RJ, Shenoi RA, Kalathottukaren MT, Kizhakkedathu JN, & Morrissey JH (2014) Nontoxic Polyphosphate Inhibitors Reduce Thrombosis While Sparing Hemostasis. *Blood* 124(22):3183-3190.

1.7. Renne T, Schmaier AH, Nickel KF, Blomback M, & Maas C (2012) In Vivo Roles of Factor XII. *Blood* 120(22):4296-4303.

1.8. Kannemeier C, Shibamiya A, Nakazawa F, Trusheim H, Ruppert C, Markart P, Song Y, Tzima E, Kennerknecht E, Niepmann M, von Bruehl ML, Sedding D, Massberg S, Gunther A, Engelmann B, & Preissner KT (2007) Extracellular RNA Constitutes a Natural Procoagulant Cofactor in Blood Coagulation. *Proc. Natl. Acad. Sci. U.S.A.* 104(15):6388-6393.

1.9. Demers M, Krause DS, Schatzberg D, Martinod K, Voorhees JR, Fuchs TA, Scadden DT, & Wagner DD (2012) Cancers Predispose Neutrophils to Release Extracellular DNA Traps That Contribute to Cancer-associated Thrombosis. *Proc. Natl. Acad. Sci. U.S.A.* 109(32):13076-13081.

1.10. Leon SA, Shapiro B, Sklaroff DM, & Yaros MJ (1977) Free DNA in the Serum of Cancer Patients and the Effect of Therapy. *Cancer Res.* 37(3):646-650.

1.11. Kopreski MS, Benko FA, Kwak LW, & Gocke CD (1999) Detection of Tumor Messenger RNA in the Serum of Patients with Malignant Melanoma. *Clin. Cancer Res.* 5(8):1961-1965.

1.12. Ng EK, Tsui NB, Lam NY, Chiu RW, Yu SC, Wong SC, Lo ES, Rainer TH, Johnson PJ, & Lo YM (2002) Presence of Filterable and Nonfilterable mRNA in the Plasma of Cancer Patients and Healthy Individuals. *Clin. Chem.* 48(8):1212-1217.

2.1. Fire A, Xu S, Montgomery MK, Kostas SA, Driver SE, & Mello CC (1998) Potent and Specific Genetic Interference by Double-stranded RNA in Caenorhabditis Elegans. *Nature* 391(6669):806-811.

2.2. Guo P, Coban O, Snead NM, Trebley J, Hoeprich S, Guo S, & Shu Y (2010) Engineering RNA for Targeted siRNA Delivery and Medical Application. *Adv. Drug Deliv. Rev.* 62(6):650-666.

2.3. Hillaireau H & Couvreur P (2009) Nanocarriers' Entry into the Cell: Relevance to Drug Delivery. *Cell. Mol. Life. Sci.* 66(17):2873-2896.

2.4. Hsu CY & Uludag H (2012) Cellular Uptake Pathways of Lipid-modified Cationic Polymers in Gene Delivery to Primary Cells. *Biomaterials* 33(31):7834-7848.

2.5. Dominska M & Dykxhoorn DM (2010) Breaking Down the Barriers: siRNA Delivery and Endosome Escape. *J. Cell Sci.* 123(Pt 8):1183-1189.

2.6. Boussif O, Lezoualc'h F, Zanta MA, Mergny MD, Scherman D, Demeneix B, & Behr JP (1995) A Versatile Vector for Gene and Oligonucleotide Transfer into Cells in Culture and In vivo: Polyethylenimine. *Proc. Natl. Acad. Sci. U.S.A.* 92(16):7297-7301.

2.7. Moret I, Esteban Peris J, Guillem VM, Benet M, Revert F, Dasi F, Crespo A, & Alino SF (2001) Stability of PEI-DNA and DOTAP-DNA Complexes: Effect of Alkaline pH, Heparin and Serum. *J. Control. Release* 76(1-2):169-181.

2.8. McCammon JA, Gelin BR, & Karplus M (1977) Dynamics of Folded Proteins. *Nature* 267(5612):585-590.

2.9. Torrie GM & Valleau JP (1977) Nonphysical Sampling Distributions in Monte Carlo Free-energy Estimation: Umbrella Sampling. *J. Comput. Phys.* 23(2):187-199.

2.10. Kumar S, Rosenberg JM, Bouzida D, Swendsen RH, & Kollman PA (1992) The Weighted Histogram Analysis Method for Free-energy Calculations on Biomolecules. I. The Method. *J. Comput. Chem.* 13(8):1011−1021.

2.11. Schlick T (2010) *Molecular Modeling and Simulation: An Interdisciplinary Guide* (Springer, New York, USA), pp 265-298.

2.12. Warshel A & Levitt M (1976) Theoretical Studies of Enzymic Reactions: Dielectric, Electrostatic and Steric Stabilization of the Carbonium Ion in the Reaction of Lysozyme. *J. Mol. Biol.* 103(2):227-249.

2.13. Groenhof G (2013) Chapter 3: Introduction to QM/MM Simulations. *Biomolecular Simulations: Methods and Protocols,* Methods in Molecular Biology, eds Monticelli L & Salonen E (Springer Science Business Media, New York), Vol 924, pp 43-66.

2.14. Takada S (2012) Coarse-grained Molecular Simulations of Large Biomolecules. *Curr. Opin. Struc. Biol.* 22(2):130-137.

2.15. Voth GA (2009) Chapter 1: Introduction. *Coarse-graining of Condensed Phase and Biomolecular Systems*, ed Voth GA (CRC Press/Taylor and Francis Group, Boca Raton).

2.16. Korolev N, Lyubartsev AP, Nordenskiold L, & Laaksonen A (2001) Spermine: An "Invisible" Component in the Crystals of B-DNA. A Grand Canonical Monte Carlo and Molecular Dynamics Simulation Study. *J. Mol. Biol.* 308(5):907-917.

2.17. Korolev N, Lyubartsev AP, Laaksonen A, & Nordenskiold L (2002) On the Competition between Water, Sodium Ions, and Spermine in Binding to DNA: A Molecular Dynamics Computer Simulation Study. *Biophys. J.* 82(6):2860-2875.

2.18. Korolev N, Lyubartsev AP, Laaksonen A, & Nordenskiold L (2003) A Molecular Dynamics Simulation Study of Oriented DNA with Polyamine and Sodium Counterions: Diffusion and Averaged Binding of Water and Cations. *Nucleic Acids Res.* 31(20):5971-5981.

2.19. Korolev N, Lyubartsev AP, Laaksonen A, & Nordenskiold L (2004) A Molecular Dynamics Simulation Study of Polyamine- and Sodium-DNA. Interplay Between Polyamine Binding and DNA Structure. *Eur. Biophys. J.* 33(8):671-682.

2.20. Korolev N, Lyubartsev AP, Laaksonen A, & Nordenskiold L (2004) Molecular Dynamics Simulation Study of Oriented Polyamine- and Na-DNA: Sequence Specific Interactions and Effects on DNA Structure. *Biopolymers* 73(5):542-555.

2.21. Ziebarth J & Wang Y (2009) Molecular Dynamics Simulations of DNA-Polycation Complex Formation. *Biophys. J.* 97(7):1971-1983.

2.22. Sun C, Tang T, Uludag H, & Cuervo JE (2011) Molecular Dynamics Simulations of DNA/PEI Complexes: Effect of PEI Branching and Protonation State. *Biophys. J.* 100(11):2754-2763.

2.23. Sun C, Tang T, & Uludag H (2012) Molecular Dynamics Simulations for Complexation of DNA with 2 kDa PEI Reveal Profound Effect of PEI Architecture on Complexation. *J. Phys. Chem. B.* 116(8):2405-2413.

2.24. Zheng M, Pavan GM, Neeb M, Schaper AK, Danani A, Klebe G, Merkel OM, & Kissel T (2012) Targeting the Blind Spot of Polycationic Nanocarrier-based siRNA Delivery. *ACS Nano* 6(11):9447-9454.

2.25. Bandyopadhyay S, Tarek M, & Klein ML (1999) Molecular Dynamics Study of a Lipid-DNA Complex. *J. Phys. Chem. B.* 103(46):10075-10080.

2.26. Braun CS, Jas GS, Choosakoonkriang S, Koe GS, Smith JG, & Middaugh CR (2003) The Structure of DNA within Cationic Lipid/DNA Complexes. *Biophys. J.* 84(2):1114-1123.

2.27. Ouyang D, Zhang H, Parekh HS, & Smith SC (2011) The Effect of pH on PAMAM Dendrimer-siRNA Complexation: Endosomal Considerations as Determined by Molecular Dynamics Simulation. *Biophys. Chem.* 158(2-3):126-133.

2.28. Pavan GM, Posocco P, Tagliabue A, Maly M, Malek A, Danani A, Ragg E, Catapano CV, & Pricl S (2010) PAMAM Dendrimers for siRNA Delivery: Computational and Experimental Insights. *Chemistry* 16(26):7781-7795.

2.29. Karatasos K, Posocco P, Laurini E, & Pricl S (2012) Poly(amidoamine)-based Dendrimer/siRNA Complexation Studied by Computer Simulations: Effects of pH and Generation on Dendrimer Structure and siRNA Binding. *Macromol. Biosci.* 12(2):225-240.

2.30. Pavan GM, Danani A, Pricl S, & Smith DK (2009) Modeling the Multivalent Recognition between Dendritic Molecules and DNA: Understanding How Ligand "Sacrifice" and Screening Can Enhance Binding. *J. Am. Chem. Soc.* 131(28):9686-9694.

2.31. Nandy B & Maiti PK (2011) DNA Compaction by a Dendrimer. *J. Phys. Chem. B.* 115(2):217-230.

2.32. Mills M, Orr BG, Banaszak Holl MM, & Andricioaei I (2013) Attractive Hydration Forces in DNA-Dendrimer Interactions on the Nanometer Scale. *J. Phys. Chem. B.* 117(4):973-981.

2.33. Pavan GM, Albertazzi L, & Danani A (2010) Ability to Adapt: Different Generations of PAMAM Dendrimers Show Different Behaviors in Binding siRNA. *J. Phys. Chem. B.* 114(8):2667-2675.

2.34. Jensen LB, Mortensen K, Pavan GM, Kasimova MR, Jensen DK, Gadzhyeva V, Nielsen HM, & Foged C (2010) Molecular Characterization of the Interaction between siRNA and PAMAM G7 Dendrimers by SAXS, ITC, and Molecular Dynamics Simulations. *Biomacromolecules* 11(12):3571-3577.

2.35. Jensen LB, Pavan GM, Kasimova MR, Rutherford S, Danani A, Nielsen HM, & Foged C (2011) Elucidating the Molecular Mechanism of PAMAM-siRNA Dendriplex Self-assembly: Effect of Dendrimer Charge Density. *Int. J. Pharm.* 416(2):410-418.

2.36. Pavan GM, Mintzer MA, Simanek EE, Merkel OM, Kissel T, & Danani A (2010) Computational Insights into the Interactions between DNA and siRNA with "Rigid" and "Flexible" Triazine Dendrimers. *Biomacromolecules* 11(3):721-730.

2.37. Maiti PK & Bagchi B (2006) Structure and Dynamics of DNA-Dendrimer Complexation: Role of Counterions, Water, and Base Pair Sequence. *Nano Lett.* 6(11):2478-2485.

2.38. Ouyang D, Zhang H, Herten DP, Parekh HS, & Smith SC (2010) Structure, Dynamics, and Energetics of siRNA-Cationic Vector Complexation: A Molecular Dynamics Study. *J. Phys. Chem. B.* 114(28):9220-9230.

2.39. Vasumathi V & Maiti PK (2010) Complexation of siRNA with Dendrimer: A Molecular Modeling Approach. *Macromolecules* 43:8264–8274.

2.40. Elder RM, Emrick T, & Jayaraman A (2011) Understanding the Effect of Polylysine Architecture on DNA Binding Using Molecular Dynamics Simulations. *Biomacromolecules* 12(11):3870-3879.

2.41. Ouyang D, Zhang H, Parekh HS, & Smith SC (2010) Structure and Dynamics of Multiple Cationic Vectors-siRNA Complexation by All-atomic Molecular Dynamics Simulations. *J. Phys. Chem. B.* 114(28):9231-9237.

2.42. Jones SP, Pavan GM, Danani A, Pricl S, & Smith DK (2010) Quantifying the Effect of Surface Ligands on Dendron-DNA Interactions: Insights into Multivalency through a Combined Experimental and Theoretical Approach. *Chemistry* 16(15):4519-4532.

2.43. Pavan GM, Kostiainen MA, & Danani A (2010) Computational Approach for Understanding the Interactions of UV-degradable Dendrons with DNA and siRNA. *J. Phys. Chem. B.* 114(17):5686-5693.

2.44. Posocco P, Pricl S, Jones S, Barnard A, & Smith DK (2010) Less Is More – Multiscale Modelling of Self-assembling Multivalency and Its Impact on DNA Binding and Gene Delivery. *Chem. Sci.* 1:393–404.

2.45. Stevens MJ (2001) Simple Simulations of DNA Condensation. *Biophys. J.* 80(1):130-139.

2.46. Dias RS, Pais AACC, Miguel MG, & Lindman B (2003) Modeling of DNA Compaction by Polycations. *J. Chem. Phys.* 119:8150-8157.

2.47. Ziebarth J & Wang Y (2010) Coarse-grained Molecular Dynamics Simulations of DNA Condensation by Block Copolymer and Formation of Core-corona Structures. *J. Phys. Chem. B.* 114(19):6225-6232.

2.48. Savelyev A & Papoian GA (2007) Inter-DNA Electrostatics from Explicit Solvent Molecular Dynamics Simulations. *J. Am. Chem. Soc.* 129(19):6060-6061.

2.49. Dai L, Mu Y, Nordenskiold L, & van der Maarel JR (2008) Molecular Dynamics Simulation of Multivalent-ion Mediated Attraction between DNA Molecules. *Phys. Rev. Lett.* 100(11):118301.

2.50. Bagai S, Sun C, & Tang T (2013) Potential of Mean Force of Polyethylenimine-mediated DNA Attraction. *J. Phys. Chem. B.* 117(1):49-56.

2.51. Sun C, Tang T, & Uludag H (2011) Molecular Dynamics Simulations of PEI Mediated DNA Aggregation. *Biomacromolecules* 12(10):3698-3707.

2.52. Sun C, Tang T, & Uludag H (2012) Probing the Effects of Lipid Substitution on Polycation Mediated DNA Aggregation: A Molecular Dynamics Simulations Study. *Biomacromolecules* 13(9):2982-2988.

2.53. Sun C, Tang T, & Uludag H (2013) A Molecular Dynamics Simulation Study on the Effect of Lipid Substitution on Polyethylenimine Mediated siRNA Complexation. *Biomaterials* 34(11):2822-2833.

2.54. Farago O, Gronbech-Jensen N, & Pincus P (2006) Mesoscale Computer Modeling of Lipid-DNA Complexes for Gene Therapy. *Phys. Rev. Lett.* 96(1):018102.

2.55. Farago O & Gronbech-Jensen N (2009) Simulation of Self-assembly of Cationic Lipids and DNA into Structured Complexes. *J. Am. Chem. Soc.* 131(8):2875-2881.

2.56. Voulgarakis NK, Rasmussen KO, & Welch PM (2009) Dendrimers as Synthetic Gene Vectors: Cell Membrane Attachment. *J. Chem. Phys.* 130(15):155101.

2.57. Ding HM & Ma YQ (2013) Design Maps for Cellular Uptake of Gene Nanovectors by Computer Simulation. *Biomaterials* 34(33):8401-8407.

2.58. Dinh AT, Pangarkar C, Theofanous T, & Mitragotri S (2007) Understanding Intracellular Transport Processes Pertinent to Synthetic Gene Delivery via Stochastic Simulations and Sensitivity Analyses. *Biophys. J.* 92(3):831-846.

2.59. Jorge AF, Dias RS, & Pais AA (2012) Enhanced Condensation and Facilitated Release of DNA Using Mixed Cationic Agents: A Combined Experimental and Monte Carlo Study. *Biomacromolecules* 13(10):3151-3161.

3.1. Liu Z, Zhang Z, Zhou C, & Jiao Y (2010) Hydrophobic Modifications of Cationic Polymers for Gene Delivery. *Prog. Polym. Sci.* 35:1144–1162.

3.2. Fire A, Xu S, Montgomery MK, Kostas SA, Driver SE, & Mello CC (1998) Potent and Specific Genetic Interference by Double-stranded RNA in Caenorhabditis Elegans. *Nature* 391(6669):806-811.

3.3. Boussif O, Lezoualc'h F, Zanta MA, Mergny MD, Scherman D, Demeneix B, & Behr JP (1995) A Versatile Vector for Gene and Oligonucleotide Transfer into Cells in Culture and In Vivo: Polyethylenimine. *Proc. Natl. Acad. Sci. U.S.A.* 92(16):7297-7301.

3.4. Demeneix B & Behr JP (2005) Polyethylenimine (PEI). *Adv. Genet.* 53:217-230.

3.5. Aliabadi HM, Landry B, Sun C, Tang T, & Uludag H (2012) Supramolecular Assemblies in Functional siRNA Delivery: Where Do We Stand? *Biomaterials* 33(8):2546-2569.

3.6. Godbey WT, Wu KK, & Mikos AG (1999) Size Matters: Molecular Weight Affects the Efficiency of Poly(ethylenimine) as a Gene Delivery Vehicle. *J. Biomed. Mater. Res.* 45(3):268-275.

3.7. Fischer D, Bieber T, Li Y, Elsasser HP, & Kissel T (1999) A Novel Non-Viral Vector for DNA Delivery Based on Low Molecular Weight, Branched Polyethylenimine: Effect of Molecular Weight on Transfection Efficiency and Cytotoxicity. *Pharm. Res.* 16(8):1273-1279.

3.8. Fischer D, Li Y, Ahlemeyer B, Krieglstein J, & Kissel T (2003) In Vitro Cytotoxicity Testing of Polycations: Influence of Polymer Structure on Cell Viability and Hemolysis. *Biomaterials* 24(7):1121-1131.

3.9. Neamnark A, Suwantong O, Bahadur RK, Hsu CY, Supaphol P, & Uludag H (2009) Aliphatic Lipid Substitution on 2 kDa Polyethylenimine Improves Plasmid Delivery and Transgene Expression. *Mol. Pharmaceutics* 6(6):1798-1815.

3.10. Incani V, Lavasanifar A, & Uludag H (2010) Lipid and Hydrophobic Modification of Cationic Carriers on Route to Superior Gene Vectors. *Soft Matter* 6:2124-2138.

3.11. Han S, Mahato RI, & Kim SW (2001) Water-Soluble Lipopolymer for Gene Delivery. *Bioconjugate Chem.* 12(3):337-345.

3.12. Furgeson DY, Cohen RN, Mahato RI, & Kim SW (2002) Novel Water Insoluble Lipoparticulates for Gene Delivery. *Pharm. Res.* 19(4):382-390.

3.13. Bajaj A, Kondaiah P, & Bhattacharya S (2008) Synthesis and Gene Transfection Efficacies of PEI-Cholesterol-based Lipopolymers. *Bioconjugate Chem.* 19(8):1640-1651.

3.14. Teo PY, Yang C, Hedrick JL, Engler AC, Coady DJ, Ghaem-Maghami S, George AJ, & Yang YY (2013) Hydrophobic Modification of Low Molecular Weight Polyethylenimine for Improved Gene Transfection. *Biomaterials* 34(32):7971-7979.

3.15. Pettersen EF, Goddard TD, Huang CC, Couch GS, Greenblatt DM, Meng EC, & Ferrin TE (2004) UCSF Chimera - A Visualization System for Exploratory Research and Analysis. *J. Comput. Chem.* 25(13):1605-1612.

3.16. Utsuno K & Uludag H (2010) Thermodynamics of Polyethlyenimine-DNA Binding and DNA Condensation. *Biophys. J.* 99(1):201-207.

3.17. Sun C, Tang T, & Uludag H (2013) A Molecular Dynamics Simulation Study on the Effect of Lipid Substitution on Polyethylenimine Mediated siRNA Complexation. *Biomaterials* 34(11):2822-2833.

3.18. Schrödinger Release 2014-2: Maestro V, Schrödinger, LLC, New York, NY, 2014.

3.19. Humphrey W, Dalke A, & Schulten K (1996) VMD: Visual Molecular Dynamics. *J. Mol. Graphics* 14(1):33-38.

3.20. Phillips JC, Braun R, Wang W, Gumbart J, Tajkhorshid E, Villa E, Chipot C, Skeel RD, Kale L, & Schulten K (2005) Scalable Molecular Dynamics with NAMD. *J. Comput. Chem.* 26(16):1781-1802.

3.21. Jorgensen WL, Chandrasekhar J, Madura JD, Impey RW, Klein ML (1983) Comparison of Simple Potential Functions for Simulating Liquid Water. J. Chem. Phys. 79: 926-935.

3.22. Sun C, Tang T, Uludag H, & Cuervo JE (2011) Molecular Dynamics Simulations of DNA/PEI Complexes: Effect of PEI Branching and Protonation State. *Biophys. J.* 100(11):2754-2763.

3.23. Vanommeslaeghe K, Hatcher E, Acharya C, Kundu S, Zhong S, Shim J, Darian E, Guvench O, Lopes P, Vorobyov I, & Mackerell AD, Jr. (2010) CHARMM General Force Field: A Force Field for Drug-like Molecules Compatible with the CHARMM All-atom Additive Biological Force Fields. *J. Comput. Chem.* 31(4):671-690.

3.24. Berendsen HJC, Postma JPM, von Gunsteren WF, Hermans J (1981) Interaction Models for Water in Relation to Protein Hydration. *Intermolecular Forces*, The Jerusalem Symposia on Quantum Chemistry and Biochemistry, eds Pullman B (Springer, Dordrecht, Holland), Vol 14, pp 331-342.

3.25. Mahoney MW, Jorgensen WL (2000) A Five-site Model for Liquid Water and the Reproduction of the Density Anomaly by Rigid, Nonpolarizable Potential Functions. *J. Chem. Phys.* 112: 8910-8922.

3.26. Nutt DR, Smith JC (2007) Molecular Dynamics Simulations of Proteins: Can the Explicit Water Model Be Varied? *J. Chem. Theory Comput*. 3: 1550-1560.

3.27. Brooks BR, Bruccoleri RE, Olafson BD, States DJ, Swaminathan S, & Karplus M (1983) Charmm – A Program for Macromolecular Energy, Minimization, and Dynamics Calculations. *J. Comput. Chem.* 4:187–217.

3.28. MacKerell AD, Brooks B, Brooks CL, Nilsson L, Roux B, Won Y, & Karplus M (1998) CHARMM: The Energy Function and Its Parameterization with an Overview of the Program. *The Encyclopedia of Computational Chemistry*, (John Wiley & Sons, Chichester), pp 271-277.

3.29. Foloppe N & MacKerell J, A.D. (2000) All-Atom Empirical Force Field for Nucleic Acids: I. Parameter Optimization Based on Small Molecule and Condensed Phase Macromolecular Target Data. *J. Comput. Chem.* 21:86-104.

3.30. MacKerell AD & Banavali NK (2000) All-atom Empirical Force Field for Nucleic Acids: II. Application to Molecular Dynamics Simulations of DNA and RNA in Solution. *J. Comput. Chem.* 21(2):105-120.

3.31. Darden T, York D, & Pedersen L (1993) Particle Mesh Ewald: An N · log(N) Method for Ewald Sums in Large Systems. *J. Chem. Phys.* 98:10089-10092.

3.32. Ryckaert JP, Ciccotti G, & Berendsen HJC (1977) Numerical Integration of the Cartesian Equations of Motion of a System with Constraints: Molecular Dynamics of N-alkanes. *J. Comput. Phys.* 23(3):327-341.

3.33. Blokzijl W & Engberts JBFN (1993) Hydrophobic Effects. Opinion and Facts. *Angew. Chem. Int. Ed. Engl.* 32:1545-1579.

3.34. Cheng YK & Rossky PJ (1998) Surface Topography Dependence of Biomolecular Hydrophobic Hydration. *Nature* 392(6677):696-699.

3.35. Thomas M & Klibanov AM (2002) Enhancing Polyethylenimine's Delivery of Plasmid DNA into Mammalian Cells. *Proc. Natl. Acad. Sci. U.S.A.* 99(23):14640-14645.

3.36. Posocco P, Pricl S, Jones S, Barnard A, & Smith DK (2010) Less Is More – Multiscale Modelling of Self-assembling Multivalency and Its Impact on DNA Binding and Gene Delivery. *Chem. Sci.* 1:393–404.

3.37. Frohlich E (2012) The Role of Surface Charge in Cellular Uptake and Cytotoxicity of Medical Nanoparticles. *Int. J. Nanomed.* 7:5577-5591.

4.1. Fire A, Xu S, Montgomery MK, Kostas SA, Driver SE, & Mello CC (1998) Potent and Specific Genetic Interference by Double-stranded RNA in Caenorhabditis Elegans. *Nature* 391(6669):806-811.

4.2. Davidson BL & McCray PB, Jr. (2011) Current Prospects for RNA Interference-based Therapies. *Nat. Rev. Genet.* 12(5):329-340.

4.3. Zhang S, Zhao B, Jiang H, Wang B, & Ma B (2007) Cationic Lipids and Polymers Mediated Vectors for Delivery of siRNA. *J. Control. Release* 123(1):1-10.

4.4. Boussif O, Lezoualc'h F, Zanta MA, Mergny MD, Scherman D, Demeneix B, & Behr JP (1995) A Versatile Vector for Gene and Oligonucleotide Transfer into Cells in Culture and In vivo: Polyethylenimine. *Proc. Natl. Acad. Sci. U.S.A.* 92(16):7297-7301.

4.5. Dominska M & Dykxhoorn DM (2010) Breaking Down the Barriers: siRNA Delivery and Endosome Escape. *J. Cell. Sci.* 123:1183-1189.

4.6. Czech B & Hannon GJ (2011) Small RNA Sorting: Matchmaking for Argonautes. *Nat. Rev. Genet.* 12(1):19-31.

4.7. Ding HM & Ma YQ (2012) Role of Physicochemical Properties of Coating Ligands in Receptor-mediated Endocytosis of Nanoparticles. *Biomaterials* 33(23):5798-5802.

4.8. Ding HM & Ma YQ (2013) Design Maps for Cellular Uptake of Gene Nanovectors by Computer Simulation. *Biomaterials* 34(33):8401-8407.

4.9. Ding HM & Ma YQ (2013) Controlling Cellular Uptake of Nanoparticles with pH-sensitive Polymers. *Sci. Rep.* 3:2804.

4.10. Dinh AT, Pangarkar C, Theofanous T, & Mitragotri S (2007) Understanding Intracellular Transport Processes Pertinent to Synthetic Gene Delivery via Stochastic Simulations and Sensitivity Analyses. *Biophys. J.* 92(3):831-846.

4.11. Gilleron J, Querbes W, Zeigerer A, Borodovsky A, Marsico G, Schubert U, Manygoats K, Seifert S, Andree C, Stoter M, Epstein-Barash H, Zhang L, Koteliansky V, Fitzgerald

K, Fava E, Bickle M, Kalaidzidis Y, Akinc A, Maier M, & Zerial M (2013) Image-based Analysis of Lipid Nanoparticle-mediated siRNA Delivery, Intracellular Trafficking and Endosomal Escape. *Nat. Biotechnol.* 31(7):638-646.

4.12. Sahay G, Querbes W, Alabi C, Eltoukhy A, Sarkar S, Zurenko C, Karagiannis E, Love K, Chen DL, Zoncu R, Buganim Y, Schroeder A, Langer R, & Anderson DG (2013) Efficiency of siRNA Delivery by Lipid Nanoparticles is Limited by Endocytic Recycling. *Nat. Biotechnol.* 31(7):653-658.

4.13. Behr JP (1997) The Proton Sponge: A Trick to Enter Cells the Viruses Did Not Exploit. *Chimia* 51(1-2):34-36.

4.14. Benjaminsen RV, Mattebjerg MA, Henriksen JR, Moghimi SM, & Andresen TL (2013) The Possible "Proton Sponge " Effect of Polyethylenimine (PEI) Does Not Include Change in Lysosomal pH. *Mol. Ther.* 21(1):149-157.

4.15. Won YY, Sharma R, & Konieczny SF (2009) Missing Pieces in Understanding the Intracellular Trafficking of Polycation/DNA Complexes. *J. Control. Release* 139(2):88-93.

4.16. Sasisekharan R, Shriver Z, Venkataraman G, & Narayanasami U (2002) Roles of Heparan-Sulphate Glycosaminoglycans in Cancer. *Nat. Rev. Cancer* 2:521-528.

4.17. Xu YH & Szoka FC (1996) Mechanism of DNA Release from Cationic Liposome/DNA Complexes Used in Cell Transfection. *Biochemistry* 35(18):5616-5623.

4.18. Ruponen M, Yla-Herttuala S, & Urtti A (1999) Interactions of Polymeric and Liposomal Gene Delivery Systems with Extracellular Glycosaminoglycans: Physicochemical and Transfection Studies. *Biochim. Biophys. Acta* 1415(2):331-341.

4.19. Moret I, Esteban Peris J, Guillem VM, Benet M, Revert F, Dasi F, Crespo A, & Alino SF (2001) Stability of PEI-DNA and DOTAP-DNA Complexes: Effect of Alkaline pH, Heparin and Serum. *J. Control. Release* 76(1-2):169-181.

4.20. Ruponen M, Honkakoski P, Ronkko S, Pelkonen J, Tammi M, & Urtti A (2003) Extracellular and Intracellular Barriers in Non-viral Gene Delivery. *J. Control. Release* 93(2):213-217.

4.21. Aliabadi HM, Landry B, Sun C, Tang T, & Uludag H (2012) Supramolecular Assemblies in Functional siRNA Delivery: Where Do We Stand? *Biomaterials* 33(8):2546-2569.

4.22. Calin GA & Croce CM (2006) MicroRNA Signatures in Human Cancers. *Nat. Rev. Cancer* 6(11):857-866.

4.23. Esquela-Kerscher A & Slack FJ (2006) Oncomirs - MicroRNAs with a Role in Cancer. *Nat. Rev. Cancer* 6(4):259-269.

4.24. Lagos-Quintana M, Rauhut R, Lendeckel W, & Tuschl T (2001) Identification of Novel Genes Coding for Small Expressed RNAs. *Science* 294(5543):853-858.

4.25. Krichevsky AM & Gabriely G (2009) miR-21: A Small Multi-faceted RNA. *J. Cell. Mol. Med.* 13(1):39-53.

4.26. Abbasi M, Lavasanifar A, Berthiaume LG, Weinfeld M, & Uludag H (2010) Cationic Polymer-mediated Small Interfering RNA Delivery for P-glycoprotein Down-regulation in Tumor Cells. *Cancer* 116(23):5544-5554.

4.27. Utsuno K & Uludag H (2010) Thermodynamics of Polyethlyenimine-DNA Binding and DNA Condensation. *Biophys. J.* 99(1):201-207.

4.28. Sun C, Tang T, & Uludag H (2013) A Molecular Dynamics Simulation Study on the Effect of Lipid Substitution on Polyethylenimine Mediated siRNA Complexation. *Biomaterials* 34(11):2822-2833.

4.29. Sun C, Tang T, Uludag H, & Cuervo JE (2011) Molecular Dynamics Simulations of DNA/PEI Complexes: Effect of PEI Branching and Protonation State. *Biophys. J.* 100(11):2754-2763.

4.30. Vanommeslaeghe K, Hatcher E, Acharya C, Kundu S, Zhong S, Shim J, Darian E, Guvench O, Lopes P, Vorobyov I, & Mackerell AD, Jr. (2010) CHARMM General Force Field: A Force Field for Drug-like Molecules Compatible with the CHARMM All-atom Additive Biological Force Fields. *J. Comput. Chem.* 31(4):671-690.

4.31. Brooks BR, Bruccoleri RE, Olafson BD, States DJ, Swaminathan S, & Karplus M (1983) Charmm – A Program for Macromolecular Energy, Minimization, and Dynamics Calculations. *J. Comput. Chem.* 4:187–217.

4.32. MacKerell AD, Brooks B, Brooks CL, Nilsson L, Roux B, Won Y, & Karplus M (1998) CHARMM: The Energy Function and Its Parameterization with an Overview of the Program. *The Encyclopedia of Computational Chemistry*, (John Wiley & Sons, Chichester), pp 271-277.

4.33. Foloppe N & MacKerell J, A.D. (2000) All-Atom Empirical Force Field for Nucleic Acids: I. Parameter Optimization Based on Small Molecule and Condensed Phase Macromolecular Target Data. *J. Comput. Chem.* 21:86-104.

4.34. MacKerell AD & Banavali NK (2000) All-atom Empirical Force Field for Nucleic Acids: II. Application to Molecular Dynamics Simulations of DNA and RNA in Solution. *J. Comput. Chem.* 21(2):105-120.

4.35. Phillips JC, Braun R, Wang W, Gumbart J, Tajkhorshid E, Villa E, Chipot C, Skeel RD, Kale L, & Schulten K (2005) Scalable Molecular Dynamics with NAMD. *J. Comput. Chem.* 26(16):1781-1802.

4.36. Jorgensen WL (1981) Quantum and Statistical Mechanical Studies of Liquids .10. Transferable Intermolecular Potential Functions for Water, Alcohols, and Ethers - Application to Liquid Water. *J. Am. Chem. Soc.* 103(2):335-340.

4.37. Balasubramanian C, Ojha RP, Maiti S, & Desideri A (2010) Sampling the Structure of the Noncanonical lin-4:lin-14 microRNA:mRNA Complex by Molecular Dynamics Simulations. *J. Phys. Chem. B* 114(49):16443-16449.

4.38. Darden T, York D, & Pedersen L (1993) Particle Mesh Ewald: An N · log(N) Method for Ewald Sums in Large Systems. *J. Chem. Phys.* 98:10089-10092.

4.39. Ryckaert JP, Ciccotti G, & Berendsen HJC (1977) Numerical Integration of the Cartesian Equations of Motion of a System with Constraints: Molecular Dynamics of N-alkanes. *J. Comput. Phys.* 23(3):327-341.

4.40. Humphrey W, Dalke A, & Schulten K (1996) VMD: Visual Molecular Dynamics. *J. Mol. Graphics* 14(1):33-38.

4.41. Sun C, Tang T, & Uludag H (2011) Molecular Dynamics Simulations of PEI Mediated DNA Aggregation. *Biomacromolecules* 12(10):3698-3707.

4.42. Ouyang D, Zhang H, Parekh HS, & Smith SC (2011) The Effect of pH on PAMAM Dendrimer-siRNA Complexation: Endosomal Considerations as Determined by Molecular Dynamics Simulation. *Biophys. Chem.* 158(2-3):126-133.

4.43. Karatasos K, Posocco P, Laurini E, & Pricl S (2012) Poly(amidoamine)-based Dendrimer/siRNA Complexation Studied by Computer Simulations: Effects of pH and Generation on Dendrimer Structure and siRNA Binding. *Macromol. Biosci.* 12(2):225-240.

4.44. Pavan GM, Albertazzi L, & Danani A (2010) Ability to Adapt: Different Generations of PAMAM Dendrimers Show Different Behaviors in Binding siRNA. *J. Phys. Chem. B.* 114(8):2667-2675.

4.45. Pavan GM, Kostiainen MA, & Danani A (2010) Computational Approach for Understanding the Interactions of UV-degradable Dendrons with DNA and siRNA. *J. Phys. Chem. B.* 114(17):5686-5693.

4.46. Jensen LB, Mortensen K, Pavan GM, Kasimova MR, Jensen DK, Gadzhyeva V, Nielsen HM, & Foged C (2010) Molecular Characterization of the Interaction between siRNA and PAMAM G7 Dendrimers by SAXS, ITC, and Molecular Dynamics Simulations. *Biomacromolecules* 11(12):3571-3577.

4.47. Ouyang D, Zhang H, Parekh HS, & Smith SC (2010) Structure and Dynamics of Multiple Cationic Vectors-siRNA Complexation by All-atomic Molecular Dynamics Simulations. *J. Phys. Chem. B.* 114(28):9231-9237.

4.48. Ouyang D, Zhang H, Herten DP, Parekh HS, & Smith SC (2010) Structure, Dynamics, and Energetics of siRNA-Cationic Vector Complexation: A Molecular Dynamics Study. *J. Phys. Chem. B.* 114(28):9220-9230.

4.49. Vasumathi V & Maiti PK (2010) Complexation of siRNA with Dendrimer: A Molecular Modeling Approach. *Macromolecules* 43:8264–8274.

4.50. Ziebarth J & Wang Y (2009) Molecular Dynamics Simulations of DNA-Polycation Complex Formation. *Biophys. J.* 97(7):1971-1983.

4.51. Elder RM, Emrick T, & Jayaraman A (2011) Understanding the Effect of Polylysine Architecture on DNA Binding Using Molecular Dynamics Simulations. *Biomacromolecules* 12(11):3870-3879.

5.1. Rabenstein DL (2002) Heparin and Heparan Sulfate: Structure and Function. *Nat. Prod. Rep.* 19(3):312-331.

5.2. Kreuger J, Spillmann D, Li JP, & Lindahl U (2006) Interactions Between Heparan Sulfate and Proteins: The Concept of Specificity. *J. Cell. Biol.* 174(3):323-327.

5.3. Gandhi NS & Mancera RL (2008) The Structure of Glycosaminoglycans and Their Interactions with Proteins. *Chem. Biol. Drug Des.* 72(6):455-482.

5.4. Sasisekharan R & Venkataraman G (2000) Heparin and Heparan Sulfate: Biosynthesis, Structure and Function. *Curr. Opin. Chem. Biol.* 4(6):626-631.

5.5. Sasisekharan R, Shriver Z, Venkataraman G, & Narayanasami U (2002) Roles of Heparan-sulphate Glycosaminoglycans in Cancer. *Nat. Rev. Cancer* 2(7):521-528.

5.6. Lamari FN, Militsopoulou M, Mitropoulou TN, Hjerpe A, & Karamanos NK (2002) Analysis of Glycosaminoglycan-derived Disaccharides in Biologic Samples by Capillary Electrophoresis and Protocol for Sequencing Glycosaminoglycans. *Biomed. Chromatogr.* 16(2):95-102.

5.7. Perrimon N & Bernfield M (2000) Specificities of Heparan Sulphate Proteoglycans in Developmental Processes. *Nature* 404(6779):725-728.

5.8. Iozzo RV & San Antonio JD (2001) Heparan Sulfate Proteoglycans: Heavy Hitters in the Angiogenesis Arena. *J. Clin. Invest.* 108(3):349-355.

5.9. Sasisekharan R, Ernst S, & Venkataraman G (1997) On the Regulation of Fibroblast Growth Factor Activity by Heparin-like Glycosaminoglycans. *Angiogenesis* 1(1):45-54.

5.10. Machovich R (1975) Mechanism of Action of Heparin Through Thrombin on Blood Coagulation. *Biochim. Biophys. Acta* 412(1):13-17.

5.11. Jaques LB (1979) Heparin: An Old Drug with a New Paradigm. *Science* 206(4418):528-533.

5.12. Verli H & Guimarães JA (2004) Molecular Dynamics Simulation of a Decasaccharide Fragment of Heparin in Aqueous Solution. *Carbohydr. Res.* 339(2):281-290.

5.13. Munoz-Garcia JC, Corzana F, de Paz JL, Angulo J, & Nieto PM (2013) Conformations of the Iduronate Ring in Short Heparin Fragments Described by Time-averaged Distance Restrained Molecular Dynamics. *Glycobiology* 23(11):1220-1229.

5.14. Verli H & Guimarães JA (2005) Insights into the Induced Fit Mechanism in Antithrombin-Heparin Interaction Using Molecular Dynamics Simulations. *J. Mol. Graph. Model.* 24(3):203-212.

5.15. Canales A, Lozano R, Lopez-Mendez B, Angulo J, Ojeda R, Nieto PM, Martin-Lomas M, Gimenez-Gallego G, & Jimenez-Barbero J (2006) Solution NMR Structure of a Human FGF-1 Monomer, Activated by a Hexasaccharide Heparin-analogue. *FEBS J.* 273(20):4716-4727.

5.16. Barnard A, Posocco P, Pricl S, Calderon M, Haag R, Hwang ME, Shum VW, Pack DW, & Smith DK (2011) Degradable Self-assembling Dendrons for Gene Delivery: Experimental and Theoretical Insights into the Barriers to Cellular Uptake. *J. Am. Chem. Soc.* 133(50):20288-20300.

5.17. Guvench O, Mallajosyula SS, Raman EP, Hatcher E, Vanommeslaeghe K, Foster TJ, Jamison FW, 2nd, & Mackerell AD, Jr. (2011) CHARMM Additive All-atom Force

Field for Carbohydrate Derivatives and Its Utility in Polysaccharide and Carbohydrate-Protein Modeling. *J. Chem. Theory Comput.* 7(10):3162-3180.

5.18. Mallajosyula SS, Guvench O, Hatcher E, & MacKerell AD (2012) CHARMM Additive All-Atom Force Field for Phosphate and Sulfate Linked to Carbohydrates. *J. Chem. Theory Comput.* 8(2):759-776.

5.19. Mulloy B, Forster MJ, Jones C, & Davies DB (1993) N.M.R. and Molecular-modelling Studies of the Solution Conformation of Heparin. *Biochem. J.* 293 (Pt 3):849-858.

5.20. Schrödinger Release 2015-4: Maestro, Schrödinger, LLC, New York, NY, 2015.

5.21. Yu WB, He XB, Vanommeslaeghe K, & MacKerell AD (2012) Extension of the CHARMM General Force Field to Sulfonyl-containing Compounds and Its Utility in Biomolecular Simulations. *J. Comput. Chem.* 33(31):2451-2468.

5.22. Frisch MJT, G. W.; Schlegel, H. B.; Scuseria, G. E.; Robb, M. A.; Cheeseman, J. R.; Scalmani, G.; Barone, V.; Mennucci, B.; Petersson, G. A.; Nakatsuji, H.; Caricato, M.; Li, X.; Hratchian, H. P.; Izmaylov, A. F.; Bloino, J.; Zheng, G.; Sonnenberg, J. L.; Hada, M.; Ehara, M.; Toyota, K.; Fukuda, R.; Hasegawa, J.; Ishida, M.; Nakajima, T.; Honda, Y.; Kitao, O.; Nakai, H.; Vreven, T.; Montgomery, Jr., J. A.; Peralta, J. E.; Ogliaro, F.; Bearpark, M.; Heyd, J. J.; Brothers, E.; Kudin, K. N.; Staroverov, V. N.; Kobayashi, R.; Normand, J.; Raghavachari, K.; Rendell, A.; Burant, J. C.; Iyengar, S. S.; Tomasi, J.; Cossi, M.; Rega, N.; Millam, J. M.; Klene, M.; Knox, J. E.; Cross, J. B.; Bakken, V.; Adamo, C.; Jaramillo, J.; Gomperts, R.; Stratmann, R. E.; Yazyev, O.; Austin, A. J.; Cammi, R.; Pomelli, C.; Ochterski, J. W.; Martin, R. L.; Morokuma, K.; Zakrzewski, V. G.; Voth, G. A.; Salvador, P.; Dannenberg, J. J.; Dapprich, S.; Daniels, A. D.; Farkas, Ö.; Foresman, J. B.; Ortiz, J. V.; Cioslowski, J.; Fox, D. J. (2009) Gaussian 09 (Gaussian Inc. , Wallingford, CT), Revision A.1.

5.23. Case DA, Darden TA, Cheatham TE, III , Simmerling CL, Wang J, Duke RE, Luo R, Walker RC, Zhang W, Merz KM, Roberts B, Hayik S, Roitberg A, Seabra G, Swails J, Götz AW, Kolossváry I, Wong KF, Paesani F, Vanicek J, Wolf RM, Liu J, Wu X, Brozell SR, Steinbrecher T, Gohlke H, Cai Q, Ye X, Wang J, Hsieh M-J, Cui G, Roe DR, Mathews DH, Seetin MG, Salomon-Ferrer R, Sagui C, Babin V, Luchko T, Gusarov S, Kovalenko A, & Kollman PA (2012) AmberTools 13 (University of California, San Francisco).

5.24. Guvench O, Hatcher E, Venable RM, Pastor RW, & MacKerell AD (2009) CHARMM Additive All-Atom Force Field for Glycosidic Linkages between Hexopyranoses. *J. Chem. Theory Comput.* 5(9):2353-2370.

5.25. Vanommeslaeghe K, Hatcher E, Acharya C, Kundu S, Zhong S, Shim J, Darian E, Guvench O, Lopes P, Vorobyov I, & MacKerell AD (2010) CHARMM General Force Field: A Force Field for Drug-Like Molecules Compatible with the CHARMM All-Atom Additive Biological Force Fields. *J. Comput. Chem.* 31(4):671-690.

5.26. Phillips JC, Braun R, Wang W, Gumbart J, Tajkhorshid E, Villa E, Chipot C, Skeel RD, Kale L, & Schulten K (2005) Scalable Molecular Dynamics with NAMD. *J. Comput. Chem.* 26(16):1781-1802.

5.27. Darden T, York D, & Pedersen L (1993) Particle Mesh Ewald - an N.Log(N) Method for Ewald Sums in Large Systems. *J. Chem. Phys.* 98(12):10089-10092.

5.28. Ryckaert JP, Ciccotti G, & Berendsen HJC (1977) Numerical-Integration of Cartesian Equations of Motion of a System with Constraints - Molecular-Dynamics of N-Alkanes. *J. Comput. Phys.* 23(3):327-341.

5.29. Sanderson PN, Huckerby TN, & Nieduszynski IA (1987) Conformational Equilibria of Alpha-L-iduronate Residues in Disaccharides Derived from Heparin. *Biochem. J.* 243(1):175-181.

5.30. van Aalten DM, Bywater R, Findlay JB, Hendlich M, Hooft RW, & Vriend G (1996) PRODRG, A Program for Generating Molecular Topologies and Unique Molecular Descriptors from Coordinates of Small Molecules. *J. Comput. Aided Mol. Des.* 10(3):255-262.

6.1. Gandhi NS & Mancera RL (2008) The Structure of Glycosaminoglycans and Their Interactions with Proteins. *Chem. Biol. Drug. Des.* 72(6):455-482.

6.2. Belting M & Petersson P (1999) Protective Role for Proteoglycans Against Cationic Lipid Cytotoxicity Allowing Optimal Transfection Efficiency In Vitro. *Biochem. J.* 342 (Pt 2):281-286.

6.3. Belting M & Petersson P (1999) Intracellular Accumulation of Secreted Proteoglycans Inhibits Cationic Lipid-mediated Gene Transfer. Co-transfer of Glycosaminoglycans to the Nucleus. *J. Biol. Chem.* 274(27):19375-19382.

6.4. Gallagher JT, Lyon M, & Steward WP (1986) Structure and Function of Heparan Sulphate Proteoglycans. *Biochem. J.* 236(2):313-325.

6.5. Kjellen L & Lindahl U (1991) Proteoglycans: Structures and Interactions. *Annu. Rev. Biochem.* 60:443-475.

6.6. Raman R, Sasisekharan V, & Sasisekharan R (2005) Structural Insights into Biological Roles of Protein-Glycosaminoglycan Interactions. *Chem. Biol.* 12(3):267-277.

6.7. Mislick KA & Baldeschwieler JD (1996) Evidence for the Role of Proteoglycans in Cation-mediated Gene Transfer. *Proc. Natl. Acad. Sci. U.S.A.* 93(22):12349-12354.

6.8. Mounkes LC, Zhong W, Cipres-Palacin G, Heath TD, & Debs RJ (1998) Proteoglycans Mediate Cationic Liposome-DNA Complex-based Gene delivery In Vitro and In Vivo. *J. Biol. Chem.* 273(40):26164-26170.

6.9. Humphries DE & Silbert JE (1988) Chlorate: A Reversible Inhibitor of Proteoglycan Sulfation. *Biochem. Biophys. Res. Commun.* 154(1):365-371.

6.10. Ruponen M, Yla-Herttuala S, & Urtti A (1999) Interactions of Polymeric and Liposomal Gene Delivery Systems with Extracellular Glycosaminoglycans: Physicochemical and Transfection Studies. *Biochim. Biophys. Acta* 1415(2):331-341.

6.11. Xu Y & Szoka FC, Jr. (1996) Mechanism of DNA Release from Cationic Liposome/DNA Complexes Used in Cell Transfection. *Biochemistry* 35(18):5616-5623.

6.12. Wiethoff CM, Smith JG, Koe GS, & Middaugh CR (2001) The Potential Role of Proteoglycans in Cationic Lipid-mediated Gene Delivery. Studies of the Interaction of

Cationic Lipid-DNA Complexes with Model Glycosaminoglycans. *J. Biol. Chem.* 276(35):32806-32813.

6.13. Liu Y & Reineke TM (2006) Poly(glycoamidoamine)s for Gene Delivery: Stability of Polyplexes and Efficacy with Cardiomyoblast Cells. *Bioconjug. Chem.* 17(1):101-108.

6.14. Ruponen M, Ronkko S, Honkakoski P, Pelkonen J, Tammi M, & Urtti A (2001) Extracellular Glycosaminoglycans Modify Cellular Trafficking of Lipoplexes and Polyplexes. *J. Biol. Chem.* 276(36):33875-33880.

6.15. Ruponen M, Honkakoski P, Tammi M, & Urtti A (2004) Cell-surface Glycosaminoglycans Inhibit Cation-mediated Gene Transfer. *J. Gene Med.* 6(4):405-414.

6.16. Nomani A, Hyvonen Z, Pulkkinen E, Hiekkala M, & Ruponen M (2014) Intracellular Gene Delivery is Dependent on the Type of Non-viral Carrier and Defined by the Cell Surface Glycosaminoglycans. *J. Control. Release* 187:59-65.

6.17. Barnard A, Posocco P, Pricl S, Calderon M, Haag R, Hwang ME, Shum VW, Pack DW, & Smith DK (2011) Degradable Self-assembling Dendrons for Gene Delivery: Experimental and Theoretical Insights into the Barriers to Cellular Uptake. *J. Am. Chem. Soc.* 133(50):20288-20300.

6.18. Abbasi M, Lavasanifar A, Berthiaume LG, Weinfeld M, & Uludag H (2010) Cationic Polymer-mediated Small Interfering RNA Delivery for P-glycoprotein Down-regulation in Tumor Cells. *Cancer* 116(23):5544-5554.

6.19. Meneksedag-Erol D, Tang T, & Uludag H (2015) Probing the Effect of miRNA on siRNA-PEI Polyplexes. *J. Phys. Chem. B* 119(17):5475-5486.

6.20. Utsuno K & Uludag H (2010) Thermodynamics of Polyethylenimine-DNA Binding and DNA Condensation. *Biophys. J.* 99(1):201-207.

6.21. Sun C, Tang T, & Uludag H (2011) Molecular Dynamics Simulations of PEI Mediated DNA Aggregation. *Biomacromolecules* 12(10):3698-3707.

6.22. Sun C, Tang T, & Uludag H (2012) Molecular Dynamics Simulations for Complexation of DNA with 2 kDa PEI Reveal Profound Effect of PEI Architecture on Complexation. *J. Phys. Chem. B* 116(8):2405-2413.

6.23. Phillips JC, Braun R, Wang W, Gumbart J, Tajkhorshid E, Villa E, Chipot C, Skeel RD, Kale L, & Schulten K (2005) Scalable Molecular Dynamics with NAMD. *J. Comput. Chem.* 26(16):1781-1802.

6.24. Sun C, Tang T, Uludag H, & Cuervo JE (2011) Molecular Dynamics Simulations of DNA/PEI Complexes: Effect of PEI Branching and Protonation State. *Biophys. J.* 100(11):2754-2763.

6.25. Vanommeslaeghe K, Hatcher E, Acharya C, Kundu S, Zhong S, Shim J, Darian E, Guvench O, Lopes P, Vorobyov I, & MacKerell AD (2010) CHARMM General Force Field: A Force Field for Drug-Like Molecules Compatible with the CHARMM All-Atom Additive Biological Force Fields. *J. Comput. Chem.* 31(4):671-690.

6.26. Darden T, York D, & Pedersen L (1993) Particle Mesh Ewald - an N.Log(N) Method for Ewald Sums in Large Systems. *J. Chem. Phys.* 98(12):10089-10092.

6.27. Ryckaert JP, Ciccotti G, & Berendsen HJC (1977) Numerical-Integration of Cartesian Equations of Motion of a System with Constraints - Molecular-Dynamics of N-Alkanes. *J. Comput. Phys.* 23(3):327-341.

6.28. Humphrey W, Dalke A, & Schulten K (1996) VMD: Visual Molecular Dynamics. *J. Mol. Graph.* 14(1):33-38, 27-38.

6.29. Schlick T (2010) Chapter 10: Nonbonded Computations. *Molecular Modeling and Simulation: An Interdisciplinary Guide* (Springer, New York, USA), pp 311-312.

6.30. González MA (2011) Force Fields and Molecular Dynamics Simulations. *Collection SFN* 12:169–200.

6.31. Sun C, Tang T, & Uludag H (2013) A Molecular Dynamics Simulation Study on the Effect of Lipid Substitution on Polyethylenimine Mediated siRNA Complexation. *Biomaterials* 34(11):2822-2833.

6.32. Smith SA, Choi SH, Collins JN, Travers RJ, Cooley BC, & Morrissey JH (2012) Inhibition of Polyphosphate as a Novel Strategy for Preventing Thrombosis and Inflammation. *Blood* 120(26):5103-5110.

6.33. Wang HM, Loganathan D, & Linhardt RJ (1991) Determination of the pKa of Glucuronic Acid and the Carboxy Groups of Heparin by ^{13}C-Nuclear-Magnetic-Resonance Spectroscopy. *Biochem. J.* 278 (Pt 3):689-695.

6.34. Park JW & Chakrabarti B (1978) Optical Characteristics of Carboxyl Group in Relation to the Circular Dichroic Properties and Dissociation Constants of Glycosaminoglycans. *Biochim. Biophys. Acta* 544(3):667-675.

6.35. Chevalier F, Lucas R, Angulo J, Martin-Lomas M, & Nieto PM (2004) The Heparin-Ca(2^{+}) Interaction: The Influence of the O-sulfation Pattern on Binding. *Carbohydr. Res.* 339(5):975-983.

6.36. Ferro DR, Provasoli A, Ragazzi M, Casu B, Torri G, Bossennec V, Perly B, Sinay P, Petitou M, & Choay J (1990) Conformer Populations of L-iduronic Acid Residues in Glycosaminoglycan Sequences. *Carbohydr. Res.* 195(2):157-167.

6.37. Mulloy B & Forster MJ (2000) Conformation and Dynamics of Heparin and Heparan Sulfate. *Glycobiology* 10(11):1147-1156.

6.38. Danielsen S, Strand S, de Lange Davies C, & Stokke BT (2005) Glycosaminoglycan Destabilization of DNA-Chitosan Polyplexes for Gene Delivery Depends on Chitosan Chain Length and GAG Properties. *Biochim. Biophys. Acta* 1721(1-3):44-54.

6.39. Nel AE, Madler L, Velegol D, Xia T, Hoek EM, Somasundaran P, Klaessig F, Castranova V, & Thompson M (2009) Understanding Biophysicochemical Interactions at the Nano-bio Interface. *Nat. Mater.* 8(7):543-557.

6.40. Kopatz I, Remy JS, & Behr JP (2004) A Model for Non-viral Gene Delivery: Through Syndecan Adhesion Molecules and Powered by Actin. *J. Gene Med.* 6(7):769-776.

6.41. Esko JD, Kimata K, & Lindahl U (2009) Chapter 16: Proteoglycans and Sulfated Glycosaminoglycans. *Essentials of Glycobiology*, eds Varki A, Cummings RD, Esko JD, Freeze HH, Stanley P, Bertozzi CR, Hart GW, & Etzler ME (Cold Spring Harbor Laboratory Press, Cold Spring Harbor (NY)), 2nd Ed.

7.1. Rickles FR & Edwards RL (1983) Activation of Blood coagulation in Cancer: Trousseau's Syndrome Revisited. *Blood* 62(1):14-31.

7.2. Francis JL, Biggerstaff J, & Amirkhosravi A (1998) Hemostasis and Malignancy. *Semin Thromb. Hemost.* 24(2):93-109.

7.3. Kvolik S, Jukic M, Matijevic M, Marjanovic K, & Glavas-Obrovac L (2010) An Overview of Coagulation Disorders in Cancer Patients. *Surg. Oncol.* 19(1):e33-46.

7.4. Anderson JA & Weitz JI (2013) Chapter 142: Hypercoagulable States, Part XII: Hemostasis and Thrombosis. *Hematology: Basic Principles and Practice*, eds Hoffman R, Benz Jr. EJ, Silberstein LE, Heslop H, Weitz JI, & Anastasi J (Elsevier Saunders Philadelphia, United States), 6th Ed., pp 2013-2024.

7.5. Cronin-Fenton DP, Sondergaard F, Pedersen LA, Fryzek JP, Cetin K, Acquavella J, Baron JA, & Sorensen HT (2010) Hospitalisation for Venous Thromboembolism in Cancer Patients and the General Population: A Population-based Cohort Study in Denmark, 1997-2006. *Br. J. Cancer* 103(7):947-953.

7.6. Walker AJ, Card TR, West J, Crooks C, & Grainge MJ (2013) Incidence of Venous Thromboembolism in Patients with Cancer - A Cohort Study Using Linked United Kingdom Databases. *Eur. J. Cancer* 49(6):1404-1413.

7.7. Horsted F, West J, & Grainge MJ (2012) Risk of Venous Thromboembolism in Patients with Cancer: A Systematic Review and Meta-analysis. *PLoS Med* 9(7):e1001275.

7.8. Timp JF, Braekkan SK, Versteeg HH, & Cannegieter SC (2013) Epidemiology of Cancer-associated Venous Thrombosis. *Blood* 122(10):1712-1723.

7.9. Heit JA (2003) Risk Factors for Venous Thromboembolism. *Clin. Chest. Med.* 24(1):1-12.

7.10. Prandoni P, Lensing AW, Piccioli A, Bernardi E, Simioni P, Girolami B, Marchiori A, Sabbion P, Prins MH, Noventa F, & Girolami A (2002) Recurrent Venous Thromboembolism and Bleeding Complications During Anticoagulant Treatment in Patients with Cancer and Venous Thrombosis. *Blood* 100(10):3484-3488.

7.11. Schafer AI, Levine MN, Konkle BA, & Kearon C (2003) Thrombotic Disorders: Diagnosis and Treatment. *Hematology Am. Soc. Hematol. Educ. Program*:520-539.

7.12. Geddings JE & Mackman N (2014) New Players in Haemostasis and Thrombosis. *Thromb. Haemost.* 111(4):570-574.

7.13. Van Dam-Mieras MCE & Muller AD (1986) Blood Coagulation as A Part of the Haemostatic System. *New Compherensive Biochemistry,* Blood Coagulation, eds Neuberger A & Van Deenen LLM (Elsevier Science Publisher B. V. (Biomedical Division)), Vol 13, pp 1-13.

7.14. Armstrong AW & Golan DE (2008) Chapter 22: Pharmacology of Hemostasis and Thrombosis. *Principles of Pharmacology: The Pathophysiologic Basis of Drug Therapy*, eds Golan DE, Tashjian J, A. H. , Armstrong EJ, & Armstrong AW (Lippincott Williams & Wilkins, U. S. A.), 2nd Ed., pp 387-416.

7.15. Gawaz M (2001) Chapter 1: Physiology of Hemostasis. *Blood Platelets: Physiology, Pathophysiology, Membrane Receptors, Antiplatelet Principles, and Therapy for Atherothrombotic Diseases* (Thieme, Stuttgart, New York), pp 1-3.

7.16. Smith SA, Travers RJ, & Morrissey JH (2015) How It All Starts: Initiation of the Clotting Cascade. *Crit. Rev. Biochem. Mol. Biol.* 50(4):326-336.

7.17. Ondrush J & Junker C (2007) Disseminated Intravascular Coagulation. *Trauma: Critical Care*, eds Wilson WC, Grande CM, & Hoyt DB (CRC Press), pp 1039-1055.

7.18. Davie EW, Fujikawa K, & Kisiel W (1991) The Coagulation Cascade: Initiation, Maintenance, and Regulation. *Biochemistry* 30(43):10363-10370.

7.19. Bhagavan NV & Ha C-E (2015) Chapter 34: Biochemistry of Hemostasis. *Essentials of Medical Biochemistry with Clinical Cases* (Academic Press) 2nd Ed., pp 637-660.

7.20. Heimark RL, Kurachi K, Fujikawa K, & Davie EW (1980) Surface Activation of Blood Coagulation, Fibrinolysis and Kinin Formation. *Nature* 286(5772):456-460.

7.21. Moore GW, Knight G, & Blann AD (2016) Chapter 14: Bleeding Disorders and Their Laboratory Investigation. *Haematology (Fundamentals of Biomedical Science)* (Oxford University Press) 2nd Ed., pp 461-506.

7.22. Burger D, Schleuning WD, & Schapira M (1986) Human Plasma Prekallikrein. Immunoaffinity Purification and Activation to Alpha- and Beta-kallikrein. *J. Biol. Chem.* 261(1):324-327.

7.23. Schmaier AH (2012) Overview of Hemostasis. *Concise Guide to Hematology*, eds Schmaier AH & Lazarus HM (Wiley-Blackwell), pp 91-102.

7.24. Muller F, Mutch NJ, Schenk WA, Smith SA, Esterl L, Spronk HM, Schmidbauer S, Gahl WA, Morrissey JH, & Renne T (2009) Platelet Polyphosphates are Proinflammatory and Procoagulant Mediators In Vivo. *Cell* 139(6):1143-1156.

7.25. Danese E, Montagnana M, Fava C, & Guidi GC (2014) Circulating Nucleic Acids and Hemostasis: Biological Basis Behind Their Relationship and Technical Issues in Assessment. *Semin. Thromb. Hemost.* 40(7):766-773.

7.26. Kannemeier C, Shibamiya A, Nakazawa F, Trusheim H, Ruppert C, Markart P, Song Y, Tzima E, Kennerknecht E, Niepmann M, von Bruehl ML, Sedding D, Massberg S, Gunther A, Engelmann B, & Preissner KT (2007) Extracellular RNA Constitutes a Natural Procoagulant Cofactor in Blood Coagulation. *Proc. Natl. Acad. Sci. U.S.A.* 104(15):6388-6393.

7.27. DeSancho MT & Rand JH (2003) Physiology of Normal Hemostasis. *Holland-Frei Cancer Medicine*, eds Kufe DW, Pollock RE, Weichselbaum RR, Bast Jr. RC, & Gansler TS (BC Decker Inc., Hamilton, Ontario, Canada), 6th Ed., Vol 2.

7.28. Brandt JT (2002) Overview of Hemostasis. *Clinical Laboratory Medicine*, ed McClatchey KD (Lippincott Williams & Wilkins), 2nd Ed, pp 987-1009.

7.29. Rodak BF, Fritsma GA, & Doig K (2007) Part IX: Hemostasis and Thrombosis, Chapter 40: Normal Hemostasis and Coagulation. *Hematology: Clinical Principles and Applications* (Saunders) 3rd Ed., pp 571-587.

7.30. Matthey F (2016) Anticoagulation and Transfusion. *Oxford Desk Reference: Acute Medicine*, eds Leach R, Bell D, & Moore K (Oxford University Press), pp 532-558.

7.31. Fareed J & Iqbal O (2016) Physiology of Hemostasis. *Anticoagulation and Hemostasis in Neurosurgery*, ed Loftus CM, (Springer International Publishing, Switzerland), pp 3-16.

7.32. Hallett JW, Brewster DC, & Rasmussen TE (2001) Chapter 25:Coagulation Disorders. *Handbook of Patient Care in Vascular Diseases* (Lippincott Williams & Wilkins) 4th Ed., pp 295-300.

7.33. Palta S, Saroa R, & Palta A (2014) Overview of the Coagulation System. *Indian J. Anaesth.* 58(5):515-523.

7.34. Rogers HJ, Bakdash S, Nakashima MO, & Kottke-Marchant K (2014) Laboratory Analysis of Coagulation. *The Coagulation Consult: A Case-Based Guide*, eds Lichtin A & Bartholomew J (Springer), pp 1-38.

7.35. Rosendaal FR (2009) Chapter 1: Causes of Venous Thrombosis. *Deep Vein Thrombosis and Pulmonary Embolism*, eds Van Beek EJR, Buller HR, & Oudkerk M (Wiley-Blackwell), pp 3-26.

7.36. Marlar RA (2003) The Hypercoagulable State. *Hematology/Oncology Secrets*, eds Wood ME & Philips GK (Hanley & Belfus), 3rd Ed, pp 89-95.

7.37. Furie B & Furie BC (2006) Cancer-associated Thrombosis. *Blood Cells Mol. Dis.* 36(2):177-181.

7.38. Hisada Y, Geddings JE, Ay C, & Mackman N (2015) Venous Thrombosis and Cancer: From Mouse Models to Clinical Trials. *J. Thromb. Haemost.* 13(8):1372-1382.

7.39. Gordon SG & Cross BA (1981) A Factor X-Activating Cysteine Protease from Malignant Tissue. *J. Clin. Invest.* 67(6):1665-1671.

7.40. Pieno GF, Brain MC, Gallus AS, Hirsh J, Hatton MWC, & Regoeczi E (1974) Tumors, Mucus Production, and Hypercoagulability. *Ann. N. Y. Acad. Sci.* 230:262-270.

7.41. Bick RL (2003) Cancer-associated Thrombosis. *N. Engl. J. Med.* 349(2):109-111.

7.42. Noble S & Pasi J (2010) Epidemiology and Pathophysiology of Cancer-associated Thrombosis. *Br. J. Cancer* 102 Suppl 1:S2-9.

7.43. Leon SA, Shapiro B, Sklaroff DM, & Yaros MJ (1977) Free DNA in the Serum of Cancer Patients and the Effect of Therapy. *Cancer Res.* 37(3):646-650.

7.44. Schwarzenbach H, Hoon DS, & Pantel K (2011) Cell-free Nucleic Acids as Biomarkers in Cancer Patients. *Nat. Rev. Cancer* 11(6):426-437.

7.45. Shapiro B, Chakrabarty M, Cohn EM, & Leon SA (1983) Determination of Circulating DNA Levels in Patients with Benign or Malignant Gastrointestinal Disease. *Cancer* 51(11):2116-2120.

7.46. Kopreski MS, Benko FA, Kwak LW, & Gocke CD (1999) Detection of Tumor Messenger RNA in the Serum of Patients with Malignant Melanoma. *Clin. Cancer Res.* 5(8):1961-1965.

7.47. Ng EK, Tsui NB, Lam NY, Chiu RW, Yu SC, Wong SC, Lo ES, Rainer TH, Johnson PJ, & Lo YM (2002) Presence of Filterable and Nonfilterable mRNA in the Plasma of Cancer Patients and Healthy Individuals. *Clin. Chem.* 48(8):1212-1217.

7.48. Swystun LL, Mukherjee S, & Liaw PC (2011) Breast Cancer Chemotherapy Induces the Release of Cell-free DNA, a Novel Procoagulant Stimulus. *J. Thromb. Haemost.* 9(11):2313-2321.

7.49. Amulic B & Hayes G (2011) Neutrophil Extracellular Traps. *Curr. Biol.* 21(9):R297-298.

7.50. Renne T, Schmaier AH, Nickel KF, Blomback M, & Maas C (2012) In Vivo Roles of Factor XII. *Blood* 120(22):4296-4303.

7.51. Gansler J, Jaax M, Leiting S, Appel B, Greinacher A, Fischer S, & Preissner KT (2012) Structural Requirements for the Procoagulant Activity of Nucleic Acids. *PLoS One* 7(11):e50399.

7.52. Ruiz FA, Lea CR, Oldfield E, & Docampo R (2004) Human Platelet Dense Granules Contain Polyphosphate and are Similar to Acidocalcisomes of Bacteria and Unicellular Eukaryotes. *J. Biol. Chem.* 279(43):44250-44257.

7.53. Smith SA, Choi SH, Collins JN, Travers RJ, Cooley BC, & Morrissey JH (2012) Inhibition of Polyphosphate as a Novel Strategy for Preventing Thrombosis and Inflammation. *Blood* 120(26):5103-5110.

7.54. Smith SA, Choi SH, Davis-Harrison R, Huyck J, Boettcher J, Rienstra CM, & Morrissey JH (2010) Polyphosphate Exerts Differential Effects on Blood Clotting, Depending on Polymer Size. *Blood* 116(20):4353-4359.

7.55. Smith SA, Mutch NJ, Baskar D, Rohloff P, Docampo R, & Morrissey JH (2006) Polyphosphate Modulates Blood Coagulation and Fibrinolysis. *Proc. Natl. Acad. Sci. U.S.A.* 103(4):903-908.

7.56. Choi SH, Smith SA, & Morrissey JH (2011) Polyphosphate is a Cofactor for the Activation of Factor XI by Thrombin. *Blood* 118(26):6963-6970.

7.57. Smith SA & Morrissey JH (2008) Polyphosphate Enhances Fibrin Clot Structure. *Blood* 112(7):2810-2816.

7.58. Nickel KF, Ronquist G, Langer F, Labberton L, Fuchs TA, Bokemeyer C, Sauter G, Graefen M, Mackman N, Stavrou EX, Ronquist G, & Renne T (2015) The Polyphosphate-factor XII Pathway Drives Coagulation in Prostate Cancer-associated Thrombosis. *Blood* 126(11):1379-1389.

7.59. Aalberts M, Stout TA, & Stoorvogel W (2014) Prostasomes: Extracellular Vesicles from the Prostate. *Reproduction* 147(1):R1-14.

7.60. Lee AY & Peterson EA (2013) Treatment of Cancer-associated Thrombosis. *Blood* 122(14):2310-2317.

7.61. Weitz JI (2013) Antithrombotic Drugs. *Hematology: Basic Principles and Practice*, eds Hoffman R, Benz Jr. EJ, Silberstein LE, Heslop H, Weitz JI, & Anastasi J (Elsevier Saunders), 6th Ed, pp 2102-2119.

7.62. Linhardt RJ & Gunay NS (1999) Production and Chemical Processing of Low Molecular Weight Heparins. *Semin. Thromb. Hemost.* 25 Suppl 3:5-16.

7.63. Schulman S, Zondag M, Linkins L, Pasca S, Cheung YW, de Sancho M, Gallus A, Lecumberri R, Molnar S, Ageno W, Le Gal G, Falanga A, Hulegardh E, Ranta S, Kamphuisen P, Debourdeau P, Rigamonti V, Ortel TL, & Lee A (2015) Recurrent Venous Thromboembolism in Anticoagulated Patients with Cancer: Management and Short-term Prognosis. *J. Thromb. Haemost.* 13(6):1010-1018.

7.64. Renne T, Pozgajova M, Gruner S, Schuh K, Pauer HU, Burfeind P, Gailani D, & Nieswandt B (2005) Defective Thrombus Formation in Mice Lacking Coagulation Factor XII. *J. Exp. Med.* 202(2):271-281.

7.65. Cheng Q, Tucker EI, Pine MS, Sisler I, Matafonov A, Sun MF, White-Adams TC, Smith SA, Hanson SR, McCarty OJ, Renne T, Gruber A, & Gailani D (2010) A Role for Factor XIIa-mediated Factor XI Activation in Thrombus Formation In Vivo. *Blood* 116(19):3981-3989.

7.66. Kleinschnitz C, Stoll G, Bendszus M, Schuh K, Pauer HU, Burfeind P, Renne C, Gailani D, Nieswandt B, & Renne T (2006) Targeting Coagulation Factor XII Provides Protection from Pathological Thrombosis in Cerebral Ischemia Without Interfering with Hemostasis. *J. Exp. Med.* 203(3):513-518.

7.67. Matafonov A, Leung PY, Gailani AE, Grach SL, Puy C, Cheng Q, Sun MF, McCarty OJ, Tucker EI, Kataoka H, Renne T, Morrissey JH, Gruber A, & Gailani D (2014) Factor XII Inhibition Reduces Thrombus Formation in a Primate Thrombosis Model. *Blood* 123(11):1739-1746.

7.68. Jain S, Pitoc GA, Holl EK, Zhang Y, Borst L, Leong KW, Lee J, & Sullenger BA (2012) Nucleic Acid Scavengers Inhibit Thrombosis Without Increasing Bleeding. *Proc. Natl. Acad. Sci. U.S.A.* 109(32):12938-12943.

7.69. Travers RJ, Shenoi RA, Kalathottukaren MT, Kizhakkedathu JN, & Morrissey JH (2014) Nontoxic Polyphosphate Inhibitors Reduce Thrombosis While Sparing Hemostasis. *Blood* 124(22):3183-3190.

7.70. Shenoi RA, Kalathottukaren MT, Travers RJ, Lai BF, Creagh AL, Lange D, Yu K, Weinhart M, Chew BH, Du C, Brooks DE, Carter CJ, Morrissey JH, Haynes CA, & Kizhakkedathu JN (2014) Affinity-based Design of a Synthetic Universal Reversal Agent for Heparin Anticoagulants. *Sci. Transl. Med.* 6(260):260ra150.

7.71. Sun C, Tang T, Uludag H, & Cuervo JE (2011) Molecular Dynamics Simulations of DNA/PEI Complexes: Effect of PEI Branching and Protonation State. *Biophys. J.* 100(11):2754-2763.

7.72. Vanommeslaeghe K, Hatcher E, Acharya C, Kundu S, Zhong S, Shim J, Darian E, Guvench O, Lopes P, Vorobyov I, & Mackerell AD, Jr. (2010) CHARMM General Force Field: A Force Field for Drug-like Molecules Compatible with the CHARMM All-atom Additive Biological Force Fields. *J. Comput. Chem.* 31(4):671-690.

7.73. Sun C, Tang T, & Uludag H (2011) Molecular Dynamics Simulations of PEI Mediated DNA Aggregation. *Biomacromolecules* 12(10):3698-3707.

7.74. Sun C, Tang T, & Uludag H (2012) Molecular Dynamics Simulations for Complexation of DNA with 2 kDa PEI Reveal Profound Effect of PEI Architecture on Complexation. *J. Phys. Chem. B* 116(8):2405-2413.

7.75. Hart K, Foloppe N, Baker CM, Denning EJ, Nilsson L, & Mackerell AD, Jr. (2012) Optimization of the CHARMM Additive Force Field for DNA: Improved Treatment of the BI/BII Conformational Equilibrium. *J Chem Theory Comput* 8(1):348-362.

7.76. Phillips JC, Braun R, Wang W, Gumbart J, Tajkhorshid E, Villa E, Chipot C, Skeel RD, Kale L, & Schulten K (2005) Scalable Molecular Dynamics with NAMD. *J. Comput. Chem.* 26(16):1781-1802.

7.77. Darden T, York D, & Pedersen L (1993) Particle Mesh Ewald - an N.Log(N) Method for Ewald Sums in Large Systems. *J. Chem. Phys.* 98(12):10089-10092.

7.78. Ryckaert JP, Ciccotti G, & Berendsen HJC (1977) Numerical-Integration of Cartesian Equations of Motion of a System with Constraints - Molecular-Dynamics of N-Alkanes. *J. Comput. Phys.* 23(3):327-341.

7.79. Humphrey W, Dalke A, & Schulten K (1996) VMD: Visual Molecular Dynamics. *J. Mol. Graph.* 14(1):33-38, 27-38.

7.80. Korolev N, Lyubartsev AP, Nordenskiold L, & Laaksonen A (2001) Spermine: An "Invisible" Component in the Crystals of B-DNA. A Grand Canonical Monte Carlo and Molecular Dynamics Simulation Study. *J. Mol. Biol.* 308(5):907-917.

7.81. Korolev N, Lyubartsev AP, Laaksonen A, & Nordenskiold L (2002) On the Competition Between Water, Sodium Ions, and Spermine in Binding to DNA: A Molecular Dynamics Computer Simulation Study. *Biophys. J.* 82(6):2860-2875.

7.82. Korolev N, Lyubartsev AP, Laaksonen A, & Nordenskiold L (2003) A Molecular Dynamics Simulation Study of Oriented DNA with Polyamine and Sodium Counterions: Diffusion and Averaged Binding of Water and Cations. *Nucleic Acids Res.* 31(20):5971-5981.

7.83. Korolev N, Lyubartsev AP, Laaksonen A, & Nordenskiold L (2004) A Molecular Dynamics Simulation Study of Polyamine- and Sodium-DNA. Interplay Between Polyamine Binding and DNA Structure. *Eur. Biophys. J.* 33(8):671-682.

7.84. Korolev N, Lyubartsev AP, Laaksonen A, & Nordenskiold L (2004) Molecular Dynamics Simulation Study of Oriented Polyamine- and Na-DNA: Sequence Specific Interactions and Effects on DNA Structure. *Biopolymers* 73(5):542-555.

7.85. Ziebarth J & Wang Y (2009) Molecular Dynamics Simulations of DNA-Polycation Complex Formation. *Biophys. J.* 97(7):1971-1983.

7.86. Jeffrey GA & Saenger W (1994) Chapter 2: Definitions and Concepts. *Hydrogen Bonding in Biological Structures* (Springer-Verlag, Heidelberg, Germany), pp 15-48.

7.87. Baker EN & Hubbard RE (1984) Hydrogen Bonding in Globular Proteins. *Prog. Biophys. Mol. Biol.* 44(2):97-179.

7.88. Takeuchi H, Watanabe N, Satoh Y, & Harada I (1989) Effects of Hydrogen Bonding on the Tyrosine Raman Band in the 1300-1150 cm-1 Region. *J.Raman Spectrosc.* 20:233-237.

7.89. Bohm HJ (1992) LUDI: Rule-based Automatic Design of New Substituents for Enzyme Inhibitor Leads. *J. Comput. Aided Mol. Des.* 6(6):593-606.

8.1. Whitehead KA, Langer R, & Anderson DG (2009) Knocking Down Barriers: Advances in siRNA Delivery. *Nat. Rev. Drug Discov.* 8(2):129-138.

8.2. Croce CM (2009) Causes and Consequences of microRNA Dysregulation in Cancer. *Nat. Rev. Genet.* 10(10):704-714.

8.3. Mitchell PS, Parkin RK, Kroh EM, Fritz BR, Wyman SK, Pogosova-Agadjanyan EL, Peterson A, Noteboom J, O'Briant KC, Allen A, Lin DW, Urban N, Drescher CW, Knudsen BS, Stirewalt DL, Gentleman R, Vessella RL, Nelson PS, Martin DB, & Tewari M (2008) Circulating microRNAs as Stable Blood-based Markers for Cancer Detection. *Proc. Natl. Acad. Sci. U.S.A.* 105(30):10513-10518.

8.4. Brase JC, Johannes M, Schlomm T, Falth M, Haese A, Steuber T, Beissbarth T, Kuner R, & Sultmann H (2011) Circulating miRNAs are Correlated with Tumor Progression in Prostate Cancer. *Int. J. Cancer* 128(3):608-616.

8.5. Corcoran C, Friel AM, Duffy MJ, Crown J, & O'Driscoll L (2011) Intracellular and Extracellular microRNAs in Breast Cancer. *Clin. Chem.* 57(1):18-32.

8.6. Kosaka N, Iguchi H, & Ochiya T (2010) Circulating microRNA in Body Fluid: A New Potential Biomarker for Cancer Diagnosis and Prognosis. *Cancer Sci.* 101(10):2087-2092.

8.7. Zelphati O, Uyechi LS, Barron LG, & Szoka FC, Jr. (1998) Effect of Serum Components on the Physico-chemical Properties of Cationic Lipid/Oligonucleotide Complexes and on Their Interactions with Cells. *Biochim. Biophys. Acta* 1390(2):119-133.

8.8. Oupicky D, Konak C, Dash PR, Seymour LW, & Ulbrich K (1999) Effect of Albumin and Polyanion on the Structure of DNA Complexes with Polycation Containing Hydrophilic Nonionic Block. *Bioconjug. Chem.* 10(5):764-772.

8.9. Esko JD & Lindahl U (2001) Molecular Diversity of Heparan Sulfate. *J. Clin. Invest.* 108(2):169-173.

8.10. Turnbull J, Powell A, & Guimond S (2001) Heparan Sulfate: Decoding a Dynamic Multifunctional Cell Regulator. *Trends Cell Biol.* 11(2):75-82.

8.11. Ruponen M, Yla-Herttuala S, & Urtti A (1999) Interactions of Polymeric and Liposomal Gene Delivery Systems with Extracellular Glycosaminoglycans: Physicochemical and Transfection Studies. *Biochim. Biophys. Acta* 1415(2):331-341.

8.12. Ito T, Iida-Tanaka N, & Koyama Y (2008) Efficient In Vivo Gene Transfection by Stable DNA/PEI Complexes Coated by Hyaluronic Acid. *J. Drug Target.* 16(4):276-281.

8.13. He Y, Cheng G, Xie L, Nie Y, He B, & Gu Z (2013) Polyethyleneimine/DNA Polyplexes with Reduction-sensitive Hyaluronic Acid Derivatives Shielding for Targeted Gene Delivery. *Biomaterials* 34(4):1235-1245.

8.14. Choudhury CK, Kumar A, & Roy S (2013) Characterization of Conformation and Interaction of Gene Delivery Vector Polyethylenimine with Phospholipid Bilayer at Different Protonation State. *Biomacromolecules* 14(10):3759-3768.

8.15. Tarek M (2005) Membrane Electroporation: A Molecular Dynamics Simulation. *Biophys. J.* 88(6):4045-4053.

8.16. Breton M, Delemotte L, Silve A, Mir LM, & Tarek M (2012) Transport of siRNA through Lipid Membranes Driven by Nanosecond Electric Pulses: An Experimental and Computational Study. *J. Am. Chem. Soc.* 134(34):13938-13941.

8.17. Beddoes CM, Case CP, & Briscoe WH (2015) Understanding Nanoparticle Cellular Entry: A Physicochemical Perspective. *Adv. Colloid Interface Sci.* 218:48-68.

8.18. Voulgarakis NK, Rasmussen KO, & Welch PM (2009) Dendrimers as Synthetic Gene Vectors: Cell Membrane Attachment. *J. Chem. Phys.* 130(15):155101.

8.19. Ding HM & Ma YQ (2013) Design Maps for Cellular Uptake of Gene Nanovectors by Computer Simulation. *Biomaterials* 34(33):8401-8407.

8.20. Vacha R, Martinez-Veracoechea FJ, & Frenkel D (2011) Receptor-Mediated Endocytosis of Nanoparticles of Various Shapes. *Nano Lett.* 11(12):5391-5395.

8.21. Ding HM & Ma YQ (2012) Role of Physicochemical Properties of Coating Ligands in Receptor-mediated Endocytosis of Nanoparticles. *Biomaterials* 33(23):5798-5802.

8.22. Ouyang D, Zhang H, Parekh HS, & Smith SC (2011) The Effect of pH on PAMAM Dendrimer-siRNA Complexation: Endosomal Considerations as Determined by Molecular Dynamics Simulation. *Biophys. Chem.* 158(2-3):126-133.

8.23. Pavan GM, Posocco P, Tagliabue A, Maly M, Malek A, Danani A, Ragg E, Catapano CV, & Pricl S (2010) PAMAM Dendrimers for siRNA Delivery: Computational and Experimental Insights. *Chemistry* 16(26):7781-7795.

8.24. Karatasos K, Posocco P, Laurini E, & Pricl S (2012) Poly(amidoamine)-based Dendrimer/siRNA Complexation Studied by Computer Simulations: Effects of pH and Generation on Dendrimer Structure and siRNA Binding. *Macromol. Biosci.* 12(2):225-240.

8.25. Boussif O, Lezoualc'h F, Zanta MA, Mergny MD, Scherman D, Demeneix B, & Behr JP (1995) A Versatile Vector for Gene and Oligonucleotide Transfer into Cells in Culture and In vivo: Polyethylenimine. *Proc. Natl. Acad. Sci. U.S.A.* 92(16):7297-7301.

8.26. Khandogin J & Brooks CL (2005) Constant pH Molecular Dynamics with Proton Tautomerism. *Biophys. J.* 89(1):141-157.

8.27. Baptista AM, Teixeira VH, & Soares CM (2002) Constant-pH Molecular Dynamics Using Stochastic Titration. *J. Chem. Phys.* 117(9):4184-4200.

8.28. Mongan J, Case DA, & McCammon JA (2004) Constant pH Molecular Dynamics in Generalized Born Implicit Solvent. *J. Comput. Chem.* 25(16):2038-2048.

8.29. Wallace JA & Shen JK (2011) Continuous Constant pH Molecular Dynamics in Explicit Solvent with pH-Based Replica Exchange. *J. Chem. Theory Comput.* 7(8):2617-2629.

8.30. Goh GB, Knight JL, & Brooks CL (2012) Constant pH Molecular Dynamics Simulations of Nucleic Acids in Explicit Solvent. *J. Chem. Theory Comput.* 8(1):36-46.

8.31. Donnini S, Tegeler F, Groenhof G, & Grubmuller H (2011) Constant pH Molecular Dynamics in Explicit Solvent with lambda-Dynamics. *J. Chem. Theory Comput.* 7(6):1962-1978.

8.32. Sugita Y & Okamoto Y (1999) Replica-exchange Molecular Dynamics Method for Protein Folding. *Chem. Phys. Lett.* 314(1-2):141-151.

8.33. Hamelberg D, Mongan J, & McCammon JA (2004) Accelerated Molecular Dynamics: A Promising and Efficient Simulation Method for Biomolecules. *J. Chem. Phys.* 120(24):11919-11929.

8.34. Laio A & Parrinello M (2002) Escaping Free-energy Minima. *Proc. Natl. Acad. Sci. U.S.A.* 99(20):12562-12566.

8.35. Tsallis C & Stariolo DA (1996) Generalized Simulated Annealing. *Phys. A Stat. Theor. Phys.* 233:395–406.

8.36. Levitt M (1976) A Simplified Representation of Protein Conformations for Rapid Simulation of Protein Folding. *J. Mol. Biol.* 104(1):59-107.

8.37. Goula D, Remy JS, Erbacher P, Wasowicz M, Levi G, Abdallah B, & Demeneix BA (1998) Size, Diffusibility and Transfection Performance of Linear PEI/DNA Complexes in the Mouse Central Nervous System. *Gene Ther.* 5(5):712-717.

8.38. Sun C, Tang T, & Uludag H (2013) A Molecular Dynamics Simulation Study on the Effect of Lipid Substitution on Polyethylenimine Mediated siRNA Complexation. *Biomaterials* 34(11):2822-2833.

8.39. Travers RJ, Shenoi RA, Kalathottukaren MT, Kizhakkedathu JN, & Morrissey JH (2014) Nontoxic Polyphosphate Inhibitors Reduce Thrombosis While Sparing Hemostasis. *Blood* 124(22):3183-3190.

APPENDIX A: Supplementary Information for Chapter 3

A.1. Polymer Synthesis and Characterization

PrA moieties were grafted onto 1.2 kDa PEI via *N*-acylation. ^{1}H-NMR spectrum of PrA substituted PEIs showed characteristic proton resonance peaks of PEI at 2.40 to 3.50 ppm, and that of PrA at 1.05 ppm and 2.11 ppm, confirming the substitution reactions. The substitution amount of PrAs onto PEIs was increased with the increase in the PrA feeding ratio (PrA/PEI, mol/mol). The highest amount of PrA grafted onto PEI was 1.59 (PrA/PEI, mol/mol), from the reaction with feed ratio of 4 (PrA/PEI, mol/mol); this corresponds to consumption of 15.9% of the primary amines. The efficacy of substitution is defined based on the ratio of the substitution amounts calculated from the ^{1}H-NMR spectrum (α) to the PrA feeding ratios, and represented as percentages. The efficacy of PrA substitution was the highest (~70%) when the feed ratio was 1, and it gradually decreased to ~40% with the further increase in the feed ratio (Figure A.1). All the designed polymers were readily soluble in water.

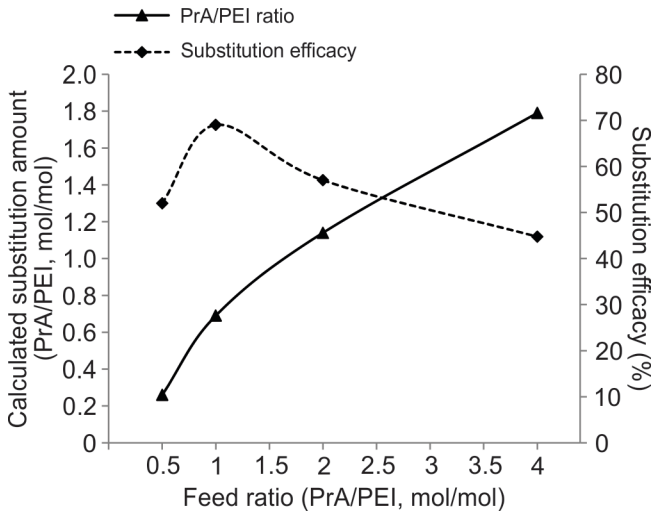

Figure A.1. Summary of polymer synthesis. The amount of PrA substitution is calculated from ^{1}H-NMR spectrum, and the substitution efficacy is defined based on the ratio of calculated PrA substitution amount to the feed ratios.

A.2. Comparison of the Efficacy and Cytotoxicity of PrA-Modified LMW PEIs with 25 kDa PEI

The performance of the native and PrA conjugated 1.2 kDa PEIs were compared to that of 25 kDa PEI in K562 cells. Polymers with low PrA substitution amounts, $\alpha = 0.26$ and $\alpha = 0.69$, displayed comparable performances to 25 kDa PEI, while further increase in the substitution amount caused a significant reduction in the siRNA delivery efficacy of 1.2 kDa PEI. In comparison with 25 kDa PEI, there was a ~0.5-fold decrease in MFI of the systems $\alpha = 0.26$ and $\alpha = 0.69$ (Figure A.2a); 48.4 ± 2.5% and 44.1 ± 0.5% of the cells were FAM-siRNA positive in these systems while delivery with 25 kDa PEI resulted in 62.1 ± 1.0% of the population to be FAM-siRNA positive (Figure A.2b). We further compared the efficacy of these polymers for silencing activity of siRNA. Among other PrA conjugated systems, $\alpha = 0.69$ delivered the best performance in terms of siRNA's silencing activity; decrease in green fluorescence protein (GFP) mean fluorescence intensity (MFI) was 32.9 ± 2.5%, 44.2 ± 3.3% and 31.2 ± 1.0% after 3, 6 and 9 of treatment, respectively; while delivery with 25 kDa PEI resulted in 50.2 ± 1.8%, 73.8 ± 6.0% and 71.2 ± 2.4% decrease in GFP MFI (Figure A.2c). Decrease in GFP-positive cell population (Figure A.2d) was well correlated with the decrease in GFP MFI, and $\alpha = 0.69$ again delivered a comparable albeit not superior performance to that of 25 kDa PEI.

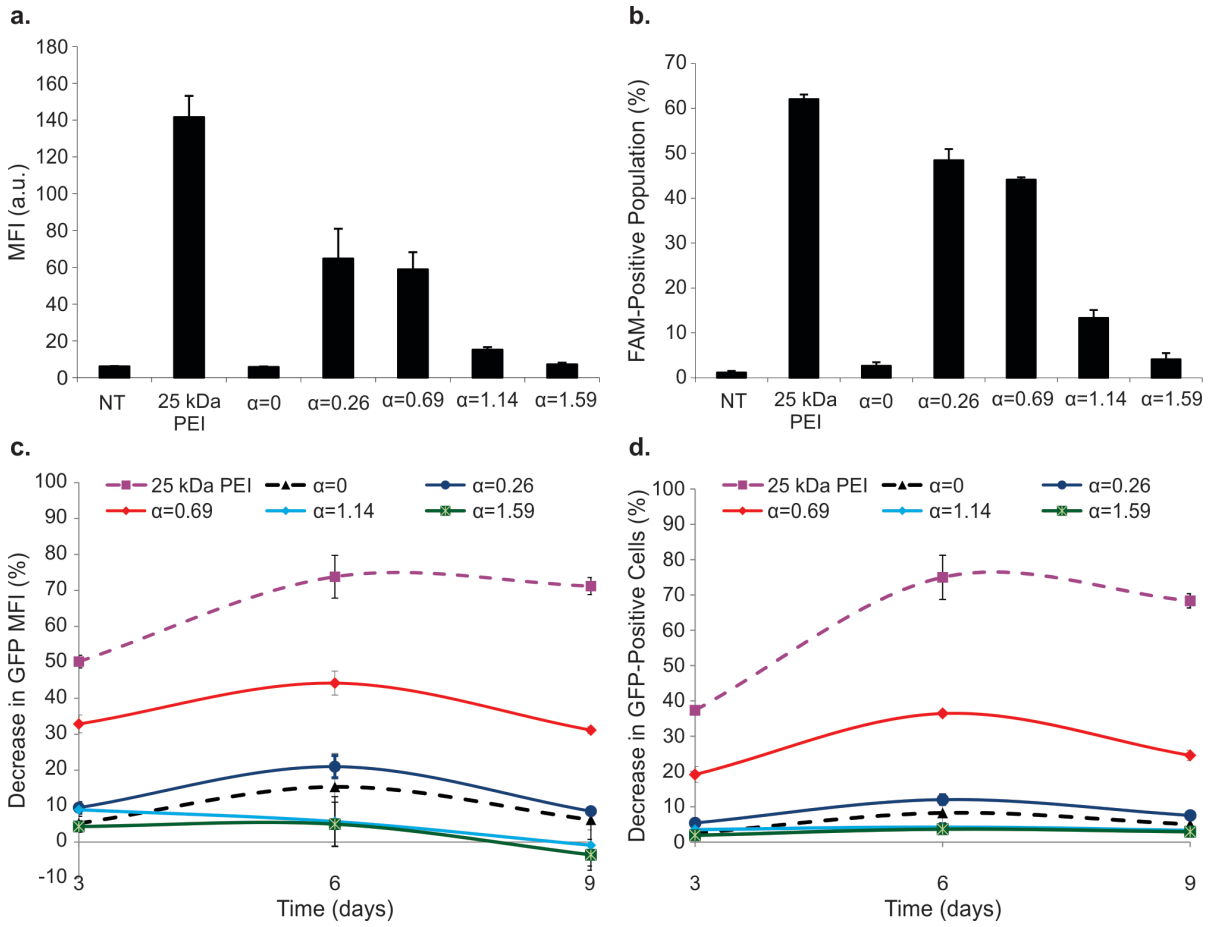

Figure A.2. (a) MFI and **(b)** percentage of FAM-siRNA positive K562 cells after 24 h exposure to complexes prepared with FAM-labeled siRNA and 25 kDa PEI, native or PrA conjugated 1.2 kDa PEIs at polymer:siRNA ratio of 6:1 (w/w), with final siRNA concentration of 60 nM. **(c)** Decrease in mean GFP fluorescence and, **(d)** decrease in GFP-positive cell population after 3, 6 and 9 days of treatment with final siRNA concentration of 60 nM at polymer:siRNA ratio of 6:1 (w/w).

We also compared the cytotoxicity of the native and PrA-modified PEIs to 25 kDa PEI (Figure A.3). The cytotoxic profile of 25 kDa PEI was similar to that of native and/or PrA-modified PEIs at the low polymer:siRNA weight ratios tested (2.5:1, 5:1, 7.5:1 and 10:1), where all the studied polymers displayed minor toxicities with cell viability of ~80%. At higher polymer concentrations (polymer:siRNA w:w = 20:1 and 40:1), 25 kDa PEI induced the highest toxicity of all, with cell viabilities of 11.5 ± 2.4% and 7.5 ± 0.3%, respectively. In comparison

with LMW PEIs, 25 kDa PEI reduced the cell viability at least 7- and 4-fold at these two highest polymer concentrations.

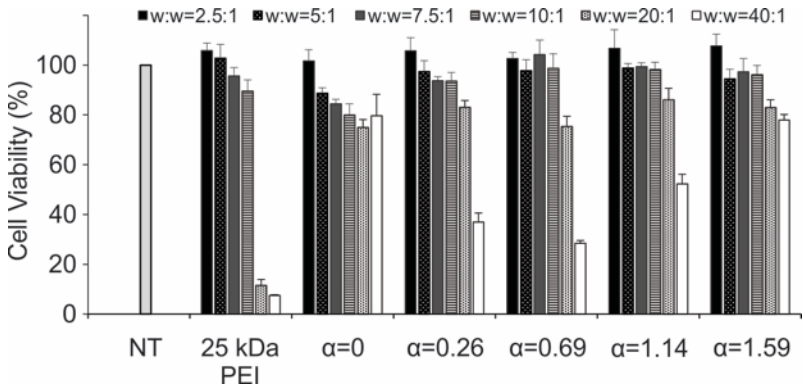

Figure A.3. Relative K562 cell viabilities after 72 h exposure to complexes of 25 kDa PEI and 1.2 kDa PEIs with different PrA substitution amounts, prepared at various polymer:siRNA (w:w) ratios.

A.3. Compactness of the Complexes

In order to explore the influence of PrA substitution on the compactness of the complexes, we calculated the radius of gyration (R_g) of the complexes by including all the 4 siRNAs and 16 native and/or modified PEIs in the calculation (Figure A.4a). The kinetics of complexation displayed similarities between the systems $\alpha = 0$, $\alpha = 0.25$ and $\alpha = 2$, while $\alpha = 0.75$ and $\alpha = 1$ showed slightly different characteristics within the first ~120 ns. In the system $\alpha = 0.75$, two of the PrA substituted PEIs were observed to be fully solvated and loose during the first 110 ns, as opposed to all the native and/or modified PEIs being in contact with the siRNAs in other systems shortly after minimization and heating. These loose PEIs managed to establish contacts with the complex until 150 ns, and remained intact till the end of simulation time. Hence, the higher trend of the system $\alpha = 0.75$ within the first ~120 ns could be attributed to this observed behavior. Despite the different trends observed in the kinetics of complexation, all systems reached

dynamic equilibrium by 120 ns. The average R_g values of the complexes were calculated to be 27.96 ± 0.20 Å, 27.88 ± 0.22 Å, 28.40 ± 0.33 Å, 28.06 ± 0.24 Å, 27.79 ± 0.13 Å for the systems α = 0, α = 0.25, α = 0.75, α = 1 and α = 2, respectively (Figure A.4b). The similar R_g values of the complexes indicate the almost negligible effect of PrA substitution on the compactness of the complexes.

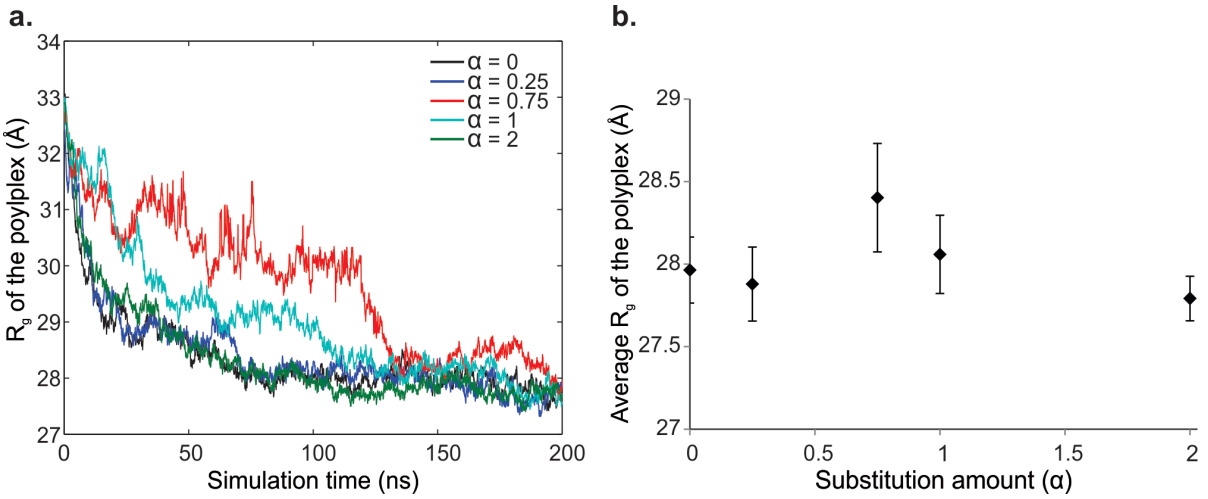

Figure A.4. (a) R_g of the complexes as a function of simulation time, and **(b)** average R_g values of the complexes calculated over the last 80 ns of the simulations as a function of substitution amount.

We have also investigated the sizes of the complexes in experiments, prepared at polymer:siRNA weight ratio of 6:1 (Figure A.5). The measured hydrodynamic diameter of the complexes were 140.1 ± 26, 266.4 ± 70, 269.6 ± 57.6, 407.5 ± 124.1 and 297.6 ± 72.7 nm for systems α = 0, α = 0.26, α = 0.69, α = 1.14 and α = 1.59, respectively. The sizes of the PrA-modified systems are slightly higher than the unmodified system, α = 0, although the difference was insignificant. Increasing the extent of PrA modification did not seem to have a systematic influence on the particle sizes.

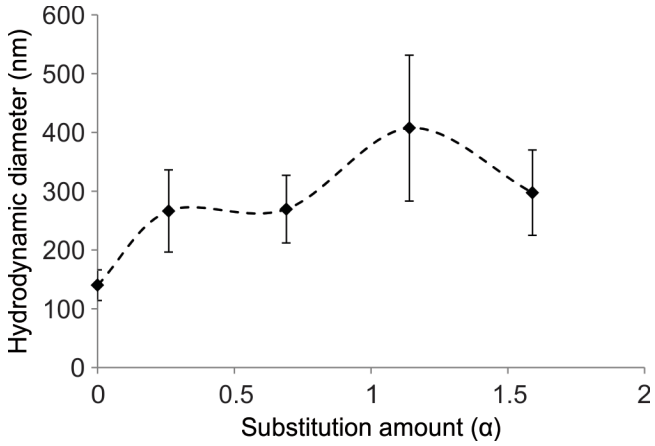

Figure A.5. Hydrodynamic diameter of the complexes with different PrA substitution amounts prepared at polymer:siRNA weight ratio of 6:1.

A.4. Calculation of PrA Surface Density

For the calculation of surface density of PrA moieties, we approximated each complex by a sphere and determined the radius of the sphere from the equality of Eqn. A.1 and Eqn. A.2, which both define the moment of inertia of a solid sphere about its center of mass:

$$I = \frac{2}{5}mR^2 \qquad \text{(Eqn. A.1)}$$

$$I = mR_g{}^2 \qquad \text{(Eqn. A.2)}$$

where I is the moment of inertia, m is the mass, R is the radius, and R_g is the radius of gyration. The final equation used in the calculation of the radius of the complexes is given in Eqn. A.3:

$$R = \sqrt{\frac{5}{2}}R_g \qquad \text{(Eqn. A.3)}$$

From the radial distribution function (RDF) calculations, we then determined the distance closest to the radius of the sphere, and assigned that as the cut-off for the definition of the complex surface. The number of PrA carbon atoms residing inside the complex is determined from the number integral over RDF of the PrA carbons (Figure A.6) in each system, and the

amount of PrA carbon atoms outside the spherical surface is calculated by subtracting the number of PrA carbons inside the complex from the total number of PrA carbon atoms (12, 36, 48 and 96 for systems α = 0.25, α = 0.75, α = 1 and α = 2, respectively) in each system. The resulting number is then divided by the surface area of each sphere to get the surface density of PrA moieties. Calculated radii and number of PrA carbon atoms inside and outside the spherical surface, percentage of the PrA carbons residing inside the complex along with the surface densities are given in Table A.1.

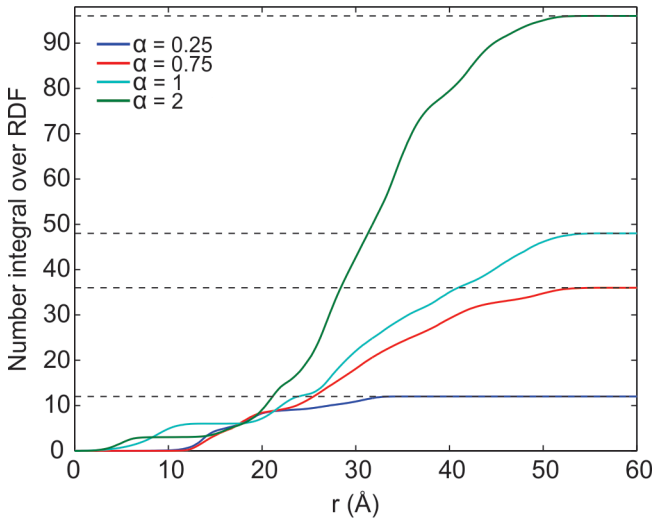

Figure A.6. Number integral over the RDF of PrA carbon atoms as a function of the distance from the COM of the complex. The black dashed lines represent the total number of PrA carbon atoms in each system: 12, 36, 48 and 96 for the systems α = 0.25, α = 0.75, α = 1 and α = 2, respectively.

Table A.1. Details of the calculation of surface density of the PrA moieties.

System	R_g (Å)	R (Å)	Cut-off (Å)	Number integral at the cut-off	Number of PrA Cs outside the surface	% of PrA Cs residing inside the complex	Surface density of PrA moieties (x 10^{-4}) (Number of PrA/Å^2)
α = 0.25	27.88	44.05	44.13	12.00	0.00	100.00	0
α = 0.75	28.40	44.87	44.88	32.68	3.32	90.78	1.31
α = 1	28.06	44.33	44.38	39.35	8.65	81.98	3.50
α = 2	27.79	43.91	44.13	88.77	7.23	92.47	2.96

A.5. Location of Water Molecules and Hydration of Complexes

Association of solutes in aqueous environments results in dislocation of water molecules. In order to monitor the motion of water molecules during complexation process, we investigated the change in the water distribution. We plotted the RDF of water molecules from the center of mass (COM) of the complex in the initial configuration (Figure A.7, left panel) and over the dynamic equilibrium (last 80 ns) (Figure A.7, right panel). The distribution in the initial configurations is quite similar within the studied systems, except the differences in the location of the first sharp peaks. The highest peaks are located at 1.38 Å, 1.88 Å, 2.74 Å, 0.88 Å and 5.13 Å in systems α = 0, α = 0.25, α = 0.75, α = 1 and α = 2, respectively; indicating the high probability of finding water molecules at the given distances. Water distribution decreases after the first sharp peaks until ~25 Å, due to having the majority of the siRNA and PEI atoms within this region making it harder for waters to get in. After 25 Å, distribution starts to increase slowly, and then levels off at 40 Å. The analysis over the dynamic equilibrium (Figure A.7, right panel) shows that complex formation decreases the water distribution in general (note the scale difference between Figure A.7 left and right panels) and makes it more featureless and homogenous (i.e. no particular peaks indicating a more structured distribution). In comparison with all the other systems, it is almost 5 to 10 times less likely to find water molecules close to the COM of the complex in system α = 2. This could be attributed to: (*i*) slightly smaller initial

water distribution close to COM (Figure A.7e, left panel), and (*ii)* migration of PrAs moieties (along with their PEIs) into the core of the complex, hence leaving less space for water to occupy. In all the systems, there is a decreasing trend until 20 Å (in α = 2, starting from 7 Å), due to water molecules being dislocated from their initial positions with complex formation. Since the majority of the complex atoms are located within the first 20-25 Å, there is an increase in water distribution past this point until 40 Å. Finally, the distribution levels off beyond 40 Å.

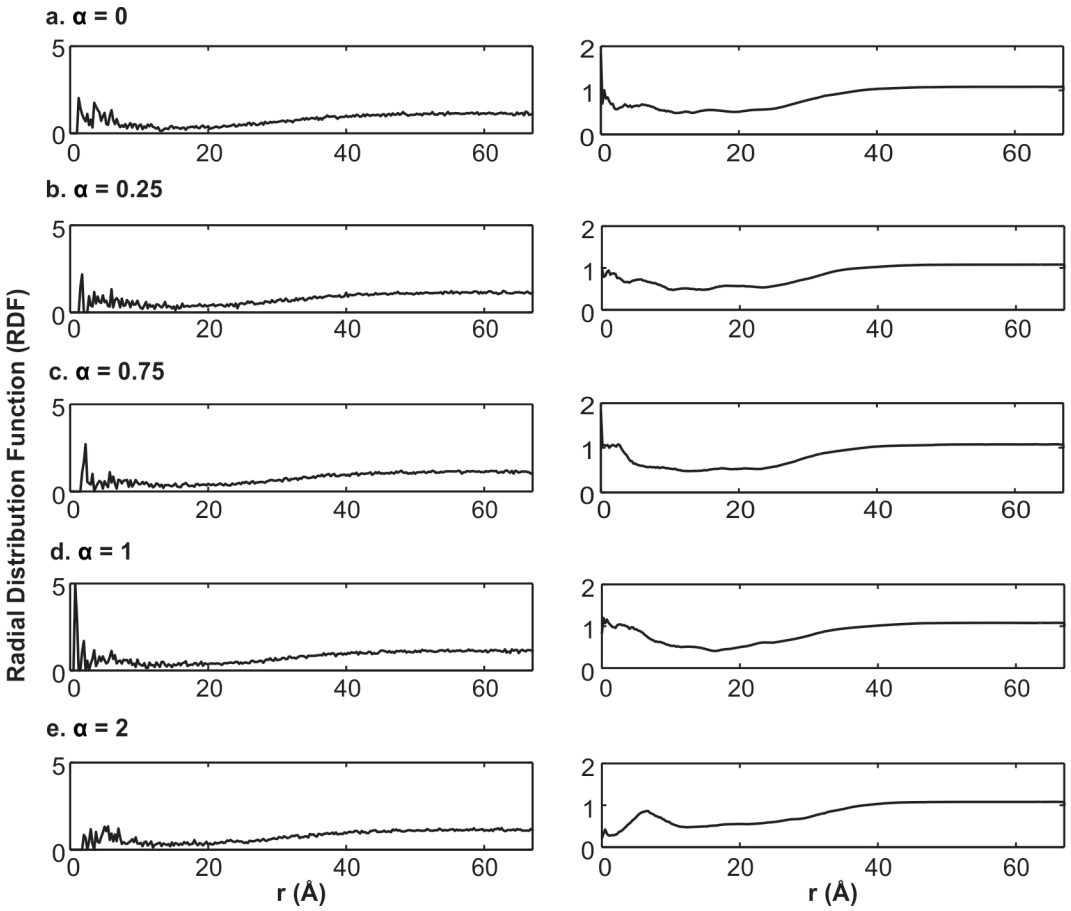

Figure A.7. Radial distribution function of water molecules, in the initial configuration (left panel), and the average over the last 80 ns of the simulations (right panel), in systems **(a)** α = 0, **(b)** α = 0.25, **(c)** α = 0.75, **(d)** α = 1, **(e)** α = 2.

We then explored the number of water molecules in the hydration shell of siRNAs and PEIs. Here, we defined the hydration shell to be 3 Å from any siRNA/PEI atom. In Figure A.8, we plot the number of water molecules in the hydration shell as a function of simulation time. The curves follow a decreasing trend within the first ~100 ns in all the systems, again confirming the dislocation of water molecules previously adhering to the siRNA and PEI surfaces to the periphery as the complex forms. All the curves reach plateau past 100 ns, indicating that the simulations come to dynamic equilibrium.

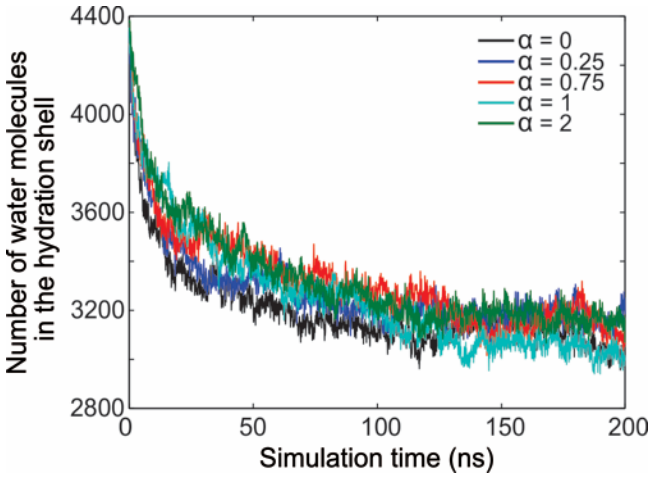

Figure A.8. Number of water molecules in the hydration shell of siRNAs/PEIs as a function of simulation time.

A.6. PEI Binding Dynamics

To see the effect of PrA substitutions on the binding capability of PEI to siRNA, we plot the number of PEI Ns in close contact with siRNAs (Figure A.9a). The close contact distance was defined to be within 4 Å of any siRNA N/Os. The increasing trend in the number of close contacts established between PEIs and siRNAs within the first ~120 ns in all the simulated systems indicates the formation of complexes. While the systems α = 0, α = 0.25, α = 0.75 and

α = 1 displayed similar trends, the number of close contact PEI Ns is higher in system α = 2 in the last ~50 ns.

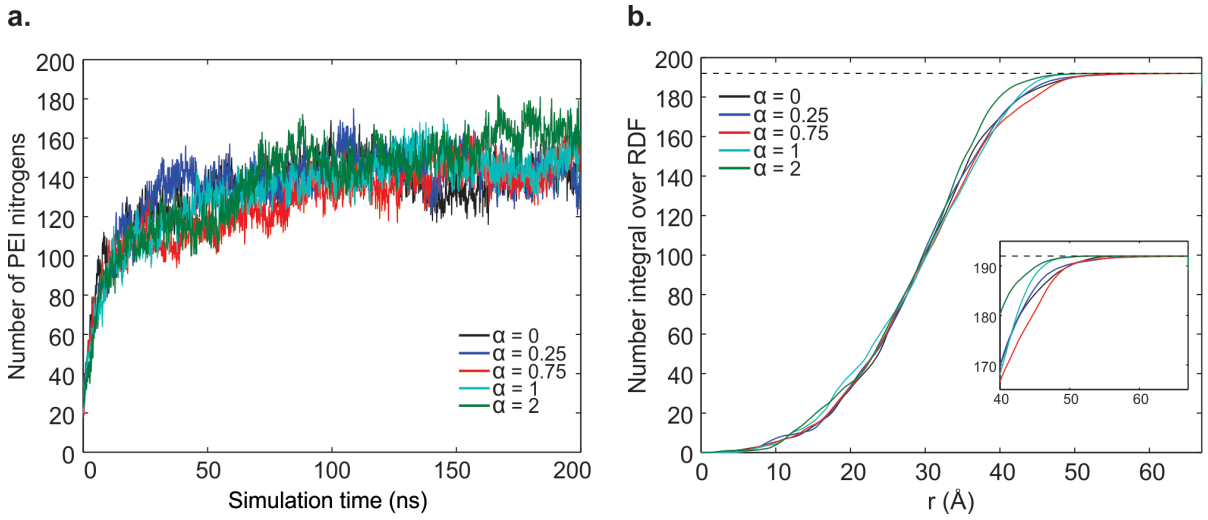

Figure A.9. (a) Number of PEI nitrogens in close contact with siRNA as a function of simulation time. **(b)** Number integral over the RDF of protonated PEI nitrogens as a function of the distance from the COM of the complex. The black dashed line represents the total number of protonated PEI nitrogens (192) in each system. The inset shows the close-up of the distribution past 40 Å.

Migration of PrA moieties into the core area of the complex made us wonder about its possible effect on the cationic surface charge of the complexes. Following the same procedure in Section A.4 for the definition of the complex surface, we calculated the number of PEI's protonated amine groups (N^+s) on the surface of the particles from the number integral of N^+s (Figure A.9b) at the defined cut-off. The higher number of PEI N^+s past 40 Å in the systems α = 1 and α = 2 (Figure A.9b, inset) indicates that majority of the PEI N^+s are enclosed inside the complex in comparison to the systems with lower PrA substitution amounts, leaving less cationic groups on the surface of the particles.

A.7. Stability of siRNAs

The alterations in siRNA structure due to polymer binding are investigated by examining the H-bonding pattern between the two strands of siRNAs throughout the simulations. Each system has 4 siRNA molecules, so each curve in Figure A.10a represents the number of H-bonds summed over 4 siRNAs. In all the systems, H-bonds follow a decreasing trend within the first ~100 ns, indicating the changes in siRNA structure due to complex formation; and systems reach plateau after ~120 ns. Among others, it is apparent that system $\alpha = 2$ has the least number of H-bonds, indicating the migration of PrA moieties along with their associated PEIs to the core of the complex affecting the stability of siRNAs, hence altering their structure.

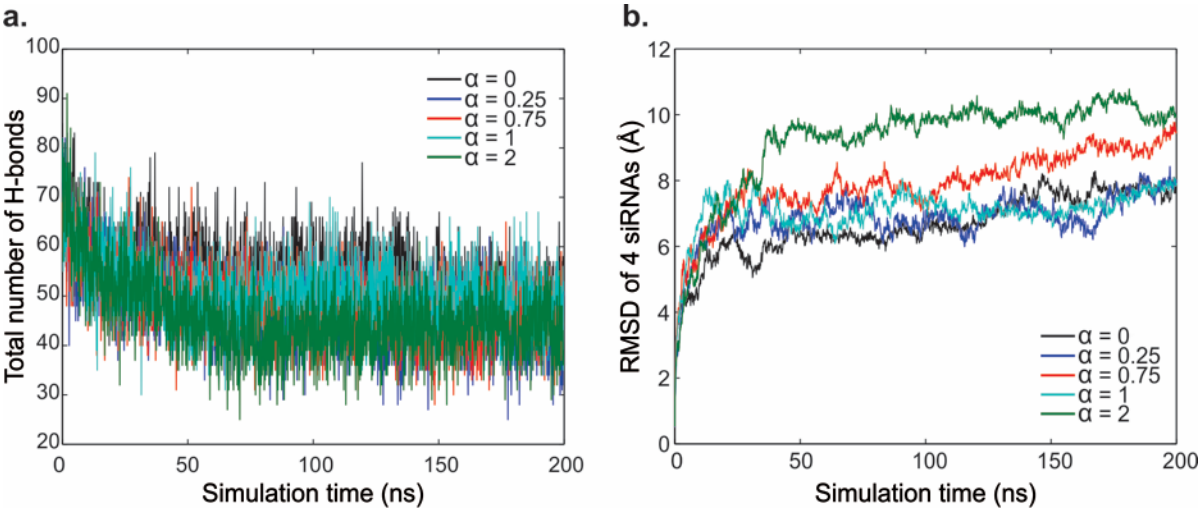

Figure A.10. (a) Total number of H-bonds established between the two strands of each siRNA and **(b)** RMSD of the 4 siRNAs in each system as a function of the simulation time.

To further confirm the structural changes of siRNAs, we investigated the root mean square deviation (RMSD) of the 4 siRNAs with respect to their initial configurations in each system, as a function of the simulation time (Figure A.10b). As a result of complex formation, RMSD values increase within the first ~120 ns in all the studied systems. Similar RMSD trends are apparent among systems $\alpha = 0$, $\alpha = 0.25$ and $\alpha = 1$, and the first ~100 ns of system $\alpha = 0.75$. Past

~100 ns, the RMSD of system α = 0.75 started to increase and remained higher than those of α = 0, α = 0.25 and α = 1 in the rest of the simulation time. This could be attributed to the different complexation kinetics of system α = 0.75, i.e. two loose PrA substituted PEIs establishing contacts with the complex around ~110 and ~140 ns, respectively. Having more PEIs in contact caused siRNAs to be more deviated. System α = 2 displayed the highest deviation, again confirming the presence of PrA moieties in the core area of the complex affecting the stability of siRNA structure.

APPENDIX B: Supplementary Information for Chapter 4

B.1. Pre-equilibration of miRNA

miRNAs comprise loop and bulge regions in their structure, which are formed by base pair mismatches. These mismatches were reported to be the thermodynamic destabilizing elements in miRNAs [1]. To capture possible structural changes due to presence of bulge and mismatches, the initial structure of miRNA generated with make-na server (http://structure.usc.edu/make-na/) (Figure B.1a) was equilibrated prior to main simulations. A single miRNA was solvated in a cubic box of TIP3P water [2] and neutralized with the addition of 41 K^+ ions. A simulation was performed with NAMD [3] with a time step of 2 fs, periodic boundary conditions (PBC), electrostatics with particle mesh Ewald (PME) [4], cut-off of 12 Å for van der Waals and pairwise electrostatic interactions, and SHAKE algorithm [5] to constrain bonds involving hydrogen atoms. The system was first minimized for 5000 steps, and then heated from 0 K to 300 K with a harmonic restraint (10 kcal/mol·$Å^2$) on non-hydrogen atoms of the solute for 20 ps. After minimization and heating, the restraint was kept for 10 ns, and then removed for 60 ns NPT simulation. Temperature and pressure control was carried out with Langevin dynamics thermostat and Nosé-Hoover Langevin barostat. Trajectory was visualized and analyzed with VMD [6].

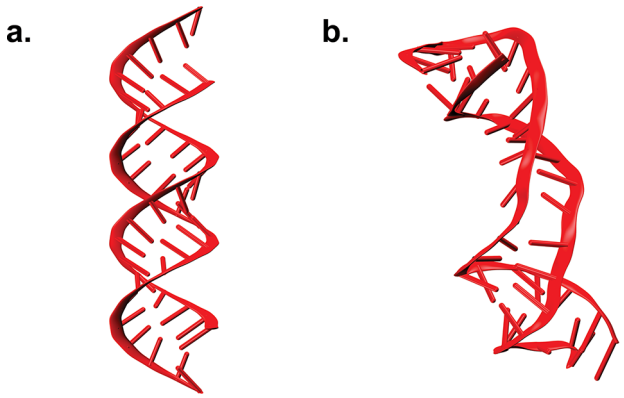

Figure B.1. Initial **(a)** and final **(b)** configurations of miRNA.

Visual inspection of the final configuration of miRNA (Figure B.1b) revealed the distorted, kinked miRNA structure; with 5′ and 3′ ends orienting to different directions. These observed structural features are in agreement with the previously reported duplex structures formed by miRNA and mRNA strands [7]. Stability of miRNA's base pairs was investigated via H-bond analysis, with donor-acceptor distance of 3 Å (Table B.1). H-bonding between 5′ and 3′ end bases (U1-G42, G21-C23) was not strong, as expected. Strong pairing was present till the occurrence of the bulge, A10; however base pairing was remarkably weakened between the bulge at A10 and the mismatch at G15, in agreement with the previously reported observations on the stability of loop and bulge regions [7].

Table B.1. Percentage occupancy of the H-bonds formed between base pairs**.**

sequence		**H-bonds formed between the base pairs (sense strand bases are in bold)**		
sense (5′ to 3′)	**anti-sense (3′ to 5′)**	**donor**	**acceptor**	**occupancy (%)**
-	U43	-	-	-
U1	G42	G42	**U1**	4.28
		U43	**U1**	3.57
		U1	G42	1.85
		U1	U43	1.57
		U1	A35	1.14
		U1	U36	0.14
A2	U41	U41	**A2**	52.07
		A2	U41	32.81
		G42	**A2**	15.83
		U43	**A2**	6.42
G3	C40	**G3**	C40	77.60
		C40	**G3**	31.38
		G42	**G3**	1.85
C4	G39	G39	**C4**	73.61
		C4	G39	35.09
		C4	U41	0.71
		U41	**C4**	0.57
U5	G38	**U5**	G38	35.66
		G38	**U5**	16.69
U6	G37	G37	**U6**	31.24
		U6	G37	1.71
A7	U36	**A7**	U36	40.09
		U36	**A7**	17.83
		G37	**A7**	0.14
U8	A35	**U8**	A35	50.36
		A35	**U8**	27.39
		U8	U36	0.29
		U36	**U8**	0.14
C9	G34	G34	**C9**	88.02
		C9	G34	36.23
A10	-	C33	**A10**	4.28
		A10	U32	0.14
G11	C33	**G11**	C33	11.41
		G11	U32	8.56
		U32	**G11**	3.99
		G11	G34	0.14
A12	U32	**A12**	G9	7.28
		U10	**A12**	3.57
		G9	**A12**	3.57
		A12	U10	1.57
		A12	C11	0.71
C13	G31	G31	**C13**	3.99
		U32	**C13**	3.28
		A30	**C13**	2.14
		C13	U32	1.00
		C13	G31	0.71
		C13	A30	0.29

Table B.1 (continued). Percentage occupancy of the H-bonds formed between base pairs**.**

sequence		**H-bonds formed between the base pairs (sense strand bases are in bold)**		
sense (5′ to 3′)	**anti-sense (3′ to 5′)**	**donor**	**acceptor**	**occupancy (%)**
U14	A30	**U14**	A30	2.14
		C29	**U14**	2.14
		A30	**U14**	1.71
		U14	C29	0.43
		C23	**U14**	0.14
G15	C29	**G15**	C28	34.80
		C28	**G15**	16.41
		G15	C29	6.13
		C23	**G15**	0.86
		G15	A30	0.14
		C29	**G15**	0.14
A16	C28	**A16**	C28	11.13
		A27	**A16**	0.29
U17	A27	A27	**U17**	14.69
		U17	A27	13.69
		U17	C28	7.70
		C26	**U17**	0.14
G18	C26	**G18**	C26	46.36
		A24	**G18**	7.70
		C26	**G18**	5.42
		A25	**G18**	4.28
		G18	A25	0.14
		G18	A24	0.14
U19	A25	A25	**U19**	9.99
		U19	A25	6.56
		U19	C26	0.57
U20	A24	C23	**U20**	5.28
		U20	A24	4.85
		A24	**U20**	2.28
G21	C23	**G21**	A24	7.70
		G21	C23	7.42
		C23	**G21**	4.56
		G21	A25	1.14
		A24	**G21**	0.43
A22	-	**A22**	A24	1.85
		A22	C23	1.43
		A24	**A22**	0.29
		C23	**A22**	0.14

B.2. Effect of Initial Configurations

To see the effect of initial structure on complex formation, a different initial configuration was tested, where all four PEIs were placed in the region between two siRNAs (Figure B.2a, left and middle panels). For the discussion in this section, the system simulated in Chapter 4 will be referred to as system 2s-4P-I, and the system simulated here using the second initial configuration will be referred to as system 2s-4P-II. For the investigation of miRNA's effect on siRNA-PEI complex integrity, as a second initial configuration, four miRNA molecules were introduced as to surround the final configuration of system 2s-4P-II (Figure B.2b, left and middle panels). For the discussion herein, the system simulated in Chapter 4 will be referred to as system 2s-4P-4m-I, and the system simulated here using the second initial configuration will be referred to as system 2s-4P-4m-II. Detailed information on the simulated systems is given in Table B.2. Results generated from systems 2s-4P-II and 2s-4P-4m-II are presented below and compared with those shown in Chapter 4.

Table B.2. Information on the two simulated systems in this section.

system name	molecules simulated	number of atoms	size of simulation box ($Å^3$)	number of K^+/Cl^-	simulation time restrained + free (ns)
2s-4P-II	2 siRNA, 4 PEI	80, 118	87 x 90 x 112	71/71	10 + 90
2s-4P-4m-II	2siRNA, 4PEI, 4 miRNA	210, 985	147 x 147 x 104	353/189	10 + 100

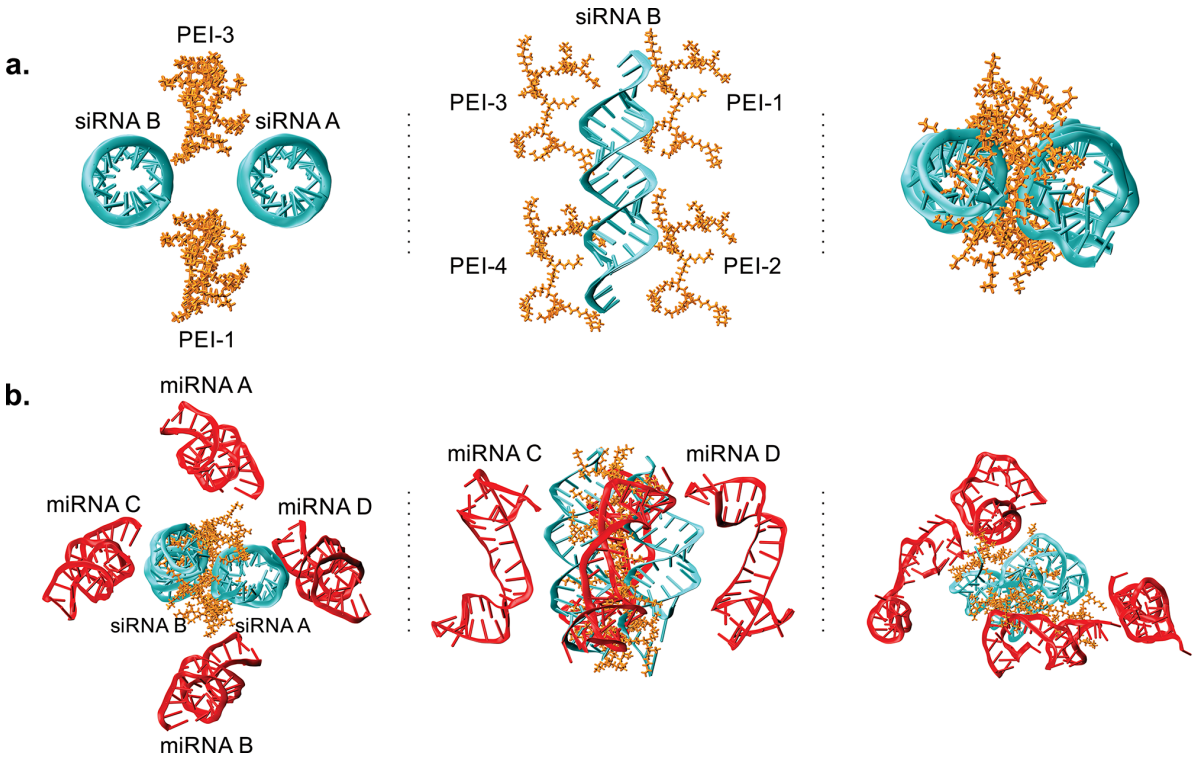

Figure B.2. Initial (left panel: top view, middle panel: side view) and final (right panel) new configurations of **(a)** 2s-4P-II, **(b)** 2s-4P-4m-II systems. siRNAs are given in cyan, while miRNAs and PEIs are represented in red and orange, respectively. Water and ions are removed for clarity.

B.2.1. PEI Binding to siRNA

Figure B.2a (right panel) shows the snapshot of the final configuration of 2s-4P-II system. All PEIs are localized in between the two siRNAs due to their initial placement, as opposed to having some PEIs surrounding centrally sequestered siRNAs as observed in 2s-4P-I system (Figure 4.3a, right panel).

In order to compare the compactness of siRNA arrangement for different initial configurations, the radius of gyration (R_g) of two siRNA in 2s-4P-II system is plotted as a function of simulation time (Figure B.3). Average R_g for the last 10 ns is 22.21±0.17 Å for 2s-4P-II system, while that in 2s-4P-I system was found to be 23.08±0.23 Å. The difference is

almost negligible (0.87 Å), and could be due to the location of PEI molecules, spanning only the region in between two siRNAs and facilitating polyion bridging of siRNAs by all PEIs.

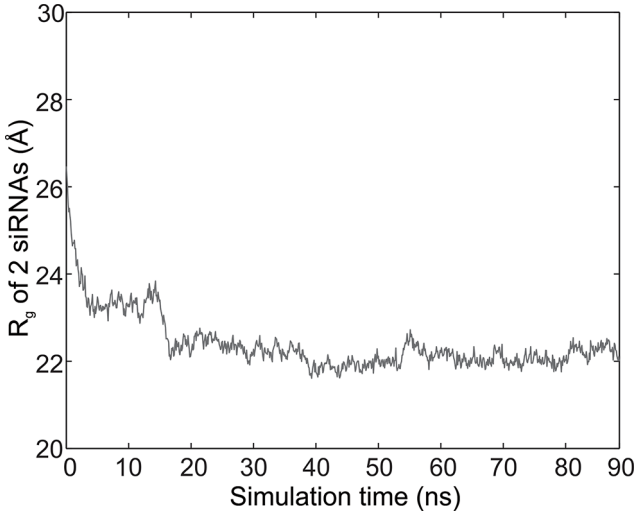

Figure B.3. R_g of two siRNAs in 2s-4P-II system as a function of simulation time.

This hypothesis can be proved by examining PEI binding dynamics to siRNA with the same procedure described in Section 4.3.1 of the Chapter 4. The four plots in each subfigure correspond to the four PEIs in the system, while two curves in each plot represent the two siRNA molecules. From Figure B.4, we have seen that all PEIs are bound to both of the siRNAs. Placing all the PEIs between the two siRNAs resulted in participation of all the PEIs in bridging of siRNAs, as opposed to the system 2s-4P-I (Figure 4.6a), showing only the contribution of PEI-1 and PEI-2 to polyion bridging.

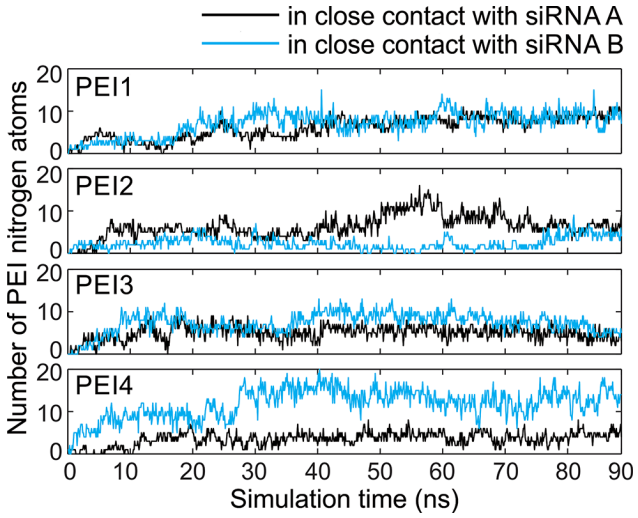

Figure B.4. Number of N atoms for each PEI within 4 Å of any siRNA N/O atoms as a function of simulation time. Four plots in each subfigure correspond to four PEIs and two curves in each plot correspond to two siRNAs.

To probe the effect of initial configuration on the electrostatic screening of siRNA charges, cumulative distributions of PEI N^+, K^+ and Cl^- atoms as well as their total net charge are plotted in Figure B.5 as a function of the distance from any siRNA C1′ atoms, averaged over the last 10 ns of the simulations. No apparent change is observed in the overall trend of individual curves, PEI N^+, K^+ and Cl^-, as well as in the behaviour of net charge, in comparison with 2s-4P-I system (Figure 4.7a). However, 100% neutralization of siRNA charges and the point of maximum over-neutralization occur at a shorter distance, 13.25 Å and 20.5 Å, respectively, in comparison with 15.99 Å and 24.25 Å, respectively, in system 2s-4P-I.

Despite the slight differences resulted from the different initial configuration of the 2s-4P system, such as participation of all PEIs into the bridging of siRNAs and screening of siRNA charges at a shorter distance; similarities were apparent between the two systems, i.e. close R_g values and similar trends of electrostatic screening. Therefore, we conclude that changing the

initial configuration of siRNA-PEI complex does not cause any significant changes in terms of structural properties of the final complexes.

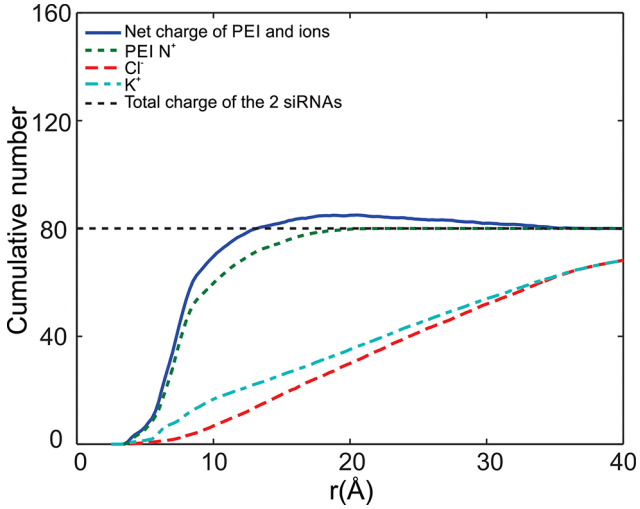

Figure B.5. Cumulative numbers of PEI N^+, K^+ and Cl^- atoms, and the total net charge of PEI and ions as a function of the distance from any siRNA C1′ atoms, averaged over the last 10 ns of the simulation. Total charge of -80 of the two siRNAs is plotted by black dashed line as a reference.

B.2.2. Effect of miRNA on siRNA-PEI Complex Integrity

Figure B.2b, right panel shows the snapshot of the final configuration for the 2s-4P-4m-II system. In comparison with 2s-4P-4m-I system (Figure 4.3c, right panel); a similar behavior is observed in miRNA A and miRNA B. However, a larger structural deformation is apparent in miRNA C, and almost no visual contacts is visible with miRNA D and the complex. Despite these differences in the behavior of individual miRNAs, the siRNAs in the complex remained intact and no apparent loosening of the complex is seen, as in system 2s-4P-4m-I.

As an indication of the compactness of siRNA arrangement in the complex upon miRNA introduction, R_g of the two siRNAs is plotted as a function of simulation time (Figure B.6). The average R_g of the two siRNAs for the last 20 ns is found to be 22.01 ± 0.17 Å, compared to that

of 22.21 ± 0.12 Å in 2s-4P-4m-I system. The difference between R_g values is negligible, indicating that regardless of the initial siRNA-PEI complex configuration, R_g of two siRNAs reach the same value upon miRNA introduction.

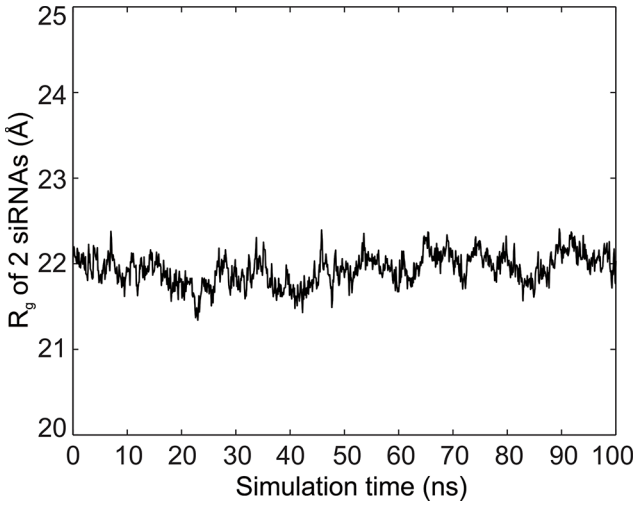

Figure B.6. R_g of two siRNAs in 2s-4P-4m-II system, as a function of simulation time.

Polyion bridging upon miRNA introduction was probed for system 2s-4P-4m-II (Figure B.7), with the same procedure described in Section 4.3.1 of Chapter 4. The four plots in each subfigure correspond to the four PEIs in the system, while six curves represent the six RNA molecules, two siRNA and four miRNA. Previously, in system 2s-4P-4m-I (Figure 4.11), PEI-1 and PEI-2 were found to simultaneously bridge three RNAs, two siRNA and one miRNA; and PEI-3 and PEI-4 were found to bridge two RNAs, one siRNA and one miRNA. It is clear from Figure B.7 that the overall pattern of polyion bridging is conserved despite the different initial configuration of the simulation system. However some differences are present between two systems in the number of close contact Ns, as well as the RNA molecules bridged (Table B.2).

Table B.2. Number of PEI Ns in close contact with RNAs, averaged over the last 20 ns of the simulations, in 2s-4P-4m-I and II systems.

	siRNA A		siRNA B		miRNA A		miRNA B		miRNA C		miRNA D	
2s-4P-4m-	I	II	I	II	I	II	I	II	I	II	I	II
PEI-1	9	4	10	7	2	-	-	7	-	-	-	-
PEI-2	10	4	8	2	-	-	4	9	-	-	-	1
PEI-3	9	5	-	10	short term	3	-	-	-	1	-	-
PEI-4	-	10	10	11	-	short term	short term	-	5	-	-	-

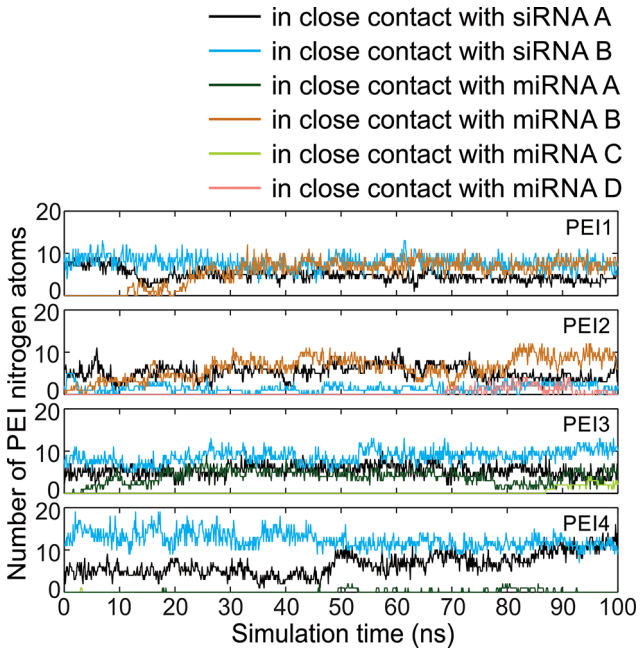

Figure B.7. Number of N atoms for each PEI within 4 Å of each siRNA and miRNA N/O atoms as a function of simulation time. Four plots in each subfigure correspond to four PEIs and six curves in each plot correspond to two siRNAs and four miRNAs in 2s-4P-4m-II system.

To examine the change in the screening of siRNA charges due to a different initial siRNA-PEI complex configuration, cumulative distributions of PEI N^+, K^+ and Cl^- and miRNA P^- atoms as well as their total net charge are plotted as a function of the distance from any siRNA C1′ atoms, averaged over the last 20 ns of the simulation (Figure B.8). No apparent change is

observed in the overall trend of individual curves, PEI N^+, miRNA P^-, K^+ and Cl^-, in comparison with 2s-4P-4m-I system (Figure 4.12). The only difference is in the total net charge; showing two maxima at 11.5 Å (charge: 79.63) and 22 Å (charge 80.01) (Figure B.8), instead of one as in 2s-4P-4m-I system (Figure 4.12). Like in system 2s-4P-4m-I, the decreasing trend of the total net charge is observed beyond 22 Å, indicating the formation of an overall negatively charged complex structure.

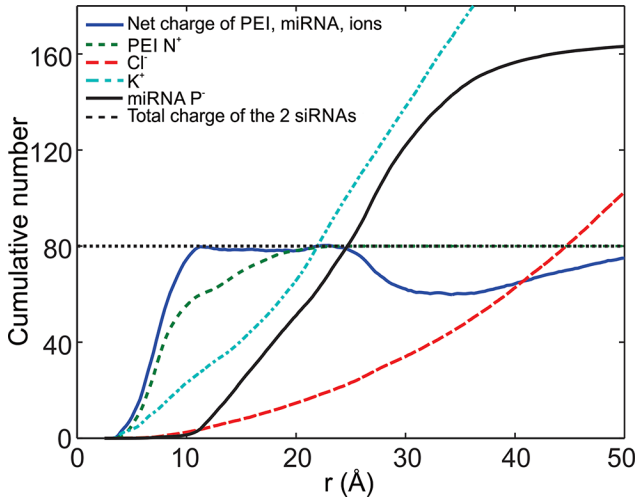

Figure B.8. Cumulative numbers of PEI N^+, K^+, Cl^- and miRNA P^- atoms, and the total net charge of PEI, miRNA and ions as a function of the distance from any siRNA C1′ atoms, averaged over the last 20 ns of 2s-4P-4m-II simulation. Total charge of -80 of the two siRNAs is plotted by a black dashed line as a reference.

In summary, analysis of the simulation trajectories revealed some differences in polyion bridging and electrostatic screening resulting from different initial configurations of 2s-4P system. However, the observed difference is insignificant, and the compactness of the two siRNAs in the complex is hardly affected. The effect of initial configuration on the integrity of complex is even smaller, and characteristics of polyion bridging and charge screening remains almost the same as the initial configuration varies. Therefore, we conclude that, for the purpose of this work, the initial configurations have negligible effect on the overall results.

B.3. ζ-Potential of the Complexes

The ζ-potential of siRNA-PEI and miRNA-PEI complexes in ddH_2O were measured at PEI:RNA weight ratios of 0.3 and 1. The results are given in Figure B.9, which clearly shows the formation of positively charged particles. Increasing the PEI:RNA weight ratio increases the ζ-potential, suggesting more PEI binding to the complexes.

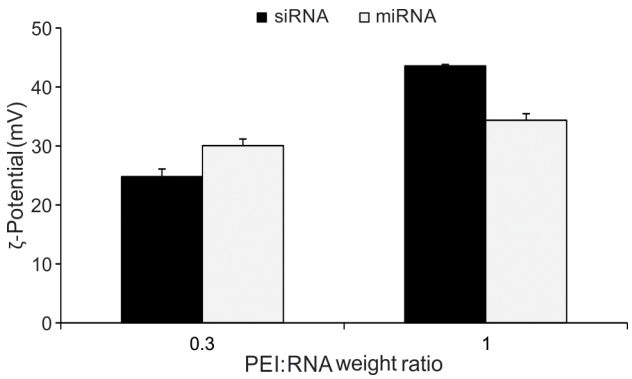

Figure B.9. ζ-potential of the siRNA-PEI and miRNA-PEI complexes prepared at PEI: RNA weight ratios of 0.3 and 1. Corresponding N:P ratios are 2.37 and 7.90, respectively.

B.4. References

1. Khvorova A, Reynolds A, & Jayasena SD (2003) Functional siRNAs and miRNAs exhibit strand bias. *Cell* 115(2):209-216.
2. Jorgensen WL (1981) Quantum and Statistical Mechanical Studies of Liquids .10. Transferable Intermolecular Potential Functions for Water, Alcohols, and Ethers - Application to Liquid Water. *J. Am. Chem. Soc.* 103(2):335-340.
3. Phillips JC, Braun R, Wang W, Gumbart J, Tajkhorshid E, Villa E, Chipot C, Skeel RD, Kale L, & Schulten K (2005) Scalable Molecular Dynamics with NAMD. *J. Comput. Chem.* 26(16):1781-1802.
4. Darden T, York D, & Pedersen L (1993) Particle Mesh Ewald: An N · log(N) Method for Ewald Sums in Large Systems. *J. Chem. Phys.* 98:10089-10092.
5. Ryckaert JP, Ciccotti G, & Berendsen HJC (1977) Numerical Integration of the Cartesian Equations of Motion of a System with Constraints: Molecular Dynamics of N-alkanes. *J. Comput. Phys.* 23(3):327-341.
6. Humphrey W, Dalke A, & Schulten K (1996) VMD: Visual Molecular Dynamics. *J. Mol. Graphics* 14(1):33-38.

7. Balasubramanian C, Ojha RP, Maiti S, & Desideri A (2010) Sampling the Structure of the Noncanonical lin-4:lin-14 microRNA:mRNA Complex by Molecular Dynamics Simulations. *J. Phys. Chem. B* 114(49):16443-16449.

APPENDIX C: Supplementary Information for Chapter 6

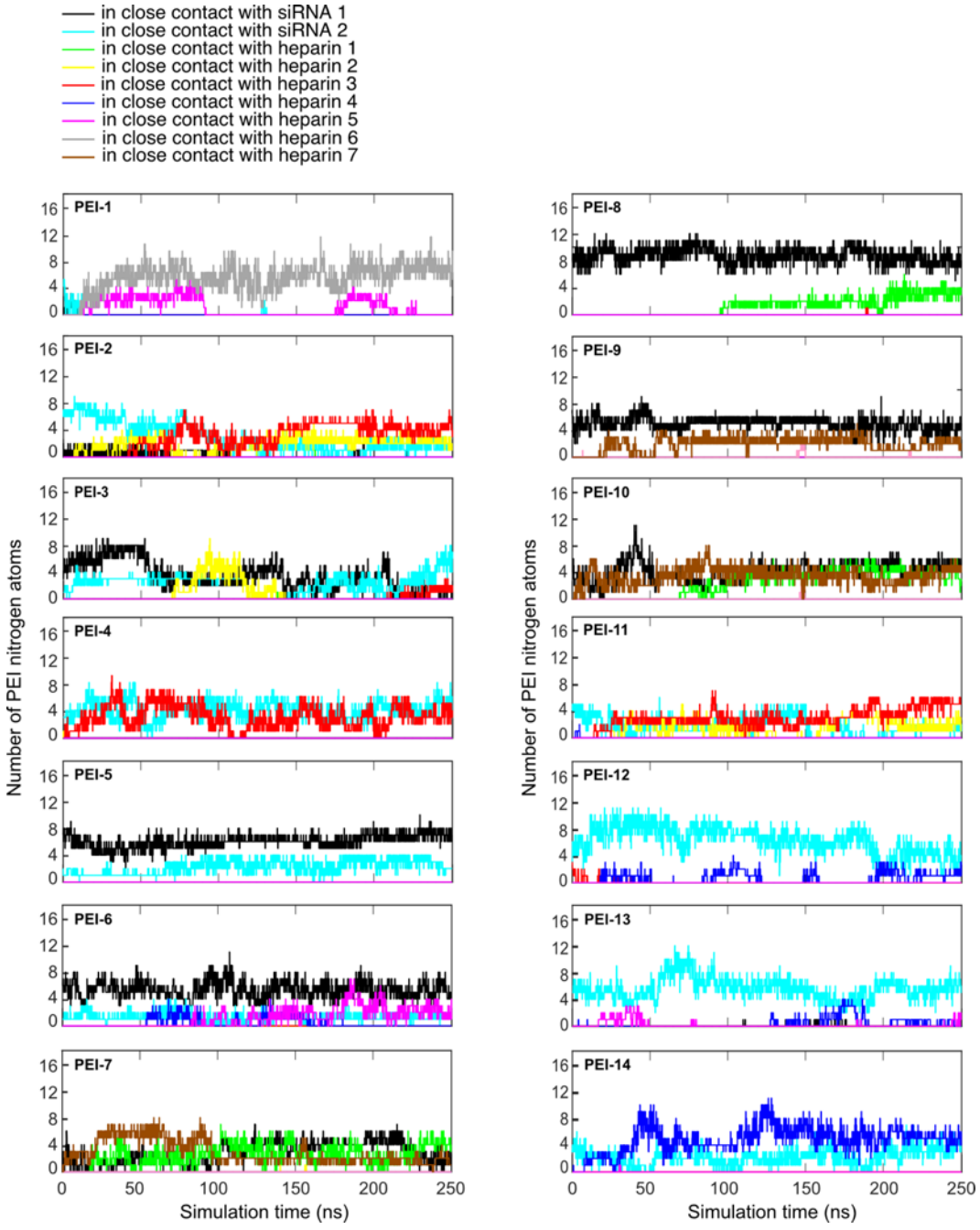

Figure C.1. Number of PEI N atoms within 4 Å of any siRNA and/or heparin N/O atoms as a function of simulation time in system C1-7sh. 14 plots represent the 14 PEI molecules, and the black and cyan curves in each plot correspond to the two siRNA molecules. Seven heparin molecules are presented with green, yellow, red, blue, purple, gray, and brown curves.

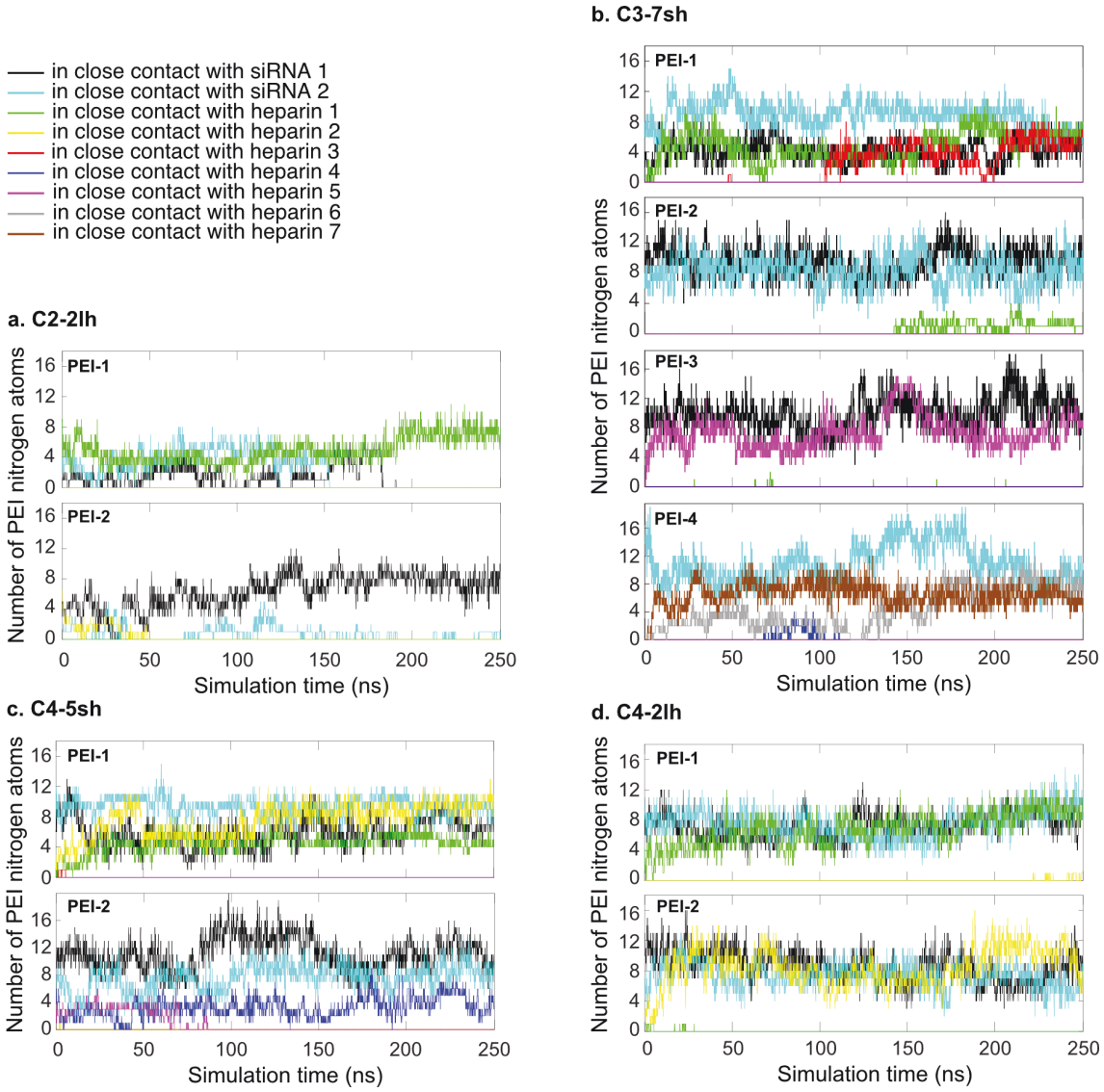

Figure C.2. Number of PEI N atoms within 4 Å of any siRNA and/or heparin N/O atoms as a function of simulation time in systems **(a)** C2-2lh, **(b)** C3-7sh, **(c)** C4-5sh, **(d)** C4-2lh. Two plots in each subfigure in **(a)**, **(c)**, **(d)** represent the two PEIs, and four plots in **(b)** represent the four PEI molecules. The black and cyan curves in each plot correspond to the two siRNA molecules. The two, five, and seven heparin molecules in systems C2-2lh, C4-2lh, C4-5sh, and C3-7sh, respectively, are presented with green, yellow, red, blue, purple, gray, and brown curves.

Table C.1. Number of PEI N and N^+ atoms within 4 Å of the individual charge groups of heparin's two building blocks, GlcNS(6S) and IdoA2S. The total number of N and N^+ atoms in each system are given in parentheses. The data presented is the average values over the last 50 ns of the simulations.

		GlcNS(6S)					IdoA2S				
Group #		1	2	3	4	5	1	2	3	4	5
C1-7sh	N (182)	12.38 ±1.80	19.56± 4.26	15.41 ±2.63	5.95 ±1.87	15.97 ±3.17	13.38 ±2.13	15.60 ±2.64	5.47 ±1.96	4.38 ±1.36	18.45 ±1.58
	N^+ (84)	8.93 ±1.41	9.67 ±2.10	10.97 ±1.70	3.50 ±1.36	9.90 ±2.23	8.65 ±1.47	10.55 ±1.76	2.35 ±1.34	2.84 ±0.96	16.51 ±1.37
C2-2sh	N (26)	0.86 ±0.37	0.12 ±0.32	0.02 ±0.13	0.02 ±0.14	2.80 ±0.79	0.24 ±0.46	3.38 ±0.74	0.97 ±0.79	1.18 ±0.83	1.76 ±0.74
	N^+ (12)	0.86 ±0.37	0.10 ±0.30	0.02 ±0.13	0.02 ±0.14	1.92 ±0.34	0.18 ±0.39	2.12 ±0.37	0.04 ±0.22	0.53 ±0.53	1.57 ±0.50
C2-5sh	N (26)	0	0	0	0	0	0	0	0	0	0
	N^+ (12)	0	0	0	0	0	0	0	0	0	0
C2-2lh	N (26)	1.97 ±0.87	3.29 ±0.95	4.55 ±1.05	0.92 ±0.48	1.77 ±0.94	3.94 ±1.04	2.58 ±0.61	0.62 ±0.75	0.87 ±0.56	4.48 ±0.61
	N^+ (12)	1.91 ±0.88	1.73 ±0.62	2.74 ±0.84	0.11 ±0.31	0.40 ±0.58	2.34 ±0.71	1.58 ±0.50	0.25 ±0.44	0.06 ±0.24	3.90 ±0.30
C3-7sh	N (172)	5.72 ±1.18	12.05 ±2.30	9.47 ±1.71	3.55 ±1.42	9.92 ±2.27	8.09 ±1.51	12.50 ±2.17	4.91 ±1.51	2.76 ±1.53	13.07 ±1.22
	N^+ (80)	5.51 ±1.11	6.90 ±1.58	7.21 ±1.35	2.78 ±1.25	6.25 ±1.73	6.59 ±1.29	9.32 ±1.58	3.43 ±1.26	2.36 ±1.29	12.41± 1.00
C4-5sh	N (86)	9.24 ±1.30	8.01 ±2.05	5.00 ±1.64	3.03 ±1.04	6.16 ±1.63	4.25 ±0.83	6.60 ±1.33	3.26 ±1.04	1.01 ±0.91	8.40 ±1.06
	N^+ (40)	7.05 ±1.14	4.70 ±1.35	4.57 ±1.23	1.60 ±0.89	5.02 ±1.31	4.14 ±0.78	4.76 ±1.08	2.27 ±0.91	0.95 ±0.88	7.78 ±0.73
C4-2lh	N (86)	6.47 ±1.22	5.82 ±1.64	4.30 ±1.35	3.17 ±1.36	9.48 ±2.12	5.35 ±1.49	4.82 ±1.50	2.44 ±1.06	1.82 ±0.91	7.53 ±1.18
	N^+ (40)	4.36 ±1.08	2.63 ±1.24	3.94 ±1.19	1.76 ±1.06	4.87 ±1.36	3.81 ±1.07	3.42 ±1.22	0.86 ±0.98	1.00 ±0.80	7.42 ±1.10

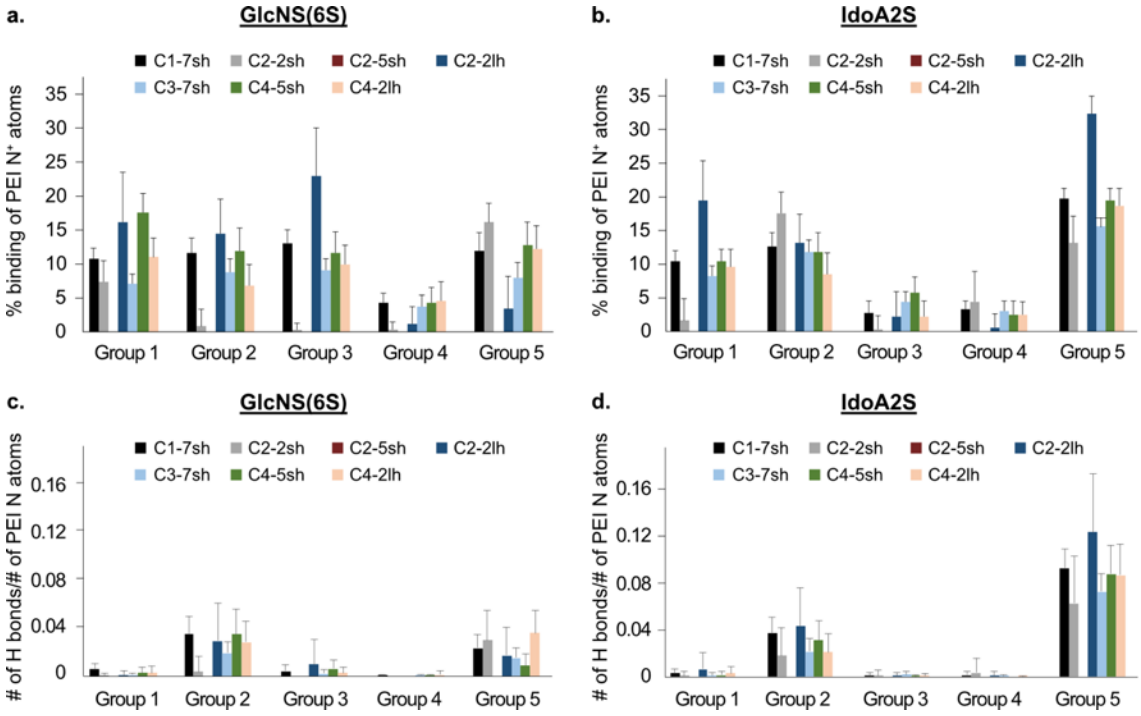

Figure C.3. Percent binding of all PEI N^+ atoms to individual charge groups of heparin's building blocks **(a)** GlcNS(6S), and **(b)** IdoA2S. The number of hydrogen bonds established between the PEI N atoms and the individual charge groups of heparin's building blocks (c) GlcNS(6S), and (d) IdoA2S. The presented data is normalized by the total number of PEI N atoms in each system. The donor-acceptor distance and angle cut-off were set to 4 Å and 20˚, respectively. All the presented data in **(a)**, **(b)**, **(c)**, **(d)** are average values over the last 50 ns of the simulations.

APPENDIX D: Supplementary Information for Chapter 7

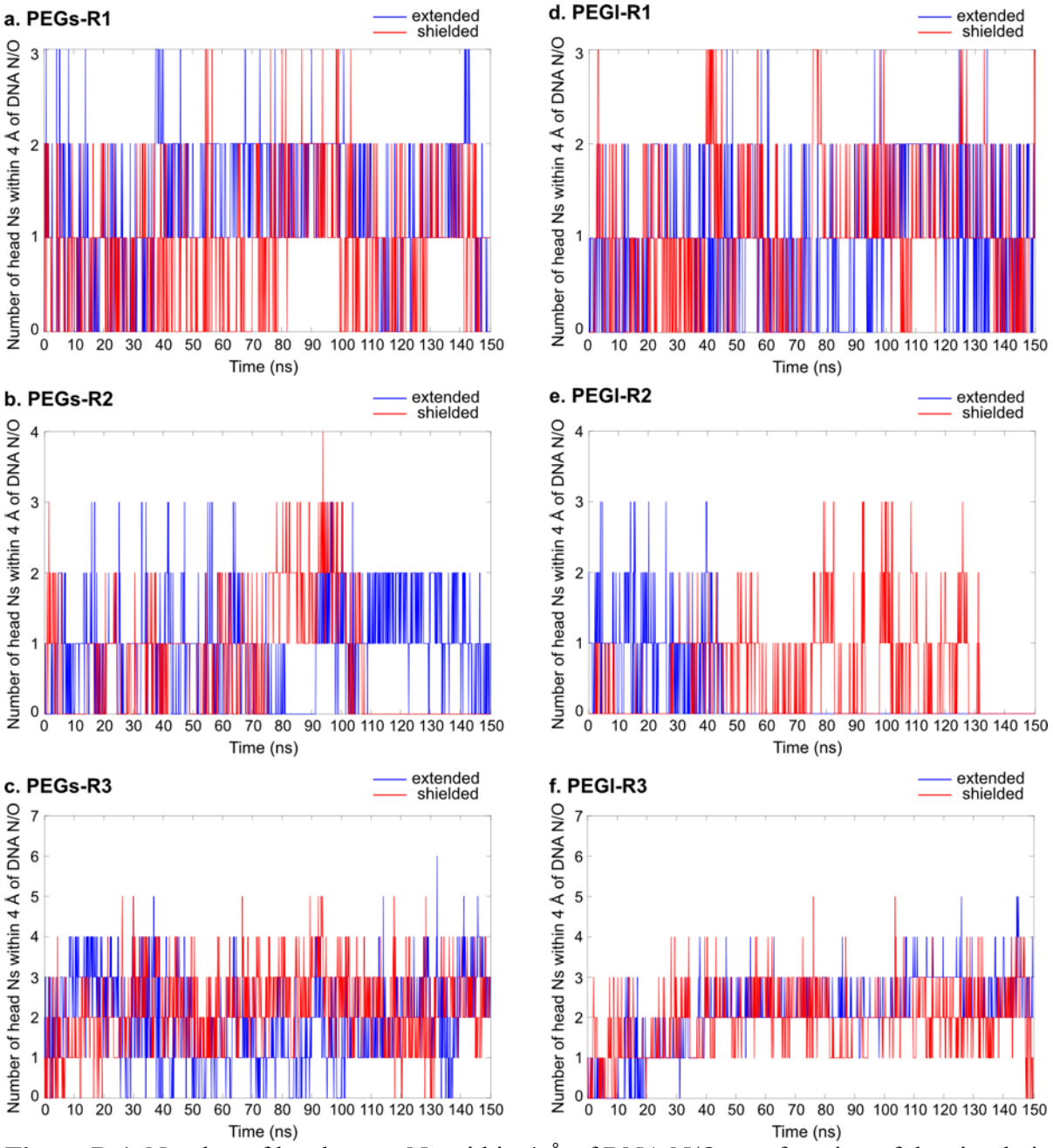

Figure D.1. Number of head group Ns within 4 Å of DNA N/O as a function of the simulation time in systems comprising DNA and **(a)** PEGs-R1, **(b)** PEGs-R2, **(c)** PEGs-R3, **(d)** PEGl-R1, **(e)** PEGl-R2, **(f)** PEGl-R3. There are two curves in each system corresponding to the two polymer initial configurations where the polymer head is in extended (blue) and shielded (red) conformation. The range of the y-scale is adjusted based on the number of Ns the head group contains in a particular system; it is set to 3 for systems with R1 in **(a)** and **(d)**, 4 for R2 in **(b)** and **(e)**, and 7 for R3 in **(c)** and **(f)**.

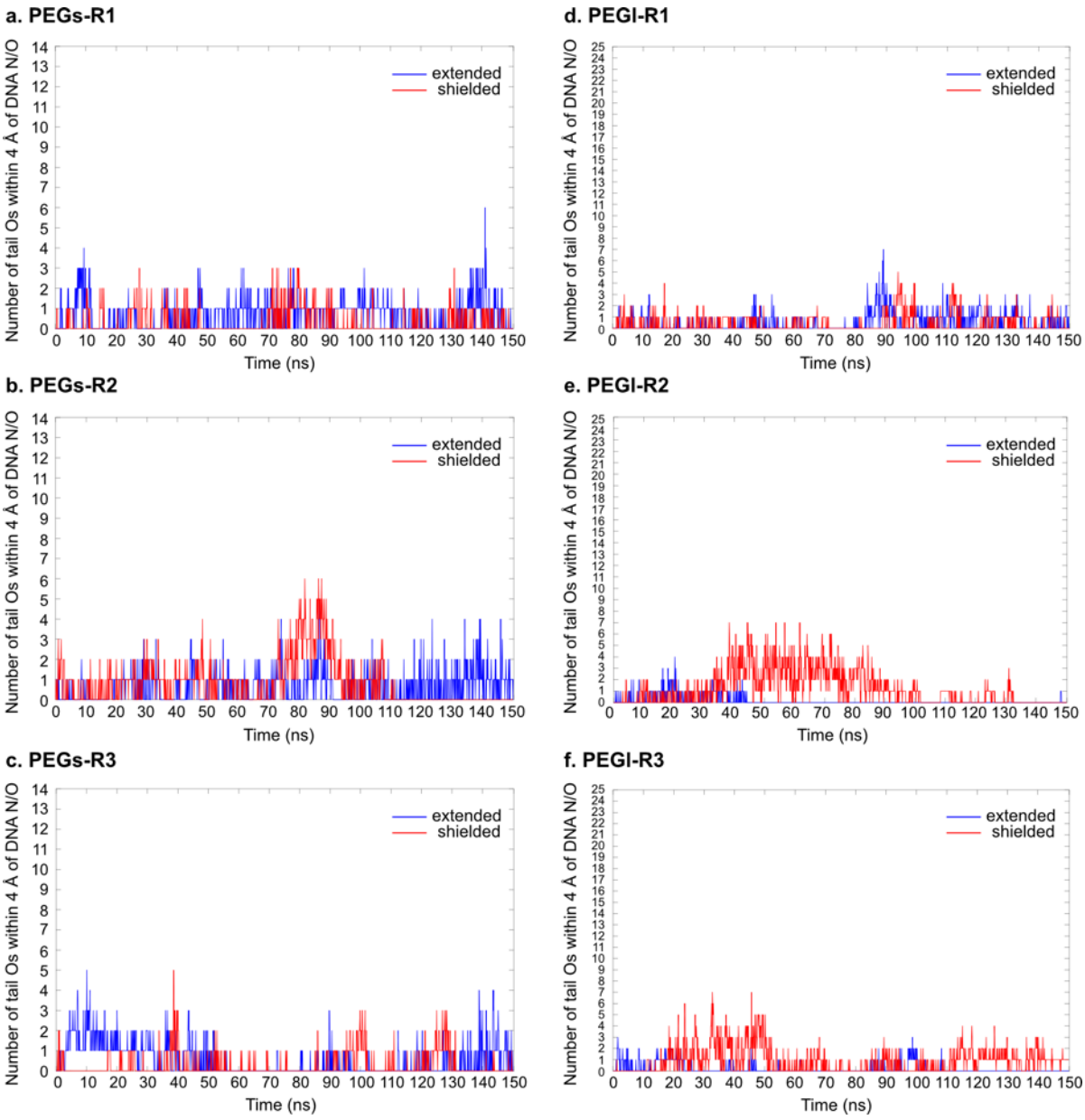

Figure D.2. Number of tail group Os within 4 Å of DNA N/O as a function of the simulation time in systems comprising DNA and **(a)** PEGs-R1, **(b)** PEGs-R2, **(c)** PEGs-R3, **(d)** PEGl-R1, **(e)** PEGl-R2, **(f)** PEGl-R3. There are two curves in each system corresponding to the two polymer initial configurations where the polymer head is in extended (blue) and shielded (red) conformation. The range of the y-scale is adjusted based on the number of Os the tail group contains in a particular system; it is set to 14 for systems with the short tail in **(a)** – **(c)**, 25 for systems with long tail in **(d)** – **(f)**.

Table D.1. Average number of N atoms of the polymer head group in close contact with DNA electronegative atoms (N/O) over the final 50 ns of the simulations.

	Backbone				Base	Whole DNA
Systems	***O1P and O2P***	***O3′ and O5′***	***O4′***	***All O***	***N/O***	***N/O***
PEGs-R1e–DNA	0.88	0.06	0	0.89	0.21	1.07
PEGs-R1s–DNA	0.76	0.06	0	0.77	0.03	0.80
PEGs-R2e–DNA	0.56	0.46	0.15	0.74	0.59	1.23
PEGs-R2s–DNA	0.14	0.02	0	0.14	0.02	0.16
PEGs-R3e–DNA	2.03	0.13	0	2.04	0.11	2.12
PEGs-R3s–DNA	2.01	0.21	0	2.03	0.16	2.19
PEGl-R1e–DNA	0.90	0.10	0	0.91	0.29	1.20
PEGl-R1s–DNA	1.03	0.08	0	1.04	0	1.04
PEGl-R2e–DNA	0	0	0	0	0	0
PEGl-R2s–DNA	0.43	0.05	0	0.44	0.002	0.44
PEGl-R3e–DNA	2.48	0.17	0.35	2.61	0.04	2.62
PEGl-R3s–DNA	2.05	0.14	0	2.09	0.002	2.09